POLITECNICO
MILANO 1863

SCUOLA DI INGEGNERIA INDUSTRIALE
E DELL'INFORMAZIONE

EXECUTIVE SUMMARY OF THE THESIS

Characterization of an austenitic lightweight steel under different thermo-mechanical and welding conditions

TESI MAGISTRALE IN MECHANICAL ENGINEERING – INGEGNERIA MECCANICA

AUTHOR: FRANCESCO PASQUALOTTO

ADVISOR: CARLO MAPELLI

ACADEMIC YEAR: 2022-2023

1. Introduction

In recent years, there has been significant interest in lightweight steels for their application in the automotive field. Their low density, combined with excellent mechanical properties, allows for reducing the weight of vehicles and increasing fuel efficiency compared to the materials currently used in this field (AHSS, HSS, and UHSS steels). [1] Lightweight steels can be divided into three categories based on the matrix phase: ferritic, austenitic, and duplex. Typically, the chemical composition of the alloy is considered to distinguish one class from another, as it significantly influences the matrix phase of the material. Specifically, austenitic steels are characterized by a higher concentration of Mn and C, which are austenite stabilizers, while ferritic steels have a higher concentration of Al, which acts a ferrite stabilizer. [1], [2] The density reduction, on the other hand, is promoted by the presence of all three elements, although C and Al have a greater impact. Among the three described classes, austenitic lightweight steels are typically preferred due to their excellent ductility combined with outstanding mechanical properties. Although the concept of lightweight steels may seem simple, the underlying metallurgical issues are complicated. In particular, in Fe-Mn-Al-C austenitic steels, it is easy to obtain precipitation of particularly fragile second phases, such as κ-carbides, β-Mn, or α-ferrite, which have a negative influence on the material's ductility. [1], [2] Among these, κ-carbides are the most common and can precipitate in two different modes: [3] as small precipitates coherent with the matrix or as larger incoherent precipitates along the boundaries of austenitic grains. Of the two cases, the latter is more dangerous as it significantly impairs the steel's ductility. Furthermore, depending on the alloy's chemical composition, austenitic lightweight steels exhibit different values of SFE (Stacking Fault Energy). This parameter is crucial as it defines the various deformation mechanisms the alloy can exhibit, including TRIP (for SFE <12 mJ/m²), TWIP (18 mJ/m² < SFE < 35 mJ/m²), SIP, and MBIP (SFE > 80 mJ/m²) [4]. It is therefore necessary to try to understand what chemical composition, deformation mechanisms and precipitate conditions are optimal to maximize the mechanical properties and ductility of the alloy. For this reason, in the present study, the microstructure

and mechanical properties of a lightweight Fe-15Mn-8Al-1C-40ppmB austenitic steel under different thermo-mechanical (hot-rolled, cold-rolled and solution treated) and welding (cladding and double-V butt welding) conditions have been investigated.

2. Experimental procedure

The material used for this analysis is a Fe-15Mn-8Al-1C-40ppmB lightweight austenitic steel produced by OCAS NV as hot-rolled sheets with a thickness of 5 mm. The actual chemical composition of the alloy was determined using the OES (Optical Emission Spectroscopy) method, and its density was measured using three different methods: hydrostatic balance, mass/volume ratio, and an equation from literature [5]. The phase diagram for the alloy was obtained using ©*Thermocalc* and is shown in Figure 1. Additionally, the microstructural characterization of the material was performed under various thermo-mechanical and welding conditions, as listed in Table 1.

$$\rho_\gamma = 8.10 - 0.101(wt.\%Al) - 0.41(wt\%C) - 0.0085(wt.\%Mn) \quad (1)$$

	Base condition	Solution treatment
Hot-rolled	5 mm	900, 950°C
Cold-rolled	2 mm	-
	1 mm	900, 925, 950, 1000, 1050°C (30 min)
		900, 925°C (15, 20, 25 min)
Welded	Cladding	-
	Double-V butt welding	-

Table 1: thermo-mechanical and welding condition analyzed

The conducted analyses included microstructural analysis using optical microscopy, SEM, EDS, EBSD and XRD. Mechanical characterization involved micro-HV tests, anisotropy tests, and bending tests on the 5 mm hot-rolled material, as well as tensile tests on the welded material. The specific parameters for each test are provided in the results section.

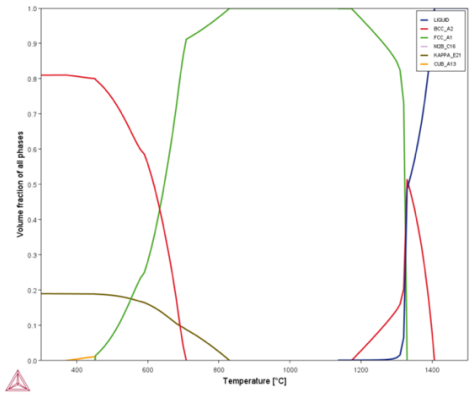

Figure 1: equilibrium phase diagram for the measured composition. (green line for austenite, red for ferrite and blue for liquid)

3. Results and discussion

3.1 Alloy design

OES analysis was used to determine the actual chemical composition of the received material in the form of hot-rolled sheets. The measured chemical composition is 15.5Mn-7.5Al-0.9C-44ppmB. There are no significant discrepancies compared to the nominal chemical composition of 15Mn-8Al-1C-40ppmB. The equilibrium phase diagram for the measured composition is shown in Figure 1. From the figure, it can be observed that in the temperature range of approximately 800°C to 1100°C, the material appears to be fully austenitic. Therefore, this temperature range seems to be the most interesting to investigate for this material.
The density obtained using each of the three methods is presented in the Table 2. It can be observed that the density of this 15Mn-8Al-1C-40ppmB lightweight steel falls within the range of 6.9 to 7.0 g/cm^3. The density reduction compared to conventionally used alloys in the automotive sector (conventional HSS: 7.8 g/cm^3; AISI 304: 7.93 g/cm^3) is therefore greater than 10%.

Measured density	Mass/volume ratio	Theoretical density
6.96 g/cm³	6.97 g/cm³	6.79 g/cm³

Table 2: comparison between the densities obtained with the different methods

3.2 Anisotropy

Anisotropy tests were conducted on samples with different relative orientations to the rolling direction: 0°, 45°, and 90°. Regarding the test

parameters, the maximum elongation was set to 10% and the deformation velocity to 3 mm/min. From the performed tests, data regarding the normal anisotropy ratio (r_m) and the planar anisotropy parameter (Δr) were collected and are reported in Table 3. It can be observed that r_m has a mean value very close to 1, indicating that the material exhibits almost complete anisotropic behavior. Furthermore, Δr is close to zero, indicating a non-earing behavior of the alloy.

r_m	Δr
1.002 ± 0.075	0.170 ± 0.111

Table 3: values for r_m and Δr calculated after the anisotropy tests

3.3 Bending tests

For the bending tests, samples with a width of 30 mm and two different thicknesses (3 mm and 5 mm) were examined, with orientations relative to the rolling direction of 0° and 90°. The tests were conducted with a distance of 70 mm between the roller supports (with a diameter of 20 mm) and a deformation velocity of 25 mm/min. The maximum bending angle used was around 75°, dictated by the machine configuration. For each condition, stress-strain bending curves were obtained, as shown in Figure 2. As can be observed, the curves are characterized by an initial linear region, followed by a change in slope until reaching the maximum stress. After the peak, there is a decrease in stress until the end of the test.

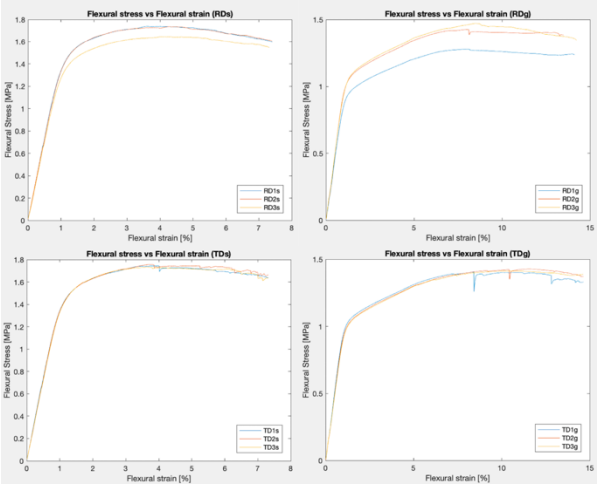

Figure 2: flexural Stress [MPa] vs Flexural Strain [%] curves obtained after the tests curves obtained after the tests for the 3 mm samples oriented along the rolling direction (RDs) and transversally (TDs); b) 5 mm samples oriented along the rolling direction (RDg) and transversally (TDg)

Furthermore, by measuring the bending angle before (α_i) and after (α_f) the release of the load, it was possible to calculate the elastic return factor $K_s=\alpha_f/\alpha_i$ for each condition. The results are shown in Table 4. As can be observed, the elastic return factor is higher for the thinner samples. The measured elastic return angles were around 9° for the thin samples and 17° for the thicker samples. Additionally, as prescribed by the standard, the samples were subjected to visual inspection after the test to check for the presence of cracks initiated by the test. However, no cracks were found in any of the samples.

Sample type	Springback Factor (K_s)
5 mm – 90°	0.782
5 mm – 0°	0.765
3 mm – 90°	0.876
3 mm – 0°	0.891

Table 4: mean K_s and for the different specimens analized

3.4 Microstructural evolution

Hot rolling → solution treatment

The microstructure of the samples obtained from the hot-rolled material (HR) and solution-treated at 900°C and 950°C (SHT900 and SHT950) is shown in Figure 3. As observed, in the untreated condition, the matrix appears to be fully austenitic, while in the other two cases, the precipitation of a very fine second phase can be seen. Specifically, in the case of the SHT950 sample, this second phase is concentrated at the edges of the sample. This hypothesis was confirmed using XRD, which showed the presence of characteristic austenite peaks in all cases, while only the two solution-treated cases exhibited a peak at 44° corresponding to ferrite. Additionally, in all conditions, a significant presence of twins resulting from the rolling process can be observed. The SEM-EDS analysis (shown in Figure 4) also revealed the presence of segregations in the material, as zones with different Mn and Fe contents were found. In particular, ferrite appears to precipitate in regions rich in Fe and poor in Mn.

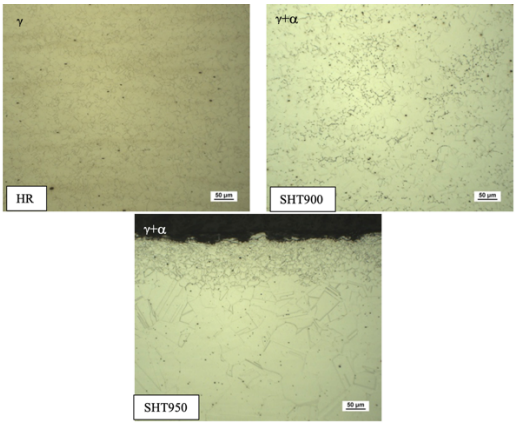

Figure 3: microstructure of the hot-rolled (HR), solutioned at 900°C (SHT900) and at 950°C (SHT950) samples at the optical microscope (200x)

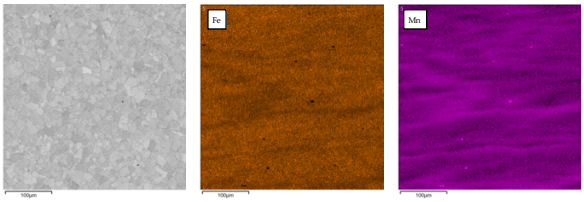

Figure 4: EDS compositional maps for the HR specimen

Hot rolling → cold rolling

The starting material, with a thickness of 5 mm, was cold-rolled to thicknesses of 2 mm (CR) and 1 mm (CRE) (corresponding to 60% and 80% thickness reduction, respectively). The observed microstructure is shown in Figure 5. After cold rolling, the grains exhibit a much smaller size compared to the initial condition, and in particular, a slight precipitation of ferrite can be observed at grain boundaries (more pronounced in the CRE sample). SEM investigations, as shown in Figure 5, highlighted the presence of a significant amount of twins and micro-bands crossing the grains.

This observation is particularly important as it suggests the activation of the two main deformation mechanisms in this material: TWIP (Twinning Induced Plasticity) and MBIP (Micro-bands Induced Plasticity). Furthermore, supporting these observations, the micro-hardness obtained in these samples is significantly higher than that of the HR material: 443 HV for CR and 510 HV for CRE, compared to ~270 HV for HR.

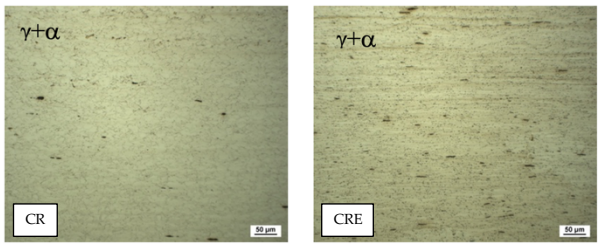

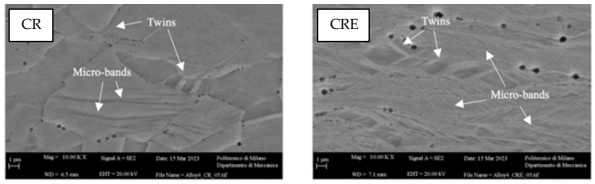

Figure 5: first raw: microstructure of the cold-rolled 2 mm (CR) and 1 mm (CRE) samples at the optical microscope; second raw: Details of the CR and CRE samples at the SEM

Cold rolling → solution treatment

The material, which was cold-rolled up to 1 mm thick, underwent solution treatments at various temperatures (900, 925, 950, 1000, 1050 °C) for 30 minutes followed by water quenching. The microstructural changes resulting from the temperature variations during the treatment are depicted in Figure 6. It can be observed that ferrite is initially present in the form of thin bands at the edges of the sample at 900°C and 925°C. Subsequently, it becomes more dispersed along the grain boundaries at 950°C and 1000°C. However, at 1050°C, the ferrite appears coarser and more concentrated in the inner part of the grain boundaries. This indicates that the solution treatment temperature significantly affects the distribution and morphology of the ferrite phase within the microstructure of the material.

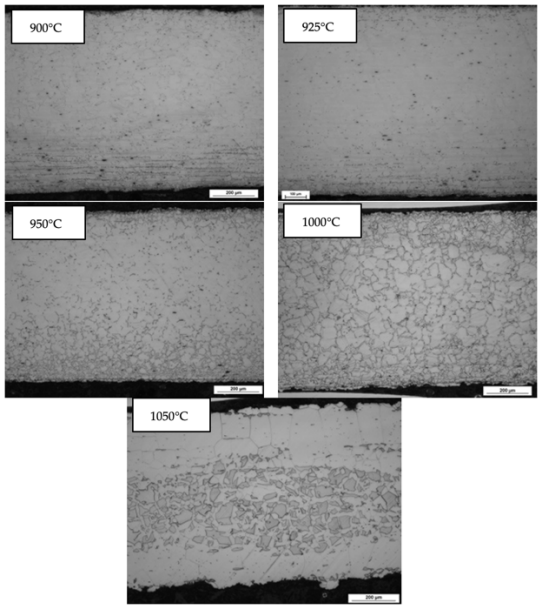

Figure 6: Microstructure of the cold-rolled and solutioned samples at the optical microscope (100x)

The microstructural analysis was performed on the 1 mm thick cold-rolled material using also solution treatments at different times. Specifically, at 900 and 925°C, the material was treated for 15, 20, and 25 minutes. The microstructural evolution is

depicted in Figure 7 and 8. It can be observed that ferrite is present in all the analyzed cases. However, the fraction of ferrite does not seem to increase linearly with the treatment time and exhibits a different trend for the two temperatures, as shown in the graph in Fig.8.

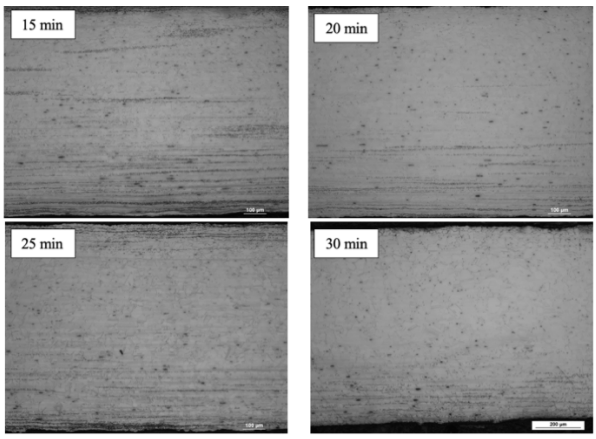

Figure 7: microstructure of the cold-rolled and solutioned samples at 900°C the optical microscope (100x)

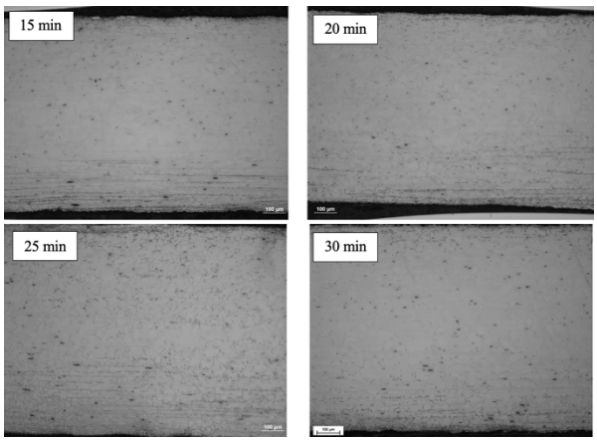

Figure 8: microstructure of the cold-rolled and solutioned samples at 925°C the optical microscope (100x)

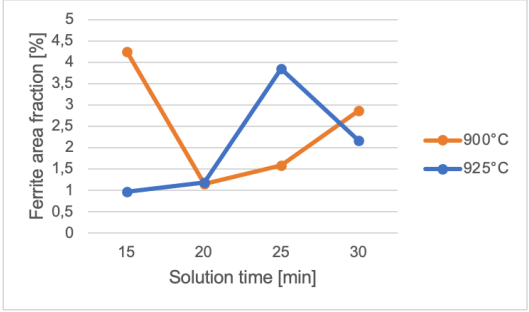

Figure 9: variation of the ferritic area fraction [%] at different sulibulization temperatures and times. The measurements were taken considering the ASTM E112-13 and the ASTM E1181-02 standards

3.6 Welding

Cladding

The cladding welds analyzed in this study were obtained using both direct current (DC), with current set at 100 A and potential at ~13 V, and alternating current (AC), with 110 A and ~16 V. For each condition, four cross sections were analyzed along the weld bead. The microstructure obtained in each of the two conditions is shown in Figure 9. From the figure, a fine dendritic microstructure can be observed in the Weld Zone (WZ), with enlarged and austenitic grains in the Heat-Affected Zone (HAZ). SEM-EDS analysis was used to determine the chemical composition of the dendrites and the WZ matrix, as shown in Figure 11. The figure reveals that the dendrite area has a much lower concentration of Mn but higher levels of Fe and Al. Therefore, it can be concluded that the dendrites are composed of ferrite, while the matrix is austenitic. Additionally, SEM-EDS analysis in the Base Metal (BM) area adjacent to the HAZ revealed the presence of some nanoscale second phases at the grain boundaries of the austenite (Figure 12). Compositional analysis conducted on these precipitates suggested that they could be κ-carbides. These phases could potentially precipitate as a result of the heating provided by the welding process in this area and may have a detrimental effect on the material's ductility. Microhardness tests performed on different welding regions indicated a trend in both conditions (DC and AC), as shown in Figure 13: the HAZ exhibited lower hardness (between 240 and 250 HV), while the base material near the HAZ showed hardness peaks, possibly attributed to the precipitation of κ-carbides in this area.

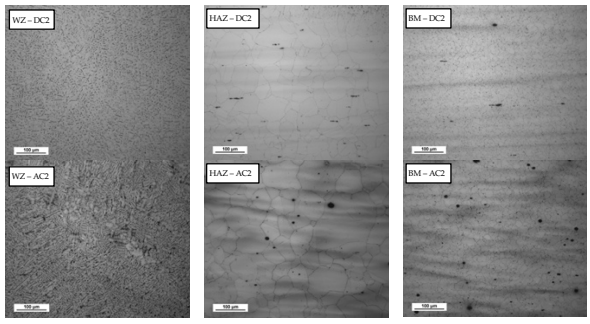

Figure 10: micrographs of one of the direct current (DC) and alternate current (AC) specimens inside the FZ, HAZ and BM at 200x

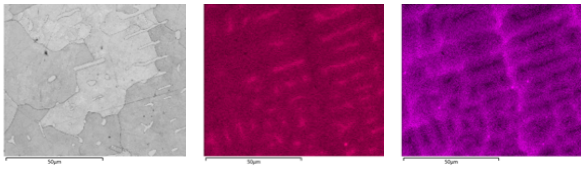

Figure 11: EDS compositional maps inside the WZ

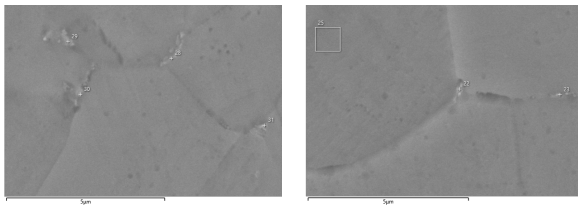

Figure 12: grain boundary precipitation of secondary phases in the zone of the BM adjacent to the HAZ

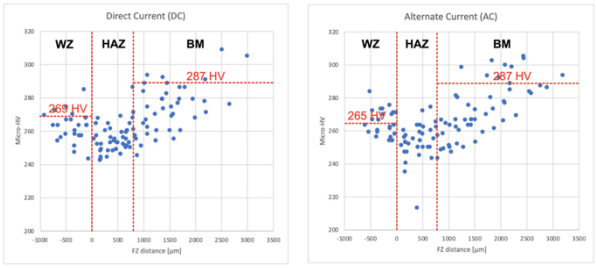

Figure 13: hardness [HV] plot of the AC and DC samples as a function of the distance from the reference FZ, obtained with a load of 300 mg and a twell time of 10 seconds

Furthermore, it is important to highlight that during the welding process, the operator noticed a higher effectiveness of the alternating current compared to direct current. To further investigate this aspect, the surface oxide development exhibited by the material after heating was analyzed. Specifically, SEM-EDS analysis revealed the presence of two distinct oxide layers on the material's surface: an inner layer of alumina and an outer layer of iron and manganese oxide. This justifies the higher effectiveness of the AC process, which has better capabilities in breaking down the oxide formed on the surface of the workpiece. [6]

Double-V Butt welds

The double-V butt welds analyzed were produced using both DC, with a current set at approximately 86 A and potential ~12 V, and AC, with ~110 A and ~15 V. In each case, four passes were performed. From each of the two welded plates, three samples were obtained for the tensile test (keeping the weld in the center of the gauge length), and four cross-sections were prepared for microstructural analysis. The microstructural analysis confirmed what was observed in the cladding case, namely the presence of a fine dendritic microstructure in the weld zone (WZ) and enlarged austenitic grains in the heat-affected zone (HAZ), with no substantial differences between DC and AC. The microhardness tests, shown in Figure 14, also revealed the previously described trend.

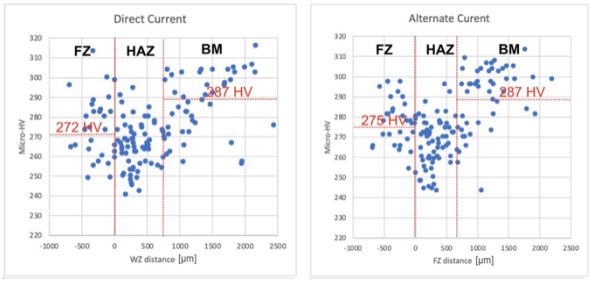

Figure 14: hardness [HV] plot of the AC and DC samples as a function of the distance from the FZ, obtained with a load of 300 mg and a twell time of 10 seconds

Regarding the tensile tests, conducted at a crosshead speed of 3 mm/min, significant differences were observed. As described earlier, AC welding exhibited higher effectiveness for this alloy, resulting in a lower occurrence of defects such as porosity and oxide inclusions. As a result, as shown in the stress vs. strain graphs in Figure 15, the AC samples demonstrated much higher elongation at fracture and ultimate tensile strength (UTS) compared to the DC samples (40-45% vs. 10-15% and 950 MPa vs. 800 MPa), with two DC samples failing precisely at the weld point. Furthermore, SEM analysis performed on the fracture surfaces revealed the presence of porosity and oxide inclusions on the failed DC samples' weld surfaces (Figure 16).

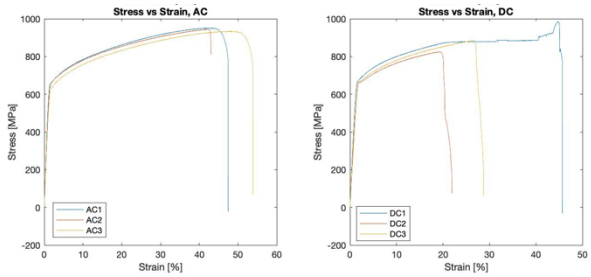

Figure 15: Stress [MPa] vs Strain [%] curves obtained for the AC and DC specimens

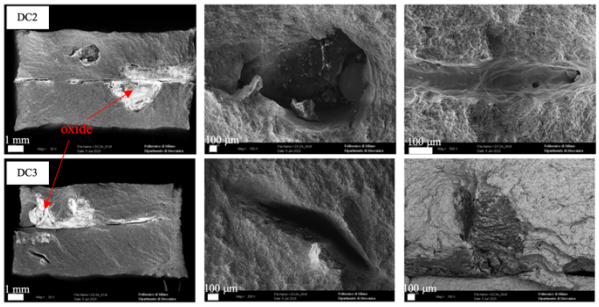

Figure 16: fracture surfaces of the two DC butt weld specimens failed in the WZ observed at the SEM

4. Conclusions

In this study, the lightweight steel Fe-15Mn-8Al-1C-40ppmB was characterized under various thermos-mechanical and welding conditions. The analysis revealed several key findings:

- the chemical composition of the alloy enables to reach a reduction in density of approximately 10% compared to the main alloys used in the automotive industry for structural components;
- the main deformation mechanisms acting on this alloy are the MBIP and the TWIP;
- the hot-rolled material exhibited a complete anisotropic behavior (r_m ~1);
- through the bending test it was possible to bend the material up to an angle of 75° without initiating any cracks on the material's surface. Furthermore, the springback factor obtained from the bending tests was 0.77 for the 5 mm specimens and 0.88 for the 3 mm specimens;
- the only rolling condition that did not show ferrite precipitation is the untreated hot-rolled state. All heat treatments performed on the hot-rolled samples resulted in ferrite precipitation, with varying forms and sizes depending on the treatment time and temperature;
- AC has been demonstrated to be more effective than DC for welding the Fe-15Mn-8Al-1C-40ppmB steel. Alternate current has shown the capability to break down the oxide layer present on the material's surface, which could potentially consist of a combination of alumina and iron manganese oxide;
- SEM analysis has demonstrated that the dendrites in the weld zone primarily consist of ferrite. Furthermore, in the region of the base material adjacent to the HAZ, nanoscale κ-carbides have been observed.

5. Bibliography

[1] S. Chen, R. Rana, A. Haldar, and R. K. Ray, "Current state of Fe-Mn-Al-C low density steels," *Progress in Materials Science*, vol. 89. Elsevier Ltd, pp. 345–391, Aug. 01, 2017. doi: 10.1016/j.pmatsci.2017.05.002.

[2] O. A. Zambrano, "A General Perspective of Fe-Mn-Al-C Steels."

[3] G. Zhang *et al.*, "Investigation on the microstructural evolution and mechanical properties of partially recrystallized Fe-27Mn-10Al-1.4C steel," *Materials Science and Engineering A*, vol. 833, Jan. 2022, doi: 10.1016/j.msea.2021.142545.

[4] H. Kim, D. W. Suh, and N. J. Kim, "Fe-Al-Mn-C lightweight structural alloys: A review on the microstructures and mechanical properties," *Science and Technology of Advanced Materials*, vol. 14, no. 1. Feb. 2013. doi: 10.1088/1468-6996/14/1/014205.

[5] J. Xing, Y. Wei, and L. Hou, "An Overview of the Effects of Alloying Elements on the Properties of Lightweight Fe-(15–35) Mn-(5–12) Al-(0.3–1.2) C Steel," *JOM*, vol. 70, no. 6. Minerals, Metals and Materials Society, pp. 929–937, Jun. 01, 2018. doi: 10.1007/s11837-018-2837-9.

[6] F. Miyasaka, T. Okuda, and T. Ohji, "Effect of current wave form on AC TIG welding for aluminum alloys," *Yosetsu Gakkai Ronbunshu/Quarterly Journal of the Japan Welding Society*, vol. 22, no. 3, pp. 364–368, 2004, doi: 10.2207/qjjws.22.364.

POLITECNICO
MILANO 1863

SCHOOL OF INDUSTRIAL AND INFORMATION ENGINEERING

Master of Science in Mechanical Engineering

Characterization of an austenitic lightweight steel under different thermo-mechanical and welding conditions

Advisor: prof. Carlo MAPELLI
Co-advisor: Giacomo VILLA

Francesco PASQUALOTTO
ID Code:10867876

Academic Year 2022/2023

Abstract

In recent years, there has been great interest in lightweight Fe-Mn-Al-C steels, especially for their applications as structural components in the automotive industry. The most important aspect of this type of steels is their lower density compared to the alloys typically used in this field (AHSS, HSS, UHSS) together with their excellent combination of ductility and mechanical properties. However, their production is very complex due to various metallurgical complications, such as the frequent precipitation of secondary phases that can affect the properties of the final material.

In this project, the microstructure and mechanical properties of an Fe-15Mn-8Al-1C-40ppmB alloy were analyzed under different thermomechanical and welding conditions. Specifically, the focus was placed on investigating the precipitation of secondary phases and grain evolution during hot and cold rolling, as well as solution treatment (with different time and temperature treatments). Regarding welding, the study focused on cladding techniques and double-V butt welds, tested using both direct and alternate current. In this context, particular attention was given to the microstructural evolution of the welded region affected by the welding operation. Additionally, tensile tests were performed on specimens with a double-V butt weld positioned at their center. Analytical methods used included optical microscopy, X-ray diffraction, scanning electron microscopy and average grain size analysis. Additionally, the anisotropy of the alloy in the hot-rolled condition was calculated, Vickers micro-hardness, bending and potentiodynamic corrosion tests were used to assess the alloy's properties.The analysis demonstrates that the Fe-15Mn-8Al-1C-40ppmB composition enables a density reduction of approximately 10% compared to conventional steels. In all the rolling conditions analyzed, except for hot-rolled without heat treatment, the microstructure exhibited an austenitic matrix with varying forms and quantities of ferrite precipitation, depending on the condition. Specifically, it was observed that the majority of ferrite precipitates after solution treatments. Furthermore, no κ-carbides were detected under any condition. With regards to welds, the microstructural analysis and tensile tests has revealed that alternating current is more effective compared to direct current due to its superior capability to breakdown the oxide layer on the material's surface. At the microstructural level, the weld zone exhibited a dendritic microstructure with an austenitic matrix. Furthermore, the precipitation of secondary phases, particularly κ-carbides, was observed in the base material adjacent to the heat-affected zone.

Abstract in italiano

Negli ultimi anni c'è stato un grande interesse per gli acciai leggeri Fe-Mn-Al-C, specialmente per le loro applicazioni come componenti strutturali nell'industria automobilistica. L'aspetto più importante di questo tipo di acciai è la loro minore densità rispetto alle leghe tipicamente utilizzate in questo settore (AHSS, HSS, UHSS), insieme alla loro eccellente combinazione di duttilità e proprietà meccaniche. Tuttavia, la loro produzione è molto complessa a causa di varie complicazioni metallurgiche, come la frequente precipitazione di fasi secondarie che ne possono influenzare le proprietà del materiale finale. In questo progetto sono state analizzate la microstruttura e le proprietà meccaniche di una lega Fe-15Mn-8Al-1C-40ppmB in diverse condizioni termomeccaniche e di saldatura. In particolare, l'attenzione è stata focalizzata sull'indagine della precipitazione di fasi secondarie e sull'evoluzione dei grani durante la laminazione a caldo e a freddo, nonché durante il trattamento termico di soluzione. Per quanto riguarda la saldatura, lo studio si è concentrato sulle tecniche di cladding e sulle saldature di testa a doppia V, testate utilizzando sia corrente diretta che alternata. In questo contesto, particolare attenzione è stata dedicata all'evoluzione microstrutturale della zona saldata influenzata dall'operazione di saldatura. Inoltre, sono state effettuate prove di trazione su provini con una saldatura a doppia V posizionata al centro. I metodi analitici utilizzati includono la microscopia ottica, la diffrazione dei raggi X, la microscopia elettronica a scansione e l'analisi della dimensione media dei grani. Inoltre, è stata calcolata l'anisotropia della lega nello stato laminato a caldo, sono state utilizzate prove di microdurezza Vickers, flessione e corrosione potenziocinetica per valutare le proprietà della lega. L'analisi ha dimostrato che la composizione chimica della lega consente una riduzione di circa il 10% della densità rispetto agli acciai convenzionali. In tutte le condizioni di laminazione analizzate, tranne che nel caso di laminazione a caldo senza trattamento termico, è stata osservata una microstruttura con matrice austenitica con varie forme e quantità di precipitazione di ferrite, a seconda della condizione. In particolare, si è osservato che la maggior parte della ferrite precipita dopo i trattamenti di soluzione. Inoltre, non sono stati rilevati carburi κ in nessuna delle condizioni. Per quanto riguarda le saldature, l'analisi microstrutturale e i test di trazione hanno rivelato che la corrente alternata è più efficace rispetto alla corrente continua grazie alla sua migliore capacità di rimuovere lo strato di ossido sulla superficie del materiale. A livello microstrutturale, la zona di saldatura ha mostrato una microstruttura dendritica con una matrice austenitica. Inoltre, è stata osservata la precipitazione di fasi secondarie, in particolare carburi κ, nel materiale di base adiacente alla zona termicamente alterata.

Summary

List of figures

List of tables

Introduction

In recent years, research has been focusing on reducing the emission of greenhouse gases to counter rising temperatures. In this context, reducing the weight of vehicles could play a relevant role in the automotive industry, in order to improve the fuel efficiency and to reduce the exhaust gas emissions.
To do this, it is important to start from the selection of the material: material for automotive applications must be lightweight and, at the same time, it must have a combination of high specific strength and ductility, to sustain the structure and for forming complex shapes.
A first alternative is related to emerging light alloys, such as aluminum and magnesium alloys, which, however, have several problems mainly related to their high cost and their performances, which are generally worse than that of steels.
Another simple strategy for reducing the overall weight of components is to select higher-performance alloys, such as high-strength steels (HSS), ultra-high-strength steels (UHSS) and advanced high-strength steels (AHSS). These alloys allow for thinner and smaller parts to be used for a given application. However, reducing the thickness and size of parts comes with disadvantages. This includes decreased stiffness, ductility, and dent resistance, as well as increased susceptibility to buckling and low-cycle fatigue.
Another alternative is given by novel lightweight Fe-Mn-Al-C steels, which are obtained by adding light elements such as Mn and Al to steel, with the aim of decreasing the density of the alloy. However, even if the concept of lightweight steel seems quite simple, the underlying metallurgical issues are complicated. This is because, depending on contents of primary alloying elements of C, Mn or Al, they can have a ferritic, austenitic, or multiphase structure with very different properties.
Due to their high specific strength and ductility coupled with their lower alloying element content, austenitic lightweight steels have proven to be the most attractive ones for structural parts in the automotive industry.
Nevertheless, depending on the chemical composition, these alloys can have different stacking fault energy (SFE) values, to which correspond different deformation mechanisms and thus different material responses.
In addition, it is necessary to consider the two main precipitates that are obtained in austenitic lightweight steels: κ-carbides and α-ferrite. Depending on their volume fraction, distribution and size, the mechanical properties of the alloy can vary significantly.

It is therefore necessary to try to understand what chemical composition, deformation mechanisms and precipitate conditions are optimal to maximize the mechanical properties and ductility of the alloy.
In the present study, the microstructure and mechanical properties of a lightweight Fe-15Mn-8Al-1C-40ppmB austenitic steel under different thermo-mechanical (hot-rolled, cold-rolled and solution treated) and welding (cladding and double-V butt welding) conditions have been investigated.

Chapter 1

Lightweight steels and their various forms

1.1 Historical background

Lightweight steels have a long history of development, dating back to 1890 when Robert Hadfield patented in 1890 some earliest Fe-Mn-Al-C steels.
Early work in the 1950s, 60s, and 70s focused on the physical metallurgy of these alloys. Since the 1980s, they were considered as potential substitutes for conventional stainless steels due to the lower cost of Mn and Al, which have similar effects to Ni and Cr, respectively [1], [2].
Despite initial optimism, subsequent studies have shown that they are not suitable replacements for stainless steels due to their lower corrosion resistance [3], [4]. Nonetheless, over the years, their high ductility and good mechanical properties have made them an attractive solution for structural components in the automotive industry. Their use in this sector, however, remained limited until the 2000s, when an understanding of the mechanisms of deformation and their relationship to mechanical properties was finally achieved [1].
In recent years, there has been a significant increase in interest in these steels. This is mainly due to the need to reduce greenhouse gas emissions in the automotive sector. Reducing the weight of vehicles is beneficial for both electric and conventional vehicles. In the case of electric vehicles, it is necessary to balance the additional weight of batteries, and in the case of conventional vehicles, reducing weight is essential for lowering fuel consumption and increasing efficiency [5], [6].
Fe-Mn-Al-C alloys can be a viable alternative to their main counterparts, including light alloys such as aluminum and magnesium alloys, as well as high-strength steels (HSS) and ultra-high-strength steels (UHSS). Light alloys have high cost and low mechanical properties when compared to ferrous alloys, which limits their applicability. HSS and UHSS steels, on the other hand, offer higher performance and allow for reduced component thickness, which reduces the weight of the vehicle. However, this approach has negative effects, including decreased stiffness, ductility, and dent resistance, as well as increased susceptibility to buckling and low-cycle fatigue. Fe-Mn-Al-C alloys, on the other hand, can overcome these limitations and offer a balance of high strength, ductility, and formability. They also have good corrosion resistance (even if lower respect stainless steels) and can be cost-effective compared to some alternatives [1], [2], [5], [7].

1.2 Lightweight steels classification

Depending on the matrix phase, three different types of lightweight steels can be distinguished [8]: ferritic (α), duplex ($\alpha+\gamma$) and austenitic (γ). As it is possible to observe from Tab.1 [8], ferrite based lightweight steels contain a lower amount of Mn and C. Contrary, austenitic based steels have an higher amount of alloying elements (Mn between 15 and 30%, C between 0.5 and 1.2%, Al between 8-12%).
In each of them it is common to get a type of precipitate called κ-carbide ($(Fe,Mn)_3AlC_x$), which plays an important role in the mechanical properties of the alloy.

Type	Composition range	Matrix phase	Precipitates
Ferrite based	(5-8)Al, (0-0.3)C, (0-8)Mn	Ferrite	κ-carbide (when C and Mn are added)
Duplex	(3-10)Al, (0.1-0.7)C, (5-30)Mn	Austenite + Ferrite	κ-carbide
Austenite based	(8-12)Al, (0.5-1.2)C, (15-30)Mn	Austenite	κ-carbide

Table 1: Microstructure constituents in lightweight alloys (approximate ranges in wt%).

In general, austenitic steels are the most promising in terms of properties and processing. In fact, in hot-rolled conditions they can reach up to 1500 MPa of ultimate tensile strength (UTS) and a very high value of total elongation (up to 80%) [9], [10], [11].

Ferritic Lightweight steel

Lightweight ferritic steels contain a high amount of Al and low amounts of C and Mn. Aluminum acts as a ferrite-stabilizer, so during the alloy production process, ferrite is directly formed from the liquid during casting.
However, the Al content in the alloy should be limited to less than 6.5 wt. % to prevent short range ordering (SRO). SRO is a phenomenon characterized by the non-random arrangement of atoms over a limited range of distances at the atomic scale. In the case of Fe-Mn-Al-C ferritic steels, SRO can lead to the precipitation of secondary phases, such as κ-carbides. These precipitates can have a detrimental effect on the material's formability and ductility. Moreover,

carbon (C) can help minimize SRO, making it possible to increase the Al content in the alloy. Therefore, adding C can lead to improved formability, even with higher Al content [5], [6].
Al not only extends the ferrite region to high temperatures but also increases the recrystallization temperature of ferrite. This means that the grain size of the ferrite cannot be refined sufficiently through dynamic recrystallization during hot rolling. As a result, ferrite is elongated along the rolling direction and forms band-like structures (Fig.1 [9]), that are detrimental for the anisotropy and ductility of the material.
Moreover, if the cooling rate is slow, coarse κ-carbides can form along the original ferrite grain boundaries during the subsequent cooling process. These κ-carbides in the ferritic matrix are semi coherent and have a thick, elongated, rod-like shape.
For these reasons, lightweight ferritic steels cannot be produced through hot rolling. Cold rolling is generally used for their production [9].

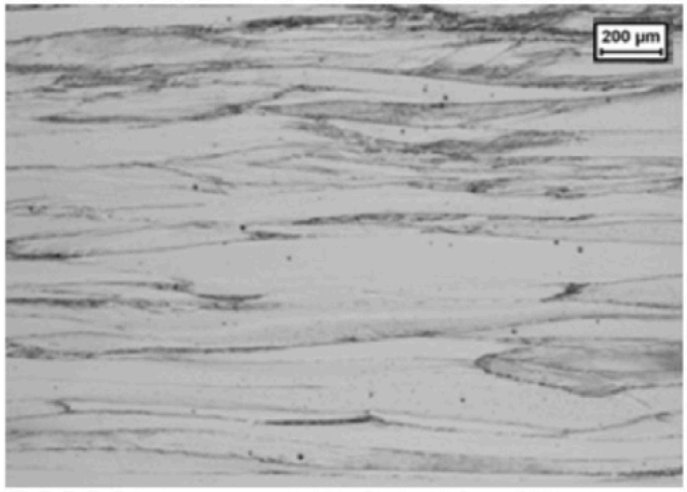

Figure 1: The characteristic microstructure of the optical microstructures of a low density ferritic steel (Fe-7Al) after hot rolling.

Duplex lightweight steels

Lightweight duplex steels are Fe-Mn-Al-C alloys with both, ferrite and austenite phases. As it can be observed in Fig.2 [9] they can consist of either an austenitic (austenite-based duplex steels) or a ferritic matrix (ferrite-based duplex steels), depending on their chemical composition. In austenitic duplex steels, the Mn and C content is typically higher as they act as a stabilizer of austenite, while in ferritic duplex steels the Mn and C content is usually lower but there is a higher concentration of Al, which acts as a ferrite-stabilizer. The stability of austenite is relatively low in both types of duplex steels due to the low content of alloying elements [5], [8], [9]. As depicted in the Fig.3 [9], in

general, their mechanical properties are inferior to those of austenitic steels [12].

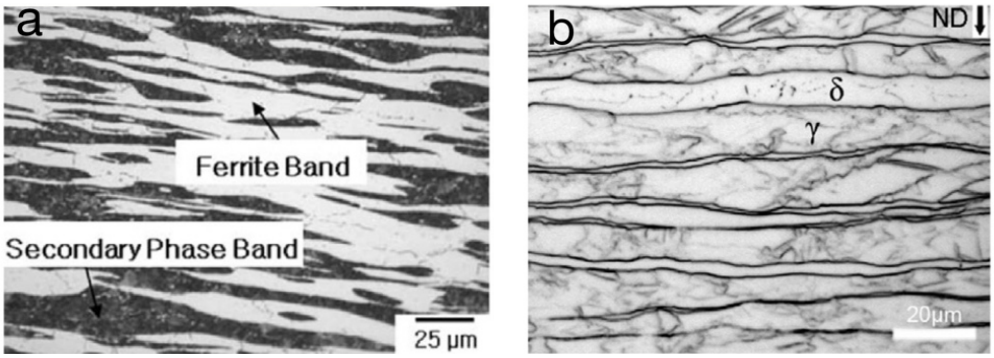

Figure 2: The characteristic microstructure of the optical microstructures of: a) ferrite based duplex after hot rolling; b) austenite based duplex after rolling.

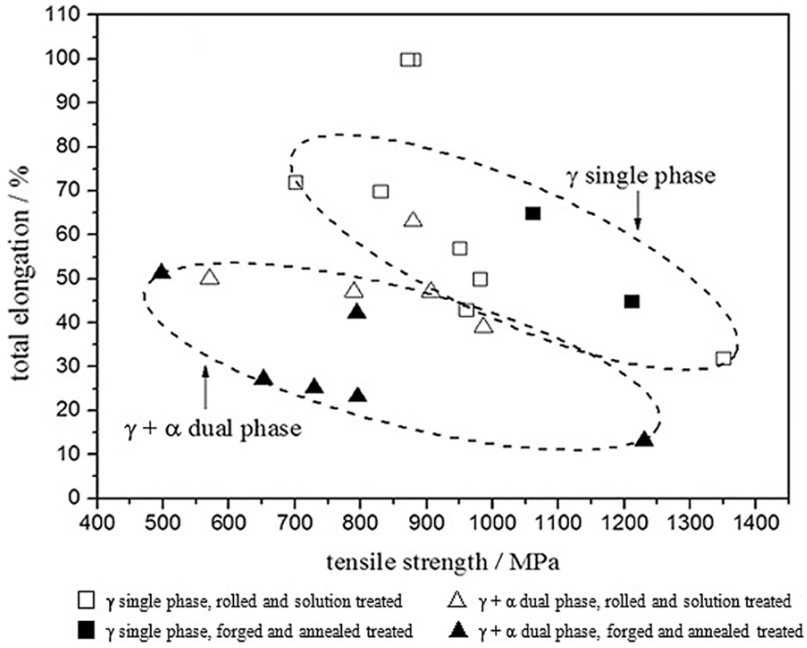

Figure 3: The relationship between tensile strength and total elongation in Fe-Mn-Al-C steel after different pre-treatment.

Austenitic lightweight steels

Austenitic steels are characterized by a high concentration of manganese and carbon, which enable them to maintain a metastable austenitic matrix even at room temperature. This class of lightweight steels is the most complex, as their properties depend on the various types of precipitates and deformation mechanisms that can be achieved. However, they are also the most intriguing due to their exceptional combination of mechanical properties and ductility [13]. As a result, **Chapter 2** focuses entirely on this class of steels.

1.3 Influence of alloying elements on density

The density of lightweight Fe-Mn-Al-C steels varies between 6.5 and 7.0 g/cm^3 depending on the chemical composition [8]. The difference between these values and the density of pure iron (7.8 g/cm^3) is ascribed to two factors:

- the addition of alloying elements with a lower atomic weight decreases the average atomic mass;
- the lattice expansion caused by the addition of alloying elements [12]. For example, Mn has a similar atomic weight respect iron (55 g/mol against 56 g/mol respectively) but a larger atomic radius (0.134 nm against 0.124 nm). Thus, increasing the Mn content leads to a greater lattice expansion and, therefore, to a density reduction.

Some studies have found an equation that relates the density of the final alloy to the weight percentage of Al, C and Mn [12]:

$$\rho_\gamma = 8.10 - 0.101(wt.\%Al) - 0.41(wt\%C) - 0.0085(wt.\%Mn)$$

It can be noticed that the relationship is linear and, from the slope of density against alloy content, it is possible to estimate the effectiveness of each element on the density reduction. In particular, the coefficients for the Mn, Al and C content are all negative, thus the addition of these elements decreases the density. The larger effect on the density reduction is given by C, which has the greatest coefficient (in absolute value); the lower impact instead is given by Mn.

1.4 Effect of alloying elements

The chemical composition of the alloy has a direct influence on its properties. Each alloying element is added in a certain percentage to achieve specific goals. Therefore, depending on the required characteristics, the chemical composition of the alloy must be correctly designed.

Mn is an austenite-promoter and is used to obtain metastable austenite even at room temperature. In literature, it is reported that its addition results in an increase in the lattice parameter and, consequently, a reduction in the density of the steel, even if with a lesser effect compared to other elements. However, if added in excessive amounts, it can lead to the formation of a very fragile secondary phase: the β-Mn, which negatively affect the ductility of the alloy. Mn also helps to increase the alloy's oxidation resistance by forming (Fe,Mn)O. However, it has little influence on the precipitation of κ-carbides [8], [9], [12].

Al, on the other hand, is a ferrite-stabilizer. It helps achieve a significant reduction in density through a remarkable increase in lattice parameter. However, it was demonstrated that excessive addition of aluminum can lead

to the precipitation of intermetallic secondary phases, which make the material brittle. For this reason, the addition of aluminum is limited to 11-12%. Aluminum has a positive effect on the alloy's oxidation resistance by forming a protective surface layer of alumina (Al_2O_3). Additionally, it significantly increases the yield strength and reduces the elastic modulus of the alloy (a 1% addition of Al leads to a reduction in Young's modulus of 2-2.5% [9]).It is also important to note that its addition greatly increases the stacking fault energy (SFE) and has a strong influence on the precipitation of κ-carbides [8], [9], [12], [14].

C is another austenite promoter, and its addition up to a certain limit increases the ductility of steel. However, beyond a certain threshold, carbon promotes the precipitation of κ-carbides, which has a negative effect on the material's ductility. In general, carbon hinders the precipitation of β-Mn and ε-martensite phases. Additionally, as the carbon concentration increases, the stacking fault energy (SFE) also increases.

Regarding the mechanical properties, the addition of carbon increases the yield strength (about 187-300 MPa/wt% C) of steel but reduces its elastic modulus and fatigue strength. Additionally, the density of steel is strongly influenced by the presence of this element [9], [12], [15].

Boron (B) is another austenite promoter. Its segregation at grain boundaries leads to the precipitation of boro-carbides ($M_{23}(C,B)_6$), which prevent the growth of austenite grains. Furthermore, this precipitation can inhibit the formation of κ-carbides and ε-martensite [16].

Chapter 2

Austenitic Lightweight steel

Austenitic lightweight steels are characterized by a metastable austenitic matrix even at room temperature, with a face-centered cubic (FCC) crystal structure that gives them an excellent combination of ductility and mechanical properties. Their typical range of composition is: Mn between 15 and 30%, Al between 8 and 12% and C between 0.5 and 1.2%.

2.1 Microstructure

The microstructure of austenite alloys in the as-cast state is typically dendritic, due to the high degree of micro and macro segregations caused by the large amount of alloying elements [9]. However, for austenitic Fe-Mn-Al-C steels, hot working (reheating and hot rolling) is typically conducted. In this way it is possible to obtain the homogenization of the elemental segregation and, in particular, recrystallization. In that case, the final microstructure is characterized by equiaxed austenitic grain structure containing annealing twins, as it is possible to observe in Fig.4 [9].
Twin boundaries are crucial for this type of alloys, as they act as nucleation sites for dislocations, but also as barriers for them. Consequently, their presence affects the material's work hardening capability ratio (WHR) and, therefore, its ductility.[10]
In addition, this type of alloy is typically fast cooled to avoid precipitation at the grain boundary and within the austenite matrix of coarse κ-carbide and/or α-ferrite particles, which can affect negatively the ductility and the toughness of the alloy.

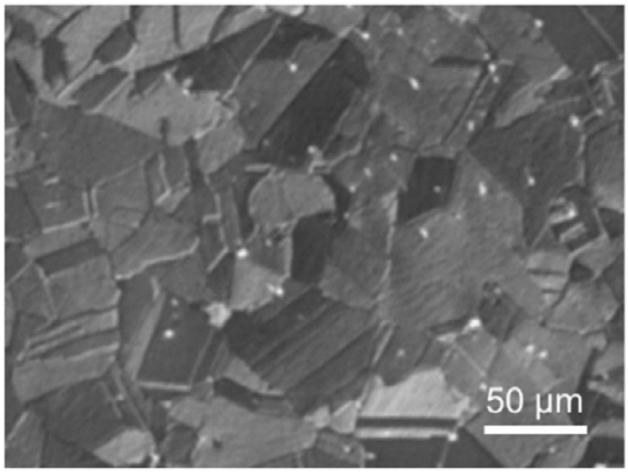

Figure 4: The characteristic of the optical microstructures of low a density austenitic steel (Fe-29Mn-6Al-0,9C) after hot rolling.

2.2 Precipitates

The main precipitates that is possible to observe in austenitic Fe-Mn-Al-C steels are the κ-carbides, the α-ferrite particles and the β-Mn [1], [5], [8]–[10], [12], [17].

κ-carbide

κ-carbide is a L'1_2 ordered face-centered cubic (FCC) carbide. Its chemical composition is $(Fe,Mn)_3AlC_x$ (with x generally less than one). Considering illustration of a κ-carbide cell (in Fig.5 [12]), it can be noticed that eight Al atoms are positioned in the corners of the lattice nodes, the single C atom is located in the octahedral interstitial site and six Fe/Mn atoms occupy the six FCC lattice nodes [12].

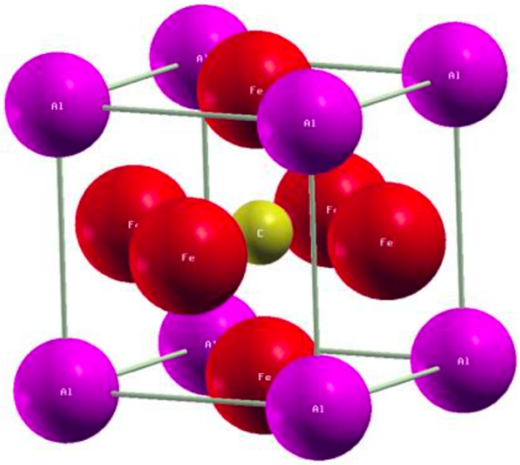

Figure 5: schematic diagram of the κ-carbide crystal cell.

It is possible to divide κ-carbides in two categories: the intragranular κ′-carbide and the intergranular κ*-carbide. Their formation mechanism as well as their contribution to the final properties of the alloy are quite different [9] [11]:

- κ '-carbide is produced homogeneously within the metal matrix and it is coherent with it. Therefore, it typically has small dimensions, as it can be observed in Fig.6 [18], and it gives a positive contribution to the alloy in terms of mechanical properties;
- κ*-carbide is produced heterogeneously along austenite grain boundaries. It is not coherent with the austenite matrix and it has larger dimensions (Fig.7 [19]), so it is very dangerous for the ductility of the alloy.

The precipitation of κ-carbide is closely related to the C and Al content of the alloy. As the concentration of C and Al increases, the driving force for its precipitation also increases. [8]
In fact, if the levels of these two alloying elements are high, κ-carbides can precipitate even with rapid cooling or even during cooling following solubilization treatment [8].
It is therefore essential to try to understand the precipitation of these particles, in order to have a better control on the material's properties.
For example, with proper solubilization treatment, followed by rapid cooling and aging at 450-650°C, it is possible to obtain κ'-carbides coherent with the austenite matrix, which have a hardening effect [9].

κ-carbide precipitation

Starting from an austenitic matrix, precipitation of κ-carbide can occur mainly in two different modes.
The first mode is based on precipitation within the matrix and involves the following series of reactions:

$$\gamma \rightarrow \gamma' + \gamma'' \rightarrow \gamma' + L1_2(SRO) \rightarrow \gamma' + \kappa'$$

During cooling, a modulation of C and Al within the austenite (γ) take place through a spinodal reaction. The high temperature γ is decomposed into two low temperature austenitic phases: the γ' (solute-lean) and the γ'' (solute rich). A further cooling promotes a short-range ordering (SRO) reaction, with the γ'' that is transformed into the metastable $(Fe, Mn)_3Al$ phase with a $L1_2$ crystal structure.
Then, a further ordering of carbon atoms leads to the transformation of the $L1_2$ phase into the $(Fe, Mn)_3AlC_x$ phase, also called κ-carbide, with a $L'1_2$ crystal structure. The carbide obtained as result of these reactions is the intragranular κ'-carbide [9], [18]–[20].

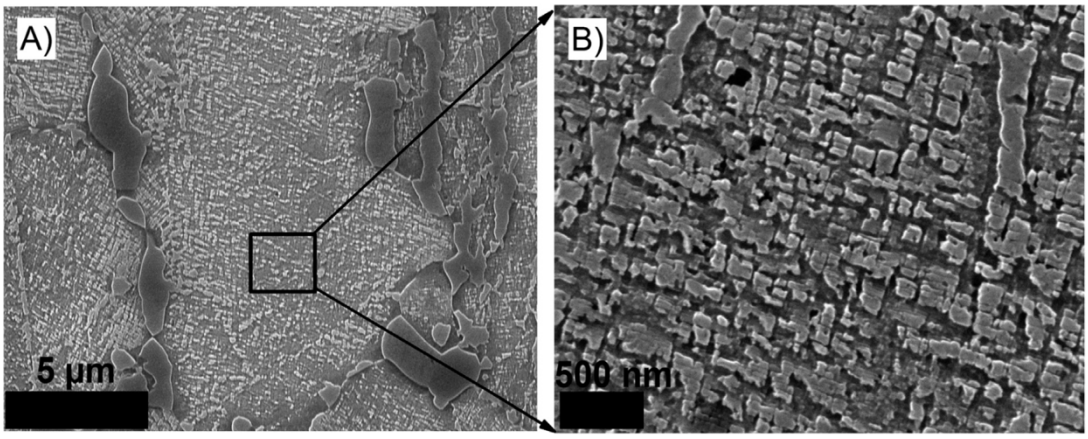

Figure 6: SEM images of κ'-carbides at (A) 5 µm and (B) 500 nm.

In over-aging conditions, the residual austenite is destabilized by a further precipitation of κ-carbides, followed by β-Mn. In that case, the sequence of reactions is:

$$\gamma \rightarrow \alpha + \beta Mn \quad or \quad \gamma \rightarrow \kappa + \alpha + \beta Mn$$

Therefore, the carbide obtained is the intergranular κ*-carbide, that precipitates at the grain boundaries incoherently with the austenite matrix in form of coarse particles [9], [21] [20].

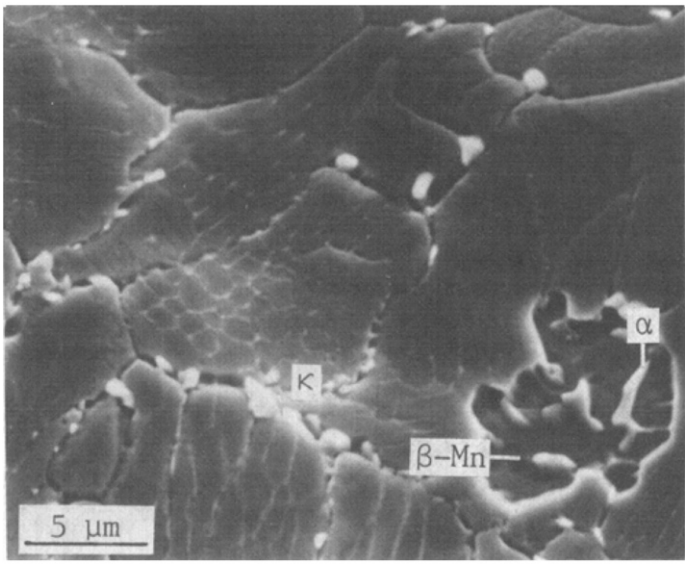

Figure 7: Scanning electron micrography of an austenitic Fe-Mn-Al-C steel after aging. The α-ferrite, β-Mn and the intergranular κ-carbide are putted in evidence.

α-ferrite

Besides κ-carbide another precipitate that can be observed after solution treatment in Fe-Mn-Al-C austenitic steels is α-ferrite. This phenomenon

depends mainly on the chemical composition of the alloy and the temperature used for treatment. It is typically observed in form of fine stringers along the austenitic grain or along the twin boundaries. Initially after solubilization treatment, these precipitates are coherent with the austenitic matrix. However, they lose coherence upon coarsening if the material is heated again (e.g. for aging) [9], [22], [23].

β-Mn

The β-Mn phase has a simple cubic A13 crystallographic structure. When the Mn concentration is very high (over 35%), the precipitation of brittle β-Mn particles occurs, causing a significant decrease in material toughness [3][8]. However, such brittle precipitates can be used to increase material hardness through aging treatments, at the expense of the material's ductility [24], [25].
In particular, the β-Mn phase tends to precipitate together with the alpha-ferrite phase during the over-aging phase, following the reactions γ→κ+α+βMn or γ→α+βMn, which produce a lamellar structure [26]. Additionally, it has been shown that its precipitation can also be accelerated by deformation, as in the case of cold rolling. In this case, precipitation occurs mainly at grain boundaries and precedes that of the alpha ferrite. The typical shape of the β-Mn precipitates obtained through this mechanism is "tunnel-like," as shown in Fig.8 [24].

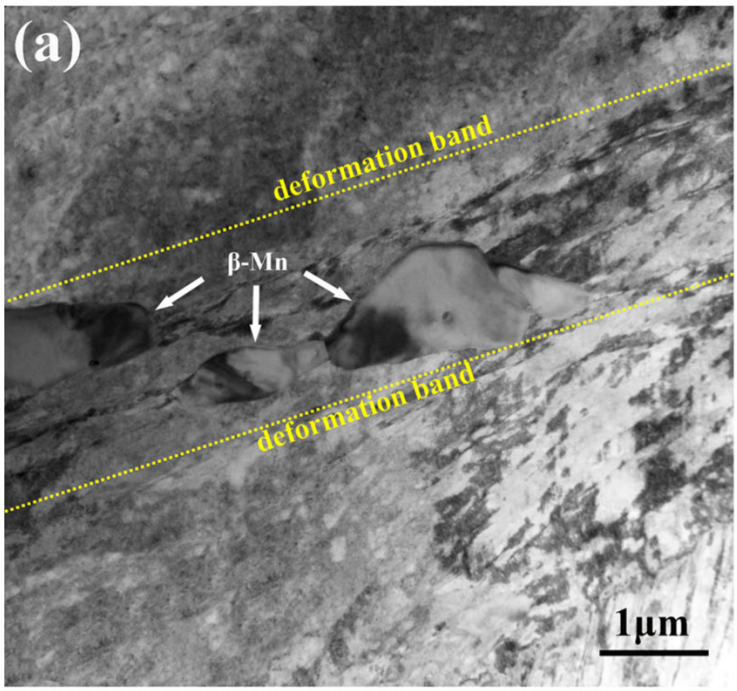

Figure 8: TEM bright-field image of the b-Mn phase in a Fe-Mn-Al-C aged steel

2.3 Stacking Fault Energy (SFE)

The activation of various deformation mechanisms in austenitic steels is related to the stacking fault energy (SFE). To define what SFE is, it is necessary to start from the perfect (or ideal) FCC crystal structure, which can be conceived as a sequence of closely stacked {111} planes arranged as ABCABCABC..., as can be observed in Fig.9. [1]

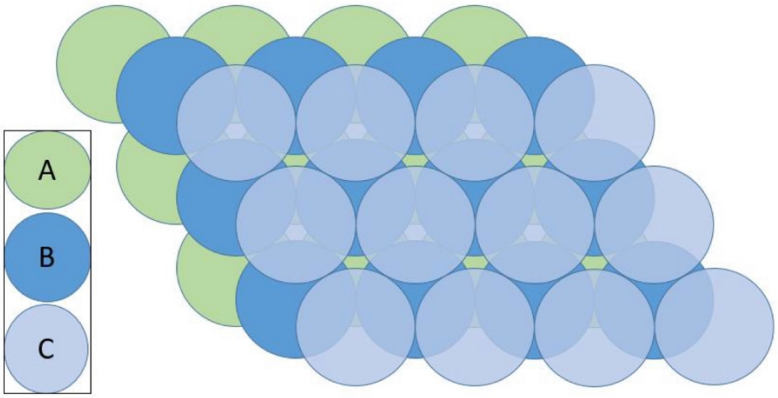

Figure 9: Schematic representation of the stacking sequence of a perfect (FCC) structure.

However, in real conditions, due to plastic deformation or the solidification process, the perfect sequence may not be preserved, and various interruptions and alterations can be observed. Each alteration compared to the ideal stacking sequence represents a stacking fault. The result is an anomalous stacking sequence, as schematically shown in Fig.10 [1].
A deviation from the equilibrium condition corresponds to an increase in the total lattice energy, which depends on the width of the stacking fault itself (indicated in the Fig.10 as 'd'). In other words, the SFE is the energy difference between the perfect stacking state and the stacking state with the fault present. Small separation distances result in high SFE values, while large distances result in low SFE values [1].

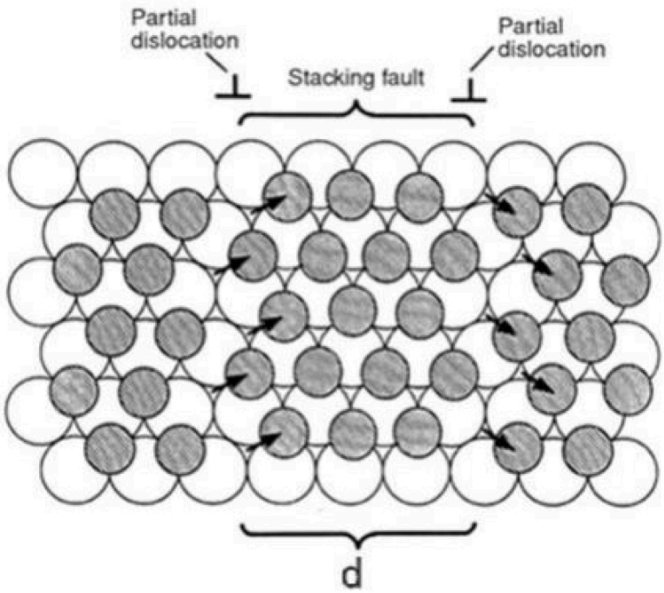

Figure 10: Schematization of the generation of the stacking fault from two partial dislocations.

Therefore, materials with low SFE hinder cross-slip and dislocation climb due to wider separation distances. Materials with high SFE, on the other hand, exhibit the opposite tendency [1].

2.5 Deformation mechanisms

As shown in Tab.2, austenitic steels can show different deformation mechanisms according to their value of stacking fault energy (SFE) [8]. Depending on the deformation mechanisms, the output of the material in terms of strength and plasticity can vary a lot. For example, a Fe–25Mn–3Si–3Al TWIP steel has a moderate tensile strength of about 650 MPa and an elongation after fracture of about 80%. Differently, an Fe–28Mn–10Al–1.0C with MBIP effect can reach a tensile strength of 840 MPa and 100% of elongation after fracture [17].
SFE depends mainly on the chemical composition even if it is also affected by the temperature, grain size and micro segregations of alloying elements. It is very important because the stability of austenite, which gives the high ductility, strength and high strain hardening rate of these steels, is controlled by the SFE [1], [17].
Hence, by optimizing these parameters, it is possible to obtain one specific deformation mechanism, which allows a greater control over the final properties of the steel.

Stacking fault energy [mJ/ $\mathbf{m^2}$]	SFE<12 $\mathrm{mJ/m^2}$	12 $\mathrm{mJ/m^2}$<SFE<18 $\mathrm{mJ/m^2}$	18 $\mathrm{mJ/m^2}$<SFE<35 $\mathrm{mJ/m^2}$	SFE>80 $\mathrm{mJ/m^2}$
Deformation mechanism	TRIP	TRIP+TWIN	TWIP	SIP or MBIP

Table 2: Deformation mechanisms for different SFE values.

- **TRIP** (transformation-induced plasticity): for SFE values lower than 12 $\mathrm{mJ/m^2}$, the metastable austenite transforms into martensite when the strain exceeds a critical value in tension. This transformation leads to a strengthening effect, given by the higher strength of martensite compared to austenite and a reduction in grain size [17]. In addition, the presence of martensite also increases the work hardening rate, improving the uniform elongation of the material. Thus, with the TRIP effect, the strength and the plasticity of the material are concurrently improved [10].
- **TWIP** (twinning-induced plasticity): When SFE value is between 18 and 35 $\mathrm{mJ/m^2}$, as strain increases during tensile stress, some oriented grains produce strain twins and twin intersections. These split the original austenite grains, refining them [17]. This is beneficial for material's properties because it leads to more barriers for dislocation's movement [10]. As a result, the strength and the plasticity of the material are increased by the TWIP effect. In general, TWIP is more beneficial to increase the ductility of the material, and the TRIP is useful for the improvement of the strength of the material [10], [13]
- **SIP** (shear-induced plasticity): When SFE has high values, shear bands (i.e., narrow zones of intense shearing strain [27]) can be observed during deformation given by a tensile stress. This result is related to the fact that, for high values of SFE, dislocations are concentrated along the κ-carbide, trying to overcome them through shear deformation. Therefore, also with the SIP, the deformation ability and the UTS of the material are increased.
- **MBIP** (microband-induced plasticity): Microbands form during deformation when the stacking fault energy (SFE) is high. This mechanism leads to an increase in dislocation density as deformation progresses. A significant number of dislocations gradually accumulate, forming clusters, a Taylor lattice, high-density dislocation walls, domain boundaries, and other structures. This accumulation results in deformation with a high density of microbands (MBIP). The outcome is an excellent combination of strength and ductility. [17] [27].

2.6 Strengthening mechanisms

In addition to the deformation mechanisms described in the previous paragraph, it is important to note that, like all metal alloys, Fe-Mn-Al-C steels have other strengthening mechanisms that allow them to increase their yield strength. Among these mechanisms, there are solid solution strengthening, grain refinement, precipitation hardening, and work hardening [1], [9], [12], [17].

The mechanism of solid solution strengthening is of fundamental importance in Fe-Mn-Al-C steels due to the high amount of alloying elements present in these alloys [6]. After the material is solutionized and tempered, aluminum, manganese, and carbon dissolve in the crystal structure of the austenite.

Some studies have shown that aluminum, due to its ability to produce a strong lattice distortion, increases the yield strength (YS), as illustrated in Fig.11, but may have a negative effect on the ultimate tensile strength (UTS) [1].

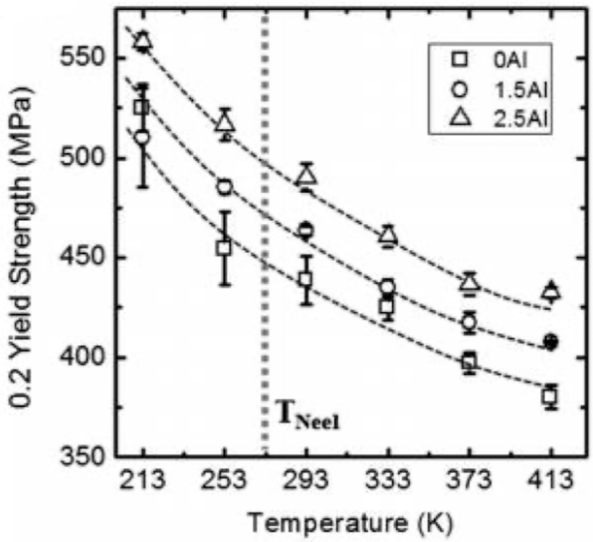

Figure 11: Effect of the Al content on the 0,2% YS of a TWIP steel.

Regarding manganese, its effect on the mechanical properties of the material depends on its content in the steel. Up to 35 wt.%. it can increase the volume fraction of austenite as well as the solubility of Al and C in the γ solid solution. However, when this limit is exceeded, it will give rise to β-Mn precipitation, causing extreme brittleness. Carbon, on the other hand, increases both the yield strength and the ultimate tensile strength of the steel [1], [9]. This trend is evident in Fig.12, where the effect of C on the tensile properties of lightweight steels with two Mn levels is shown.

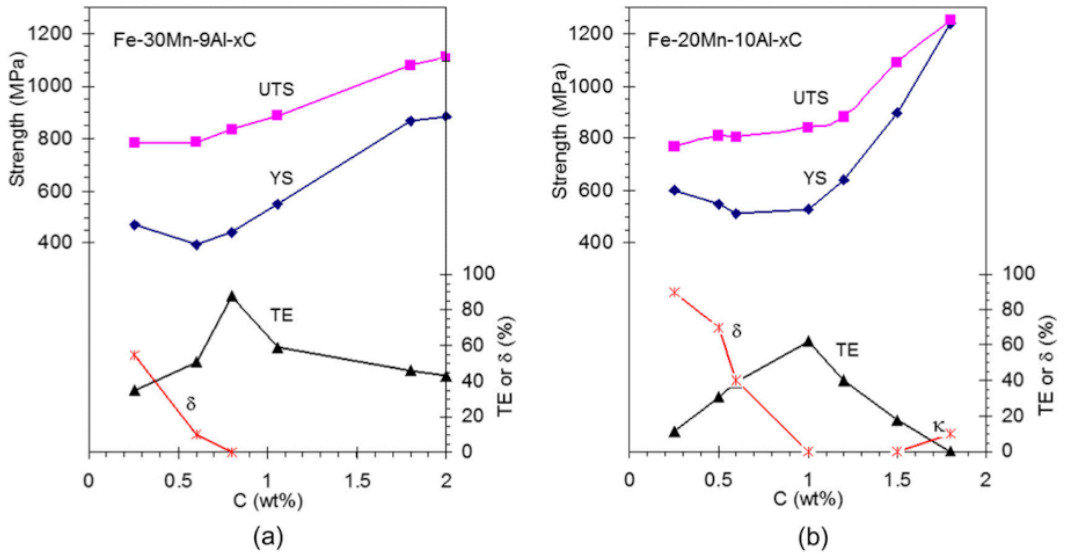

Figure 12: Effect of the carbon content on the microstructure and tensile properties of two series of Fe-Mn-Al-C steels

Regarding grain refinement, it is often achieved through cold/hot rolling or recrystallization annealing. This mechanism is also fundamental, as described in Paragraph 2.1, because due to the large amount of alloying elements, the microstructure of these steels in the as-cast state is typically dendritic [9].
Precipitation hardening is mainly related to the precipitation of κ-carbides. In Paragraph 2.3, it was seen how, depending on the cooling conditions and heat treatments used, it is possible to obtain κ'-carbides (coherent with the austenitic matrix) or κ*-carbides (incoherent with the austenitic matrix). Having coherent precipitates allows for a higher yield strength.

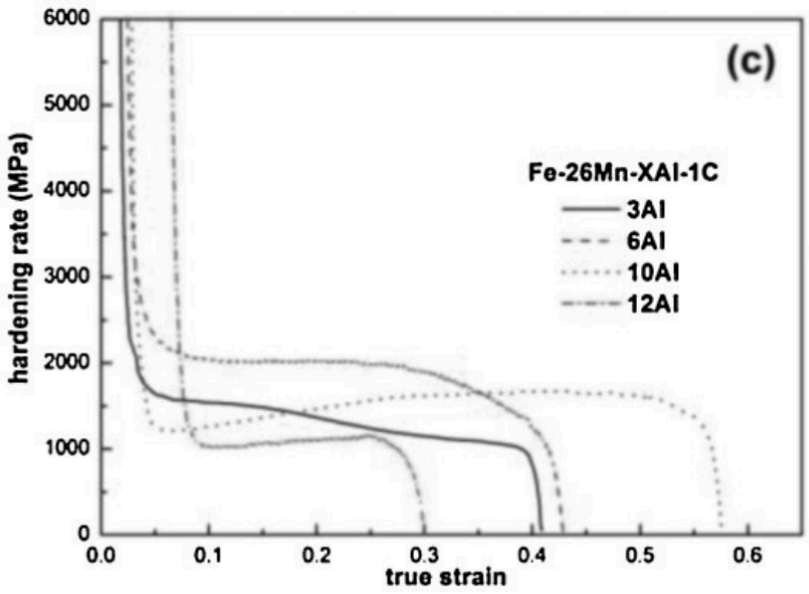

Figure 13: Variations of strain hardening rate with true strain of steels with different Al concentrations

The typical work hardening behavior of Fe-Mn-Al-C steels at room temperature can be seen in Fig.13 [28]. The curve can be divided into three stages, which vary depending on the alloy composition. The steel described in the figure is an Fe-26-XAl-1C with varying amounts of Al. As discussed in the previous paragraphs, Al has a strong influence on the SFE of the alloy, with higher Al content resulting in a higher SFE. Thus, different Al concentrations can activate different deformation mechanisms and lead to several microstructural changes [1], [28], [29].
As it can be observed in Fig.13, Stage 1 is characterized by a rapid decrease in the strain hardening rate. In the second stage, as plastic deformation increases, the strain hardening rate behaves differently depending on the alloy composition. It can either increase or decrease, but its behavior remains relatively stable (i.e., it increases or decreases only slightly). Stage 3 is the stage that leads to specimen fracture and is characterized by a rapid decrease in the strain hardening rate [12], [28], [29].

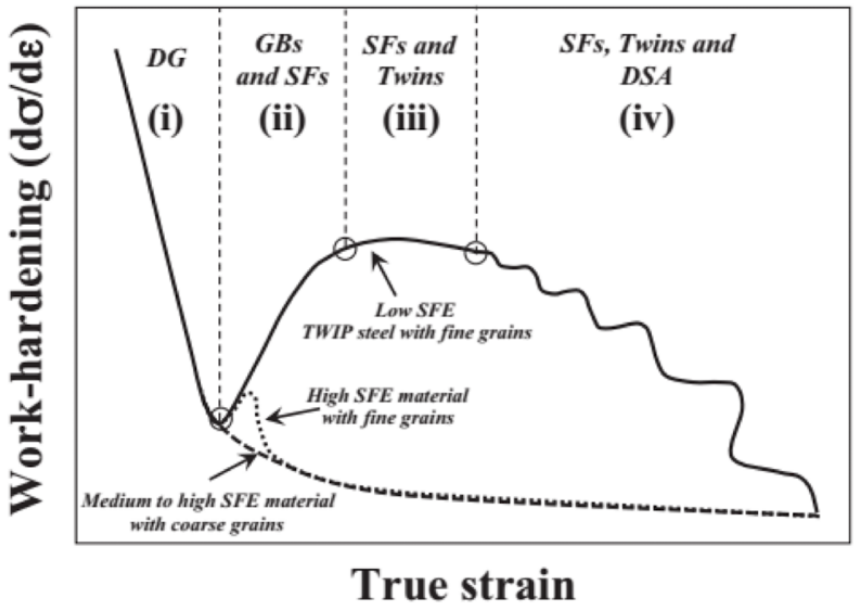

Figure 14: Work hardening behavior representation of FCC materials with different SFE

In Fig.14, it is possible to compare the typical work-hardening behavior of an alloy with low SFE, typically high-Mn steels, represented by the solid line, with that of a Fe-Mn-Al-C alloy with medium-high SFE, represented by the dashed/dotted line. It is noted how in high-Mn steels, unlike what was described previously for lightweight steels, following the rapid decrease of the strain hardening rate, there is a rapid increase that leads to a local maximum. Therefore, Fe-Mn-Al-C steels show a lower deformation-induced hardening capacity compared to high-Mn steels [1].

2.7 Application properties

In order to apply austenitic Fe-Mn-Al-C steels in the automotive sector, several important mechanical properties of this type of steel must be considered, such as toughness, fatigue strength, formability, weldability and corrosion resistance.

Various studies [30], [31] have shown that the impact toughness of austenitic lightweight steels after solubilization and water quenching treatment is higher than that of conventional HSS, but lower than that of austenitic stainless steels (as it can be observed in Fig.15). Moreover, aging hardening significantly reduces the impact toughness of these alloys, and the cooling rate after the solution treatment also has some influence on it [9]. This is mainly due to the precipitation of second phases as described in Paragraph 2.2, which makes the alloy brittle.

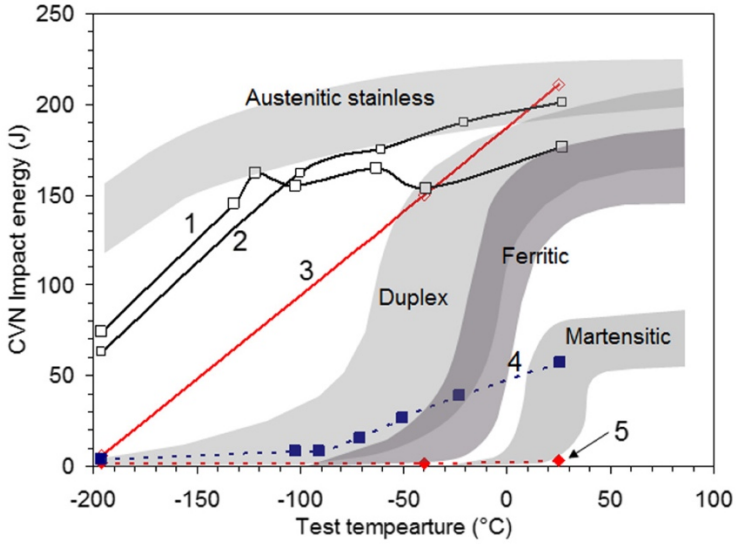

Figure 15: CVN impact energy as a function of test temperature for two austenitic steels solutionized at 1050°C: 1) Fe-28Mn-5Al-1C solutionized for 75 min; 2) Fe-28Mn-5Al-1C solutionized for 8 h; 3) Fe-30Mn-10Al-1C-1Si solutionized for 1 h; 4) Fe-28Mn-5Al-1C solutionized for 8 h and aged at 550°C for 16 h; 5) Fe-30Mn-10Al-1C-1Si solutionized for 1 h and aged at 550°C for 16 h.

Regarding the fatigue behavior, it is not yet fully clear how it is influenced by the deformation mechanisms mentioned in Paragraph 2.5. However, recent research has highlighted a direct correlation between fatigue resistance in TRIP steels and the SFE of austenite. In particular, a high SFE can provide better properties [1].

In addition, concerning the chemical composition, it has been found that the addition of carbon promotes crack propagation, thus reducing fatigue life [32]. As for aluminum, it has been shown to increase low-cycle fatigue (LCF) under cyclic loading at high strain amplitudes but decrease it at low strain amplitudes [33].

Formability is another important property for applications related to the automotive industry. Fully austenitic Fe-Mn-Al-C steels have high formability, comparable to that of high Mn steels. However, further studies are still needed to optimize the forming operation, especially to understand the effect of Al and Mn on the deformation mechanisms that occur during forming [9]. In addition, when dealing with forming or bending operations, it is necessary to carefully consider the high springback effect of these alloys.

Another important property to consider is weldability. Although this property has not yet been sufficiently studied in lightweight steels, some research suggest that these alloys may present certain challenges during welding operations [34]–[36].
In fact, the energy supplied to the material in the form of heat, can have a similar effect to that obtained in aging treatments: it is easy to promote precipitation in the heat affected zone (HAZ) and in the fused zone (FZ) of secondary phases (such as κ-carbides or β-Mn) that negatively affect the ductility of the component [35].
An example is shown in Fig.16, where the results of the Charpy test for an Fe-30Mn-XAl-0.9C alloy in the heat-affected zone (HAZ) subjected to aging treatments with three different times are displayed. It is evident that as the treatment time increases, there is a degradation in the toughness of the alloy, primarily caused by the precipitation of κ-carbides in the HAZ [36].

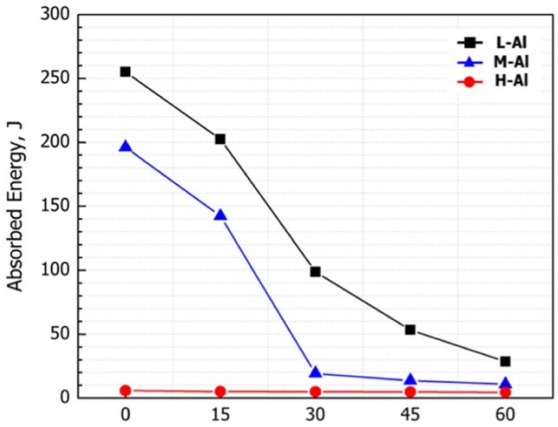

Figure 16: Cryogenic Charpy impact toughness profiles of the heat affected zones as a function of the post welding heat treatment time on a Fe-30Mn-XAl-0.9C steel (where L=9.0wt%, M=10.4wt%, H=11.4wt%)

Other typical problems that can be encountered with these alloys are chemical segregation, hot cracking, hardness variations, inclusion formation and phase transformation [35].
In particular, it is interesting to observe how the hardness profile in these alloys exhibits a fairly characteristic trend. As can be seen in Fig.17, near the HAZ, it

is possible to find a peak in hardness (local or global), mainly due to the precipitation of second phases in this region.

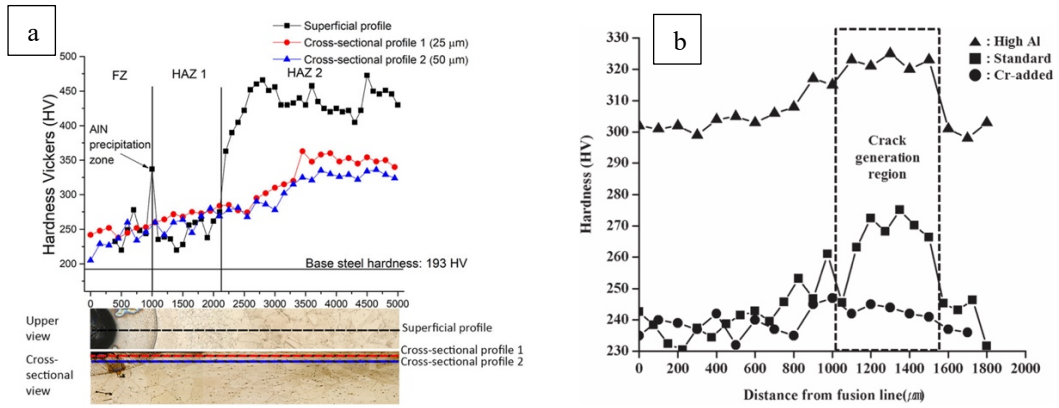

Figure 17: hardness profile vs distance from the fusion line for: a) Fe-31Mn-8Al-1.9C and b)Fe-29.8Mn-10.4Al-0.9C

To achieve a better welding result, micro-additions of titanium and boron can be used in the alloy. Ti acts not only as a deoxidizer and desulfurizer, but also as grain refiner; while boron inhibits grain growth and reacts with nitrogen to promote the formation of BN. This prevents the formation of a more detrimental compound with aluminum that could negatively impact the mechanical properties of the joint [35].
In addition, when welding with these alloys, attention must be paid to the use of post-welding heat treatments (PWHT), which can cause uncontrolled coarsening of secondary phases in the microstructure [36].

Although lightweight steels have not been able to replace stainless steels, their good corrosion resistance remains one of their main advantages [5], [9], [12]. The corrosion resistance is typically expressed as a function of two parameters: the corrosion current density I_{corr} and the corrosion potential E_{corr}. I_{corr} is used to evaluate the corrosion reaction kinetics, It is proportional to the corrosion rate of the material, meanwhile E_{corr} characterizes the difficulty of electron loss in corrosive media. Therefore, the higher the E_{corr} and the lower the I_{corr}, the greater the corrosion resistance of the alloy [37]–[41].
In lightweight Fe-Mn-Al-C steels, corrosion resistance is highly dependent on the chemical composition. In general, the addition of Al promotes the formation of a protective alumina layer on the material surface that prevents corrosion of low-density steel. As described previously, however, aluminum is a ferrite promoter, but austenitic steels are usually preferred because of their excellent combination of ductility and mechanical strength. To achieve an austenitic microstructure, C and Mn are usually added, which, however, affect the oxidation resistance of the material. In fact, manganese has a low passivity coefficient and forms an unstable manganese oxides film, decreasing E_{corr} and

increasing $I_{corr.}$ In addition, several studies have shown that the addition of C is also detrimental to the oxidation resistance of these alloys [37]–[39].

The corrosion resistance of these alloys also depends on the thermomechanical treatments to which they are subjected. In fact, it has been shown that after being subjected to solution treatment, low-density steel shows an increase in E_{corr}, a decrease in $I_{corr.}$, and higher corrosion resistance than hot-rolled steel [37].

This is mainly because the high-temperature solution treatment reduces the segregation of elements in low-density steel, improving the uniform diffusion and distribution of alloying elements, especially aluminum, and preventing aggregation. As a result, the Al_2O_3 protective film generated during electrochemical corrosion is more uniform and compact.

In conclusion, it has been widely demonstrated in the literature that lightweight Fe-Mn-Al-C steels typically have better corrosion resistance compared to conventional carbon steels, but lower compared to that of stainless steels (some examples are reported Tab.18) [37], [38].

Alloy	E_{corr} [mV]	I_{corr} [mA/cm^2]
304 SS	-360	0.0003
Mild steel	-720	0.0016
Fe-24.8Mn-7.3Al-0.90C	-570	0.003
Fe-24.4Mn-9.2Al-0.40C	-590	0.0046

Table 3: Corrosion data of an austenitic stainless steel, a mild steel and two austenitic lightweight steels

Chapter 3

Experimental procedure

The objective of this study is to perform the characterization of a lightweight Fe-Mn-Al-C austenitic steel under different conditions: hot-rolled, hot-rolled followed by a solubilization heat treatment at different temperatures, cold-rolled, cold-rolled followed by a solubilization heat treatment at different temperatures and times. Furthermore, the mechanical and microstructural properties of the alloy were also investigated under two different welding conditions: cladding welding and double V butt welding.
This alloy, with a nominal chemical composition of Fe-15Mn-8Al-1C-40ppmB, was produced by OCAS NV. It was received in the form of four sheets after hot rolling and water quenching, with a thickness of 5 mm and almost 2 mm, as shown in Fig.18. Instead, the thermal treatments were performed inside the laboratories of Politecnico di Milano.

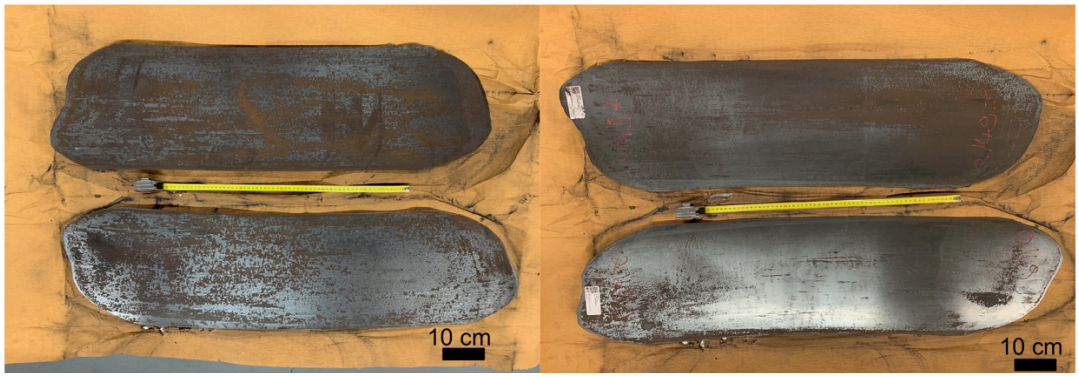

Figure 18: The sheets received from OCAS NV

The characteristics investigated include the density, mechanical properties, precipitation of κ-carbides and B-carbides, grain size and orientation of the steel and its corrosion resistance.
Fig.19 and Fig.20 show a simple schematic of the workflow adopted for this work, which will help the reader understand the steps performed for the analysis.

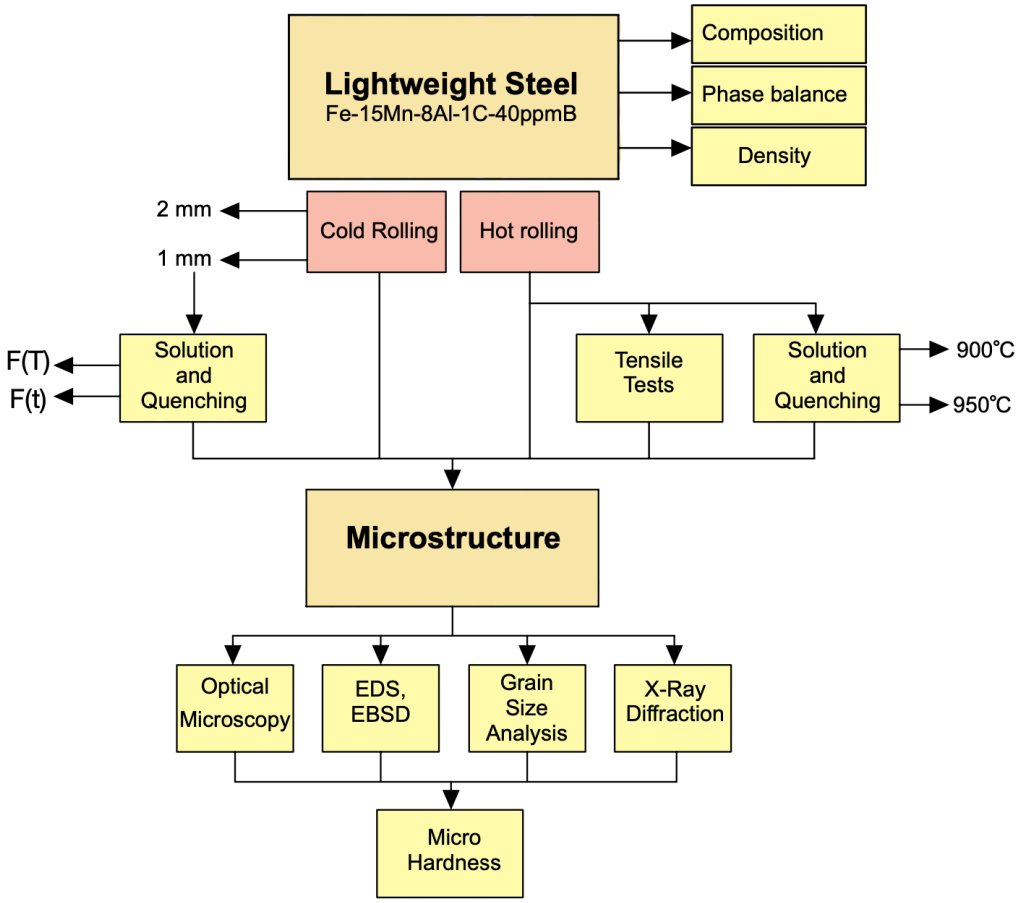

Figure 19: Schematic of the workflow adopted for the characterization of the alloy under rolling condition

Firstly, the actual chemical composition of the steel was determined using the Optical Emission Spectroscopy (OES) method and compared with the nominal composition. The equilibrium phase diagram for the real and the nominal chemical composition was then obtained with © *Thermo-Calc* and © *Jmat Pro* databases. Subsequently, the density of the steel in the hot-rolled condition was evaluated with three methods (hydrostatic balance, mass/volume ratio and with the equation in Paragraph 1.3) to highlight the impact of the chemical composition on the density reduction.

Regarding the characterization of the rolled Fe-15Mn-8Al-1C-40ppmB lightweight steel, the experimental plan was divided into two main branches: analysis under hot-rolled and cold-rolled conditions. As for the former, solution treatments were carried out at two different temperatures (900°C and 950°C) to analyze the effect of treatment temperature on the mechanical and microstructural properties of the alloy. The treatments were conducted for a duration of 30 minutes, followed by water quenching for cooling.

Anisotropy tests were then conducted on hot-rolled specimens obtained from three different orientations with respect to the normal direction to evaluate microstructural anisotropy.
Four samples were prepared for microstructural characterization, including one in the hot-rolled condition (HR), one obtained from the tensile test specimens (HRTT), one after solution treatment at 900°C (SHT900) and another at 950°C (SHT950). Sample preparation involved mounting, grinding, surface polishing, and chemical etching.
For the second branch, the starting material was cold-rolled to achieve two different thicknesses: 1 mm and 2 mm. The material rolled to 1 mm was then subjected to a solution treatment for 30 minutes at five different temperatures: 900°C, 950°C, 1000°C, 1050°C, and 1100°C, followed by quenching in water. After these operations, the samples were prepared for microstructural analysis.
In a second step, it was decided also to perform solution treatments on the 1 mm cold-rolled material at 900°C and 925°C, using different treatment times: 15, 20, 25 and 30 minutes. This decision was taken with the aim of studying the precipitation of secondary phases during the solution treatment.

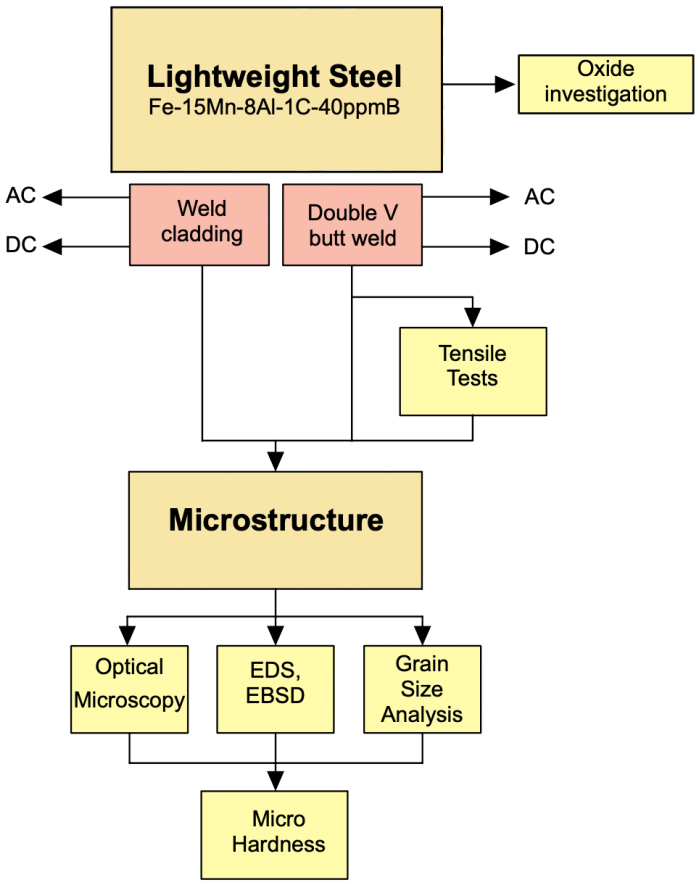

Figure 20: Schematic of the workflow adopted for the characterization of the alloy under welding condition

The preparation and mechanical, as well as microstructural, characterization of the welded joints followed the procedure depicted in Fig.20. Firstly, heating-induced surface oxide formation in the hot-rolled condition was investigated. This step was performed due to the significant impact these oxides can have on the welding quality.
Subsequently, the TIG welding technique was employed for two different types of welds: cladding welding and double V butt welding. Both types of welds were tested using both alternating current (AC) and direct current (DC). The material for the plates was obtained from one of the hot-rolled plates received from OCAS NV, while the filler material rods were obtained from leftover pieces from previous operations.
For each welding condition, four samples were taken at different distances along the weld bead and prepared for microstructural analysis through mounting, grinding, surface polishing, and chemical etching. Additionally, from two plates welded with the double V butt weld, six samples were extracted for the tensile test.
The microstructural features were fully characterized using various analytical methods, including Optical Microscopy (OM), Scanning Electron Microscopy (SEM), Electron Diffraction Spectroscopy (EDS), Electron Back Scatter Diffraction (EBSD), and X-Ray Diffraction (XRD).
Finally, Vickers micro-hardness, bending and potentiodynamic corrosion testing were used to evaluate the alloy's properties.

3.1 Samples preparation

The specimens for the anisotropy tests were obtained from the sheet metal by laser cutting, with three different orientations relative to the rolling direction (0°, 45°, and 90°), as shown in Fig.21.
The remaining material resulting from this operation, which had the typical complementary dog-bone shape of the tensile test, was then used partly to obtain samples for heat treatment and partly for the cold rolling operation.
Thus, two specimens (with an initial thickness of 5 mm) were cold-rolled with a © *OAM SM2001* machine to a thickness reduction of the 60% (2 mm final thickness) for one, and 80% (1 mm final thickness) for the other.

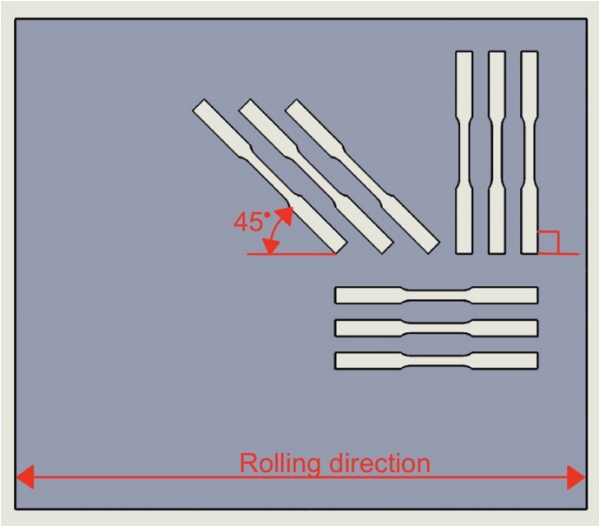

Figure 21: Example of cutting scheme showing the different orientations of the obtained specimens with respect to the rolling direction

Next, a first series of heat treatments were carried out to promote homogenization and solubilization of alloying elements in the austenitic matrix: the hot-rolled material was solutioned at 900°C and 950°C, the cold-rolled one instead at 900°C, 950°C, 1000°C, 1050°C and 1100°C. The duration of the treatment was defined as 30 minutes for both samples. Subsequently, a second series of heat treatments was carried out on the remaining cold-rolled material: three at 900°C (for a time of 15, 20 and 25 minutes respectively) and three at 925°C (for a time of 15, 20, 25 and 30 minutes respectively).
At the end of all the treatments, the pieces were quenched in water to freeze the microstructure and obtain only austenite even at room temperature. The heat treatment was carried out using a © *Lenton UAF 14/27* furnace present in the laboratories of Politecnico di Milano.
In the end, sixteen samples were obtained: one hot-rolled base and one for each treatment temperature, one cold-rolled at 2 mm and one at 1 mm, one cold-rolled for each treatment temperature and one cold-rolled for each treatment time.
Another specimen was obtained by cutting one of the 90° orientation specimens tested for anisotropy using a cutting machine.
The welding operation was carried out using the TIG welding technique, with material obtained from one of the hot-rolled plates received from the supplier. Prior to the operation, the material was cleaned of surface oxides resulting from the rolling process. Filler material rods were used, which were obtained from leftover material from the cuts made for the anisotropy test samples. The welding techniques employed included cladding welding (a single pass of filler material on a plate) and double V butt weld.

For cladding welding with alternating current, a current of 110 A and a voltage difference of ~16 V were used. For direct current, a current of 100 A and a voltage difference of ~13 V were employed. As for the double V butt welds, four passes were made (2 on each side). For alternating current, all passes were performed at 110 A and a voltage of ~15 V. For direct current, the first pass was done at 86 A and a voltage of ~12 V, followed by three subsequent passes at 82 A and a voltage of ~12 V. Finally, six tensile specimens (three for alternating current and three for direct current) were obtained from the plates welded with the double V butt weld using waterjet cutting, as shown in Fig.22.

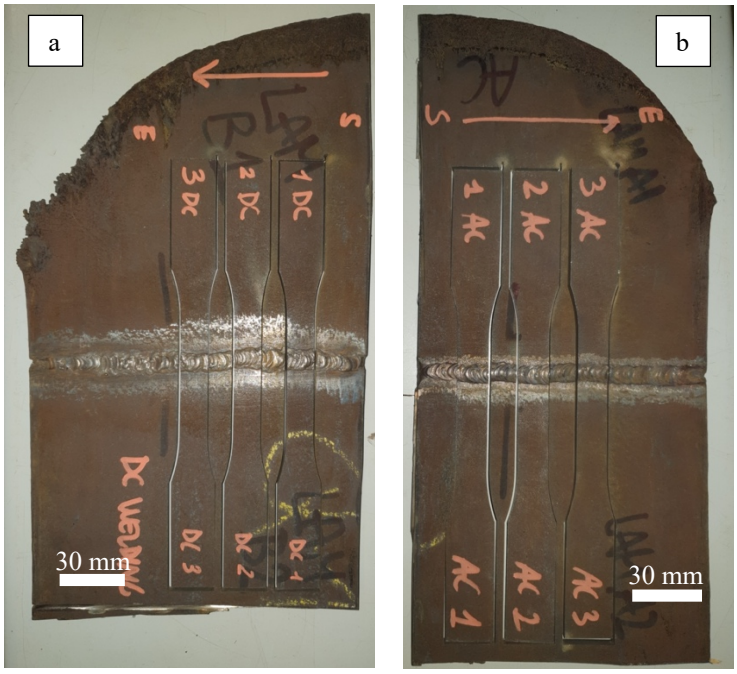

Figure 22: Tensile specimens cutted from the welded plates: a) Direct Current; b) Alternate Current

Regarding the bending tests, six specimens of dimensions 18 mm (length) x 3 mm (width) were obtained by the use of a waterjet cutter: three with a relative orientation of 0° to the rolling direction and three with a relative orientation of 90°, as shown in Fig.23a.

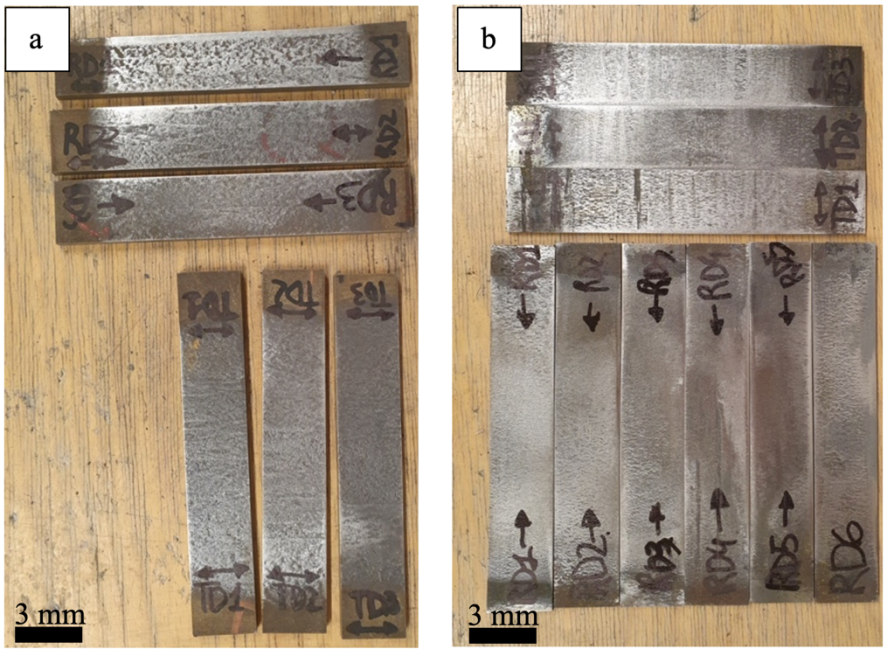

Figure 23: Samples cut for the bending tests, with a) 5 mm thickness, b) 3 mm thickness

Subsequently, another plate of the material was hot-rolled to a thickness of about 3 mm, from which six samples were obtained with a relative direction of 0° to the rolling direction and three with a transverse orientation (Fig.23b). Additionally, also nine circular samples with a diameter of 1.5 cm were cut for the corrosion test from the 3 mm plate (Fig.24a).

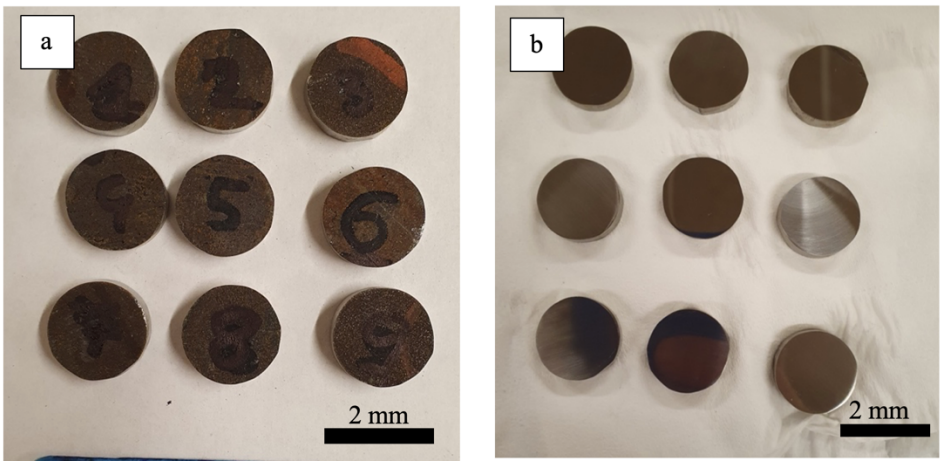

Figure 24: Specimens for corrosion test a) before and b) after grinding

3.2 Surface processing

The samples thus obtained were cut with a silicon blade using the © *Hitech Europe C301* cutting machine to obtain a cross section. Once smaller pieces were obtained, the samples were incorporated through the © *Hitech Europe EP 15* hot mounting press with a thermosetting polymer resin. The purpose of

this operation was to facilitate the analysis and handling of the samples during subsequent operations. The result obtained was cylindrical pastilles with a diameter of 30 mm. An example is shown in Fig.25.

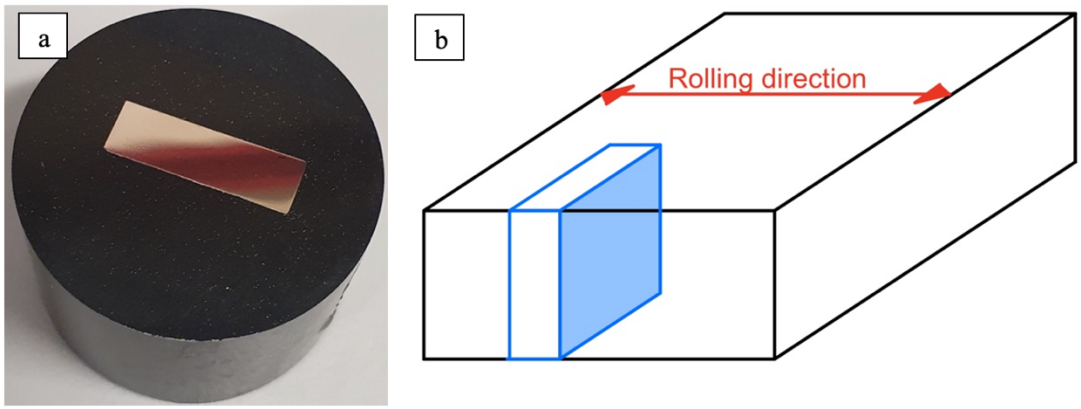

Figure 25: a) HRTT sample after mounting; b) Face of the specimen used for the microstructural analysis (highlighted in blue) respect the rolling direction

To prepare the surface for microstructural analysis, the samples were subjected to a grinding operation using rotating silicon carbide plates, with water as a lubricant, to reduce roughness from 200 µm to 10 µm. This operation was performed using either the © *Hitech Europe MP311T* or the © *Metkon Forcipol V* metallographic machines.
The next step involved polishing, which was carried out using diamond suspensions of 6 µm and then 1 µm, with lubrication on rotating cloth plates. The metallographic polishing machine used was the © *Hitech Europe MP22V*.
Finally, a chemical etching was performed on the samples to analyze with the optical microscope using a NITAL10 (10% nitric acid, 95% ethanol) or a NITAL2 (2% nitric acid, 98% ethanol) depending on the condition analyzed, which were selected based on the experience of the research team at Politecnico di Milano.
Also the samples obtained for the bending and corrosion tests were grinded, with the rectangular samples being roughly polished to remove the oxide layer in surface, while the circular samples were grinded until a roughness of 10 µm on both sides (with the exception of the sample 2, grinded until 6 µm on one side and 20 µm on the other), as reported in Fig.24b.

3.3 Test and analysis

Chemical composition and density

The real chemical composition of the alloy was determined using OES analysis and compared to the nominal composition. A total of 9 measurements were taken for this purpose.
Subsequently, the density of the steel was assessed with different methods and the results were compared, in order to determine the effectiveness of the alloying element addition on the density reduction. Firstly, the equation described in Paragraph 1.3 was used to measure the theoretical density. Secondly, 4 measurements were taken with the hydrostatic balance © *Mettler-Toledo* (which is shown in Fig.26a) for two samples shaped as rectangular cuboids of different dimensions. Finally, the density was computed as the ratio mass/volume, with the mass measured by a lab balance (3 measures for each sample) and the volume computed from the measurements taken with a caliber (3 measures for each of the 3 dimension of the samples), as shown in Fig.26b.

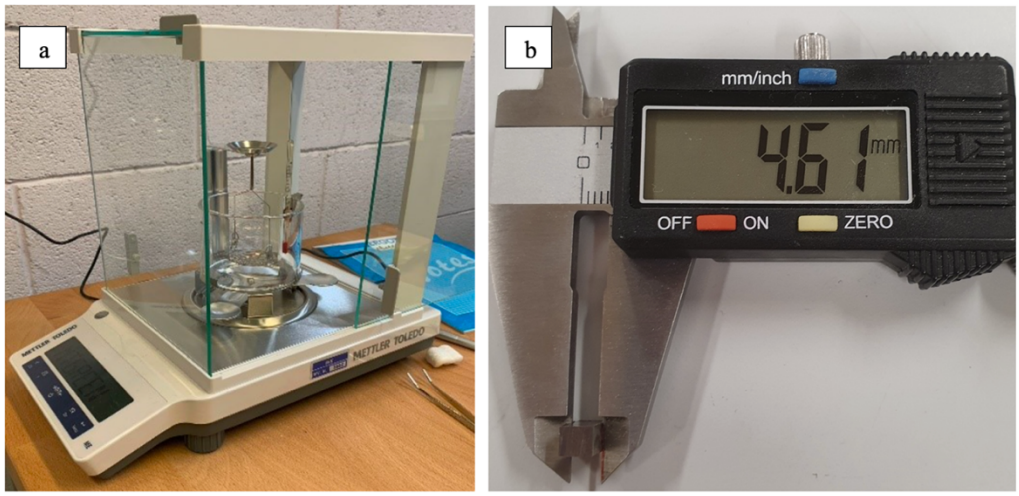

Figure 26: a) the hydrostatic balance; b) example of measurement taken with the caliber

Optical microscopy, SEM, EBSD and EDS

The optical microscope was used to collect high quality pictures, representative of the steel's microstructure, at different magnifications. In this step, the four hot-rolled samples were analyzed at 3 magnifications: 50x, 100x and 200x; the cold-rolled and the welded specimens instead at 100x, 200x and 500x. The equipment used consist in a © *Nikon Eclipse LV150NL* optical microscope, a © *Nikon Digital Sight DS-U3* camera and the © *Nikon NIS Elements v4.60 software.* In addition, to study the microstructural evolution of

the alloy as a function of the thermo-mechanical treatments applied, the average grain size and the austenitic/ferritic area fractions were calculated. The reference standards were ASTM E112-13 (*Standard Test Methods for Determining Average Grain Size*) and l'ASTM E1181-02 (*Standard Test Methods for Characterizing Duplex Grain Sizes*). To perform the calculations, images obtained by optical microscopy and the © *ImageJ* software were used. For the average grain size, the (Heyn) mean linear intercept (MLI) procedure was used; as required by standards, a magnification of 100x was adopted, and measurements were taken nine times for each sample: three times along each of the three directions (horizontal, vertical and oblique), as shown in Fig.27.

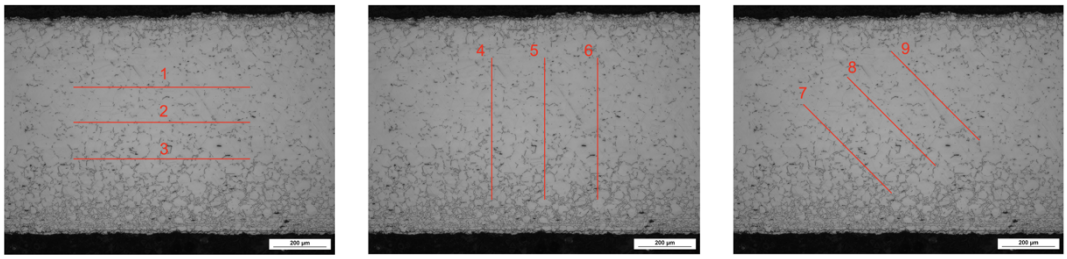

Figure 27: Measurement scheme adopted for the MLI procedure

For the study of κ-carbides and boro-carbides precipitation and the formation of secondary phases, the SEM analysis was performed using a © *Zeiss Sigma500* field emission microscope. The magnification used are: 10000x and 25000x. Moreover, the EDS analysis was exploited for identifying precipitates and secondary phases based on their chemical composition relative to the austenite matrix, providing qualitative insights. In addition, to enhance the understanding of the crystallographic characteristics of the secondary phases and the average misorientation of grains, EBSD analyses was conducted.

Vickers micro-hardness tests

Vickers micro hardness tests were performed by using a © *Future-Tech FM-810* micro-hardness tester. The reference for the choice of the regions for the execution of the measurements and for the load selection was taken from the ASTM E92-17 standard (*Standard Test Methods for Vickers Hardness and Knoop Hardness of Metallic Materials*) [42]. The testing load was set at 100 g, 300g or 1000 g depending on the specimen tested (more indications are given with the results) and the dwell time at 10 seconds. In all the hot/cold-rolled specimens at least 5 measurements were repeated on each sample for statistical significance.
For the welded specimen instead, a specific plan was adopted. For the cladding, as depicted in Fig.28, three measurements were taken in the center

of the weld zone (WZ), three in an area of the base material (BM) far from the weld, and 18-24 measurements on three lines radial to the zone of material deposition, intercepting the weld zone, the heat-affected zone (HAZ) and the base material adjacent to the HAZ.

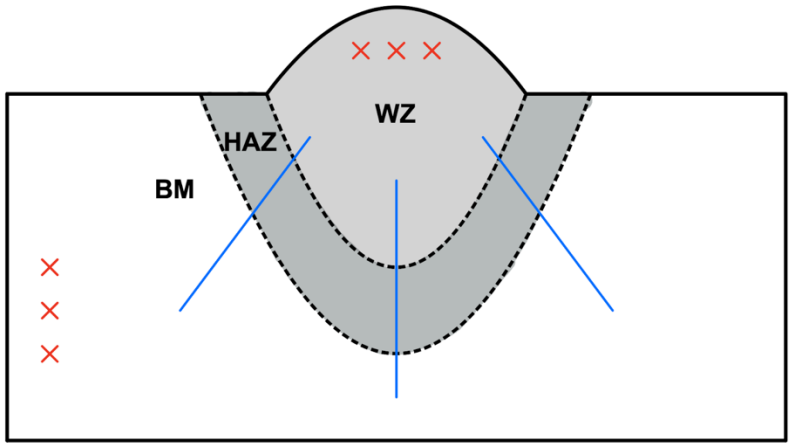

Figure 28: Schematization of the micro-HV test plan on the cladding welds

Similarly, for the double-V butt welds, three measurements were taken for each WZ, five in the HAZ and three in an area of the base material (BM) far from the weld. However, 12-16 measurements were taken as in the cladding case (on two lines radial respect the material deposition zone) and 12-16 on two horizontal lines in the inner part of the sample. A schematization of the plan is shown in Fig.29.

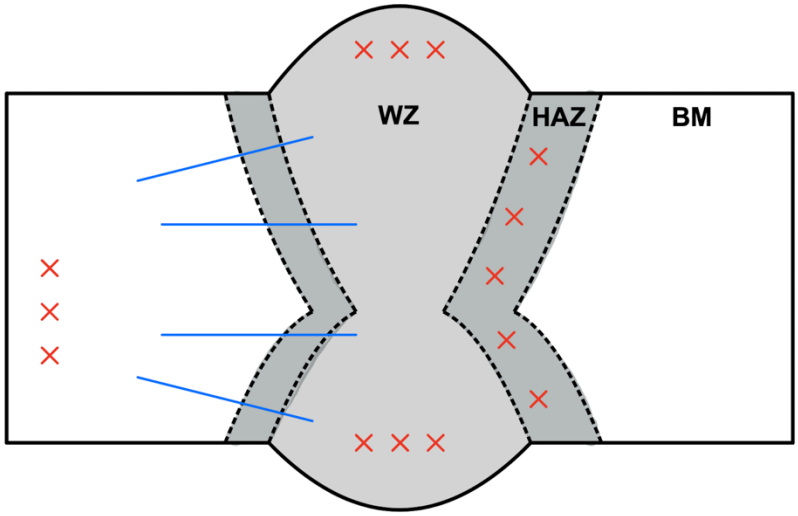

Figure 29: Schematization of the micro-HV test plan on the double-V butt welds

Anisotropy test

For the evaluation of the anisotropy of the alloy in the hot rolled condition, tensile tests at 10% elongation were conducted on three samples for each of the orientation described in Paragraph 3.1. The deformation velocity was set at 3 mm/min; the thickness and width of the specimens were measured with a micrometer at three points along the Gauge length for each specimen, both before and after the tests. The collected data were used to evaluate the plastic strain ratio (r-value), the normal anisotropy ratio (r_m), and the planar anisotropy parameter (Δr) [43].
The r-value is a coefficient used to measure the metal alloy's resistance to thinning and is the ratio between the true width strain and the true thickness strain at a specific value of longitudinal strain up to that of uniform elongation. The equation is as follows:

$$r = \left\{ \frac{ln\frac{w_f}{w_0}}{ln\frac{t_f}{t_0}} \right\}$$

where w_f = final width; w_0 = initial width; t_f = final thickness; t_0 = initial thickness;

An r-value of 1 indicates that the sheet has a similar response to deformation in both the width and thickness directions.
The r_m instead defines the ability of a material to deform in the thickness direction relative to deformation in the plane of the sheet. For complete anisotropy, r_m should be equal to 1. The equation is as follows:

$$r_m = \frac{(r_0 + 2r_{45} + r_{90})}{4}$$

Where r_x is the r-value at x° respect the rolling direction.

Finally, the Δr expresses the ability of a material to demonstrate non-earing behavior. A value close to zero indicates equal metal flow in all directions, which is desirable for operations such as deep drawing. The equation is as follows:

$$\Delta r = \frac{(r_0 - 2r_{45} + r_{90})}{2}$$

Where r_x is the r-value at x° respect the rolling direction.

Welds tensile test

The tensile strength and the elongation of the welded samples were evaluated. In particular, three samples from the AC and three from the DC welded plates, were tested. The deformation speed was set at 3 mm/min. The specimens, the test apparatus, and the set parameters were selected in accordance with the ASTM E8/E8M-21 [44] (*Standard Test Methods for Tension Testing of Metallic Materials*), ASTM A370-20 [45] (*Standard Test Methods and Definitions for Mechanical Testing of Steel Products*), and ASTM A505-16 [46] (*Standard Specification for Steel, Sheet and Strip, Alloy, Hot-Rolled and Cold-Rolled, General Requirements* for) standards.

Bending Test

For the bending test, a three-point guided test was performed using 20 mm diameter rollers as supports, with a distance of 70 mm between them. The deformation speed was set at 25 mm/min. The complete setup prior to the test is shown in the Fig.30a. For each specimen, Force (normalized on the specimen's width) [N/mm]/Displacement [mm] curves were obtained, and the following equations were used to calculate the Flexural Stress [MPa]/Flexural Strain [%] curves [47], [48]:

$$\varepsilon_f = \frac{600dh}{L^2}\%;\ \sigma_f = \frac{3FL}{2bd^2};$$

Where ε_f = flexural strain, σ_f = flexural stress [MPa], d = crosshead [mm] (function of time), h = thickness of the specimen (3 mm for the thin specimens and 5 mm for the thick specimens), L = support distance [mm], F = force [N] (function of time), b = width of test beam [mm] = 30 mm.

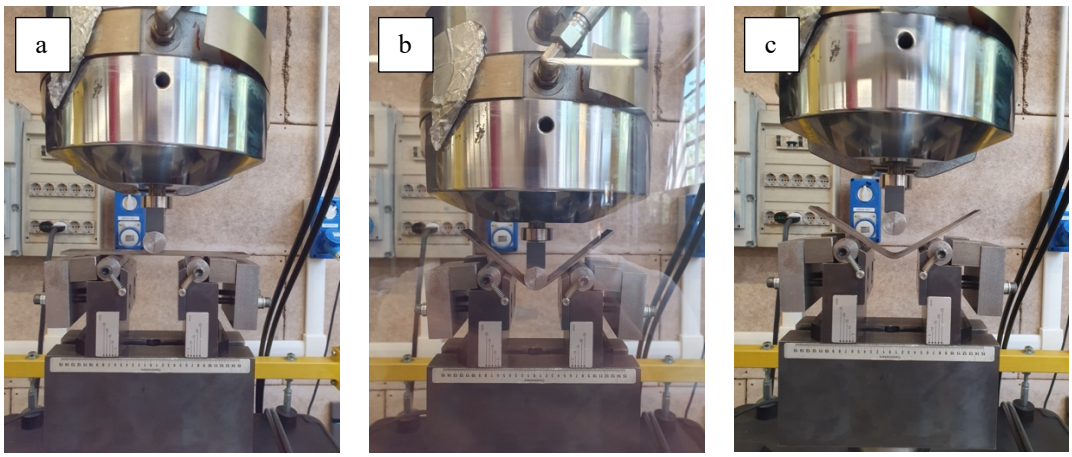

Figure 30: Setup a) before the bending test, b) with the mold closed, c) after releasing the load

Additionally, in order to evaluate the springback factor K_s, photos were taken for each sample before the test, before (Fig.30b) and after (Fig.30c) the load

was released. Using these photos, the alpha angle (bending angle) was evaluated taking three measurements for each condition using the © *ImageJ* software, as shown in the Fig.31. The springback factor was calculated using the following equation [49]:

$$K_s = \frac{\alpha_f}{\alpha_i}$$

where α_i = bending angle with closed mold (Fig.30b) [°]; α_f = bending angle after releasing the load (Fig.30c) [°].

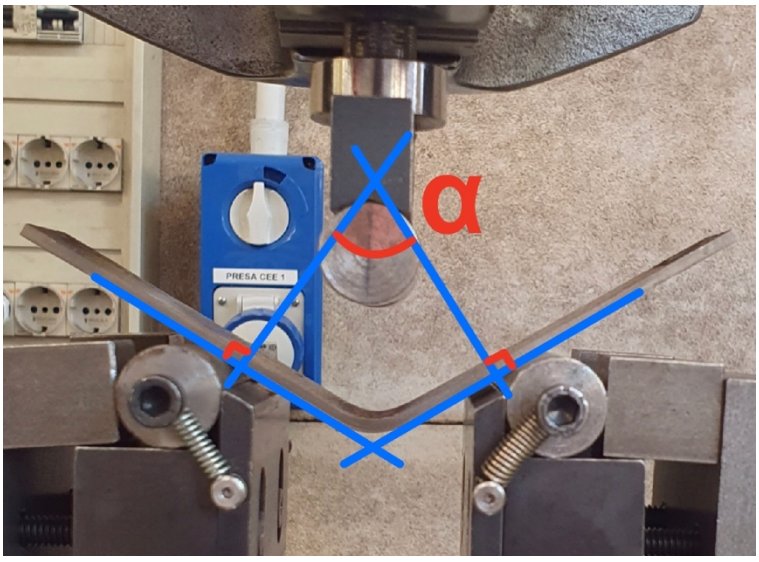

Figure 31: bending angle α (after releasing the load)

Finally, as indicated by the ASTM E290-22 standard [50] (*Standard Test Methods for Bend Testing of Material for Ductility*) the convex surface and the edges of the bent specimens were examined to detect any crack or other open defect derived from the test. For this purpose, a stereomicroscope was used.

Potentiondynamic corrosion test

A saline solution consisting of water and 0.6 mols of NaCl, prepared using 800 ml water and 28.224 g NaCl, was used for potentiodynamic anodic polarization tests. Tests were conducted at 25°C on the specimens shown in Fig.24, of

5mm thickness, by the use of a potentiostatic galvanostat © *Amel Electrochemistry MODEL 2553*.
The area of contact between the samples and the solution was of 0.785 cm^2.
The complete setup is shown in Fig.32.
Regarding the parameters:

- initial potential: -1500 mV;
- final potential: -100 mV;
- step potential: 1 mV.

From the results of the tests, polarization curves were obtained, and some important parameters were extrapolated from them, such as the corrosion potential (E_{corr}), the passivation current density (I_p) and the end-passivation potential (E_{epp}). For test set-up and data extrapolation, the reference standards were the [51] ASTM G3-14 (2019) (*Conventions Applicable to Electrochemical Measurements in Corrosion Testing*) and the [52] ASTM G5-14 (2021) (*Standard Reference Test Method for Making Potentiodynamic Anodic Polarization Measurements*).

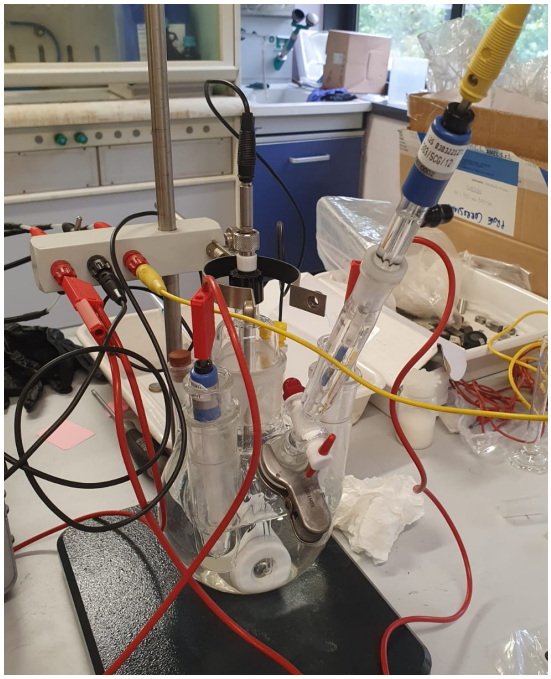

Figure 32: Potentiodynamic test at work

Chapter 4

Results

In this chapter, the main results of the study are presented and briefly commented on. For a more detailed discussion, the reader can refer to **Chapter 5**. The treatment of the topics begins with the chemical composition, density, calculation of the SFE, the anisotropy of the alloy, its corrosion resistance and the bending test results. Subsequently, the microstructure and hardness of the material are addressed, focusing on the different analyzed conditions.

Alloy composition

The OES analysis was utilized to determine the real chemical composition of the alloy. Tab.4 presents the weight fraction measured and a comparison with the nominal chemical composition for the main alloying elements (Fe, Mn, Al, C, B). There were no significant discrepancies found between the actual and nominal chemical composition. However, non-negligible traces of Ta (0.214 wt.%) and Pb (0.191 wt.%) were identified, likely resulting from the casting or rolling process. All the nine measurements taken for the entire database of elements are reported in **Appendix A**.

wt.%	Fe	Mn	Al	C	B
Real	74.94	15.53	7.581	0.994	0.0044
Nominal	75.998	15	8	1	0.0040

Table 4: Comparison between the nominal and the mean of the real chemical composition resultant from the OES analysis

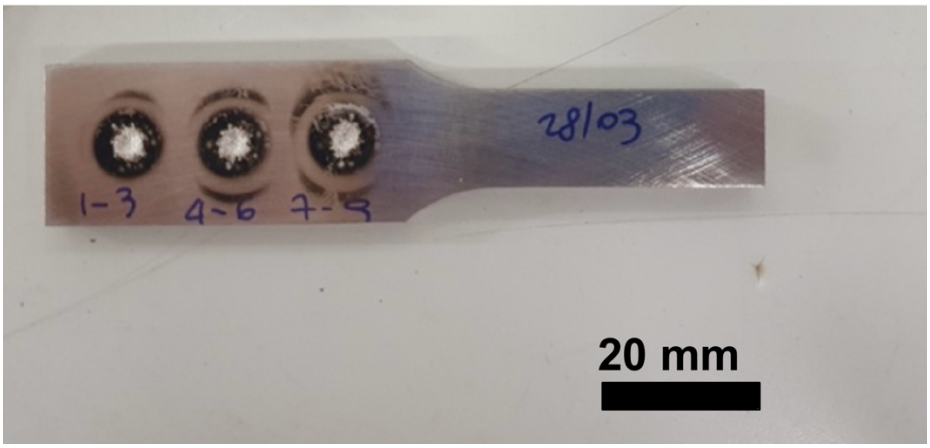

Figure 33: the specimen after the OES analysis. Three tests were conducted

Equilibrium phase diagram

The molar fraction at equilibrium of the constituent phases was predicted by the use of © *Jmat Pro* and © *Thermo-Calc* databases. Fig.34 reports the equilibrium phase diagrams obtained for the nominal and the real chemical composition of the alloy. It can be noticed that with © *Thermo-Calc*, in both cases in the interval between 900°C and 1100°C the alloy microstructure is fully austenitic (green line). A different situation is highlighted by the © *Jmat Pro* results: in the same interval ferrite (yellow line) is consistently present at the expense of the amount of austenite (in gray). No other secondary phases are expected to precipitate in either database between 900°C and 1100°C.

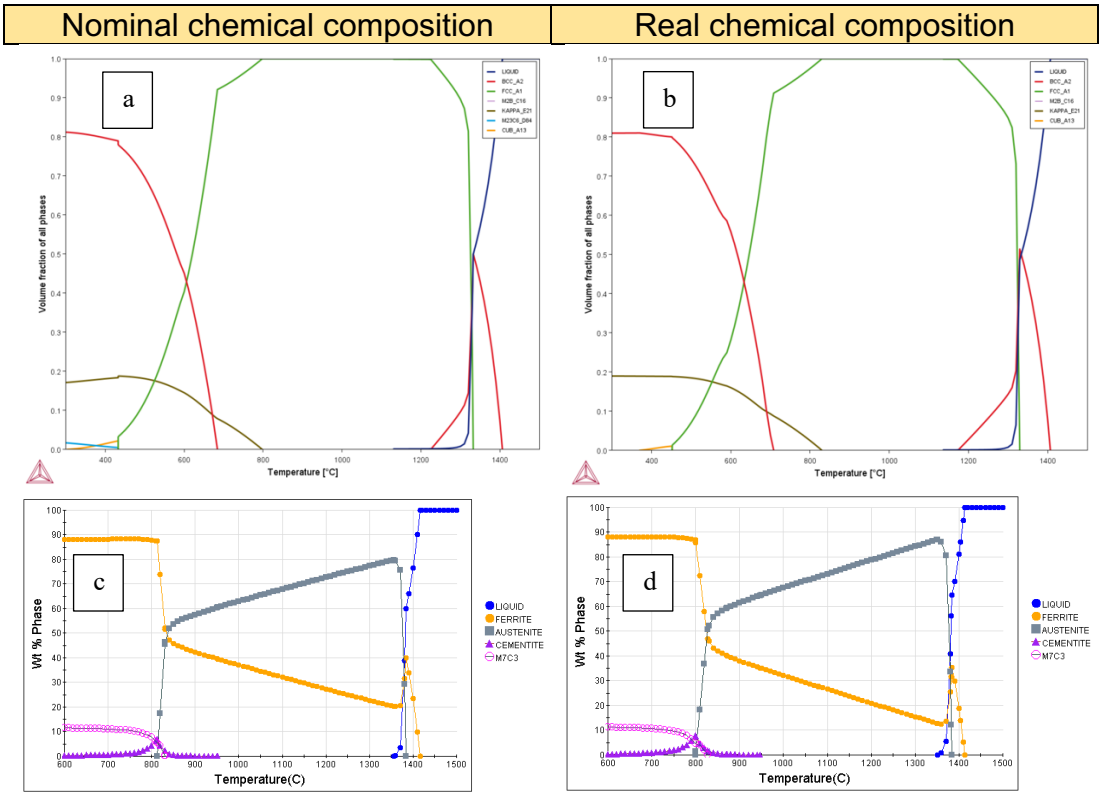

Figure 34: Equilibrium phase diagram for the real and the nominal chemical compositions, computed with a), b) © Thermo-Calc and c), d) © Jmat Pro databases

Both databases are based on experimental data and, probably, do not have a high degree of accuracy for new alloys under development, such as lightweight steels. Therefore, considering the high degree of error, it can be stated that in the above-mentioned temperature range, the microstructure of the alloy may not be fully austenitic. Similarly, this range is of particular interest for the study of this alloy as it should allow the austenite fraction to be maximized.

Density

The density of the alloy was obtained by three different methods: direct measurement (using an Archimedean water balance), calculation from volume and density measurements, and the theoretical method (using an equation from the literature [12]).
The first two methods were applied on two cuboids of different sizes. The results are shown in Tab.5; while Fig.35 shows the averages and standard deviations in two Interval Plots.

Measured density [g/cm^3]	Calculated density [g/cm^3]	Theoretical density [g/cm^3]
6.971 (A) 6.949 (B)	7.060 (A) 6.882 (B)	6.7947 (nominal c.c) 6.7947 (real c.c)

Table 5: Comparison between the densities obtained with the different methods. (A=bigger sample; B=smaller sample)

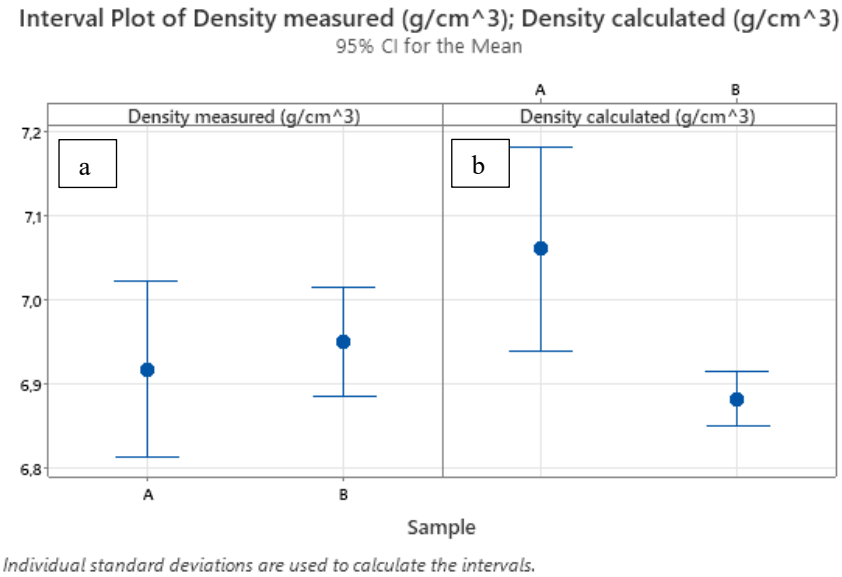

Figure 35: Interval plots for the density a) measured with the Archimedean water balance and b) density calculated using the mass and the volume of the specimens. (A=bigger sample; B=smaller sample)

It can be observed from Fig.35 that the density of the alloy can be placed in the range of 6.9 to 7.0 g/cm^3.

Material	Density	Density reduction
Fe-15Mn-8Al-1C-40ppmB	6.9 - 7.0 g/cm^3	-
Conventional austenitic steel	8.15 g/cm^3	15%
Conventional ferritic steel	7.87 g/cm^3	12%
Conventional HSS	7.80 g/cm^3	11%
AISI 304	7.93 g/cm^3	13%

Table 6: Comparison of the density of Fe-15Mn-8Al-1C-40ppmB and the density of major steels used for automotive applications

In Tab.6 [9], [53], [54], the alloy density is compared with that of the main steel grades for automotive applications. It can be seen that the density reduction compared with conventional HSS, austenitic and ferritic steels is larger than 10%.

SFE

Simulation software © *Jmat Pro* was used to calculate the value of Stacking Fault Energy (SFE) as a function of the temperature, considering the real chemical composition of the alloy, obtained by OES analysis. As shown in Fig.36, the relationship between these two parameters is linear, and at ambient temperature the SFE value is about 160 mJ/m^2. As reported in Paragraph 2.5, for values above 80 mJ/m^2, the main deformation mechanisms to be considered are Shear Induced Plasticity (SIP) and Microbands induced plasticity (MBIP). In particular, SIP is activated when κ-carbides are present in the form of precipitates in the microstructure of the alloy. In their absence, it is therefore possible to say that the dominant mechanism is the MBIP.

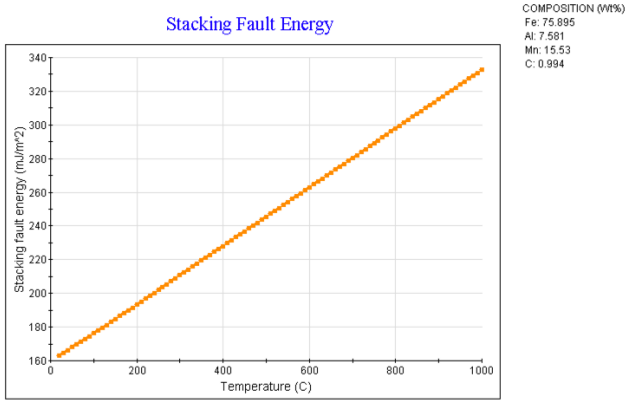

Figure 36: Relationship between temperature and SFE, calculated with the © Jmat Pro simulation software

Anisotropy

The samples used for the tensile test are shown in Fig.37a before and Fig.37b after the test.

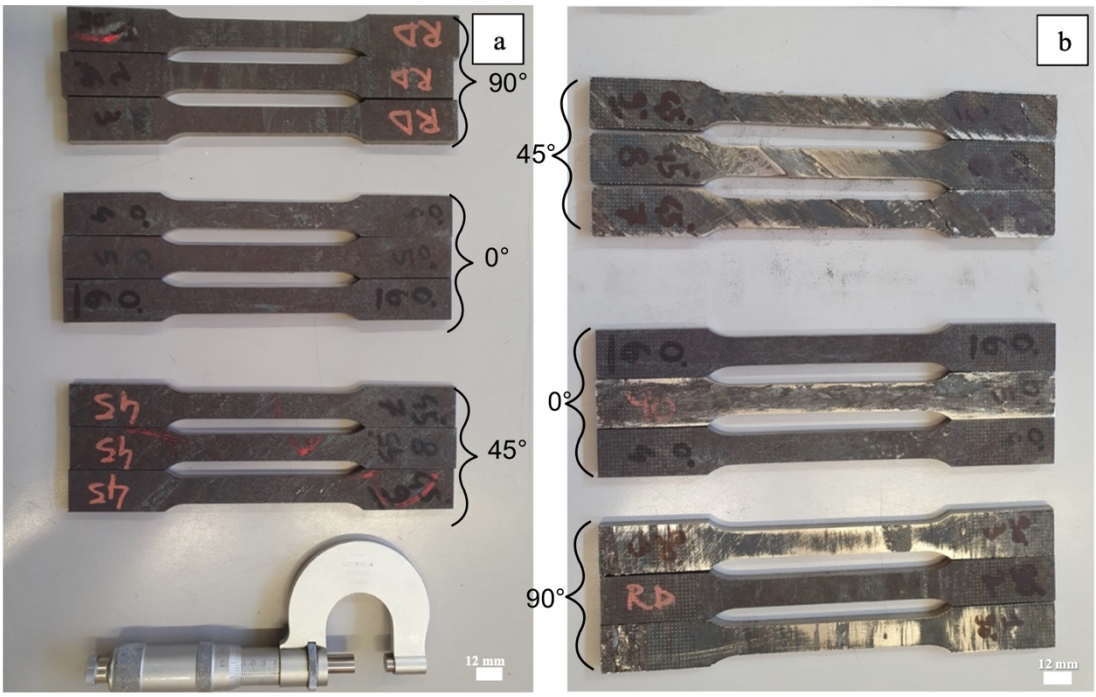

Figure 37: Tensile test specimens with their orientation respect the rolling direction: a) before and b) after the test

From the results of the tensile tests performed at 10% elongation, it was possible to calculate the values of r, r_m and Δr. Results are shown in Tab.7 and Fig.38.

As it can be observed, the mean of r is close to 1 for each direction, even if for a direction of 90° respect the rolling direction the standard deviation is quite large. Regarding r_m instead, its average value is around 1, with a small standard deviation. This indicates that the alloy has an almost completely anisotropic behavior, which is a good feature for the automotive industry, where most components are obtained by forming operation.

Finally, Δr has a mean close to zero, which indicates a non-earing behavior, although again the standard deviation is quite high.

r_{90}	r_{45}	r_0	r_m	Δr
1.034	0.891	0.897	0.928	0.075
1.413	0.935	1.045	1.082	0.293
0.855	1.070	0.995	0.998	0.144

Table 7: Values for r, r_m and Δr calculated after the tensile tests. Each row represents a different specimen

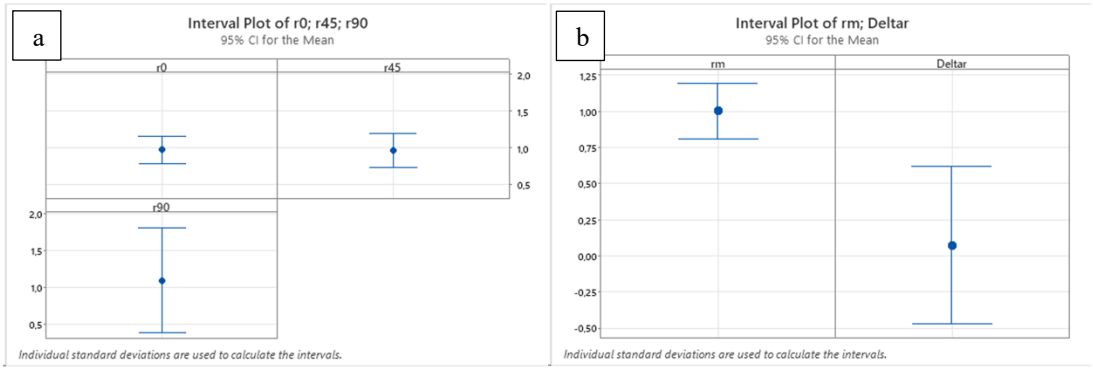

Figure 38: Interval plots for a) r-value in direction 0°, 45° and 90° respect the rolling direction and b) r_m and Δr

Bending test

Using the data obtained from the three-point guided bending test, it was possible to derive the Force normalized on the specimen's width [N/mm] vs Crosshead [mm] (Fig.39) and Flexural Stress [MPa] vs Flexural Strain [%] (Fig.40) curves for each tested specimen. In all tests carried out, the desired bending angle was approximately 75° and it was imposed by the machine configuration. As shown in the figures, all curves are characterized by an initial linear segment, followed by a change in slope until reaching the maximum force or stress. After the peak, there is a decrease in force and stress until the end of the test.

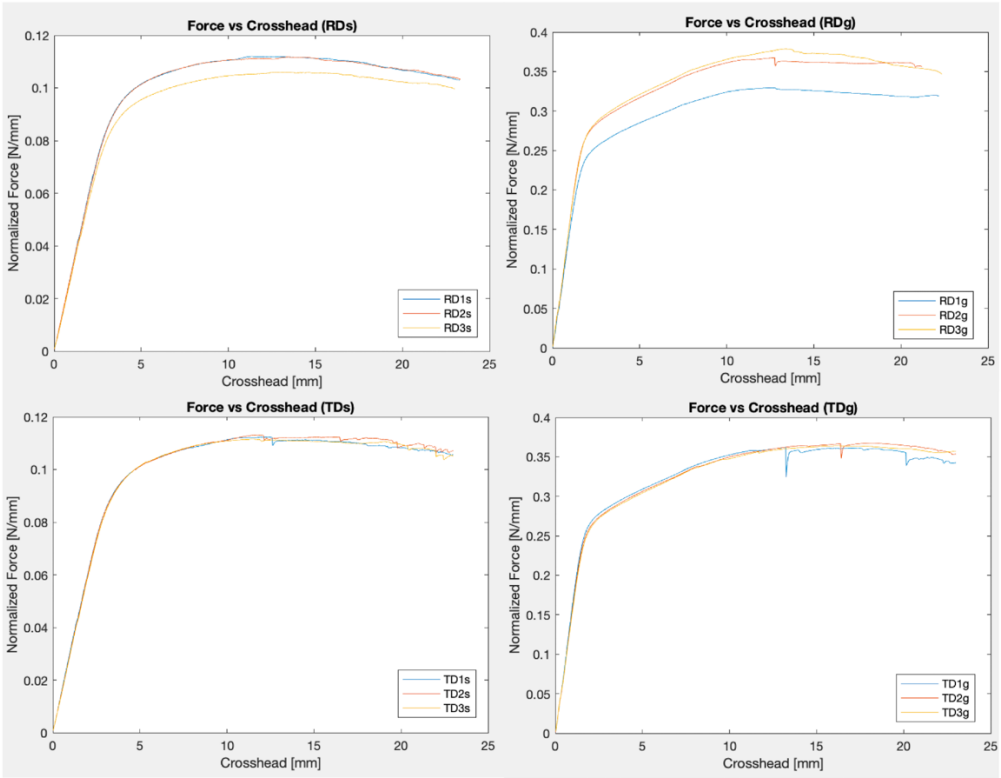

Figure 39: Normalized Force [N/mm] vs Crosshead [mm] curves obtained after the tests for the a) 3 mm samples oriented along the rolling direction (RDs); b) 5 mm samples oriented along the rolling direction (RDg); c) 3 mm samples oriented transversally respect the rolling direction (TDs) and d) 5 mm samples oriented transversally respect the rolling direction (TDg)

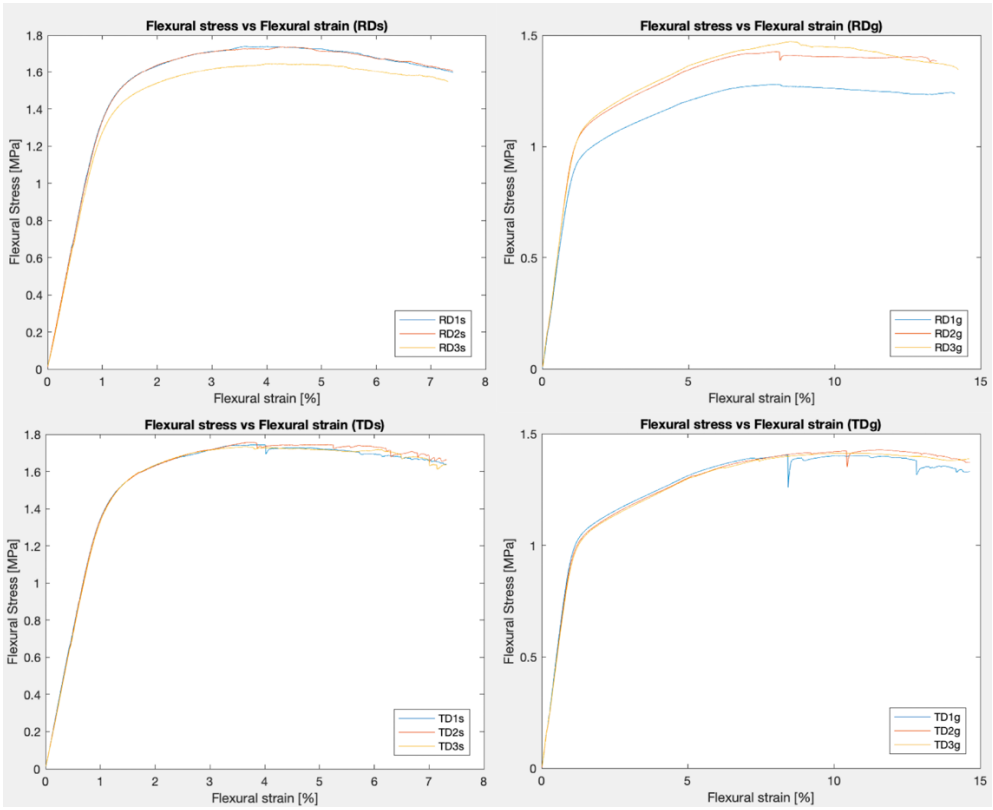

Figure 40: Flexural Stress [MPa] vs Flexural Strain [%] curves obtained after the tests for the a) 3 mm samples oriented along the rolling direction (RDs); b) 5 mm samples oriented along the rolling direction (RDg); c) 3 mm samples oriented transversally respect the rolling direction (TDs) and d) 5 mm samples oriented transversally respect the rolling direction (TDg)

Values of stress and strain at the transition point between the initial linear segment and the variable-slope line (identified in this study as σ_y and ϵ_y) and maximum stress (σ_{max}) point were then obtained from each curve and reported in Fig.41. It can be deduced from the measurements that the different orientation of the deflection with respect to the rolling direction does not affect the force or stress applied.

For the samples with a thickness of 5 mm, in the transition point σ_y is around 0.8 MPa and ϵ_y is approximately 0.85%. Additionally, the maximum stress reaches 1.4 MPa. On the other hand, for the samples of 3 mm, σ_y and ϵ_y are approximately 1.1 MPa and 0.8%, respectively, with a maximum stress of 1.7 MPa.

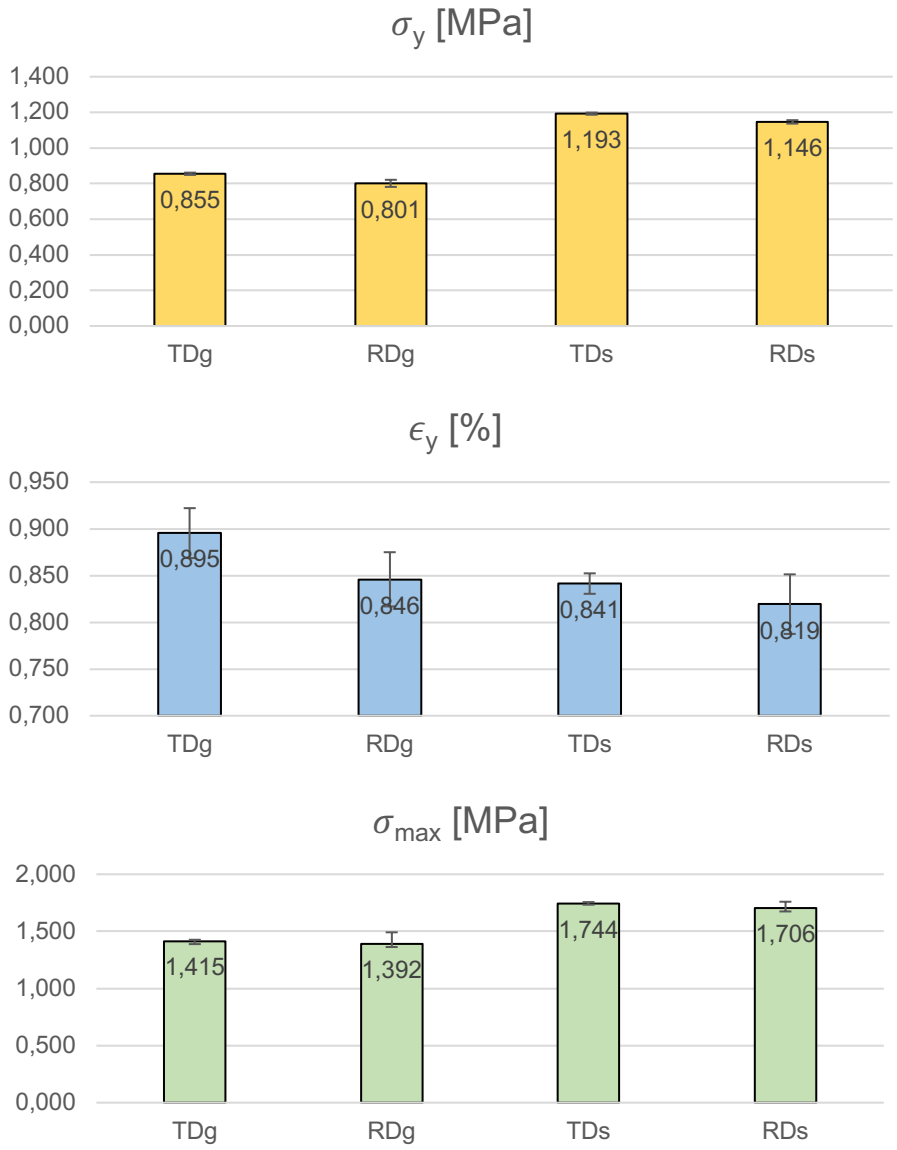

Figure 41: Mean values of Yield Stress [MPa], Yield Strain [%] and Maximum Stress [MPa] values extrapolated from the curves

Additionally, the bending angle was measured before and after the load release (as shown in Fig.42). This analysis allowed to derive the elastic return angle and the springback factor, which are shown in Tab.8 for each sample group.

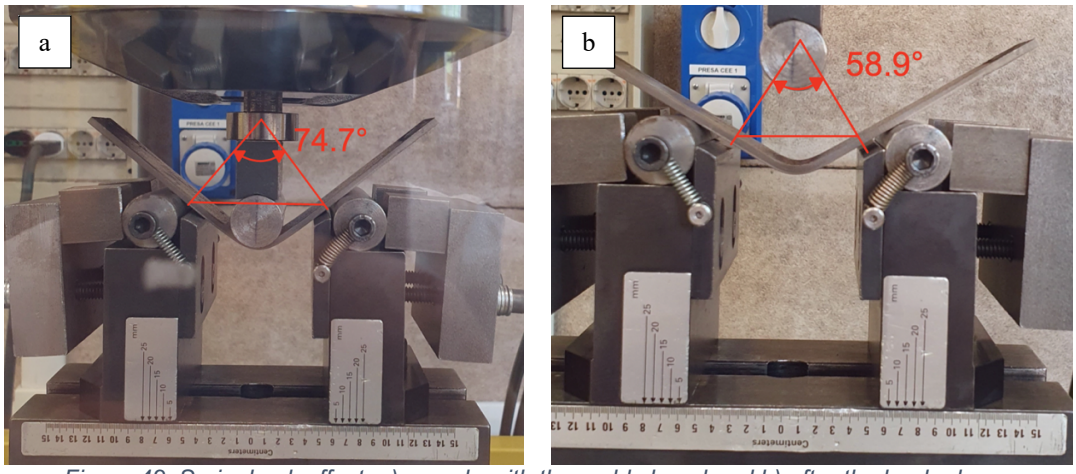

Figure 42: Springback effect: a) sample with the mold closed and b) after the load release

In particular, as described in the literature, the springback factor mainly depends on the ratio between the internal bending radius (which remained constant in these tests) and the sample thickness [49]. For the same bending radius, a greater thickness corresponds to a lower springback factor. This observation is also confirmed by the data on the elastic return angle reported in the table, where a larger elastic return was observed in the 5 mm samples compared to those of 2 mm. It is important to emphasize that the achieved bending angles of 75° before and 60-65° after load release represent an excellent result for the material, confirming its outstanding ductility.

Sample type	Springback Factor (K_s)	Elastic Return Angle [°]
TDg	0.782	16.450
RDg	0.765	17.980
TDs	0.876	9.580
RDs	0.891	8.186

Table 8: Mean K_s and Elastic Return Angle for the TDg (transverse direction – 5 mm), RDg (rolling direction – 5 mm), TDs (transverse direction – 3 mm) and RDs (rolling direction – 3 mm) specimens

Furthermore, the inspection of each sample after the test did not reveal the development of any cracks. In Fig.43 are reported the pictures taken for the inspection visual inspection of the RD1s specimen; the complete set of images is reported in **Appendix B.**

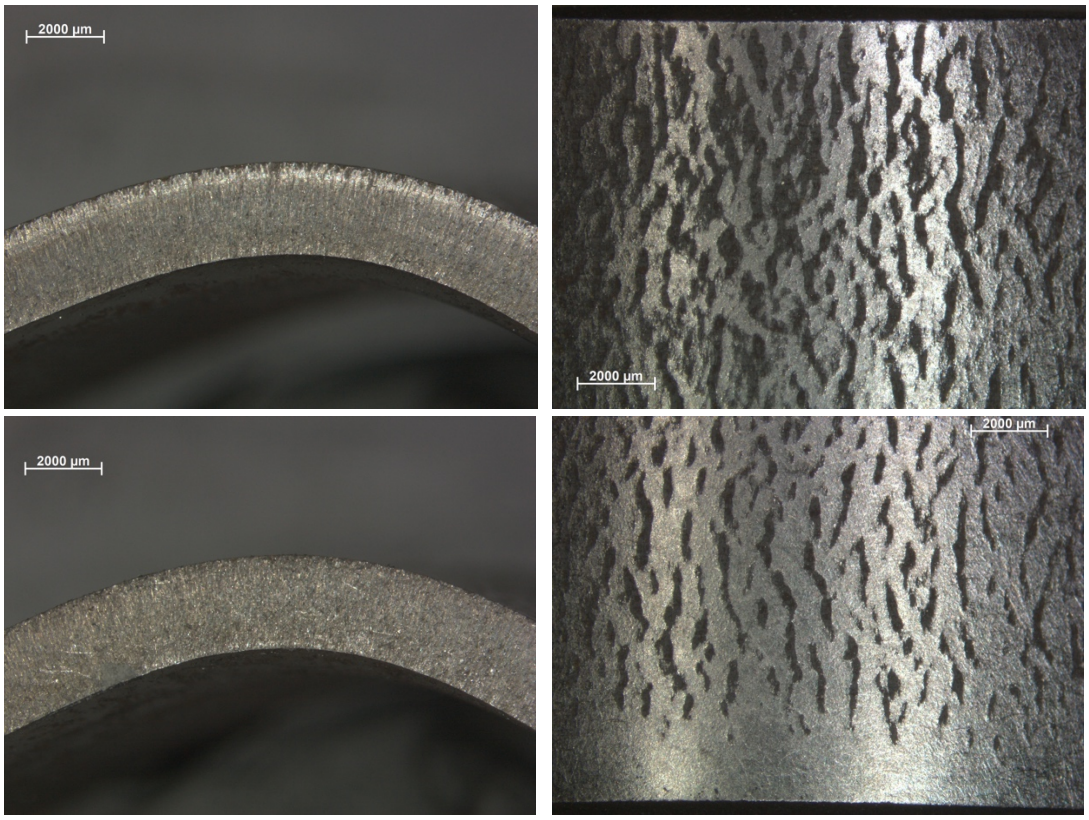

Figure 43: Images taken at the stereomicroscope for the visual inspection of cracks initialized during the test

Potentiondynamic corrosion test

All polarization curves obtained for each sample are individually shown in **Appendix C**. In Fig.44, instead, all polarization curves derived from the tests performed on both sides of the nine samples are plotted on a single graph.

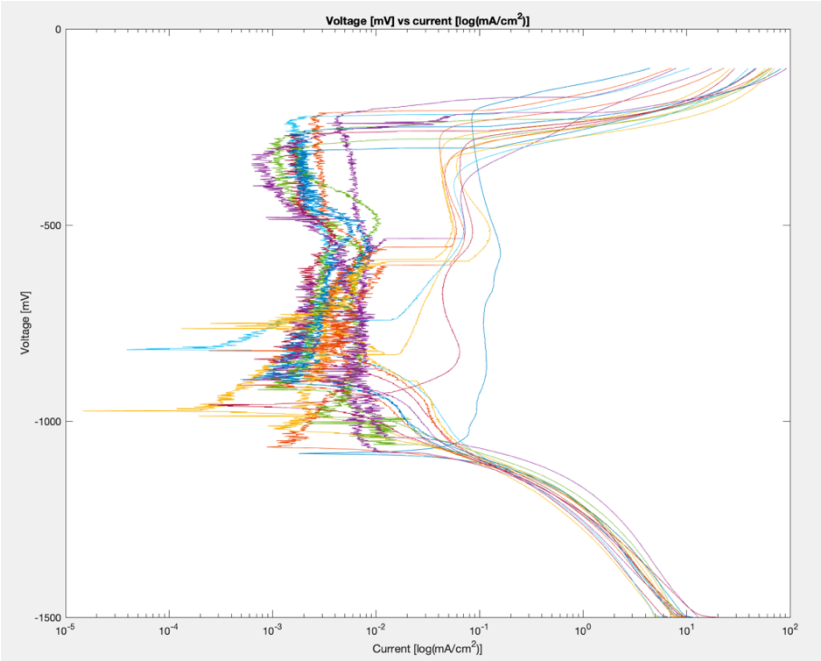

Figure 44: Polarization plots for a passive anode representing all the tests performed. Each color represents a different test

Following the indication of the standards (shown in Fig.45 [51], [52]), E_{corr} and I_p values were extrapolated from each curve. In addition, also the potential value in the transition point between the passive and the transpassive region (E_{epp}) was extrapolated.

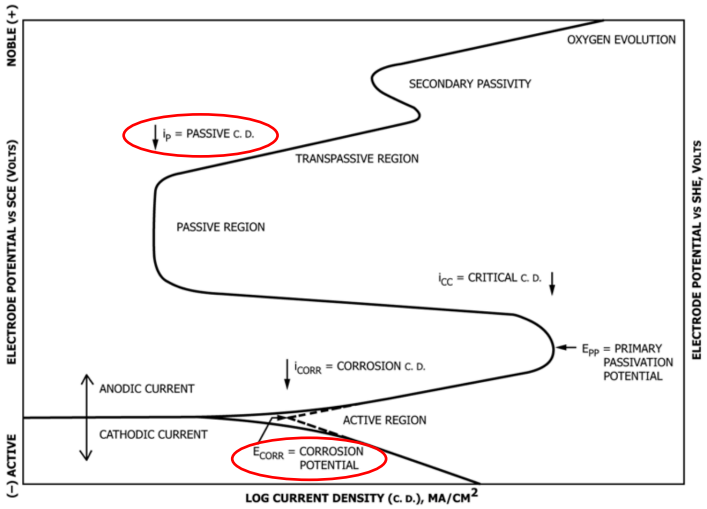

Figure 45: Hypothetical polarization plot for passive anode

From Fig.44, it can be observed that most of the curves have a very similar trend and are concentrated within the same area. However, some curves have a different trend compared to the main group and appear to be distorted. This could be related to errors in the test setup or contaminations in the solution used. Therefore, for the calculation of the average value of E_{corr}, I_p, and E_{epp} only the 14 most similar curves were considered, excluding the distorted ones. The results obtained are shown in Tab.9.

E_{corr} [mV]	I_p [$\mu A/cm^2$]	E_{epp} [mV]
-914 ± 70	0.00390 ± 0.00171	-262 ± 36

Table 9: Corrosion potential and passivation current density values extrapolated from the test plots

As also shown in Fig.46a-b-c, the range for the corrosion potential is between -984 mV and -844 mV, meanwhile the passivation current between 0.00219 $\mu A/cm^2$ and 0.00561 $\mu A/cm^2$ and the end-passivation potential between -228 mV and -226 mV.

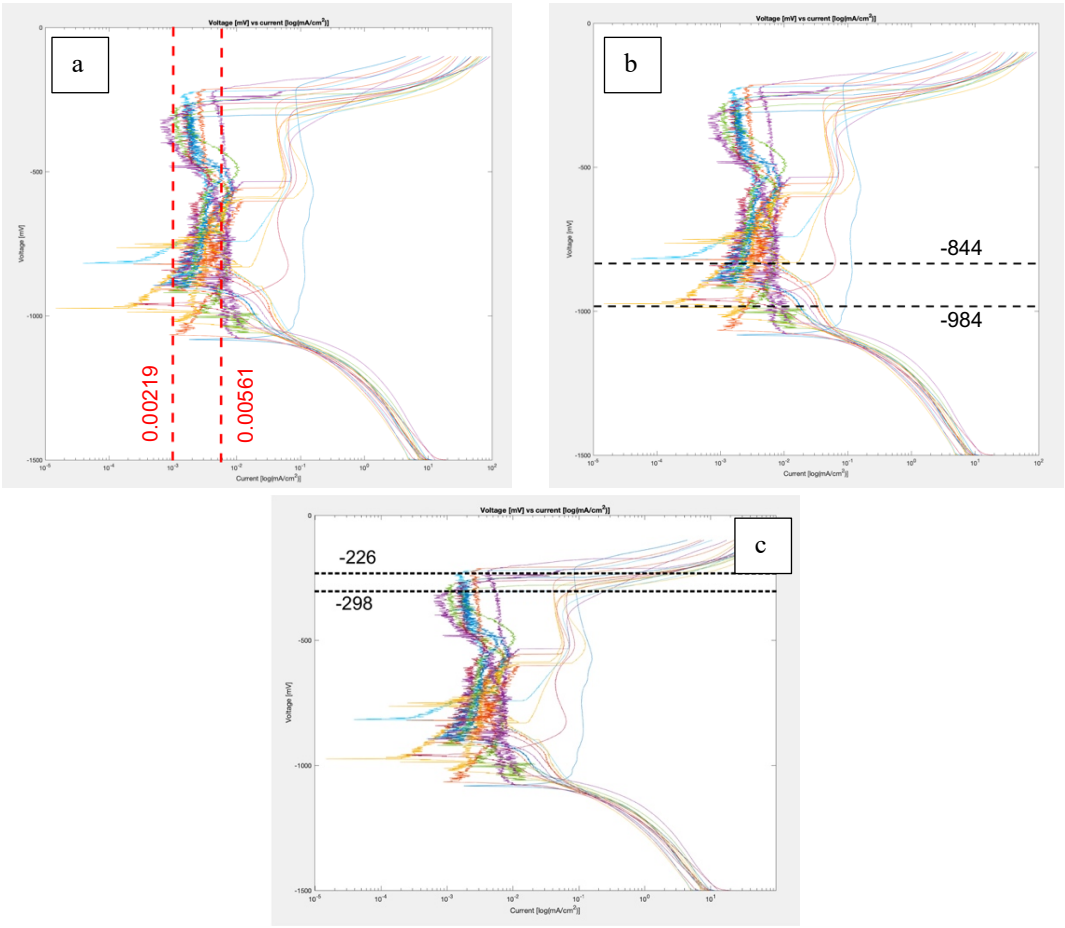

Figure 46: representation of the estimated ranges for: a) passivation current density; b) corrosion potential; c) end-passivation potential

4.1 Microstructural and mechanical evolution

In this paragraph, microstructural evolutions due to thermo-mechanical and welding processes performed on the alloy are presented. The conditions of hot-rolling (both as a base and with solution treatments), cold-rolling at different thicknesses, cold-rolling and solubilization at various temperatures and times, cladding welding and double-V butt welding are described. For each specimen, a specific section was examined, focusing on the outgoing rolling direction (as in Fig.25). Analysis results include data obtained through XRD, light microscope and SEM observations, EBSD and EDS analysis, average grain size measurements and microhardness tests. The complete set of micrographs of each sample is included in **Appendix D**.

Hot-rolled → solution treatment

The microstructural evolution of the material in the hot rolled condition and after solution treatment at two different temperatures is shown in Fig.47. From the figure, it can be noticed that in the hot-rolled condition, as received from the manufacturer, the material presents a completely austenitic structure. The grains appear to be small in size and equiaxed in structure, without any preferred grain orientations. However, after solution treatment at 900°C, fine ferrite can be identified precipitating at the grain boundaries of the austenitic matrix; it can be observed that it is randomly distributed within the sample. On the other hand, with a treatment at 950°C, the precipitated ferrite is coarser and concentrated mainly at the sample boarders. In all the three cases presented, a large number of twins can be distinguished.

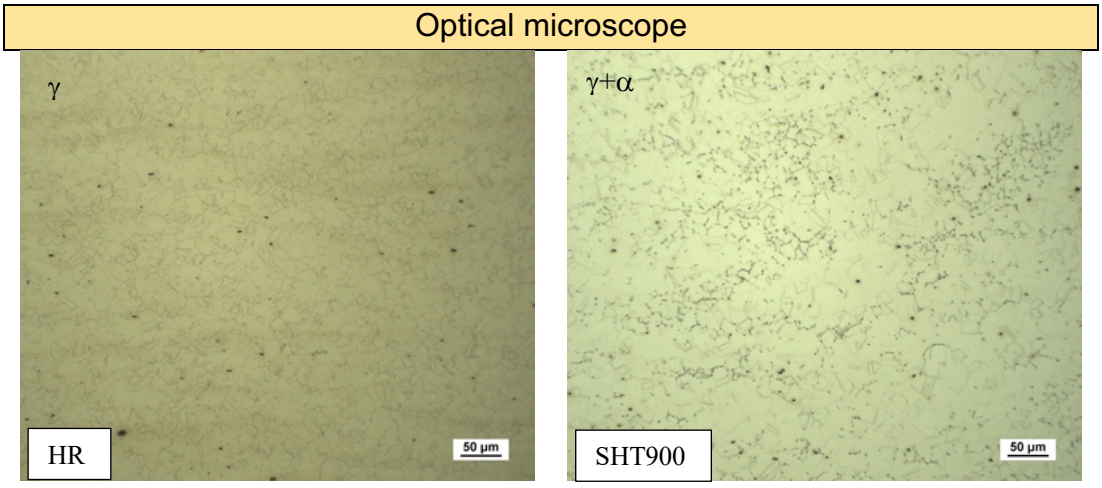

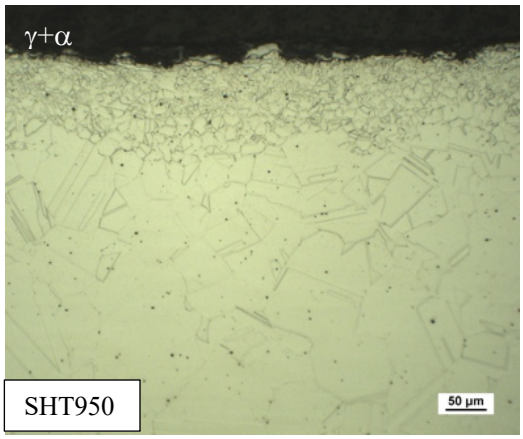

Figure 47: Microstructure of the hot-rolled (HR), solutioned at 900°C (SHT900) and at 950°C (SHT950) samples at the optical microscope (200x)

Fig.48 shows the peaks resultant from the XRD for the three specimens. Peaks at 42°, 49°, 73°, 88° and 94° are present in all the cases, indicating the presence of an austenitic matrix. Furthermore, for the solutioned samples, an additional peak is detected at 44°, which is associated with the presence of ferrite. In any case characteristic peaks of κ-carbides were not identified.

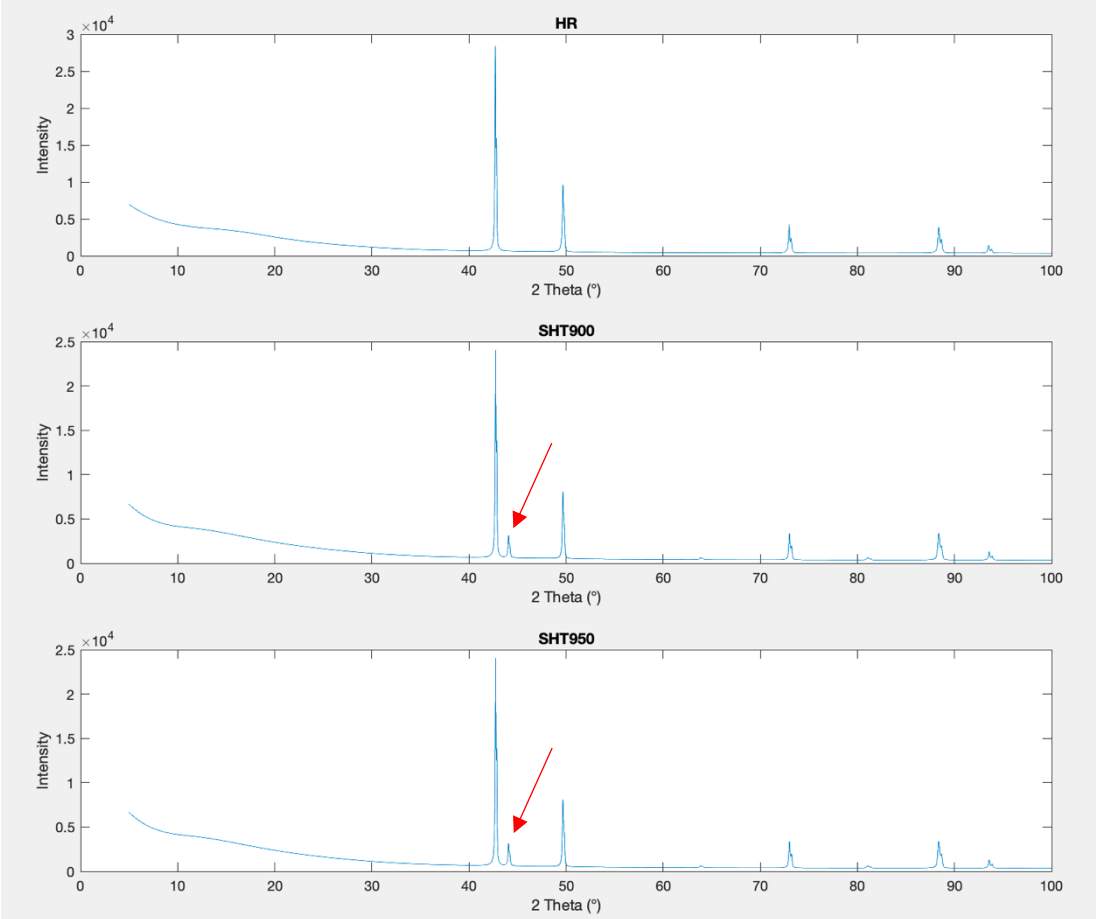

Figure 48: Peaks at the XRD for HR, SHT900 and SHT950 specimens

The results of the average grain size analysis are reported in Tab.10. The dependence of the size of austenitic grains on the solubilization temperature is shown graphically in Fig.49. In the hot rolled case, the microstructure appears to be quite fine, around 15 μm thanks to the recrystallization that occurs during the rolling process. The solution treatment, on the other hand, increases the grain size and, in particular, as the treatment temperature increases, the grain size also increases.

Average grain size		
HR	SHT900	SHT950
14.55 μm	31.93 μm	59.62 μm

Table 10: Average grain size results for the hot-rolled and solutioned samples. As described by the ASTM E1181 – 02 standard the measurement for the SHT950 (identified as cross-section condition) was done in the zone with and without ferrite

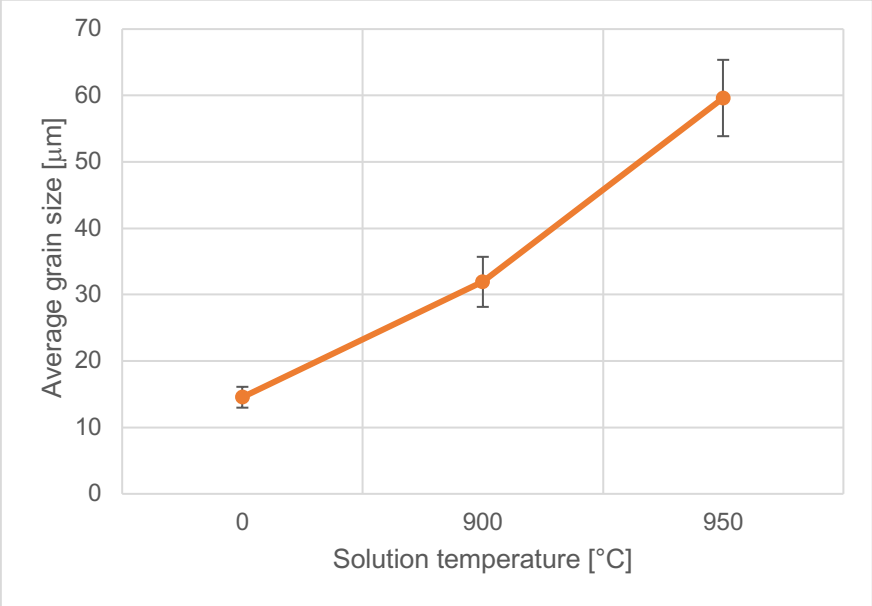

Figure 49: Average grain size plot of the hot-rolled and solutioned samples for different treating temperatures

The EDS analysis for the hot rolled sample detected significant segregations of Fe and Mn, and with less evidence, of Al (Fig.50b,c,d). In particular, it was possible to identify two types of regions with different concentrations of Mn: some Mn-rich bands, brighter in the figure (with about 17.4 wt.% of Mn), and some Mn-poor bands darker in the figure (with about 13.3 wt.% of Mn). According to the literature, the precipitation of ferrite is expected to occur within the Mn-depleted bands, while MnS precipitates within the Mn-rich bands [1], [9]. However, as observed with optical microscope, it can be seen that the identified ferrite seems to be present in very small amounts, with most of the precipitates being MnS.

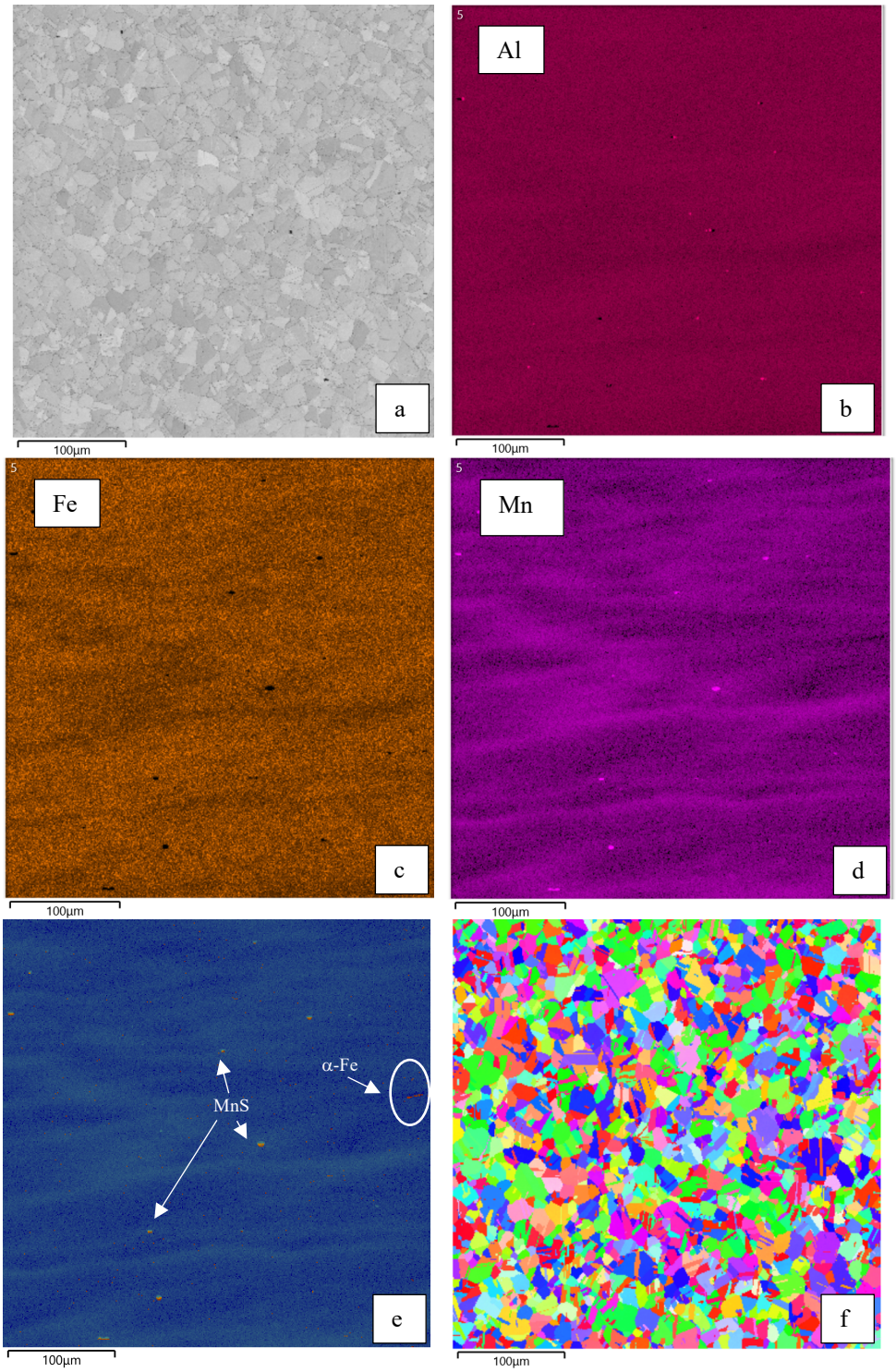

Figure 50: a) – d) EDS compositional map; e) ferrite (in red) and MnS (in yellow) identification; f) inverse pole figure map respect z axis obtained from EBSD for the hot rolled sample

Moreover, the EBSD analysis in Fig.50f had confirmed that there are no preferential grain orientations.

Also for the specimen solution treated at 900°C (SHT900), the EDS showed two regions of different Mn concentration (Fig.51): poor at 13.6 wt.% and rich at 17.2 wt.%. In this case, the presence of ferrite seems to be much more pronounced although MnS precipitates are still evident. Again, the EBSD shows no preferential grain orientations, as it can be observed in Fig.51f.

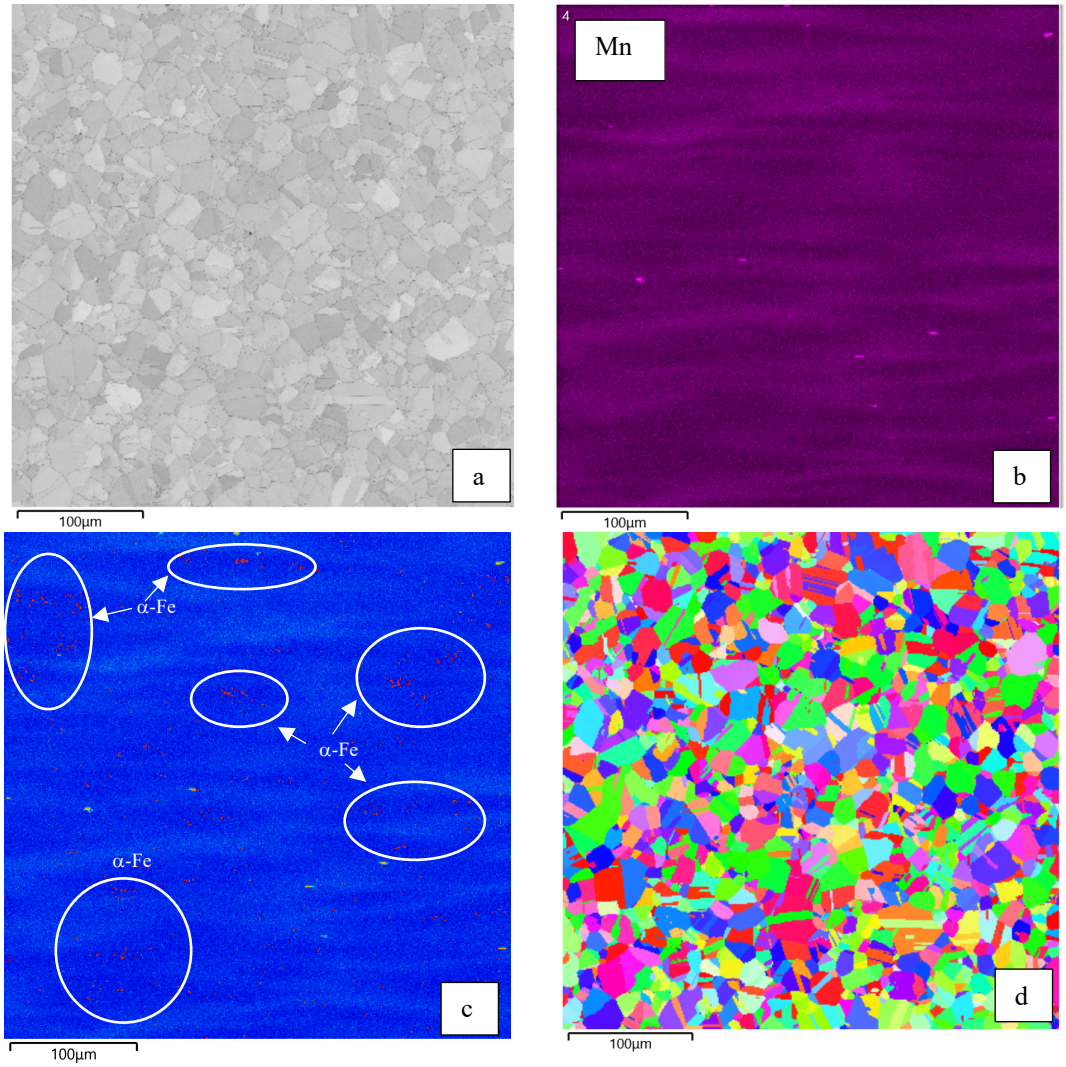

Figure 51: a) – b) EDS compositional map; e) ferrite (in red) and MnS (in yellow) identification; f) inverse pole figure map respect z axis obtained from EBSD for the sample solution treated at 900°C

Finally, hardness test results are given in Tab.11 and shown graphically as the solubilization temperature changes in Fig.52.

As expected, the highest hardness is obtained in the hot rolled condition (~265 HV) where the grains are smaller in size. With treatment at 900°C, the uniform precipitation of ferrite helps maintain hardness nearly equivalent with the untreated condition, despite the increase of the grain size. However, with the ferrite concentrated at the edges and the test always performed in the middle part of the specimen, at 950°C the hardness is the lowest of the three cases.

Micro-HV		
HR	SHT900	SHT950
263.7 HV	255.9 HV	233.7 HV

Table 11: Mean value of the hardness of the hot-rolled (HR), solutioned at 900°C (SHT900) and at 950°C (SHT950) samples obtained with a load of 1000 mg and a twell time of 10 seconds

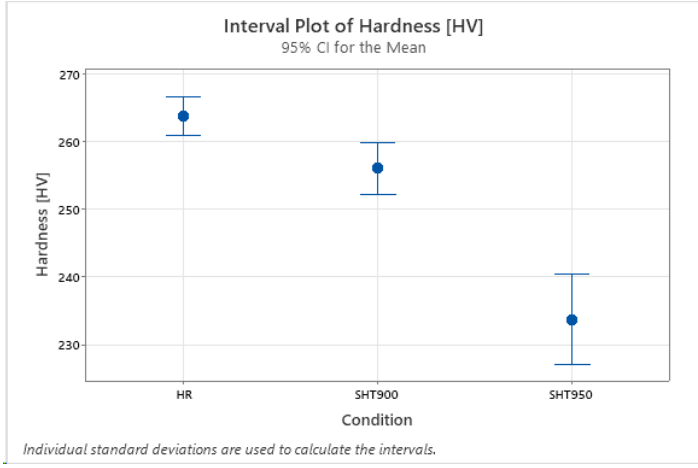

Figure 52: Hardness [HV] plot of the hot-rolled (HR), solutioned at 900°C (SHT900) and at 950°C (SHT950) samples

Hot-rolled → Tensile elongation

After conducting anisotropy tests on the hot-rolled material, a sample was extracted from one of the specimens oriented at a 90° relative angle to the rolling direction. This sample was used for microstructural analysis. The microstructure of this sample is presented in Fig.53, and it is compared with the hot-rolled condition.

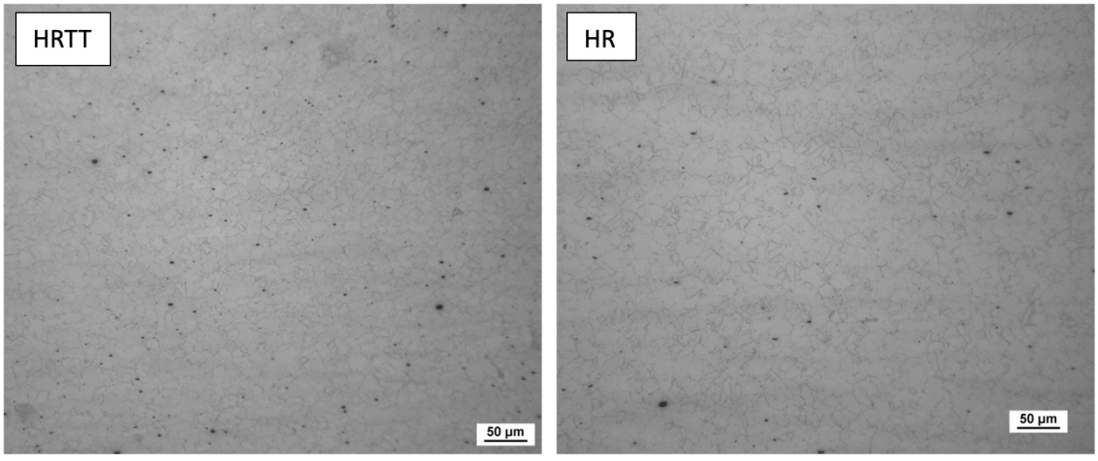

Figure 53: Microstructure of the hot-rolled anisotropy tested (HRTT) and the hot-rolled (HR) samples at the optical microscope (200x)

As depicted in the image, no substantial differences are discernible between the two samples. However, upon closer examination of the comparative micrographs, it becomes apparent that the HRTT sample exhibits a higher occurrence of twinning. These twinned regions are likely a result of the material's response to the imposed deformation during the anisotropy test.
In addition, the SEM-EDS analysis performed on this sample is reported in Fig.54.

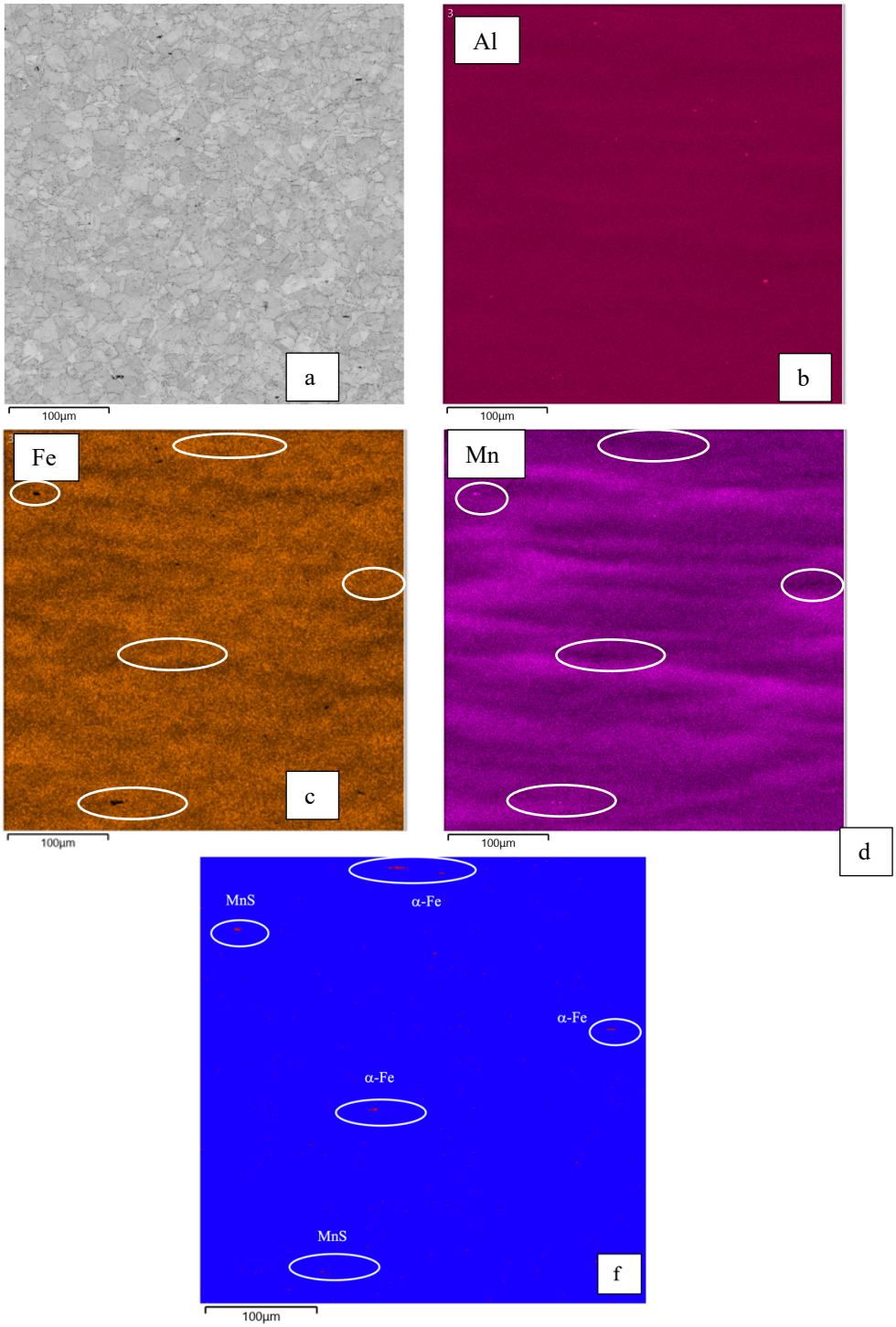

Figure 54: a) – d) EDS compositional map and e) second phases identification for the sample solution treated at 900°C

Similar to the hot-rolled material, noticeable manganese segregations are also observed in this case. Fig.54 reveals the presence of precipitates, and upon comparing the phase color map in Fig.54e with the maps for Mn and Fe, it appears that these precipitates could potentially be MnS and ferrite, similar to what was observed in the hot-rolled material.
Additionally, Tab.12 presents the average austenitic grain size of the sample compared to the calculated grain size for the material in the hot-rolled condition. It is evident that the grain size becomes finer after the elongation of the sample. This phenomenon can probably be attributed to the fact that the deformation direction is perpendicular to the analyzed section. As a result, during deformation, the grains elongate along the applied stress direction, thereby narrowing their cross-sectional area.

Austenitic average grain size	
Hot-rolled anisotropy tested	Hot-rolled
10.8 $\pm$ 2.2 μm	14.5 $\pm$ 1.5 μm

Table 12: Average grain size results for the hot-rolled anisotropy tested and the hot-rolled specimens

From the EBSD analysis of the HRTT and the hot-rolled samples, the local misorientation maps in Fig.55 were obtained.
These maps help to understand if the deformation is quite distributed or more concentrated in some regions of the specimen. In particular, by comparing the two results, it can be observed that the material's deformation is different between the two cases. In fact, in the elongated sample the majority of the misorientation is localized at grain boundaries, which can be probably associated to the grain refinement strengthening. However, no preferential grain orientation seems to be present.

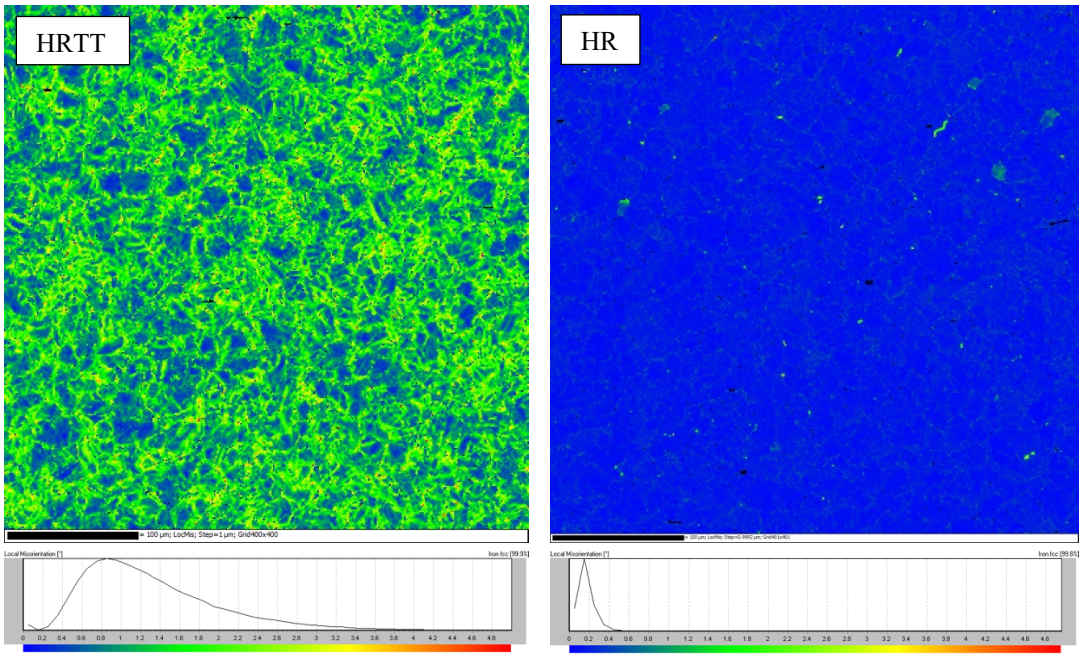

Figure 55: Local misorientation maps from the EBSD analysis for the hot-rolled anisotropy tested and the hot-rolled specimens

In conclusion, even after undergoing significant deformation (reaching an elongation of 10% during the test), the material has shown no substantial differences compared to the base hot-rolled condition, except for an increase in observed twinning and a reduction in the average grain size. Furthermore, it was observed that the deformation tends to concentrate along grain boundaries.

Hot-rolled → Cold-rolled

The starting material, with a thickness of 5 mm, was cold rolled until obtaining two specimens with different thickness: one of 2 mm (60% thickness reduction) and another of 1 mm (80% thickness reduction). In Fig.56, the microstructure observed with the optical microscope of the obtained samples is shown, compared with the hot rolled starting condition.

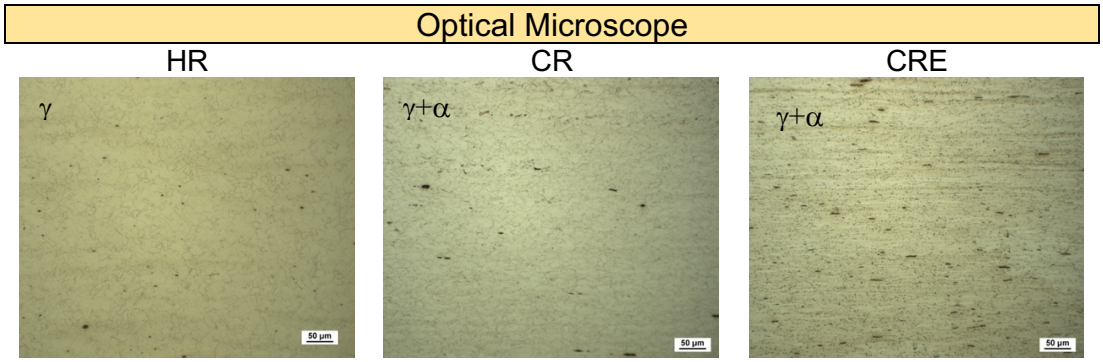

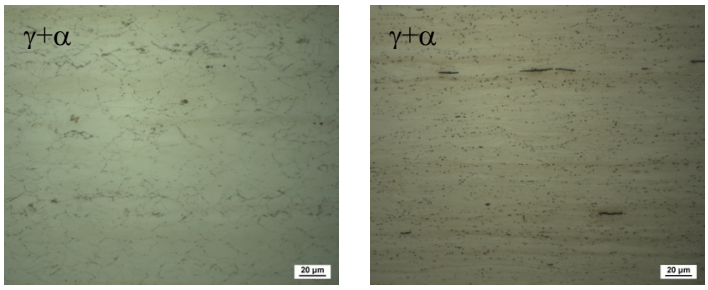

Figure 56: Microstructure of the hot-rolled (HR), cold-rolled at 2 mm (CR) and at 1 mm (CRE) samples at the optical microscope (200x and 500x)

In the sample deformed to 2 mm thickness (hereafter referred to as CR), the austenitic grains are smaller in size compared to the hot-rolled condition, and a light precipitation of fine-sized ferrite can be observed at the grain boundaries. As for the cold-rolled specimen with a thickness of 1 mm (also referred to as CRE), the grains appear to be further reduced in size, and the ferrite is precipitated much more noticeably. In both cases, the grains seems to be slightly elongated.

Unfortunately, as indicated by the ASTM E112-13 standard [55], it was not possible to calculate the average grain size under these conditions due to unfulfillable assumptions and requirements of the standard.

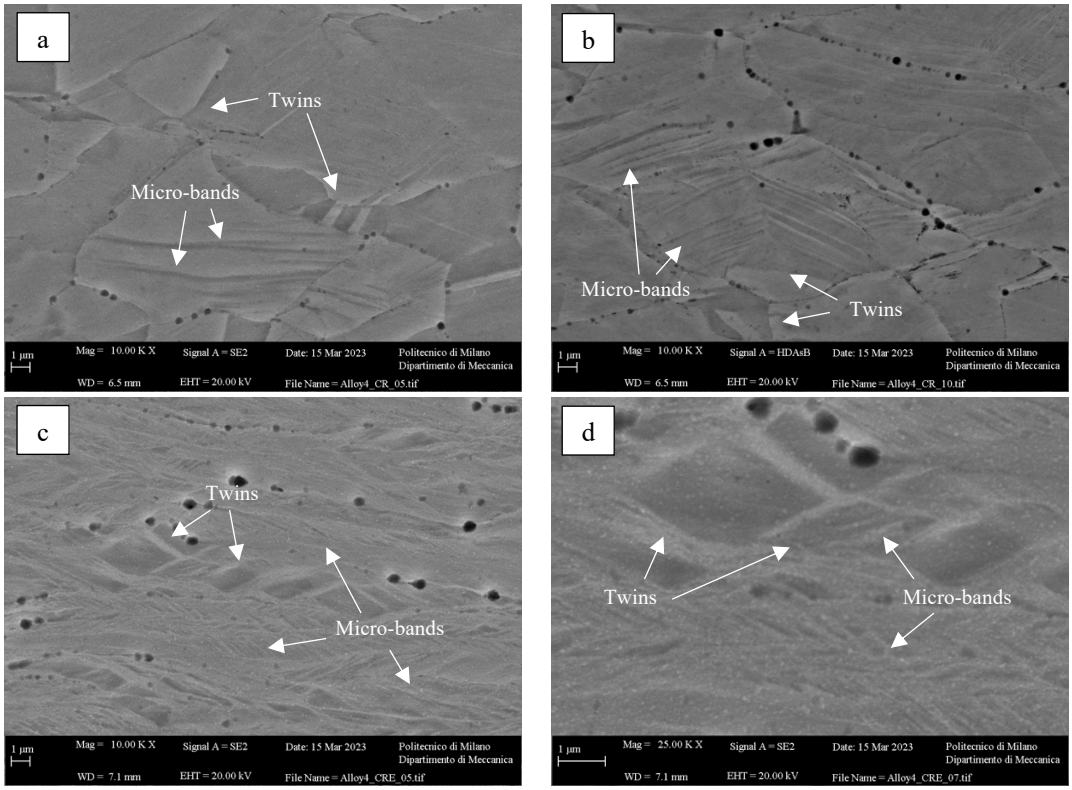

Figure 57: Details of the a),b) cold-rolled at 2 mm (CR) and c),d) at 1 mm (CRE) samples at the SEM

To further investigate the microstructure and the deformation mechanisms of these specimens, an analysis was conducted using the SEM. From Fig.57 it can be observed that the microstructure is very fine in both cases, CR and

CRE, but more so in the 1 mm sample. Furthermore, both twins and a large quantity of micro-bands crossing the grains can be observed.
This latter observation is particularly important because it suggests the deformation mechanism involved in this alloy. After calculating the SFE value for the given chemical composition, the two alternatives were SIP and MBIP. Following this analysis, it is possible to exclude SIP and affirm that MBIP is the primary deformation mechanism.
The hardness test results for these two samples are given in Tab.14 in the form of mean value and shown graphically in Fig.58 with their standard deviation.

Micro-HV		
HR	CR	CRE
263.2	443.1	510.6

Table 13: Mean value of the hardness of the hot-rolled (HR), cold rolled at 2 mm (CR) and at 1 mm (CRE) samples obtained with a load of 300 mg and a twell time of 10 seconds

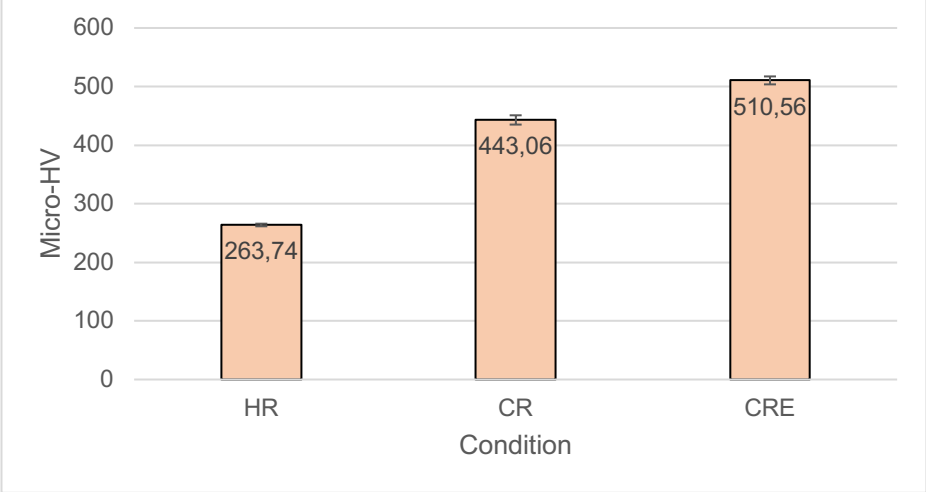

Figure 58: Hardness [HV] plot of the hot-rolled (HR), cold rolled at 2 mm (CR) and at 1 mm (CRE) samples

Cold rolling significantly increases the hardness of the alloy compared to hot rolled condition. In particular, the CRE condition offers an almost twice as high as the HR specimen (~510 HV versus ~265 HV). This can be explained both by the activation of the MBIP deformation mechanism and by the traditional strengthening mechanisms. Among these, the strain hardening and grain refinement are certainly of fundamental importance.

Cold-rolled → solution treatment

The cold-rolled material up to 1 mm thick was then subjected to solution treatments at different temperatures. The 1 mm thickness was chosen because SEM analysis revealed a dense presence of micro-bands. Hence, the

investigation aimed to assess the effectiveness of a solution treatment in removing the residual stresses and the precipitated ferrite under cold-rolled conditions.
Specifically, all treatments were conducted for a duration of 30 minutes. The temperatures used were 900, 950, 1000, 1050, and 1100°C, followed by quenching in water for cooling.
The effect of the temperature variation during the treatment on the material's microstructure is shown in Fig.59.

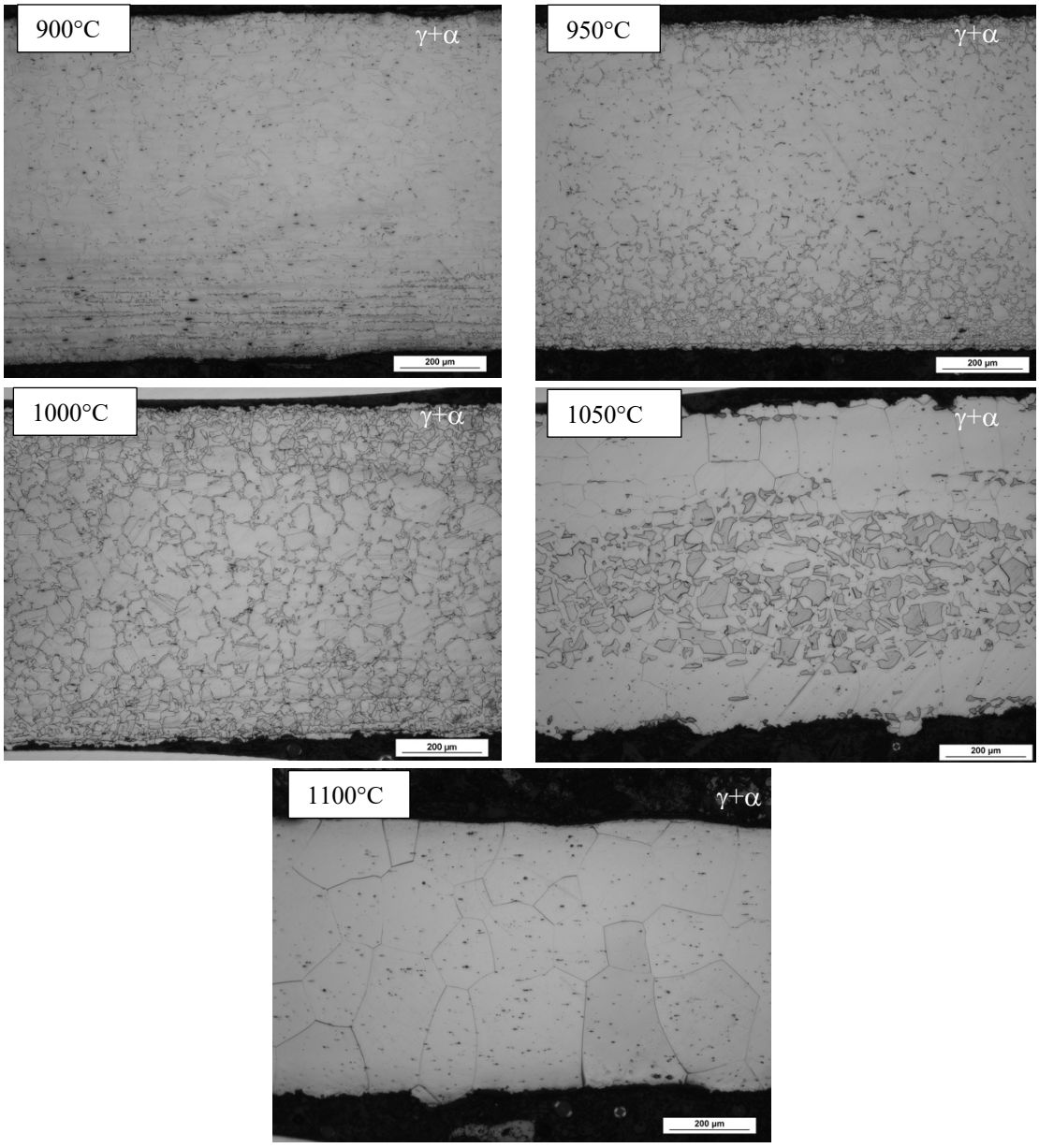

Figure 59: Microstructure of the cold-rolled and solutioned samples at the optical microscope (100x)

As can be observed in Fig.59, the only condition in which ferrite is not recognizable on visual inspection is that solubilized at 1100°C. In the other samples, in fact, ferrite can be noticed firstly in the form of thin bands on the sides of the sample (900°C) and then in a coarser and more dispersed form,

to decorate the austenitic grain boundaries (950°C and 1000°C). However, in the sample treated at 1050°C it becomes much coarser and concentrates in the inner part of the sample.
Furthermore, in the sample treated at 1100°C, several dark spots are observed. They may be fine and dispersed second-phase particles, but many may simply be a sign of pitting originating from chemical etching. In general, however, the observed austenitic grains appear to have an equiaxed structure.
To confirm the hypothesis for the 1050 and 1100°C specimens, XRD analysis was conducted on these samples. Fig.60 displays the XRD peaks obtained for the two specimens. It can be observed that, in both cases, in addition to the characteristic peaks of austenite, there is also a peak at 44°, which is associated with the presence of ferrite. This peak is particularly prominent in the case of the sample solutioned at 1100°C. As a result, it is evident that a significant fraction of ferrite is present also in the sample solutioned at 1100°C.

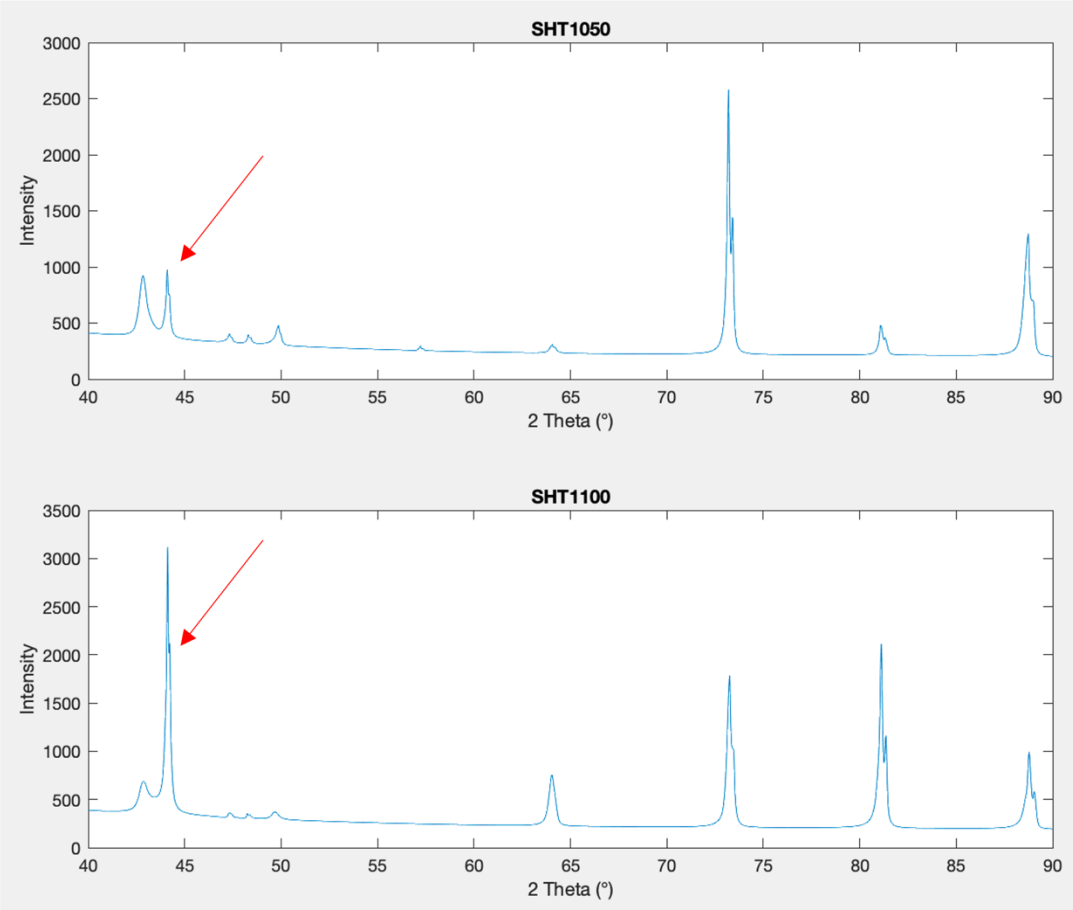

Figure 60: Peaks at the XRD for the cold rolled and solutioned samples at 1050°C and 1100°C

Austenitic average grain size				
900°C	950°C	1000°C	1050°C	1100°C
36.44 μm	40.93 μm	48.84 μm	81.17 μm	151.37 μm

Table 14: Average grain size results for the cold-rolled and solutioned samples. The measurements were taken considering the ASTM E112-13 and the ASTM E1181-02 standards

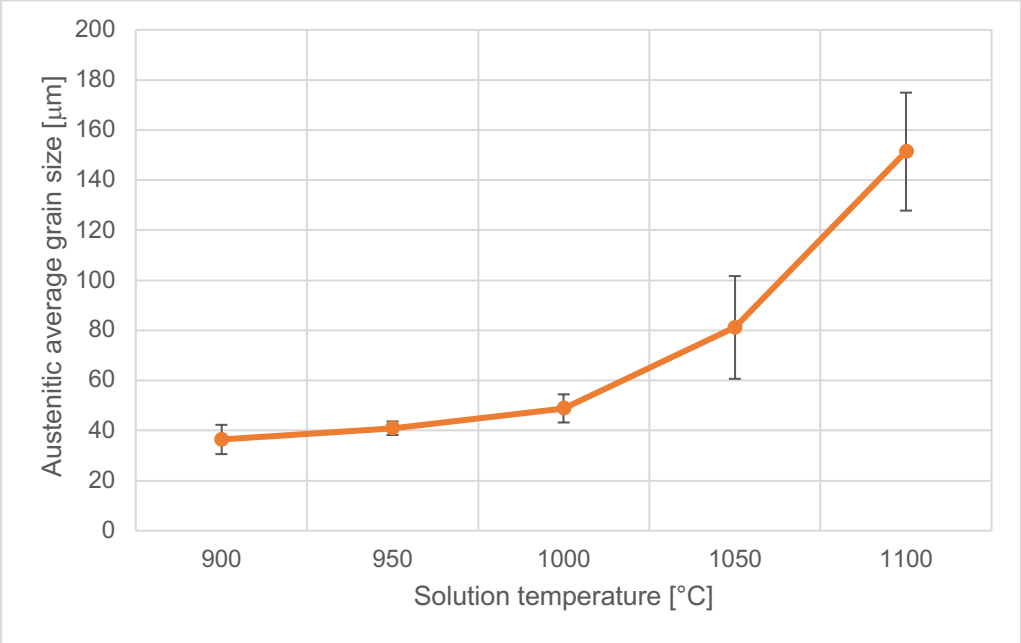

Figure 61: Average grain size plot of the cold-rolled and solutioned samples for different treating temperatures

Area Fractions					
	900°C	950°C	1000°C	1050°C	1100°C
Ferritic	2.87 %	11.9 %	20.85 %	17.84 %	0 %
Austenitic	97.13 %	88.1 %	79.15 %	82.16 %	100 %

Table 15: Austenitic and ferritic area fraction of the cold-rolled and solutioned samples at different treating temperatures. The measurements were taken considering the ASTM E112-13 and the ASTM E1181-02 standards

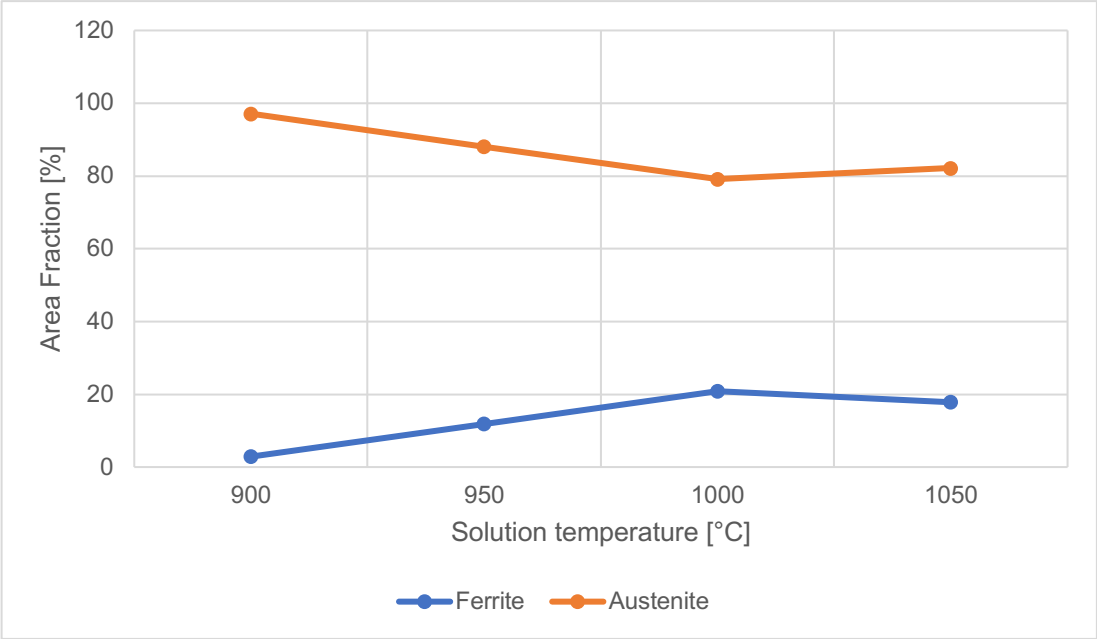

Figure 62: Variation of the ferritic and austenitic area fraction [%] at different sulibulization temperatures. The measurements were taken considering the ASTM E112-13 and the ASTM E1181-02 standards

As shown in Fig.61 and Tab.15 [43], [56], the average austenitic grain size remains almost unchanged with a treatment between 900 and 950°C. This can be attributed to both, the lower treatment temperature and the pinning effect of the small ferrite particles present at the grain boundaries: these small particles prevent the movement of the grain boundaries and thus, austenite grains do not have the opportunity to grow [57], [58].

However, starting from 1000°C, the precipitated ferrite begins to grow significantly in quantity and size (Fig.62 and Tab.16). As a result, the pinning effect becomes less and less effective [57], [58].

At 1050°C, the ferrite begins to 'withdraw' from the edges, leaving space for the growth of austenitic grains that start to reach sizes even larger than 0.2 mm. This effect becomes even more pronounced at 1100°C. However, at this temperature, it was not possible to calculate the fraction of ferrite present in the sample as the ferritic grains were not easily distinguishable.

The results of hardness tests for these samples are given in Tab.17 in the form of mean value and shown graphically in Fig.63 with their standard deviation. Tests were conducted on two different regions for each sample to better study the effect of microstructure on mechanical properties. Five tests were performed on the inner part of the samples, with a load of 300 mg, and five near the edge with a load of 100 mg. This modification in the test load was implemented to allow for approaching the sample edge as closely as possible, while still maintaining a distance from it equal to 2.5 times the diagonal length of the penetrator's impression, as indicated by the standards.

Micro-HV				
900°C	950°C	1000°C	1050°C	1100°C
223.64 HV	202.70 HV	199.26 HV	227.14 HV	268.16 HV

Table 16: Mean value of the hardness of the cold rolled at 1 mm and solutioned samples

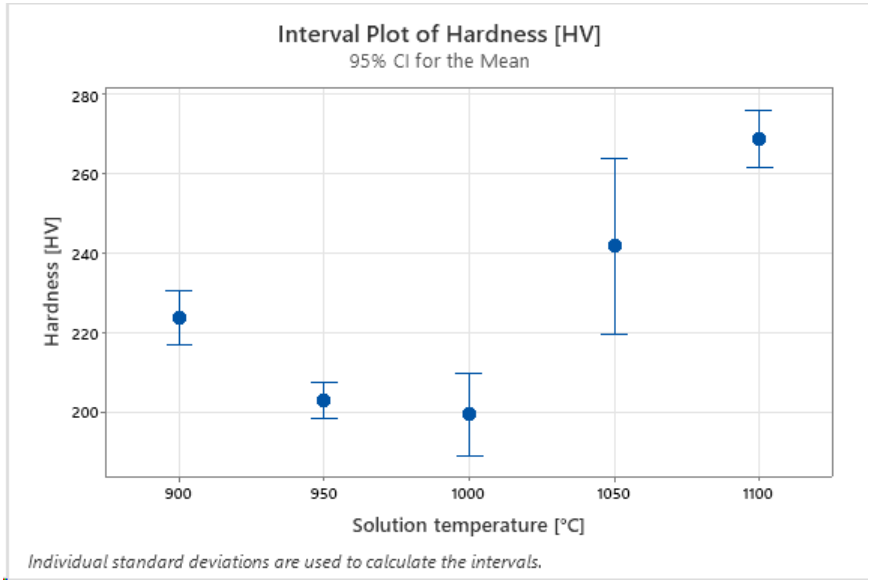

Figure 63: Hardness [HV] plot of the cold-rolled samples as a function of the solutioning temperature

It can be seen from Fig.63 that solution treatment seems to have a negative effect on the hardness of the alloy up to 1000°C, where a minimum value is present. From this temperature, the trend becomes opposite and the hardness increases rapidly, reaching a peak of about 270 HV in the solubilized sample at 1100°C.

However, relating the test results to the zones investigated (Fig.64), a discrepancy with the literature can be seen [59]. In particular, the hardness seems to be higher in areas where ferrite is not present or is present in small amounts (such as 900°C and 1050°C). Probably, the higher value at 900°C, where the fraction of ferrite is around 3% (Fig.62), than at 950°C and 1000°C is related to the fact that in each case the ferrite is very fine and homogeneously distributed; therefore, the probability of finding austenite with the indenter is much higher in each region of the samples. The result is that the final hardness is much more influenced by the grain size (which is less than 900°C) than by the fraction of ferrite.

Moreover, in the sample solubilized at 1050°C, tests in the inner region, rich in ferrite, and in the outer region, completely austenitic with coarse grains, show a higher hardness in the presence of austenite. This could be related to a different strain partitioning between austenite and ferrite. In particular, it has been shown that during cold rolling, austenite shows greater strain hardening

respect ferrite; therefore, the two phases have also a different recovery rate during solution treatment [60].
However, it was not considered appropriate to continue with the investigation, as the conditions at 1050°C and 1100°C have too large grains and were not considered applicable.

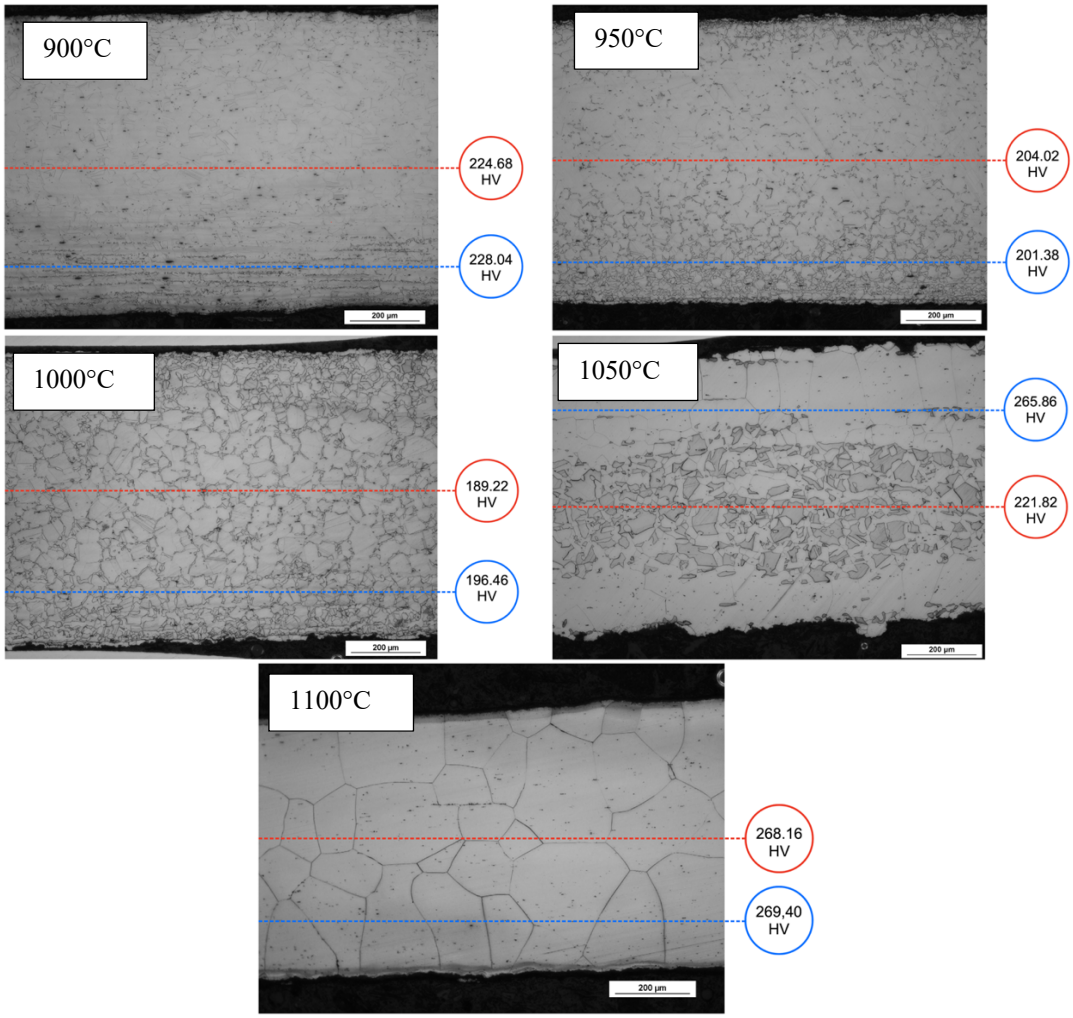

Figure 64: Average hardness value of 1 mm cold-rolled and solubilized samples as a function of temperature and test site

Cold-rolled → solution treatment (time parameter variation)

The cold-rolled material up to 1 mm thick was subjected also to solution treatments at 900°C and 925°C with different treatment times: 15 min, 20 min and 25 min. The effect of the temperature and time variation during the treatment on the material's microstructure is shown in Fig.65 and Fig.66.

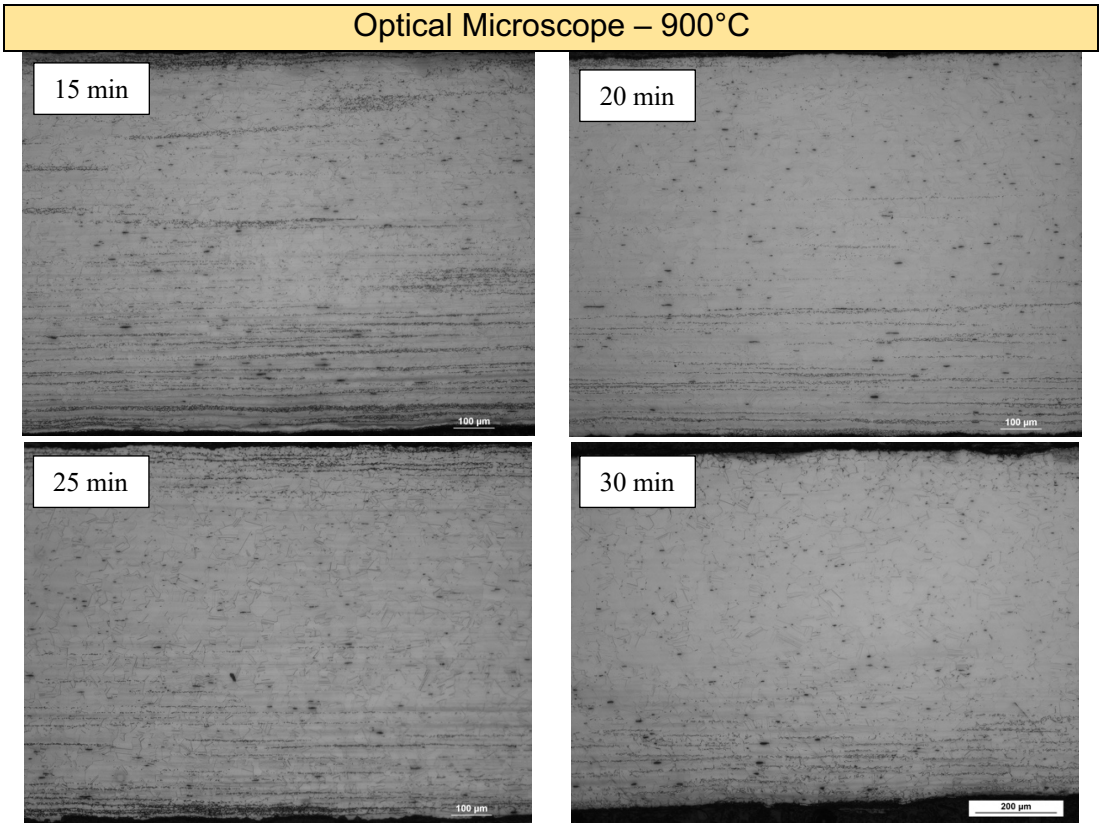

Figure 65: Microstructure of the cold-rolled and solutioned samples at 900°C the optical microscope (100x)

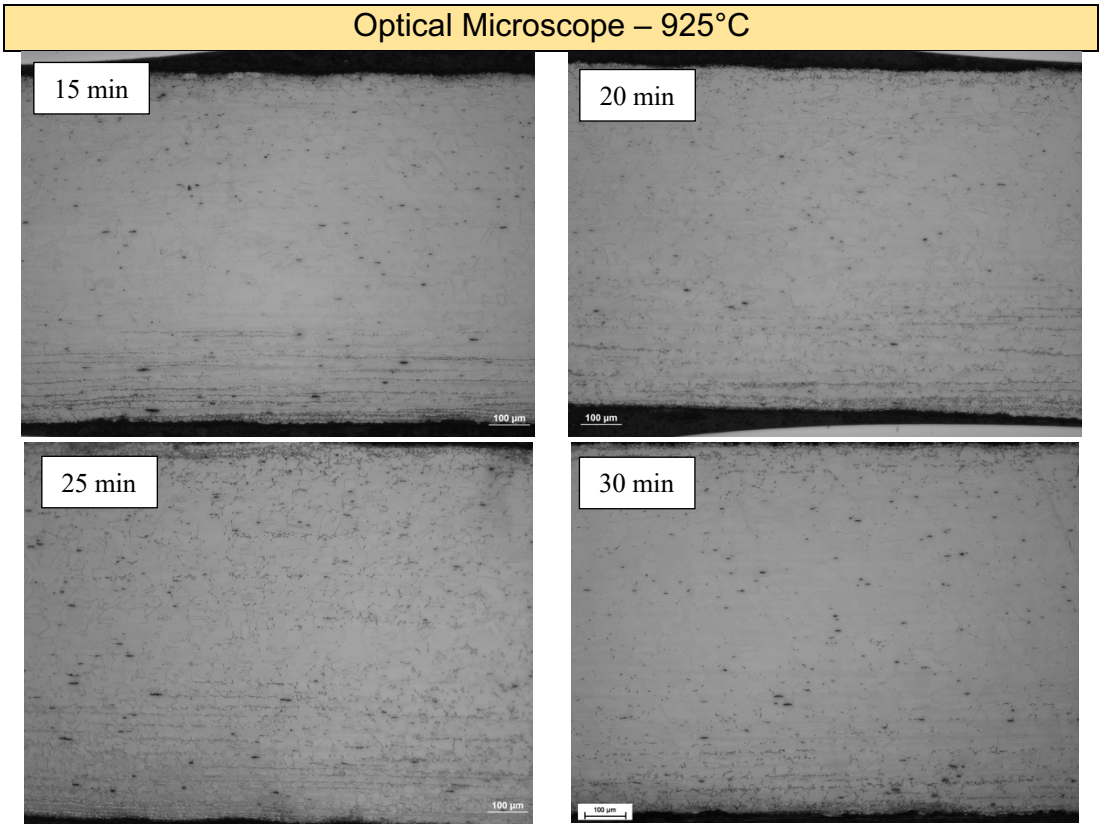

Figure 66: Microstructure of the cold-rolled and solutioned samples at 925°C the optical microscope (100x)

As can be seen in the figures, ferrite bands are present in all analyzed conditions, although in different quantities and sizes, and tend to concentrate mainly at the edges. Furthermore, a peculiar behavior of the material at 900°C can be noticed: the trend of the ferrite fraction inside the material as a function of the treatment time is not linear. In particular, at 20 minutes, there seems to be a minimum, but the amount of ferrite increases at 25 minutes and then decreases again at 30 minutes (as seen in the previous paragraph).
At 925°C, on the other hand, the amount of ferrite also increases as the treatment time increases, although at 15 and 20 minutes the situation seems to be almost unchanged. These observations are confirmed by the graph shown in Fig.67. However, the value increases significantly at 25 minutes, but then at 30 minutes, the trend reverses in a rather unusual manner.

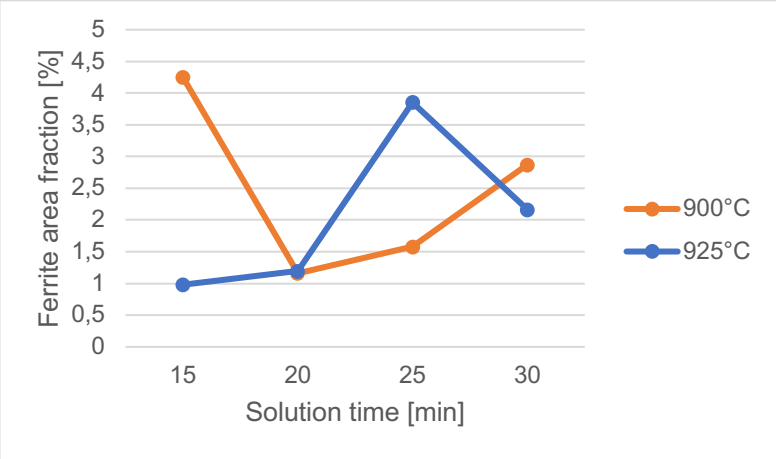

Figure 67: Variation of the ferritic area fraction [%] at different sulibulization temperatures and times. The measurements were taken considering the ASTM E112-13 and the ASTM E1181-02 standards

The average austenitic grain size is larger at the higher temperature (925°C) for any given time, as shown in Fig.68. Furthermore, increasing the treatment time also leads to an increase in the austenitic grain size.
Additionally, the optimal treatment time to minimize the amount of ferrite seems to be 20 minutes for both temperatures.

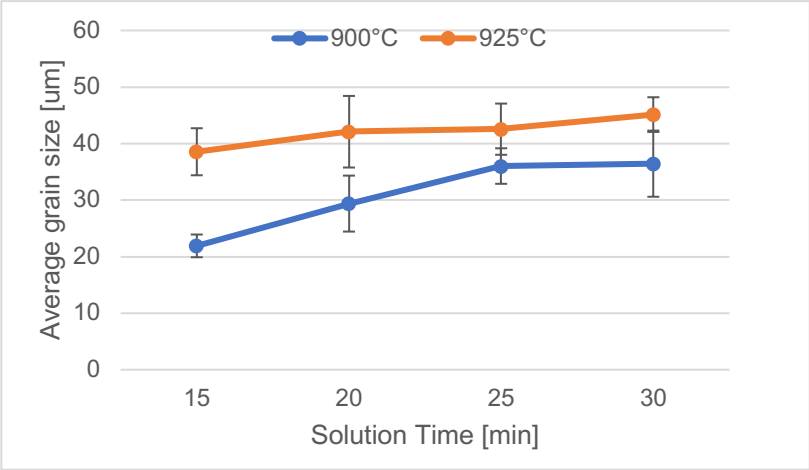

Figure 68: Average grain size plot of the cold-rolled and solutioned samples for different treating temperatures and times

The results of hardness tests for samples treated between 15 and 25 minutes are given in Tab.18 in the form of mean value and shown graphically in Fig.69 with their standard deviation.

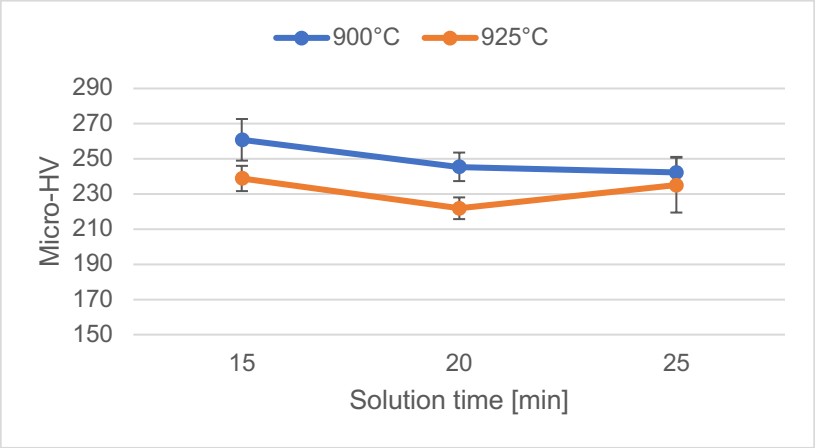

Figure 69: Hardness [HV] plot of the cold-rolled samples as a function of the solutioning temperature and time, obtained with a load of 300 mg and a twell time of 10 seconds

Micro-HV			
	15 min	20 min	25 min
900°C	260.80 HV	245.44 HV	242.258 HV
925°C	238.64 HV	221.88 HV	235.033 HV

Table 17: Mean value of the hardness of the cold rolled and solutioned samples for different treatment times

As shown in Fig.69, an increase in treatment time appears to have a negative impact on the final alloy hardness for solution treatment at 900°C. The highest hardness value (around 260 HV) is achieved with only 15 minutes of treatment, while the minimum (around 230 HV) is obtained at 25 minutes. However, the material exhibits different behavior at 925°C, as the hardness remains more stable across all analyzed conditions. Although a minimum value can be

observed at 20 minutes of treatment (with a value of 221 HV), it is significantly less pronounced than at 900°C.

Welding

Cladding

In general, in welded joints different zones can be observed: the Weld Zone (WZ), the Partially Melted Zone (PMZ), and the Heat-Affected Zone (HAZ) as well as the Base Metal (BM). The WZ is the region where the filler is deposited and the material fully melts and rapidly solidifies. The PMZ is the transitional region between the weld bead and the HAZ in the welded joint. The HAZ is adjacent to the PMZ and refers to the area of the material that experiences heating (resulting in microstructural alterations) without reaching the melting point [61].
The cladding welds analyzed in this study were obtained using both direct current, with current set at 100 A and potential at approximately 13 V, and alternating current, with 110 A and approximately 16 V. The result obtained for the two conditions is shown in Fig.70.

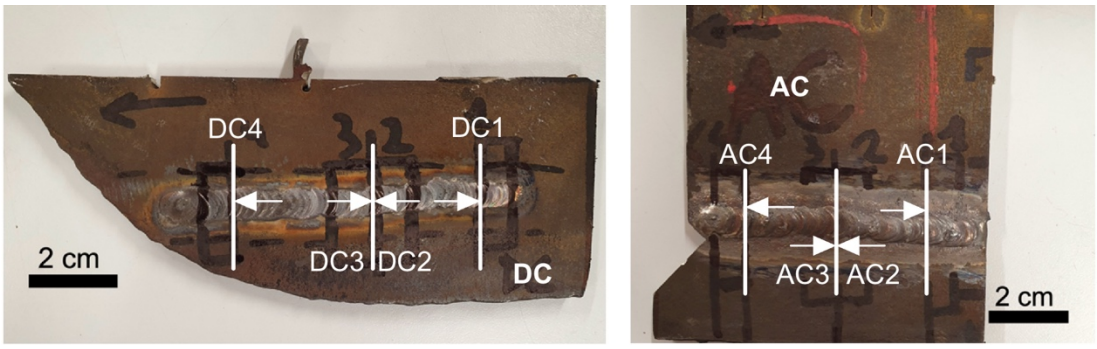

Figure 70: Sheets obtained after the welding operation, showing the cross-sections analyzed

In both cases, four cross-section samples of the joint were taken at various points along its length: two in the center and two at the material's ends, as depicted in Fig.70.
In Fig.71, the cross-sections of two of these welds (DC2 and AC2) can be observed. From the figure, a clear distinction between the weld zone and the rest of the material can be observed.

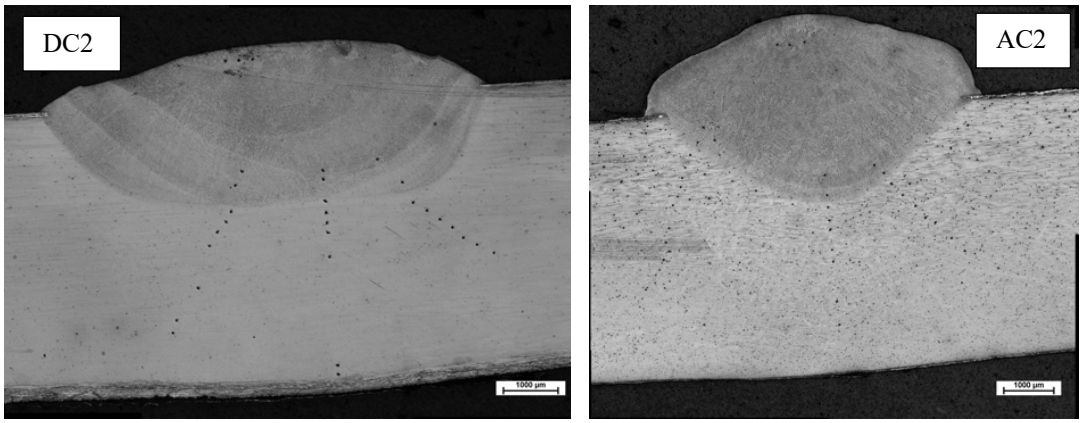

Figure 71: Micrographs of the cross sections of weld nuggets for the DC2 and AC2 specimens

Furthermore, Fig.72 presents higher magnification images of each zone for the AC2 and DC2 samples, which are considered representative of their respective conditions. However, the complete collection of images captured using the optical microscope for these specimens is provided in **Appendix D**.

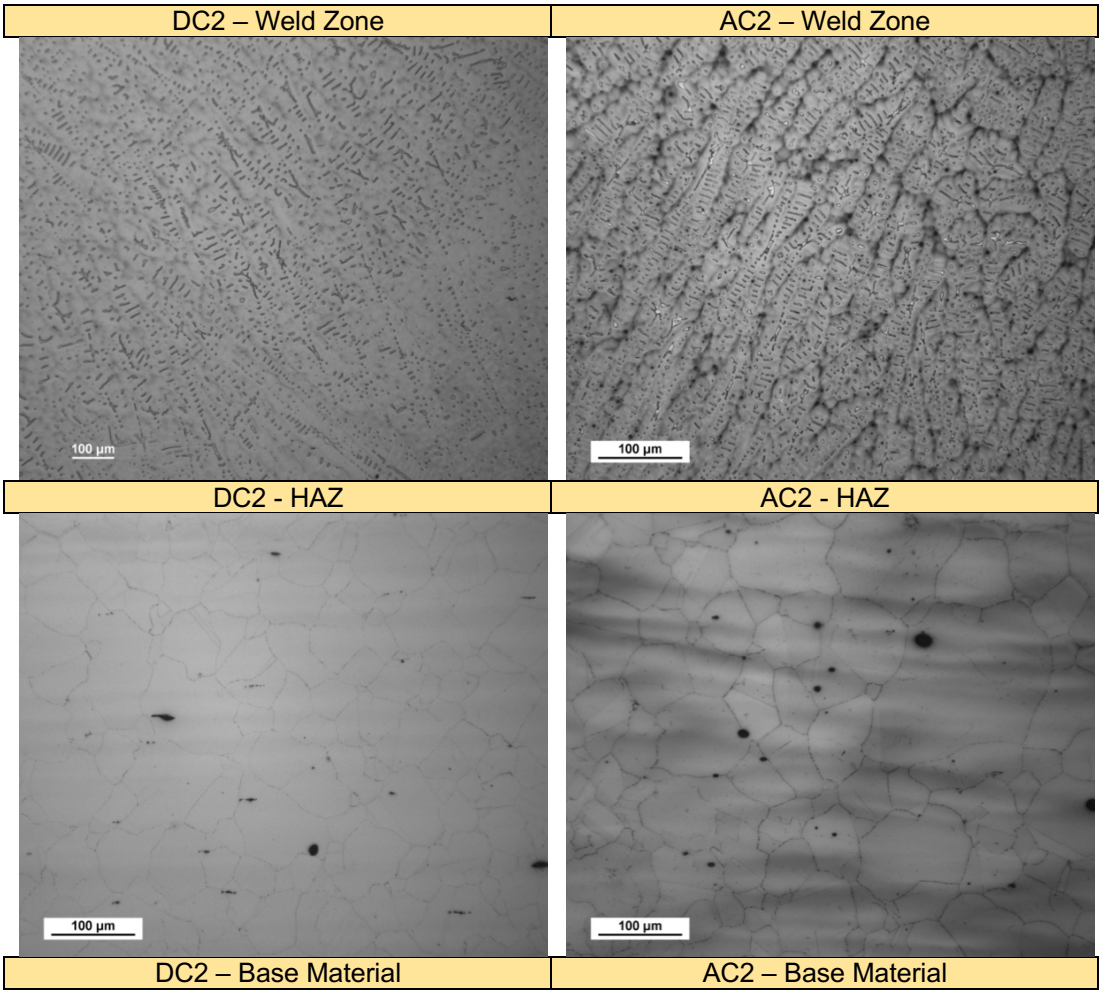

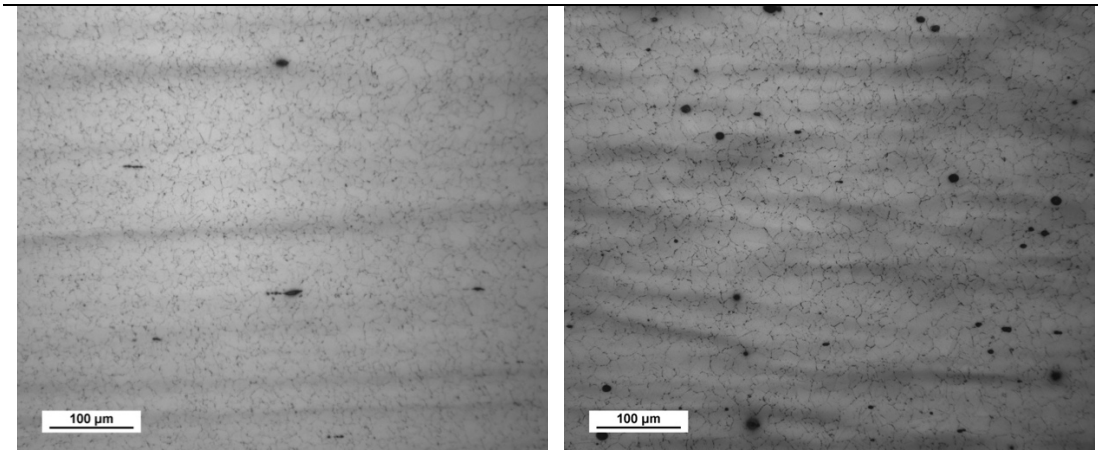

Figure 72: Micrographs of the DC2 and AC2 specimens inside the FZ, HAZ and BM at 200x

From Fig.73, a fine dendritic microstructure can be observed in the WZ. An unusual characteristic was observed in the dendrite orientation, whereby the primary branches exhibited incident angles of 60/120° or their multiples, recalling structures similar to those seen in the Widmanstatten macrostructures.

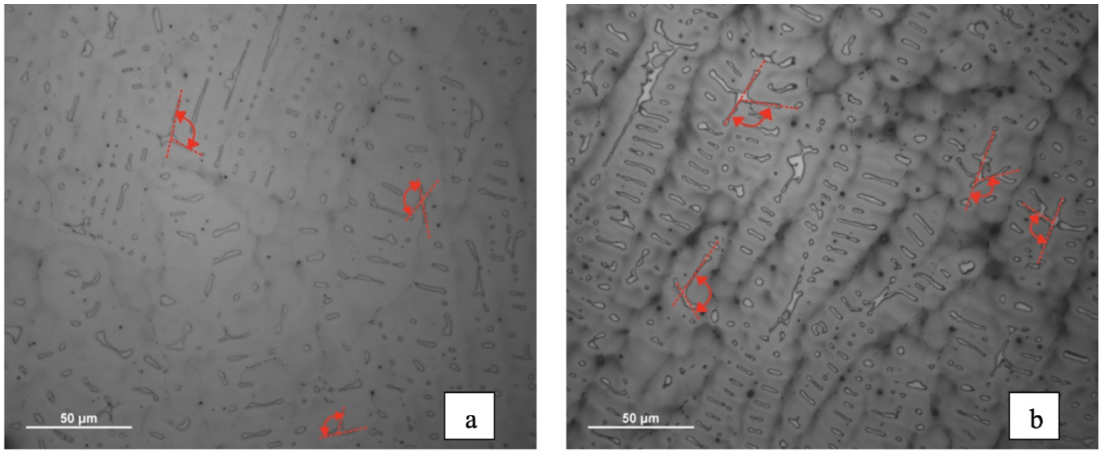

Figure 73: Dendrites orientation highlighted for the a) DC2 and b) AC2 specimens at 500x

At the border of the WZ, a transition zone can be observed where dendrites appear to become finer and exhibit a more uniform shape. This region marks the transition to the HAZ, which has been simply distinguished considering grain coarsening (Fig.74). In this zone, although the heating resulting from the welding process was not sufficient to melt the material, it was adequate to induce grain coarsening.

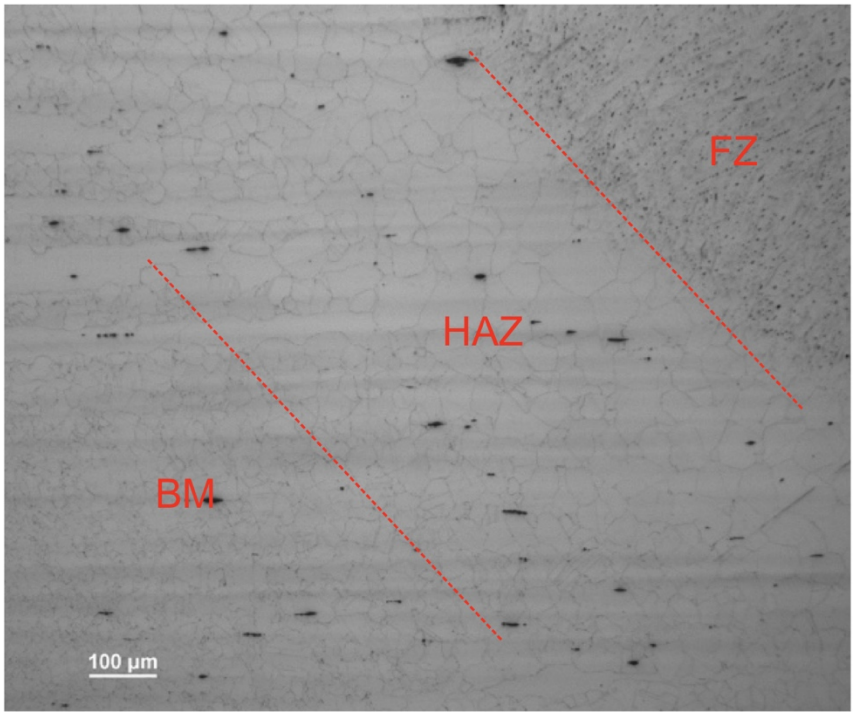

Figure 74: Distinction of the FZ, HAZ and BM in the DC2 specimen at 100x

The HAZ appears to have a length of approximately 0.6 mm. Beyond it, the base material can be observed, with dimensions that appear to be similar to those described in the initial condition (hot-rolled 5 mm).
In Tab.19, the measurements for the dimensions of the WZ described in Fig.75, are reported for each specimen.

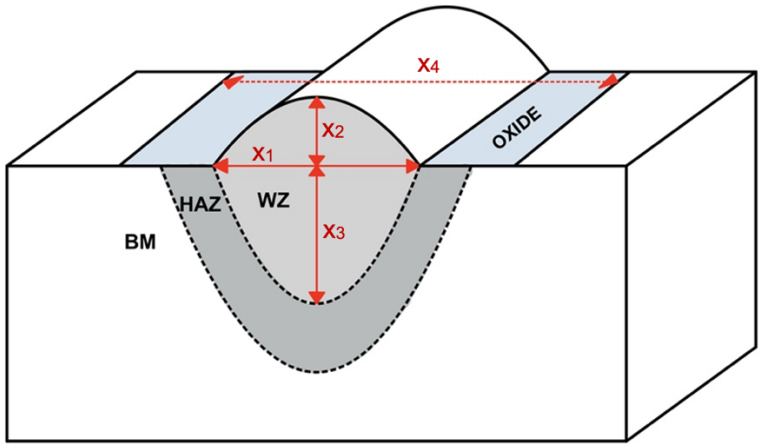

Figure 75: Legend of the measurements taken for the welds

Condition	x_1: FZ width [mm]	x_2: FZ height [mm]	x_3: FZ depth [mm]	x_4: Oxide width [mm]
AC	7.15 ± 0.25	1.65 ± 0.29	1.76 ± 0.23	19.40 ± 0.45
DC	7.65 ± 0.57	0.98 ± 0.13	1.87 ± 0.23	12.83 ± 0.65

Table 18: Values of the weld area measured from the AC and DC specimens

From the values reported in the table, it can be observed that the direct current condition generates a wider melt pool but with a smaller surface oxide layer on the sides of the weld bead. On the other hand, the alternating current condition produces a weld bead with a greater height. Regarding the depth of the Fusion Zone (FZ), the two conditions have a similar effect. Furthermore, considering the length of the two weld beads and the time required for welding each piece, it was possible to calculate the average feed rate used by the operator: 1.54 mm/s for alternating current and 1.44 mm/s for direct current.

The SEM analysis was conducted on the DC2 sample to investigate the chemical composition of the dendrites in the FZ and examine the presence of secondary phase precipitation in the region of the BM adjacent to the HAZ. In fact, the thermal energy supplied to the material during the welding operation in this zone may not be sufficient to promote the coarsening of austenitic grains. However, it could be adequate to induce a similar aging effect and lead to the precipitation of secondary phases in the material.
The SEM, EDS and EBS analysis on the DC2 sample are reported in Fig.76.

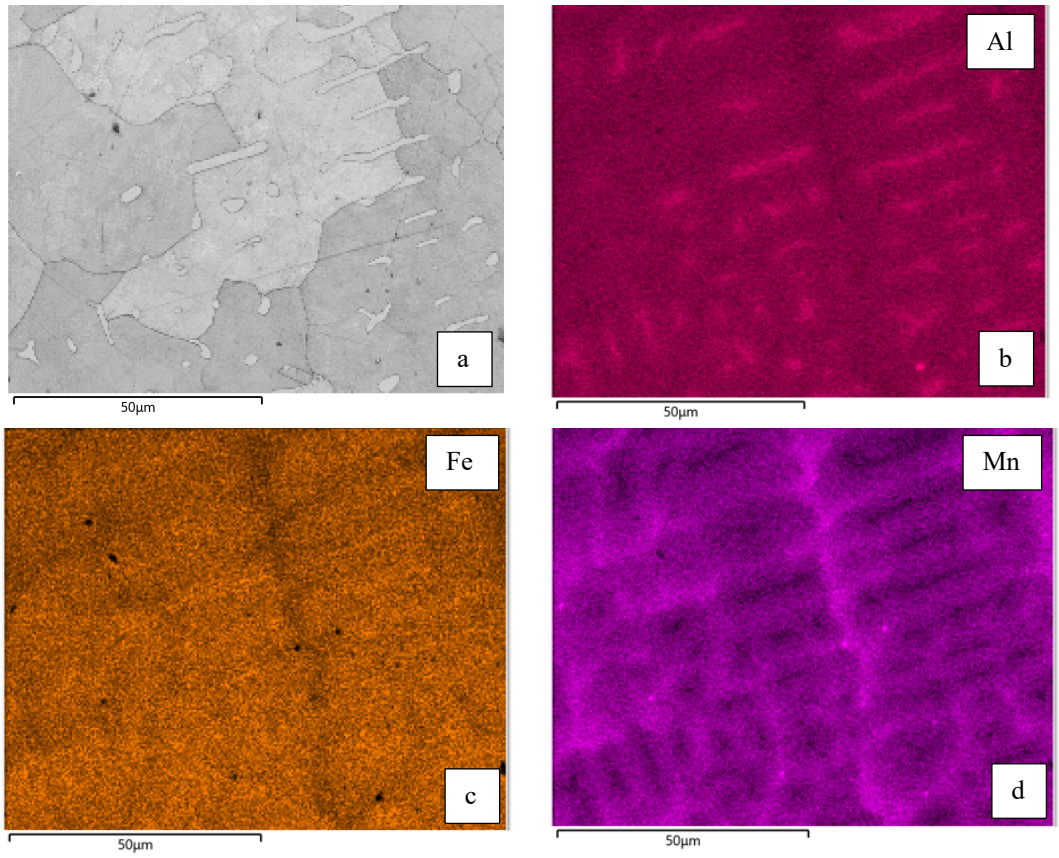

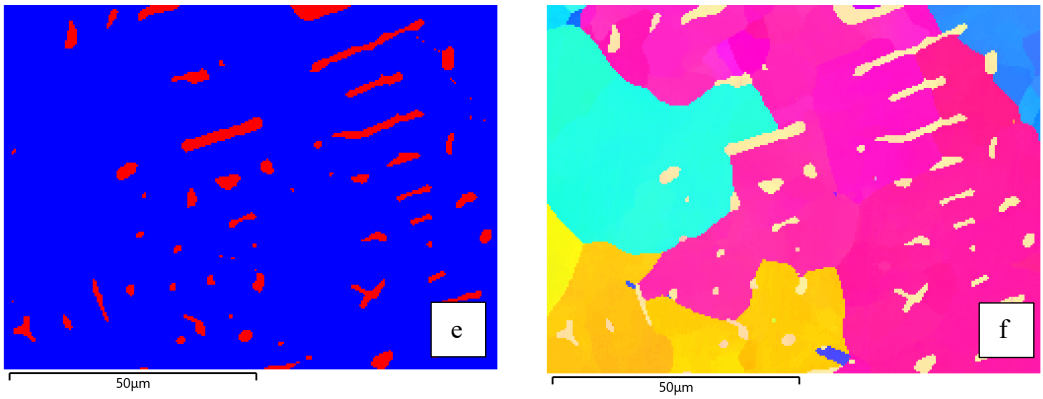

Figure 76: a) – d) EDS compositional map; e) ferrite (in red) identification; f) inverse pole figure map respect z axis obtained from EBSD for the DC2 sample

From Fig.76 it can be observed that the dendrites present in the WZ seem to be constituted by ferrite. In particular, Fig.76d-b show that dendrites grows in Mn-depleted and Al-enriched zones. Furthermore, the compositional map in Fig.76e highlights in red the ferritic fraction and in blue the austenitic matrix. The EBSD shows a preferential grain orientation for the dendrites, as it can be observed in Fig.76f.

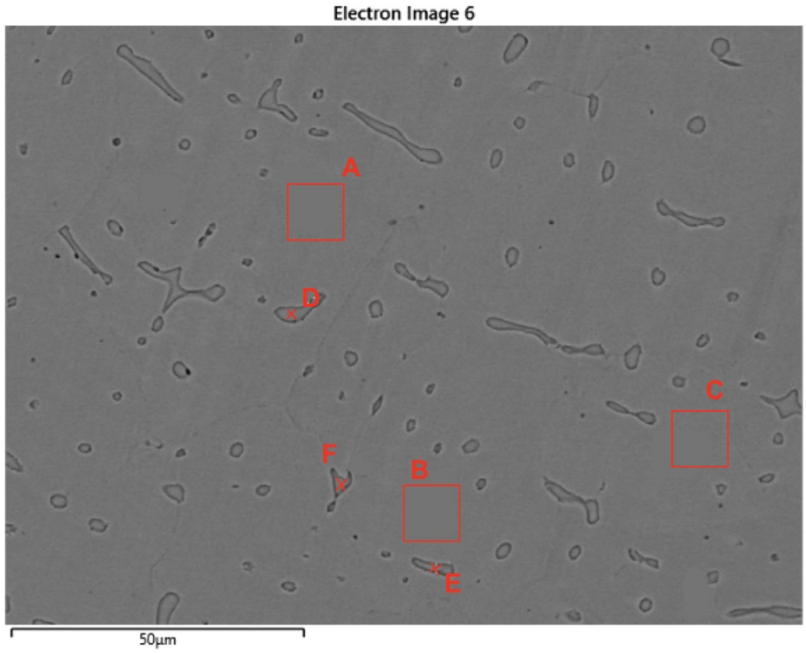

Figure 77: Areas and points investigated at the SEM-EDS in the FZ of the DC2 specimen

SEM-EDS Compositional Analysis [wt.%]				
	Fe	Mn	Al	C
A	69.6	15.8	7.1	7.4
B	71.0	13.9	7.4	7.7
C	67.2	18.2	7.7	6.9
D	71.2	9.8	9.6	9.3
E	71.2	11.0	9.2	8.6
F	71.3	10.2	9.4	9.1

Table 19: The SEM-EDS outputs of the investigated sites reported in Fig.77

The chemical composition obtained through SEM-EDS analysis of the dendrites in the WZ is presented in Tab.20. The first three rows (A, B, C) represent three areas selected from the material outside the dendrites. It can be observed from the table that in these areas, the Al composition is lower compared to the points E, F, G taken from three different dendrites. On the other hand, the Mn and C composition is higher in the matrix areas. Since Mn and C are austenite stabilizers while Al promotes ferrite, it can be concluded that this analysis confirms the observations drawn from Fig.76, namely that the dendrites are composed of ferrite and the matrix is austenitic.

In addition, the chemical composition of the base metal (BM) adjacent to the heat-affected zone (HAZ) is also reported in Tab.21. In this zone, the chemical composition of small precipitates observed at high magnification at the grain boundaries was identified. The first row (designated as A) represents the composition of a point in the matrix, which serves as a reference. Comparing the secondary phases with the reference matrix reveals that in these points, the concentration of Fe is lower, while C is higher and the variation in Mn concentration is negligible. This result is consistent with the stoichiometry of $(Fe, Mn)_3AlC$ κ-carbides and their formation in Al and C-rich regions (resulting from spinodal decomposition). Therefore, the analysis appears to confirm the presence of nanometric κ-carbides in the region of the BM adjacent to the HAZ. This hypothesis is also supported by the literature [34]–[36], as the heating applied to the base material during the welding process can promote their precipitation.

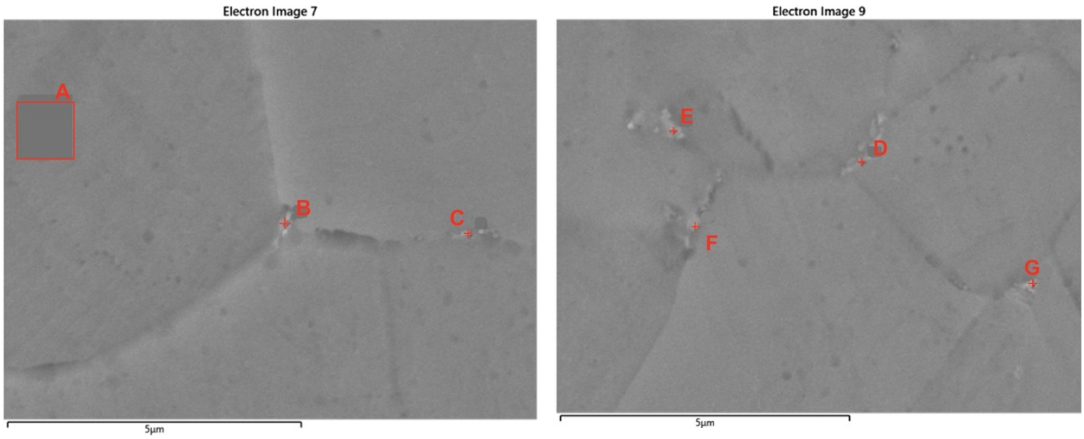

Figure 78: Grain boundary precipitation of secondary phases in the DC2 specimen, investigated at the SEM-EDS

SEM-EDS Compositional Analysis [wt.%]				
	Fe	Mn	Al	C
A	69.6	15.8	7.1	7.4
B	71.0	13.9	7.4	7.7
C	67.2	18.2	7.7	6.9
D	71.2	9.8	9.6	9.3
E	71.2	11.0	9.2	8.6
F	71.3	10.2	9.4	9.1

Table 20: The SEM-EDS outputs of the investigated sites reported in Fig.78

Fig.79 presents the values for calculating the average grain size in the regions of the base metal and the heat-affected zone for each analyzed sample. From the graphs, it can be observed that the base material has preserved the dimension that was observed in the hot-rolled condition with a thickness of 5 mm. Regarding the HAZ, in the case of alternating current (AC), the grain size is smaller in samples AC1 and AC4, likely due to the lower amount of heat absorbed by the material at the weld bead apexes.

In the case of direct current (DC) the smaller average grain size was observed in sample DC1, at the beginning of the weld bead. However, when comparing the two graphs, it can be observed that in the case of alternating current, the grains in the HAZ are typically coarser compared to the direct current case.

This phenomenon can indeed be attributed to the different parameters set in the two processes (lower current and voltage in direct current). However, it may also be due to the different impact they have on the material. In fact, during the operations, a higher effectiveness of alternating current welding has been observed, which appears to penetrate better into the oxide layer present on the material's surface.

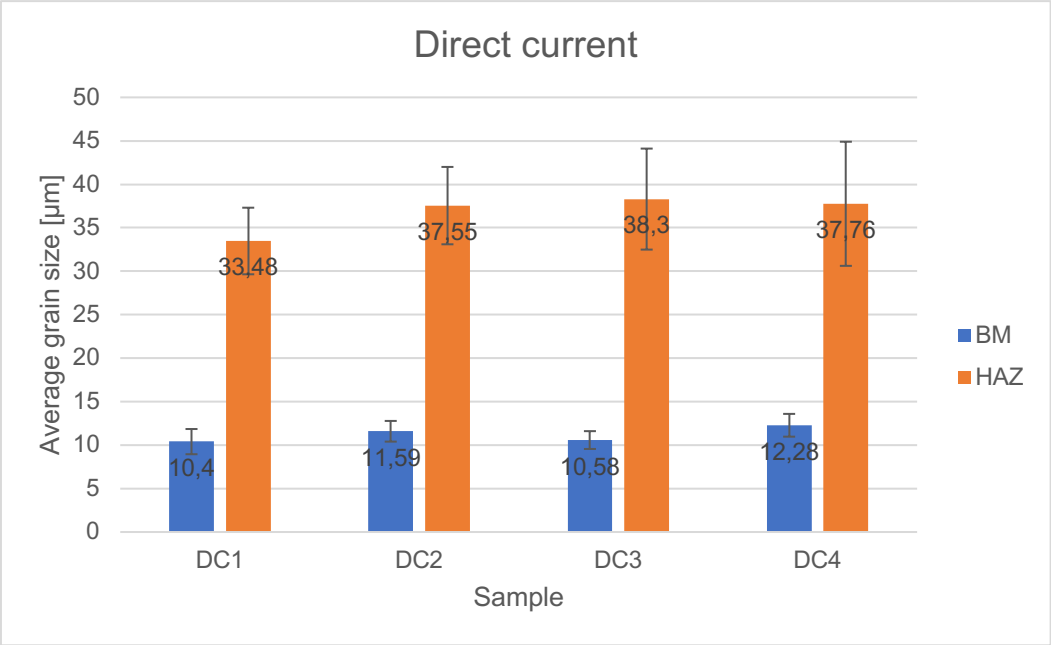

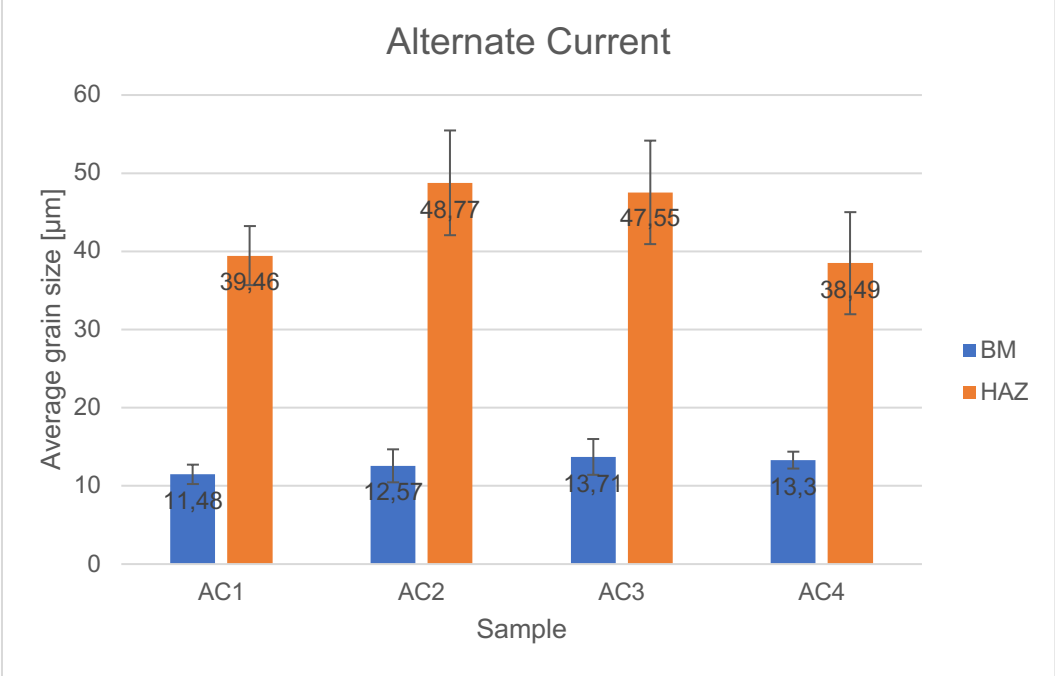

Figure 79: Average grain size plot of the Direct Current (DC) and Alternate Current (AC) samples for the BM and the HAZ

Fig.81 presents the hardness profile for each analyzed specimen in the cross-sectional area under the two welding conditions. Fig.81a depicts the direct current condition. Tests were conducted at the center of the WZ, in an area of the BM material far from the weld and on three radial lines relative to the fusion zone, as shown in Fig.28.

From the graph in Fig.81a, it can be observed that the initial hardness in the FZ stabilizes around 265 HV. Moving towards the HAZ, the hardness value decreases, reaching a range between 240 and 255 HV (at approximately 0.15-

0.2 mm distance from the initial point). This decrease is likely attributed to the presence of larger austenitic grains in this zone.
Starting from approximately 0.8-1.0 mm, the BM is reached, where the hardness reestablishes to higher values comparable to those of the base material tested in a region far from the weld (287 HV).
A similar situation was identified in the alternating current condition, as shown in Fig.81b, with very similar values in the FZ and the HAZ. The only significant discrepancy was observed in the BM adjacent to the HAZ (approximately 1.5 mm distance from the initial point), where peaks close to or exceeding 300 HV were recorded. In this case, the effect of κ-carbide precipitation was likely more pronounced, possibly due to the higher effectiveness of the alternating current condition, which, by more effectively breaking the surface oxide layer, provides greater heat to the material plate. This could result in a more evident precipitation of second phases, particularly κ-carbides.

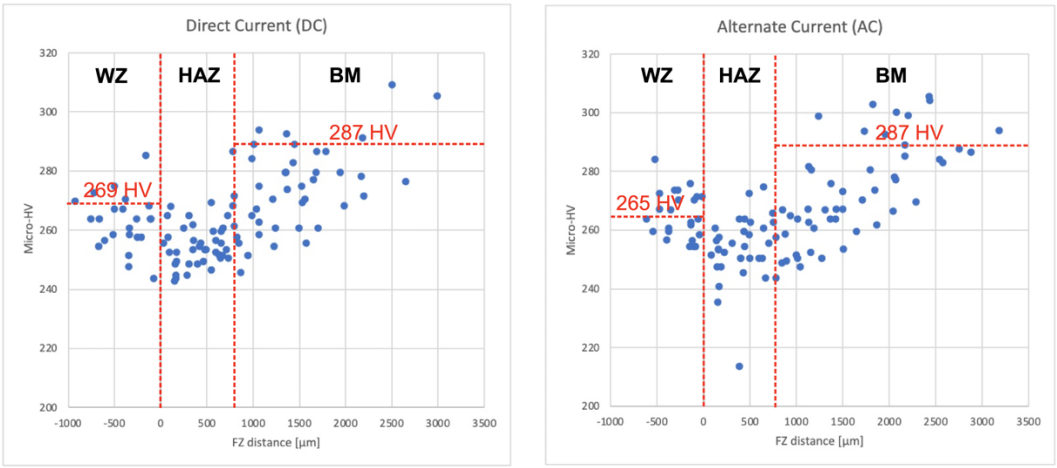

Figure 80: Hardness [HV] plot of the Alternate Current (AC) and Direct Current (DC) samples as a function of the distance from welded zone, obtained with a load of 300 mg and a twell time of 10 seconds

Oxide formation

To investigate the surface oxide formation during welding-induced heating, two samples of hot-rolled material, grinded on one side to completely remove pre-existing oxides resulting from hot rolling, were subjected to thermal treatment at 1000°C for 15 minutes. Subsequently, one sample was cooled in water, while the other was cooled in ambient air. The main objective of this procedure was to understand the composition of the different oxides formed on the material surface, in order to gain additional insights into their stability and influence during welding. To achieve this, SEM-EDS analysis was employed to examine specific areas on the edge of the sample where oxides were removed before the thermal treatment. The results of the analysis on the air quenched specimen are shown in Fig.82.

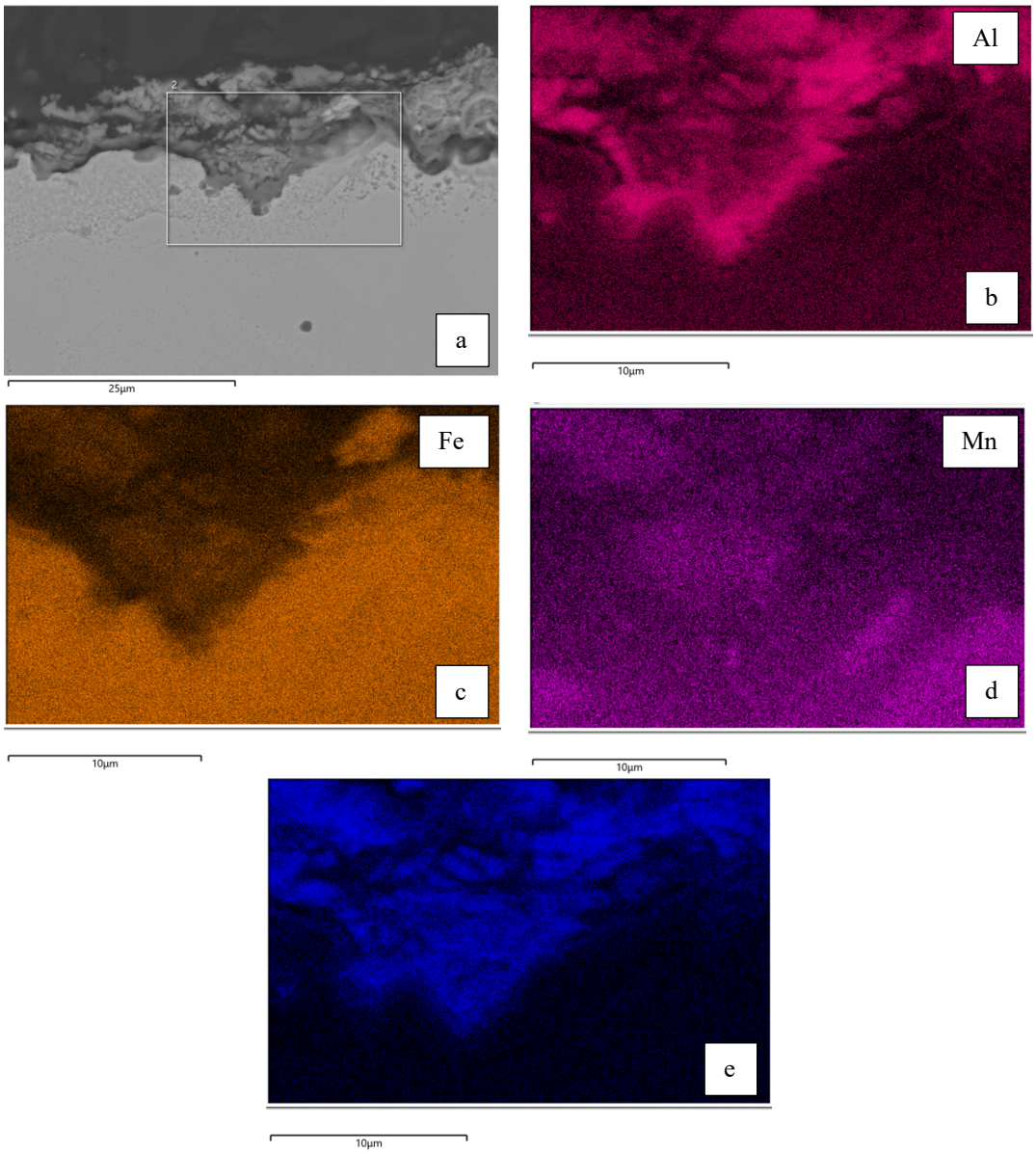

Figure 81: a) – e) EDS compositional map obtained from EBSD for the investigation on the oxide composition on the air quenched specimen

From Fig.82b-c-d, two distinct areas can be observed on the oxide layer of the air-quenched sample: a first layer rich in Al, attached to the sample's edge, and a smaller outer layer enriched with Mn. These observations suggest the presence of two different oxides on the sample's surface: alumina and iron manganese oxide [62], [63]. Among the two, alumina appears to be present in greater and more stable quantities, as it is uniformly distributed and forms a continuous layer along the sample's edge. On the other hand, iron manganese oxide exhibits more vein-like structures, indicating its potential instability (and thus susceptibility to fracture during welding).

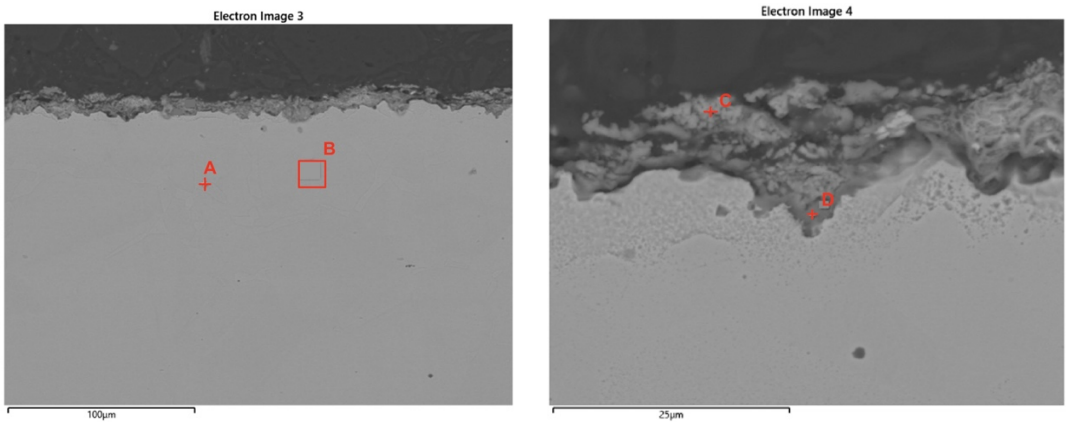

Figure 82: Oxide layer in the edge of the air quenched specimen, investigated at the SEM-EDS

SEM-EDS Compositional Analysis [wt.%]					
	Fe	Mn	Al	C	O
A	71.7	13.5	7.4	7.4	-
B	71.7	14.3	7.4	6.6	-
C	30.6	7.1	28.4	6.2	28.4
D	31.2	8.1	11.6	19.4	31.2

Figure 83: The SEM-EDS outputs of the investigated sites reported in Fig.83

The chemical composition obtained through SEM-EDS analysis of two points in the oxide layer (C and D in Fig.83) is presented in Tab.84. The first two rows (A and B) represent respectively a point and an area selected from the base material inside the air quenched specimen.

From the table, it can be observed that points C and D exhibit a significantly different chemical composition compared to the base material. Specifically, points C and D show a higher concentration of aluminum or oxygen, at the expense of iron concentration. Additionally, manganese appears to have a lower concentration compared to the base material, and point D also registers a high amount of carbon. These observations are consistent with the deductions made from the color phase map in Fig.82 and thus seem to confirm the presence of at least a significant layer of alumina.

The same investigations were then conducted on the water-quenched specimen. The results of the analysis are presented in Fig.85.

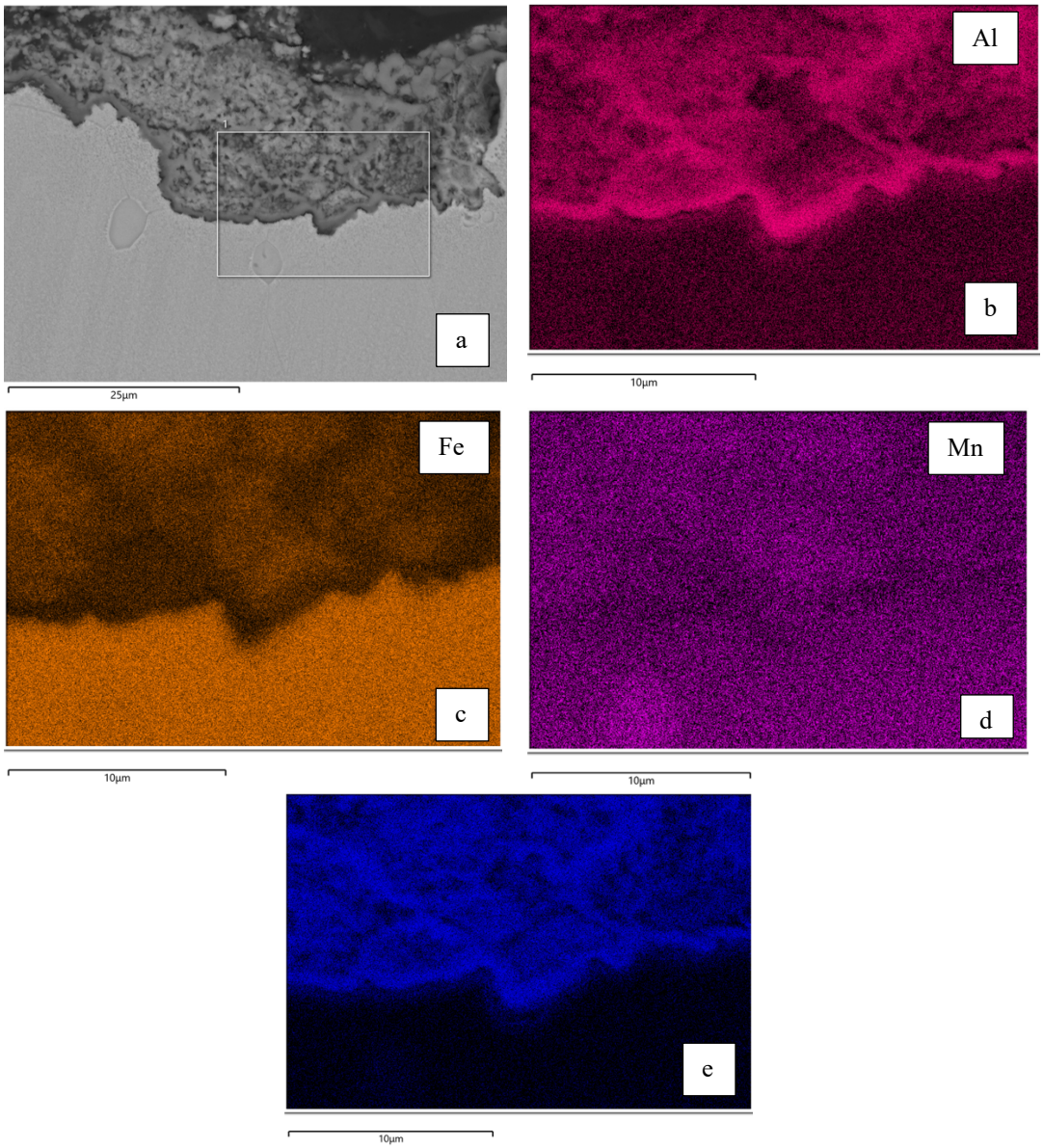

Figure 84: a) – e) EDS compositional map obtained from EBSD for the investigation on the oxide composition on the water quenched specimen

In this case, the oxide layer on the material surface appears to be much more extensive. Similar to the air-quenched specimen, the innermost layer of oxide is composed of alumina, while the outermost layer is iron manganese oxide. Once again, the alumina layer seems to be more stable and continuous, while the iron manganese layer, despite occupying a larger thickness, appears more discontinuous.

The chemical composition of 5 points in the oxide layer (in Fig.86) investigated through SEM-EDS analysis is presented in Tab.22. The first row (A) represents an area selected from the base material inside the water quenched specimen.

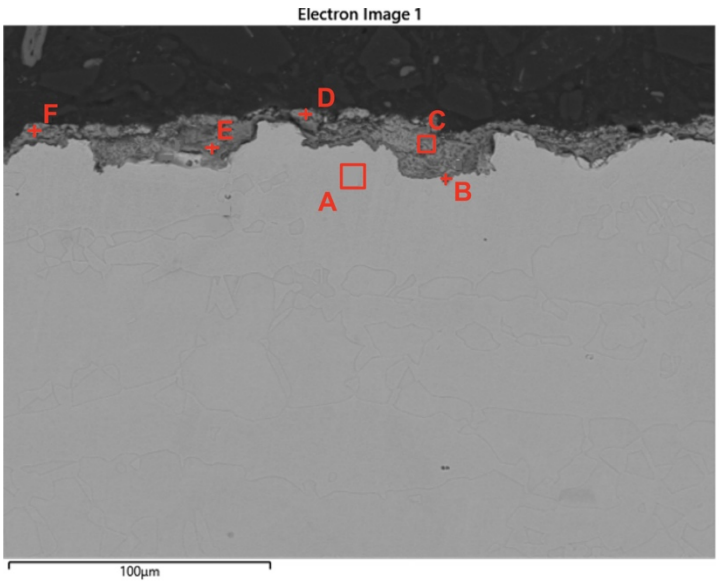

Figure 85: Oxide layer in the edge of the water quenched specimen, investigated at the SEM-EDS

SEM-EDS Compositional Analysis [wt.%]					
	Fe	Mn	Al	C	O
A	74.4	11.5	6.7	7.3	-
B	19.0	8.2	28.7	8.1	36.0
C	39.1	10.0	12.4	10.7	27.8
D	33.9	11.0	14.8	7.1	33.2
E	30.3	6.0	12.9	16.5	34.3
F	40.1	28.4	16.8	6.0	28.4

Table 21: The SEM-EDS outputs of the investigated sites reported in Fig.86

The table clearly distinguishes two points, B and F, taken from different layers of the oxide: B from the oxide layer adjacent to the base material and F from the central oxide layer. Both points exhibit a significantly different chemical composition compared to the base material. Point B shows a high concentration of aluminum and oxygen, while point F has a higher amount of manganese and oxygen. As also observed from the phase color map, these findings confirm the presence of two distinct oxides: alumina and iron manganese oxide. The other investigated points showed negligible variation in manganese concentration compared to the base material. However, they consistently displayed higher amounts of aluminum and, in some cases, carbon.

In conclusion, the cooling method does not seem to have an impact on the chemical composition of the oxide formed on the surface of the specimen. However, it is important to note that after air cooling, a portion of the oxide (likely composed primarily of iron manganese oxide) crumbled and detached from the specimen. This also explains why the observed oxide layer thickness was lower in this case. Consequently, during the welding operation on Fe-

15Mn-8Al-40ppmB, it is crucial to consider the possibility of oxide formation on the heated surface, which could adversely affect the successful outcome of the operation. Among these oxides, alumina appears to be the most problematic due to its homogeneous nature and high temperature resistance. For this reason, Tungsten Inert Gas (TIG) welding with alternating current (AC) may prove to be more effective with Fe-15Mn-8Al-1C-40ppmB alloy. In fact, during the period of positive electrode potential, the cathode spot induces the breakdown of the oxide layer that covers the surface of the material [64].

Double V butt welds

The double V butt welds analyzed were obtained using both direct current (DC) and alternating current (AC). In both cases, four passes were made to deposit the filler material between the two plates (two passes from one side and two from the other). The values of current and potential difference used for each pass are presented in Tab.23.

Direct current (DC)	Alternate current (AC)
1°: 86 A; ~12 V	1°: 110 A; ~15 V
2°: 82 A; ~12 V	2°: 110 A; ~15 V
3°: 82 A; ~12 V	3°: 110 A; ~15 V
4°: 82 A; ~12 V	4°: 110 A; ~15 V

Table 22: Welding parameters for each pass

In both cases, four cross-section of the joint were taken at various points along its length, as shown in Fig.87.

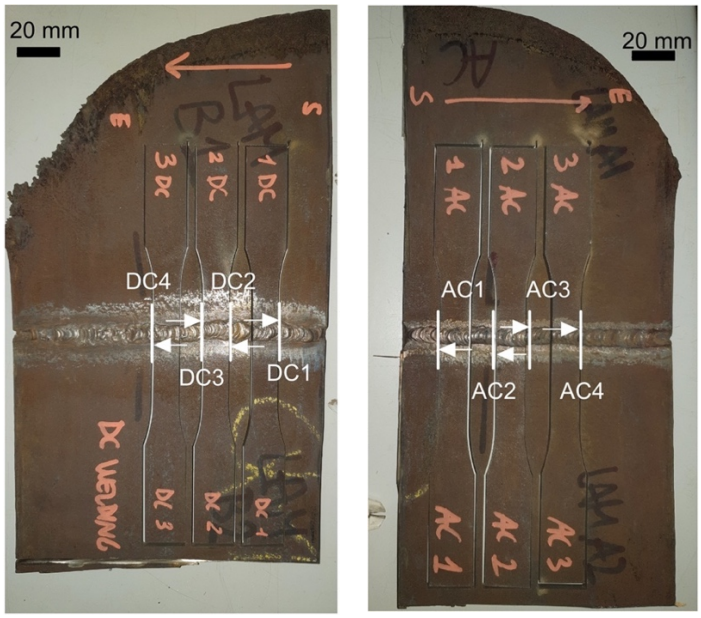

Figure 86: Sheets obtained after the double-V butt welding operation, showing the cross-sections analyzed

In Fig.88, the cross-sections of two of these welds (DC4 and AC3) can be observed. From the figure, as in the case of cladding, a clear distinction between the two fusion zones and the rest of the material can be observed.

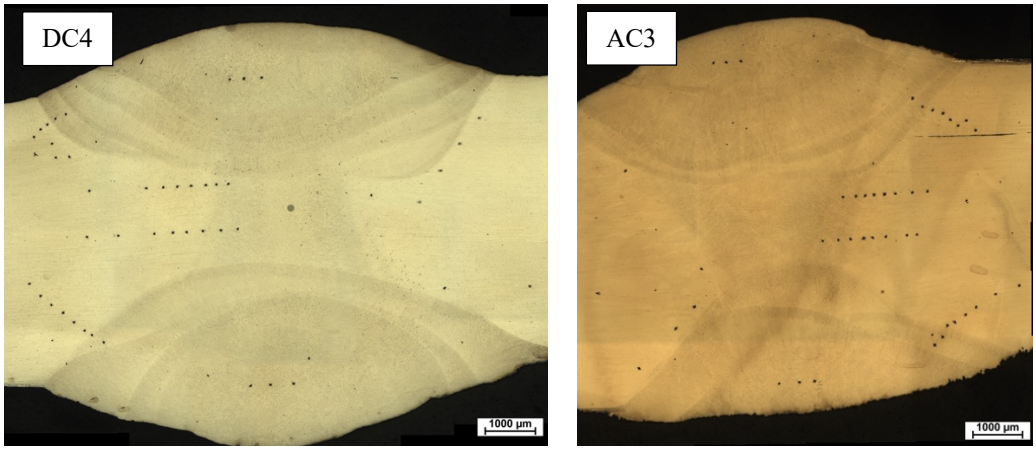

Figure 87: Micrographs of the cross sections of weld nuggets for the DC4 and AC3 specimens

Moreover, in Fig.89 higher magnification images of each zone for the AC2 and DC2 samples are presented. However, the complete collection of images captured using the optical microscope for these specimens is provided in **Appendix D**.

DC2 – Weld Zone	AC2 – Weld Zone
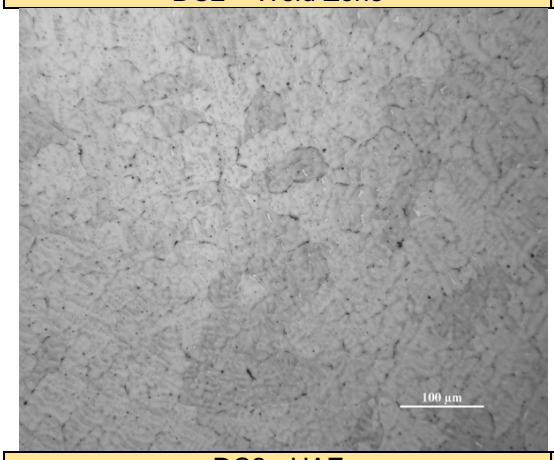	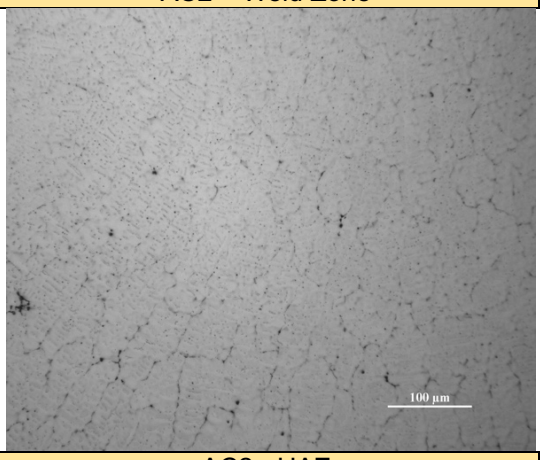
DC2 - HAZ	AC2 - HAZ

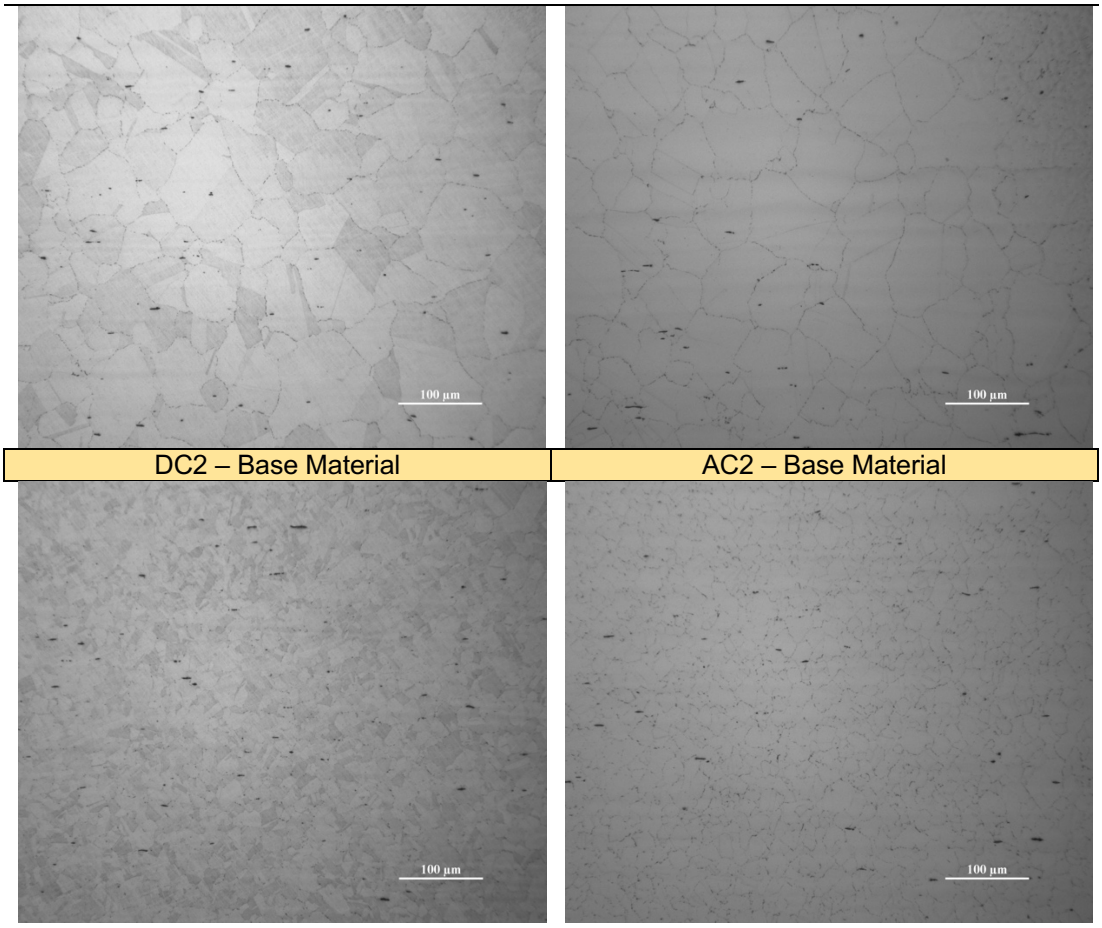

Figure 88: Micrographs of the DC2 and AC2 specimens inside the FZ, HAZ and BM at 200x

Similar to the cladding case, in Fig.89 and Fig.90, a fine dendritic microstructure can be observed within the WZ, with primary branches exhibiting incident angles of 60/120° or their multiples. However, particularly in the alternating current case, the dendrites branches appear shorter and less concentrated in this region.

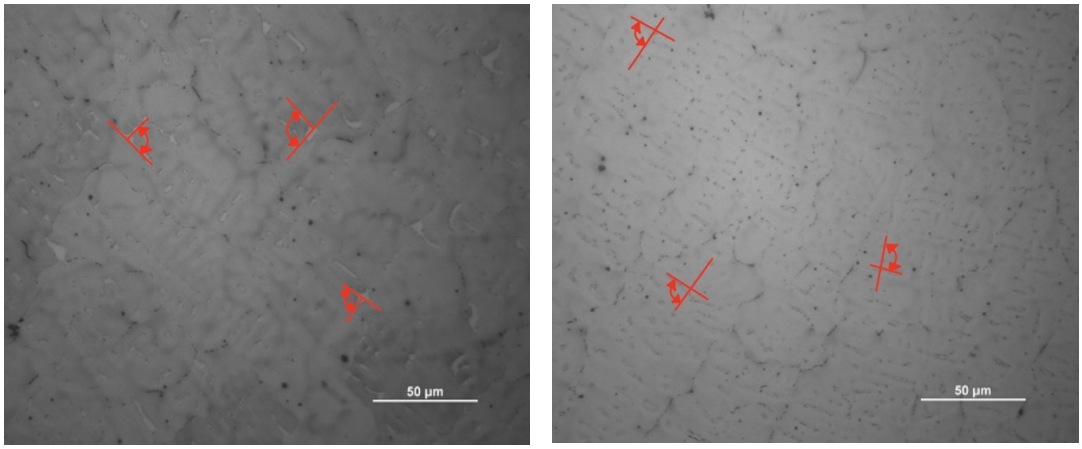

Figure 89: Dendrites orientation highlighted for the a) DC2 and b) AC2 specimens at 500x

An interesting feature was also observed in the Weld Zone (WZ) in the root gap, as shown in Fig.91. In this area, the dendrites appear to assume highly variable shapes and orientations. Specifically, as depicted in Fig.91, long

dendrites oriented horizontally and much shorter, almost globular dendrites oriented vertically were found. These different characteristics are undoubtedly associated with the specific thermal cycle to which this area is subjected during the welding operation. The molten material receives heat from both above and below, due to the different deposition of filler material, while simultaneously releasing heat to the adjacent walls of the two plates being welded.

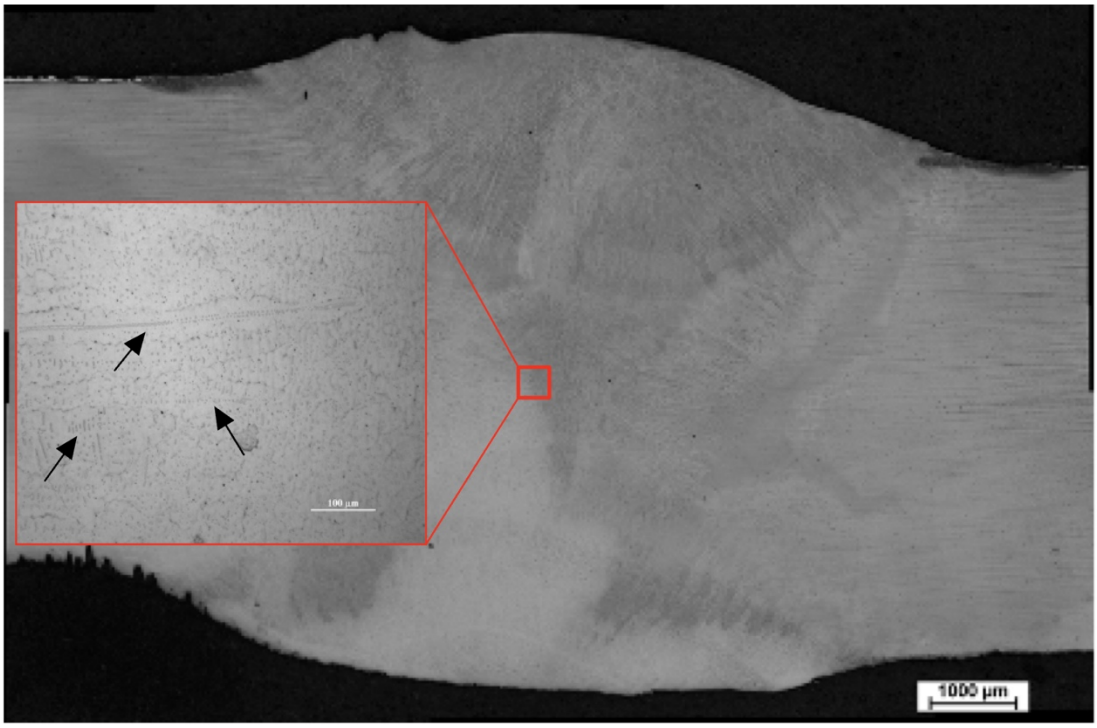

Figure 90: Root gap detail at the optical microscope (200x) for the DC4 specimen

Fig.92 displays the calculated average grain size values for the BM and the HAZ in each analyzed sample. The graphs indicate that the base material has maintained the grain size observed in the hot-rolled condition, with a thickness of 5 mm. In terms of the HAZ, a comparison between the two conditions reveals no significant variations in the average grain size dimension.

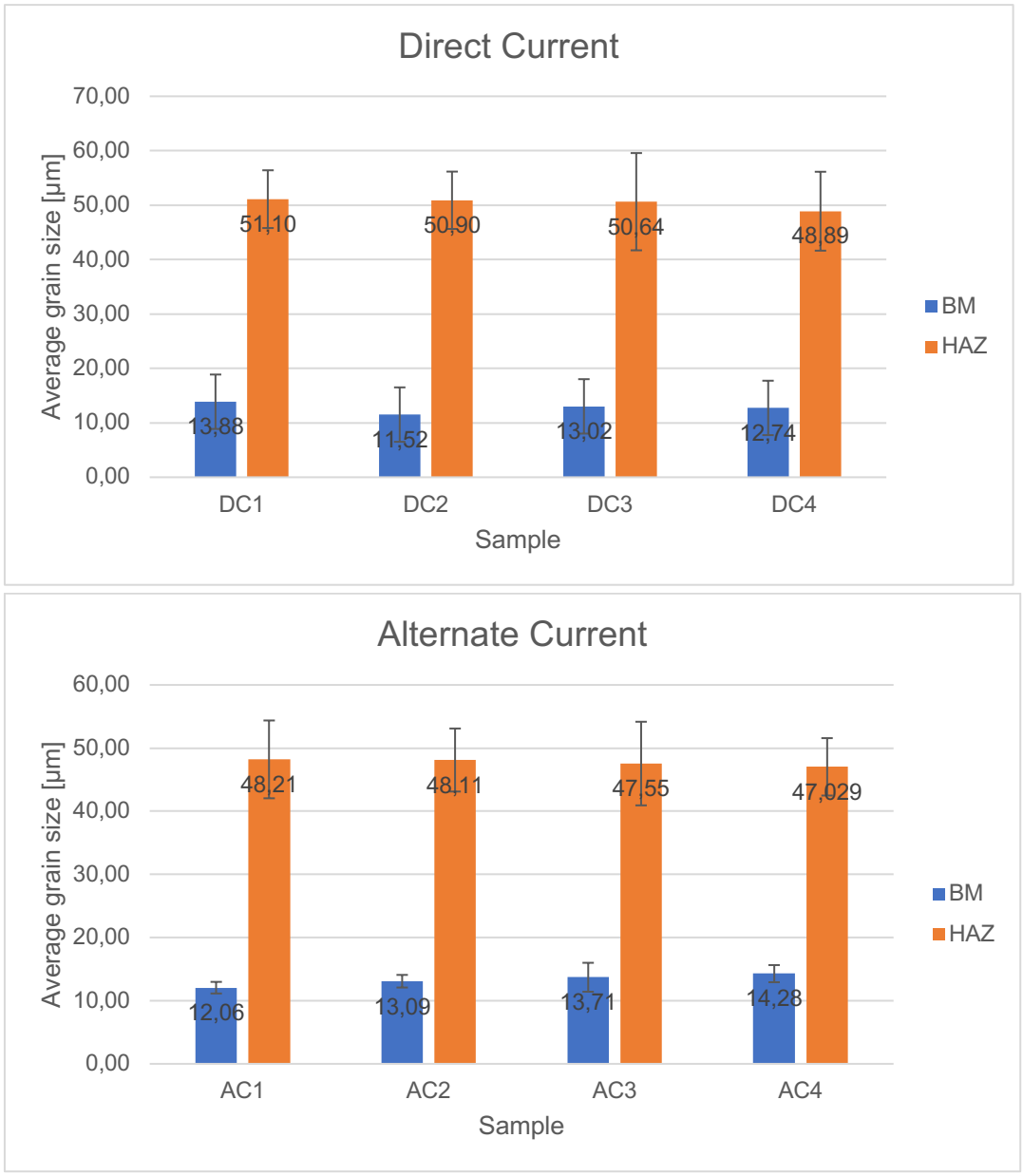

Figure 91: Average grain size plot of the Direct Current and Alternate Current) samples for the BM and the HAZ

Fig.94 presents the hardness profile for each analyzed specimen in the cross-section under the two welding conditions. Tests were conducted in the centre of the two weld zones, in the HAZ and on four radial lines starting from the WZ, as shown in Fig.93.

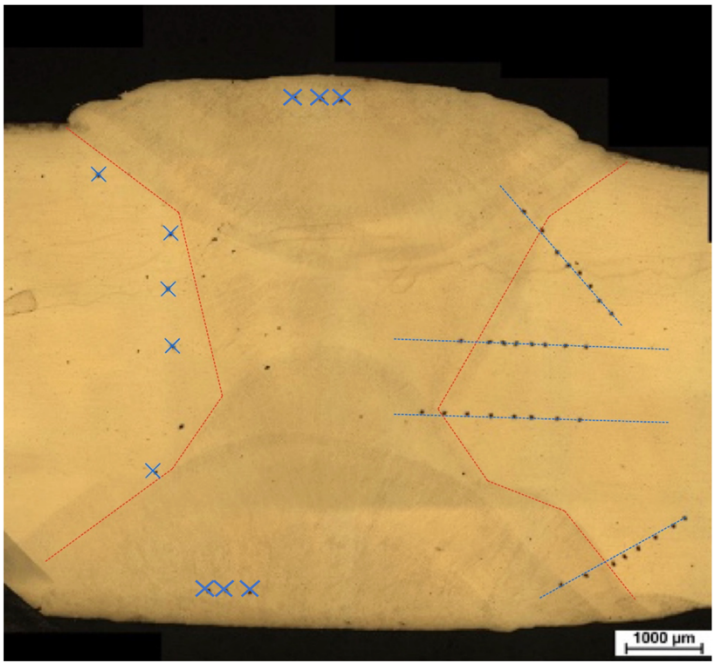

Figure 92: Micrographs of the AC1 specimen, showing locations of the four radial lines and the five HAZ's points tested

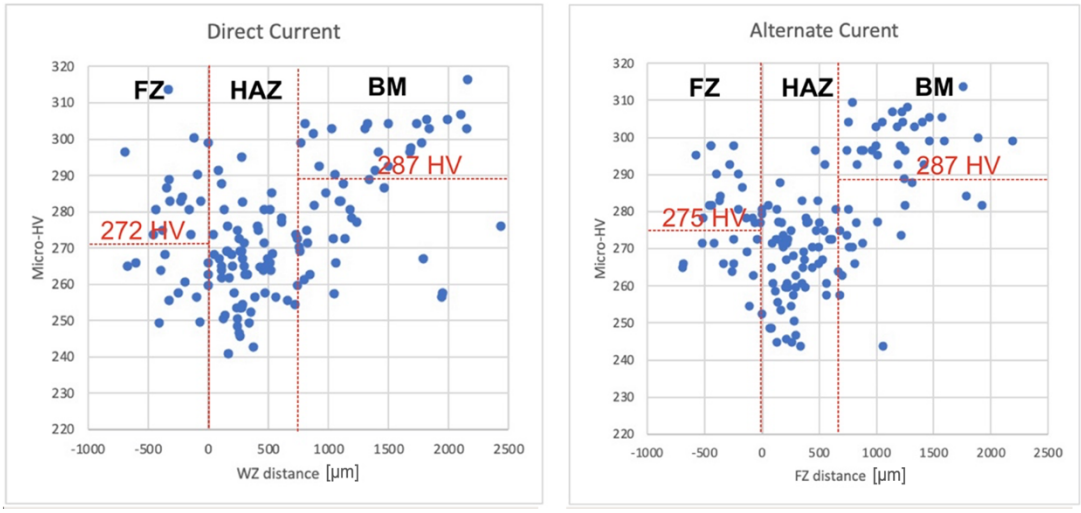

Figure 93: Hardness [HV] plot of the Alternate Current (AC) and Direct Current (DC) samples as a function of the distance from the WZ, obtained with a load of 300 mg and a twell time of 10 seconds

In both analyzed cases, direct current and alternating current, a similar behavior of the material can be observed. Specifically, within the tested points in the FZ (or WZ), the hardness values appear to concentrate in a range of approximately 260 to 300 HV. Moving towards the HAZ, there is a higher concentration of points at the lower end of this range. Additionally, within the HAZ, the hardness seems to decrease further, reaching minimum values (around 240 HV) at approximately 0.2-0.3 mm from the fusion zone. As we progress towards the Base Material (BM), the hardness appears to increase again, possibly due to the progressive reduction in size of austenitic grains. In the BM region adjacent to the HAZ, hardness values are significantly higher

than the 287 HV observed in the material's hot-rolled condition. This could be attributed to the precipitation of nano-sized κ-carbides, as observed in the cladding weld samples as well. However, the increased heat supplied to the material during the welding operation to achieve this type of joint may have further emphasized the precipitation of these secondary phases. The result is undoubtedly an increase in hardness but the presence of carbides, whether they are coherent or incoherent with the austenitic matrix, can also lead to a reduction in the ductility of the component.

Tensile tests

To investigate the tensile strength of the welds, three test specimens were cut from double-V welded plates with direct current, and three specimens from the plates welded using alternating current, as depicted in Fig.87. The specimens were cut in such a way as to maintain the weld at the center of the gauge length. The tests were conducted at a crosshead speed of 3 mm/min until complete sample fracture. The stress-force [kN] versus displacement [mm] and stress [MPa] versus strain [%] graphs obtained from the tests are presented in Fig.95. Fig.96 shows all the specimens after the test.

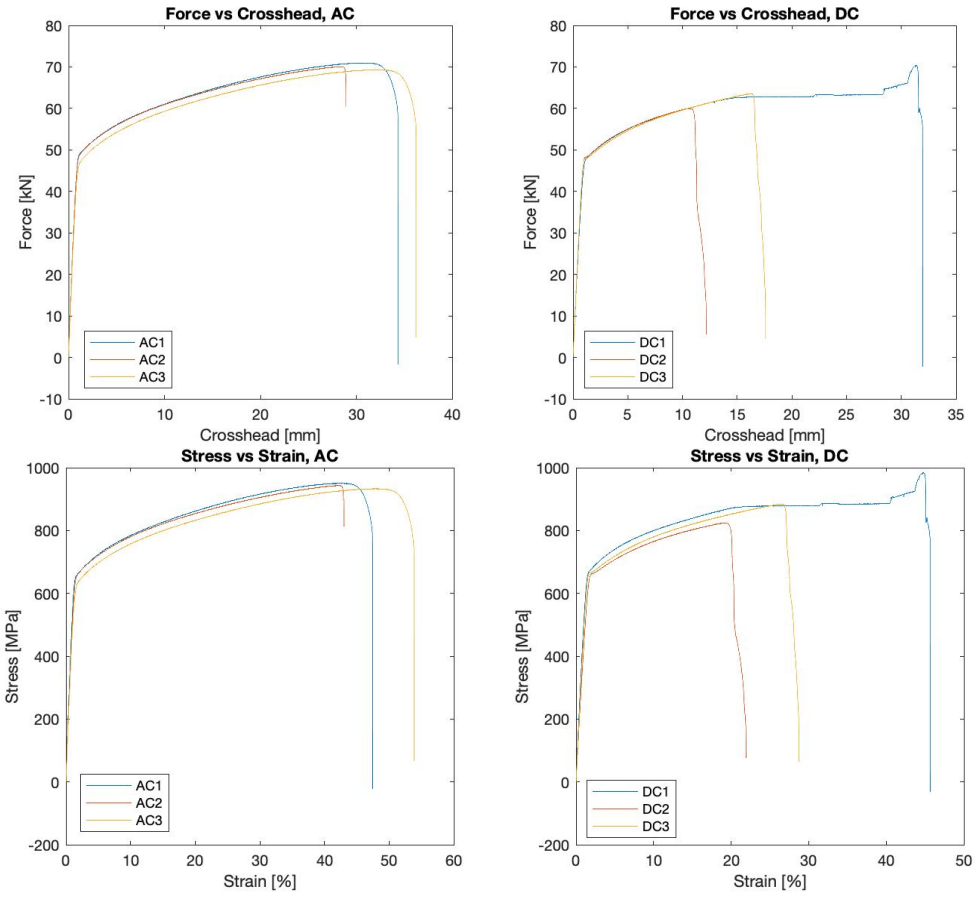

Figure 94: Force [KN] vs Crosshead [mm] and Stress [MPa] vs Strain [%] curves obtained after the tests

Figure 95: The tensile tests specimens after the failure

From Fig.96, it can be observed that two out of the three specimens extracted from the plate welded with direct current failed precisely at the center of the weld. As for the alternating current specimens, in all three cases, the fracture point is approximately at the center of the gauge length.

In Fig.95, it can be seen that in the case of direct current, the specimens that failed at the weld exhibited lower percentage elongation compared to the other cases (10-15% vs 40-45%). In general, the alternating current welds demonstrated better tensile behavior, both in terms of elongation at fracture and ultimate tensile strength (UTS).

These results confirm what was observed during the fabrication of these welds: alternating current appears to penetrate the material more easily, reducing the risk of defects such as porosity within the fusion zone. These defects, especially porosities, represent a critical issue for the material as they serve as preferential sites for crack initiation and propagation.

To better understand the fracture modes of the tested specimens, several SEM micrographs were taken at high magnifications. The obtained images are presented in Fig.97.

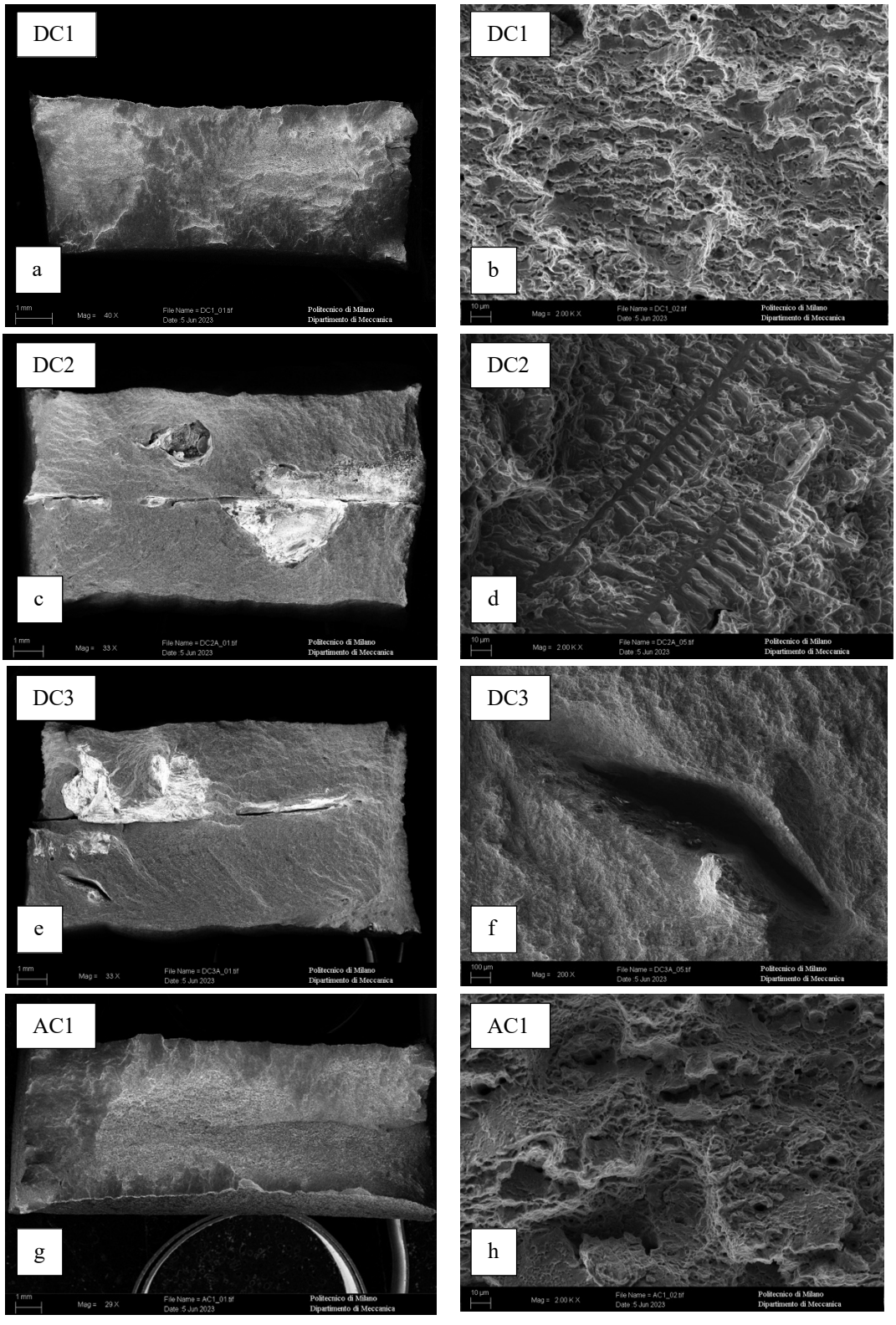
DC1
a
1 mm
Mag = 40 X
File Name = DC1_01.tif
Date :5 Jun 2023
Politecnico di Milano
Dipartimento di Meccanica
DC1
b
10 µm
Mag = 2.00 K X
File Name = DC1_02.tif
Date :5 Jun 2023
Politecnico di Milano
Dipartimento di Meccanica
DC2
c
1 mm
Mag = 33 X
File Name = DC2A_01.tif
Date :5 Jun 2023
Politecnico di Milano
Dipartimento di Meccanica
DC2
d
10 µm
Mag = 2.00 K X
File Name = DC2A_05.tif
Date :5 Jun 2023
Politecnico di Milano
Dipartimento di Meccanica
DC3
e
1 mm
Mag = 33 X
File Name = DC3A_01.tif
Date :5 Jun 2023
Politecnico di Milano
Dipartimento di Meccanica
DC3
f
100 µm
Mag = 200 X
File Name = DC3A_05.tif
Date :5 Jun 2023
Politecnico di Milano
Dipartimento di Meccanica
AC1
g
1 mm
Mag = 29 X
File Name = AC1_01.tif
Date :5 Jun 2023
Politecnico di Milano
Dipartimento di Meccanica
AC1
h
10 µm
Mag = 2.00 K X
File Name = AC1_02.tif
Date :5 Jun 2023
Politecnico di Milano
Dipartimento di Meccanica

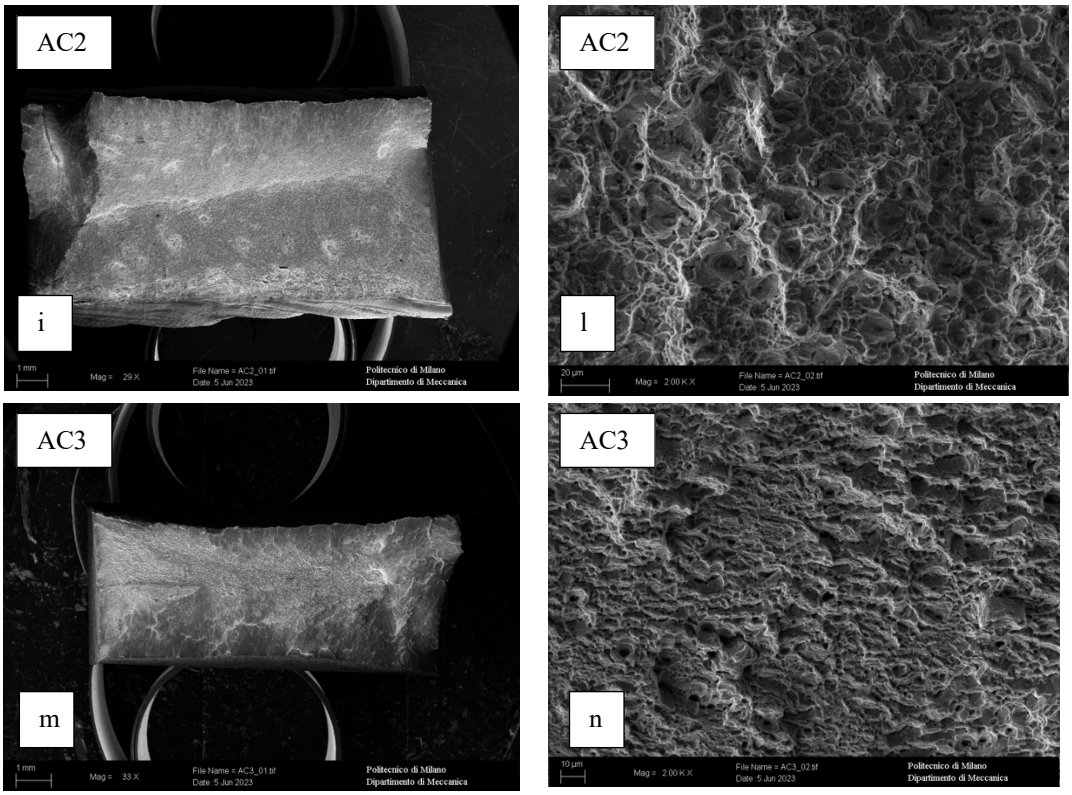

Figure 96: Fracture surfaces of the specimens at the SEM

As observed in Fig.96, the DC1, AC1, AC2, and AC3 specimens did not fail at the weld and, in general, exhibited higher elongation at fracture compared to the others. SEM images of these specimens clearly show the characteristic features of ductile fracture: dimples. On the other hand, the DC2 and DC3 specimens fractured within the weld in both cases. Fig.97d provides a clear view of dendrites that have been cut transversely on the fracture surface. As hypothesized through SEM-EDS analysis conducted in the Cladding section, these dendrites are composed of ferrite, with the surrounding matrix being austenite. Upon visual examination of their surfaces, it is evident that the ferrite and austenite phases deform in distinct manners. The surface of ferrite exhibits a flatter appearance, meanwhile the surface of austenite reveals the presence of dimples, indicating a localized plastic deformation process. Furthermore, oxide formations and porosities were detected on the fracture surfaces of both specimens. In particular, the oxide appears on the SEM as light-colored patches because it is non-conductive. These defects are likely attributed to the lower effectiveness of direct current welding on the material, as discussed earlier.

In conclusion, the tensile tests conducted on the double V butt welds also highlight how alternating current enables the achievement of higher quality joints, with an ultimate tensile strength (UTS) of approximately 900 MPa and 45% elongation at fracture.

Chapter 5

Discussion

The analysis performed has demonstrated that the microstructure of the Fe-15Mn-8Al-1C-40ppmB lightweight alloy is strongly dependent on the thermo-mechanical treatment that the material undergoes.
From the equilibrium phase diagram calculated with © *Thermo-Calc* for this chemical composition, the result expected is a fully austenitic microstructure within the temperature range of 900°C to 1100°C. However, ferrite can be observed in both hot and cold-rolled samples after the solution treatments at 900°C and 950°C. In particular, the cold-rolled specimens show a significantly higher and coarser fraction of ferrite, as can be seen in Fig.98.
This result suggests that cold-rolling may de-stabilize the austenitic matrix and promote the precipitation of secondary phases, particularly α-ferrite.
By comparing the average grain size analysis (Fig.99), it is possible to observe that in the cold-rolled case the coarsening of austenitic grains is less evident respect the hot-rolled condition ($\sim$60 μm for the hot-rolled and $\sim$40 μm for the cold-rolled). This behavior can be explained by the pinning effect, which is much more pronounced than the hot-rolled and solutioned condition due to the larger ferrite fraction.

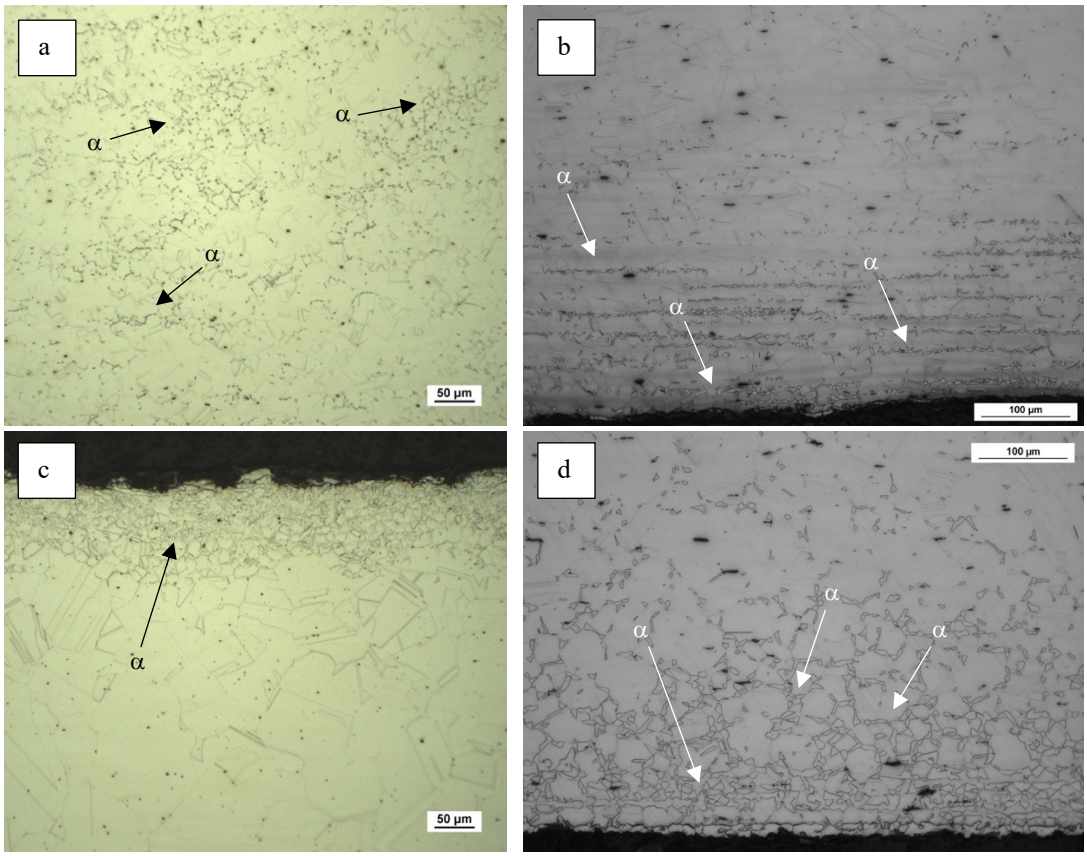

Figure 97: Microstructural evolution of hot-rolled solutioned samples at a) 900°C and c) 950°C, and of cold-rolled solutioned samples at b) 900°C and c) 950°C

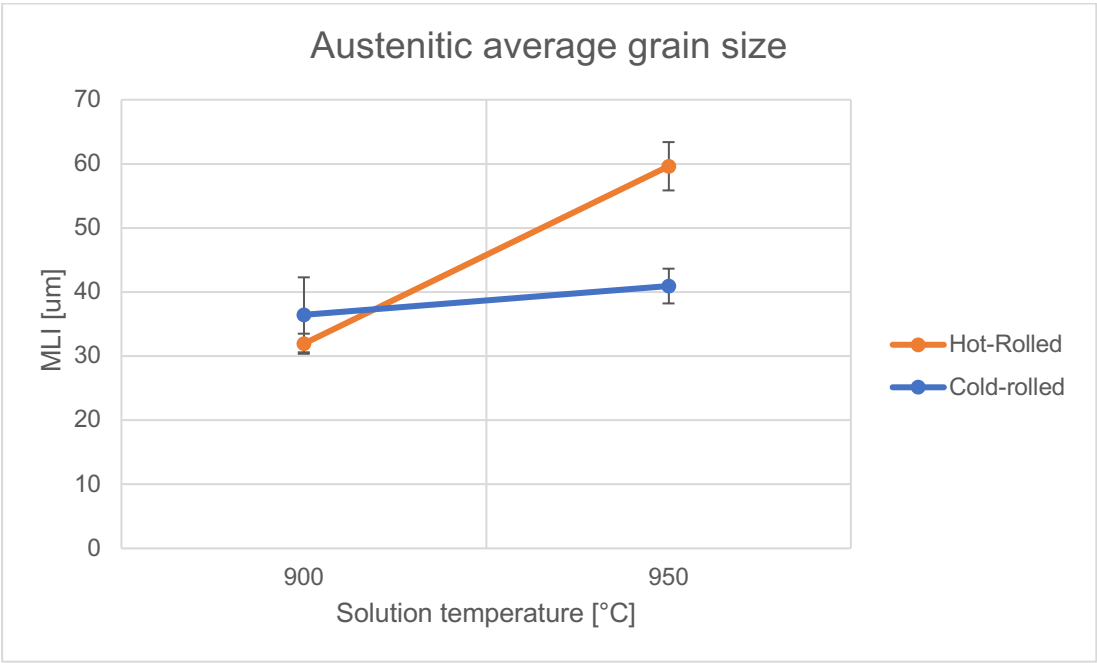

Figure 98: Average grain size evolution for hot-rolled and cold-rolled solutioned samples at 900°C and 950°C

According to literature [1], [9], [12], [13], [18], the effect of the ferrite precipitation is to increase in the yield strength (YS) and the hardness of the alloy. However, the main negative effect is the reduction in ductility. In general, ferrite is typically undesirable in lightweight austenitic steels as it has a negative impact on one of the characteristics that make these steels so important: their exceptionally high ductility.

Proceeding with the microstructure comparison, in all the analyzed cases, except for the 1 mm (80% thickness reduction) and 2 mm (60% thickness reduction) cold-rolled without heat treatments, the microstructure was found to be equiaxed. In the cold-rolled and solutioned specimens, this indicates that grain recrystallization occurred during heat treatment. This aspect is significant because it is closely related to the alloy's anisotropy. Therefore, from an industrial point of view it can be used for forming operations and then subjected to solution treatment to restore anisotropy.

Twin boundaries are detected in most of the microstructures analyzed for both hot and cold-rolled samples, as evidenced in Fig.98. They have a beneficial effect on the alloy's mechanical properties, because they obstruct the dislocations movement (as described in **Chapter 2**). In addition, the SEM analysis revealed a high amount of micro-bands crossing the grains, in particular in the cold-rolled samples. This indicates the main deformation mechanism acting on this alloy: the micro-bands induced plasticity (MBIP).

During cold deformation, in fact, dense zones of dislocations formed within the grains, easily observed at high magnifications (Fig.100). However, in the sample with an 80% reduction (CRE), the observed striations are so dense that they appear to be attributable to the typical martensite structure. However, this hypothesis was discarded because in the sample with a 60% reduction rate (CR), there is a lower amount of striations, which in this case can be easily attributed to micro-bands.

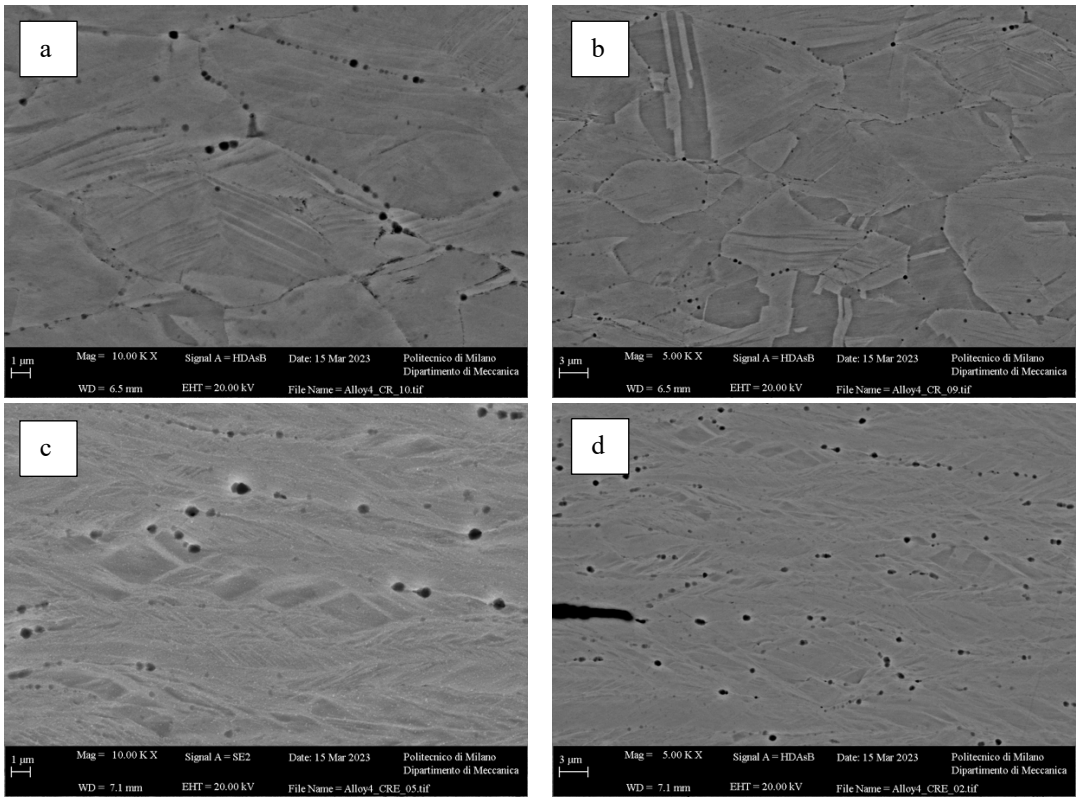

Figure 99: SEM observations for cold-rolled at a), b) 2 mm and at c), d) 1 mm specimens

None of the analyzed rolled conditions exhibited precipitation of κ-carbides. This observation can be primarily attributed to two factors: firstly, no aging treatment was conducted, secondly, the presence of 40ppm of boron in the alloy. Boron, in fact, can inhibit the formation of κ-carbides and prevent austenitic grain growth by forming boron-carbides. Two recent studies examined lightweight steels with similar chemical compositions: a Fe-15Mn-6.8Al-0.9C-0.2Ti [65] and a Fe-15Mn-8Al-2C [66] alloys; in the first case, κ-carbides were not found due to the presence of Ti, which has a similar function as B. In the second case, the microstructure was found to be composed mainly of austenite, with κ-carbide precipitation. Probably, if a certain amount of boron were added to the second alloy, it would be possible to avoid κ-carbide precipitation.

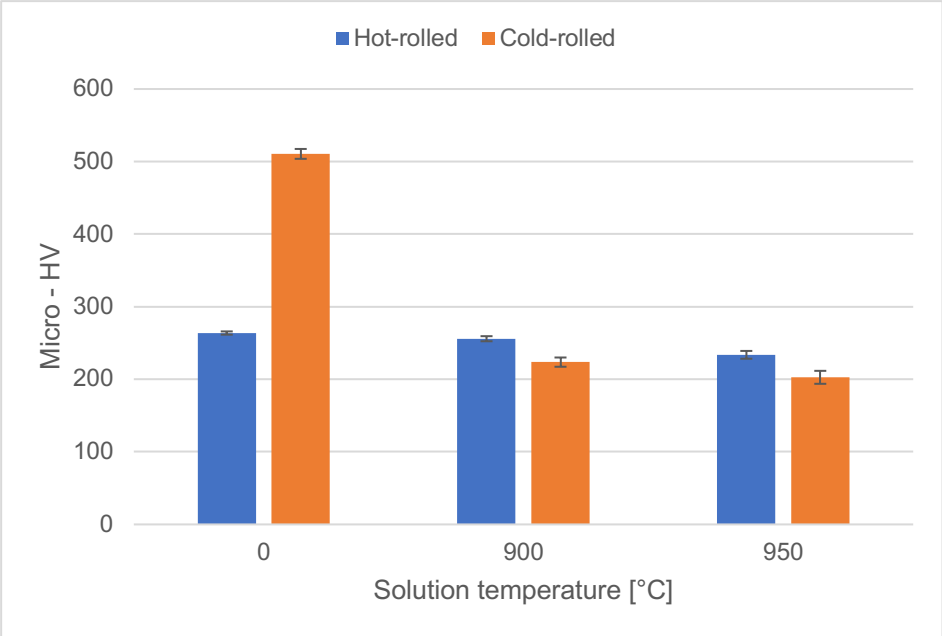

Figure 100: Micro-hardness [HV] evolution of hot-rolled and cold-rolled solutioned samples at 900°C and 950°C

Regarding the comparison of hardness between hot-rolled and cold-rolled conditions with respective solution treatments at 900°C and 950°, it can be observed in Fig.101 that the highest hardness is provided in the cold-rolled condition with a thickness reduction of 80% without heat treatment. In fact, observing the microstructure, it can be seen that the grains are very fine, and the precipitation of ferrite is highly uniform (Fig.102b). In contrast, in hot-rolled specimens, the hardness is about 50% lower, but the matrix is completely austenitic (Fig.102a). However, after heat treatments, the hardness is more constant in the case of hot-rolled specimens, while in the case of cold-rolled specimens it shows a significant reduction as early as 900°C and decreases further at 950°C.

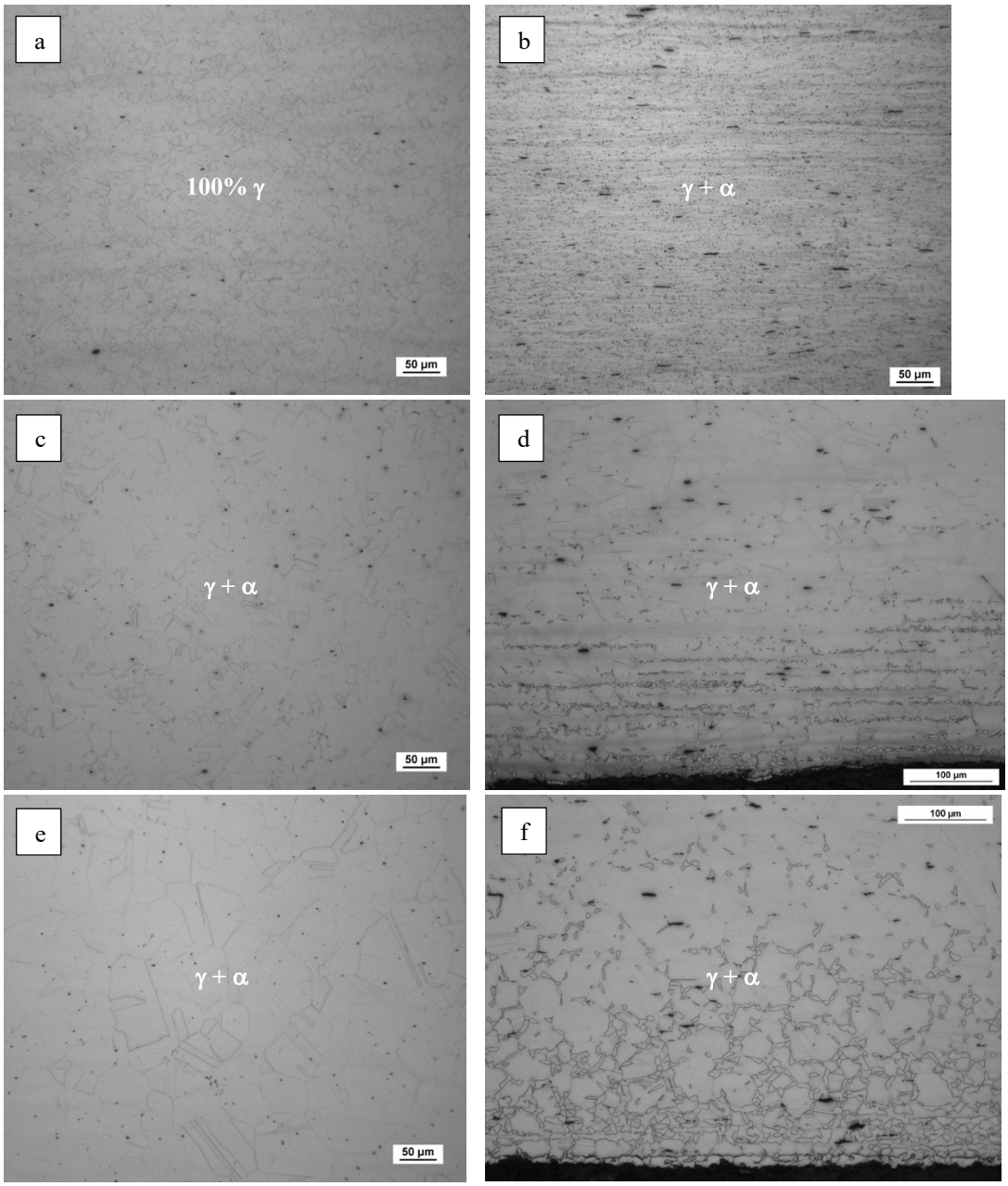

Figure 101: Microstructural evolution of a) hot-rolled and hot-rolled solutioned samples at c) 900°C and e) 950°C, and of b) cold-rolled and cold-rolled solutioned samples at d) 900°C and f) 950°C

In general, the condition which seems to give the best compromise between the desired characteristics is the hot-rolled without heat treatment. The grain is very fine, ferrite and κ-carbides are not present (according to XRD analysis), and a large amount of twins can be observed. The calculated r_m value for the anisotropy is close to 1, a very good result, and the hardness is the highest compared to all the conditions with equiaxed grains (HR, SHT900, SHT950 and CRE solution treated). Moreover, the hot-rolled material, even after solution treatments, maintains a quiet constant hardness value, and the ferrite that precipitates is fine and in lower fraction than in the cold-rolled case. This means that this material, when hot-deformed, can be solutioned to reduce

residuals stresses and promote homogenization of the microstructure with fewer problems than the cold-rolled case.

The solution treatments performed at both 900 and 925°C while varying the specimens time inside the furnace (15, 20, and 25 minutes) allowed for a more detailed study of the ferrite precipitation evolution within the austenitic matrix. In this case, the starting condition was cold-rolled to 1 mm (CRE), which, as previously described, showed uniform precipitation of fine grain boundary ferrite within the sample.
From a theoretical point of view, as indicated by the phase diagram obtained with © *Thermocalc*, by heating the samples above 800°C and then quenching them, a completely austenitic microstructure should have been obtained. Instead, the material's behavior appears to be rather unusual: for both 900°C and 925°C, after 15 minutes, ferrite bands can be identified mainly at the edges of the samples; after 20 minutes, the amount of ferrite seems to decrease, and then slightly increase again after 25 minutes.
This non-linear behavior can be probably associated to the competition of two phenomena that have an opposite effect: the recovery of the stresses resulting from the rolling process and the development of segregations resulting from the ferrite-to-austenite transformation. In fact, on the one hand, during the cold-rolling process, austenite tends to display more strain hardening compared to ferrite; during a subsequent heating, the relaxation of the stresses can induce the phase transformation of austenite into ferrite [60], [67]. On the other hand, heating above the austenitization temperature induces the transformation of ferrite into austenite. However, during this transformation, the newly formed austenite tends to reject Al, which, being a ferrite-stabilizer, is taken up by the remaining ferrite, stabilizing it [68].

The bending tests performed on samples obtained with both parallel and transverse orientation relative to the rolling direction, using two different thickness plates, have confirmed the excellent ductility of this Fe-15Mn-8Al-1C-40ppmB steel. It was possible to achieve a bending angle of approximately 75° without initiating cracks in the stressed regions of the material. Additionally, no substantial differences were observed in the response of samples with different orientations, supporting the excellent material anisotropy. Furthermore, a springback factor of ~0.7 was calculated for the 5 mm samples, while for the 3 mm samples, it was found to be ~0.8. For the industrial application of this alloy, it is therefore recommended to carefully set the forming operation, taking into consideration the sheet thickness and the consequent required overbending, in order to avoid excessive springback angles after the load is released.

Another interesting result was obtained from the corrosion tests conducted in a saline environment. As described in **Chapter 4**, the polarization curves derived from the various tests performed have shown a common trend in the material, allowing for the determination of ranges of values for the corrosion potential, E_{corr} (between -984 mV and -844 mV), the passivation current I_{pass} (between 0.00219 μA/cm^2 and 0.00561 μA/cm^2), and the end-passivation potential E_{epp} (between -298 mV and -226 mV). As described in **Chapter 2**, these values confirm the lower corrosion resistance of this alloy compared to stainless steels or other lightweight steels with higher concentrations of Al and Mn.

However, SEM-EDS analysis of the surface of the hot-rolled and heat-treated material at 1000°C has revealed the formation of two distinct oxide layers. It is hypothesized that these layers consist of an alumina layer and an iron and manganese oxide layer. Among these two, the alumina layer was found to be present as a thin, uniformly distributed layer along the material's surface. On the other hand, the iron and manganese oxide appeared more discontinuous and exhibited a vein-like structure. The presence of these oxides is important to highlight because they can influence the material's response to certain common industrial operations, such as welding.

In fact, the analyses conducted on the welds in this study have highlighted a greater effectiveness of alternating current (compared to direct current) due to its higher ability to break down the oxide layer covering the material surface. This principle is similar to the one used in welding aluminum alloys, where the breakage of the surface layer of alumina is necessary to achieve an high quality weld.

From a microstructural perspective, both types of tested welds (cladding and double V-butt weld) exhibited clear distinctions in grain structure and size among the weld zone, the heat-affected zone, and the base material zone, as observed in Fig.103.

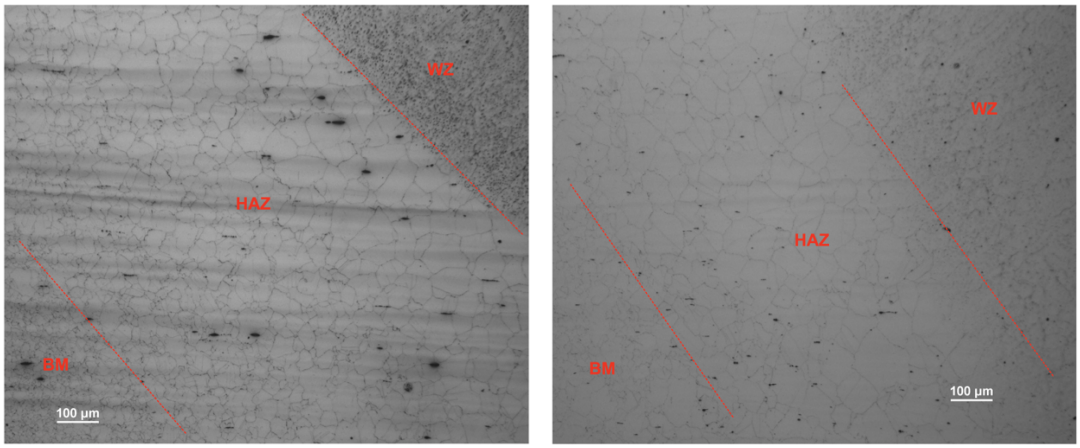

Figure 102: Distinction of the FZ, HAZ and BM in the a) DC2 cladding and b) AC2 double-V butt weld specimen at 100x

In particular, the WZ exhibited a microstructure characterized by the presence of ferrite dendrites surrounded by an austenitic matrix. The observed dendrites generally had a radial orientation relative to the material deposition zone. However, dendrites with primary branches exhibiting incident angles of 60/120° or their multiples were also observed. Regarding the HAZ, it was identified using grain size as a criterion. Between the base material and the weld zone, grains of significantly larger size were present. In all analyzed conditions, the HAZ exhibited an average grain size of approximately 50 µm. Additionally, this area showed lower hardness compared to the base material, with values reaching around 240 HV, much lower respect the 280-290 HV of the base material.

Of particular interest was the region of the base material adjacent to the HAZ. Although the average grain size in this region was comparable to that of the base material in the hot-rolled condition, SEM-EDS analysis revealed the presence of some precipitates. Specifically, nano-sized κ-carbide precipitates were observed along grain boundaries.

Presumably, the heat input in this material zone was insufficient to induce grain coarsening, but it still promoted the precipitation of these secondary phases. This results in an increase in hardness, as measured in the tests conducted (up to 310 HV), but a significant loss of ductility.

To further investigate the ductility and mechanical properties of the double-V butt welds, tensile tests were conducted, followed by SEM analysis of the resulting fracture surfaces. The results revealed superior quality of the joints produced using alternating current, exhibiting elongations at fracture of up to 45% and a higher ultimate tensile strength (UTS) exceeding 900 MPa. Specifically, for these samples, fracture did not occur within the weld, and their fracture surfaces exhibited a uniform presence of dimples. In contrast, in two out of the three samples tested using direct current, fracture occurred precisely at the center of the weld, with significantly lower elongation and stress values

compared to the previous cases. Furthermore, SEM analysis allowed for the observation of two important characteristics in these samples, as depicted in Fig.104. On the fracture surface of both samples, a distinct area affected by the presence of oxide can be observed. Additionally, horizontal cracks were found at the center of the samples, which could be attributed to lack of fusion, as well as relatively large-sized porosities located more externally.

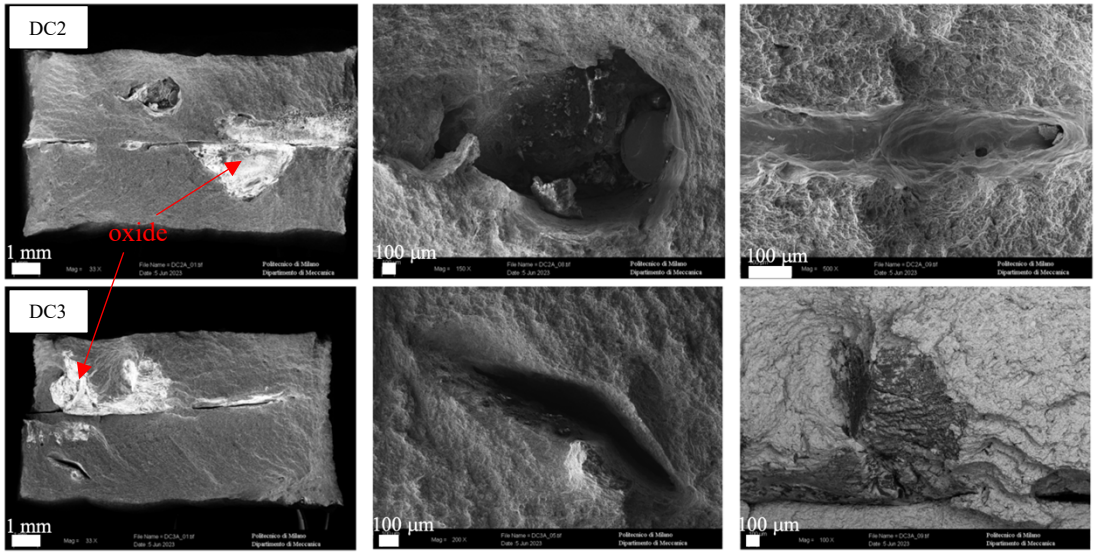

Figure 103: Fracture surfaces of the DC2 and DC3 butt weld specimens at the SEM

Furthermore, in one of these samples that failed at the center of the weld, sections of dendrites were found on the fracture surface (Fig.105). It is notable that these dendrites appear to be deformed differently compared to the surrounding material and do not exhibit dimples, which are the primary feature of ductile fracture surfaces. These observations are consistent with the previous description that the dendrites and the matrix are composed of two distinct crystalline structures, respectively ferrite and austenite.

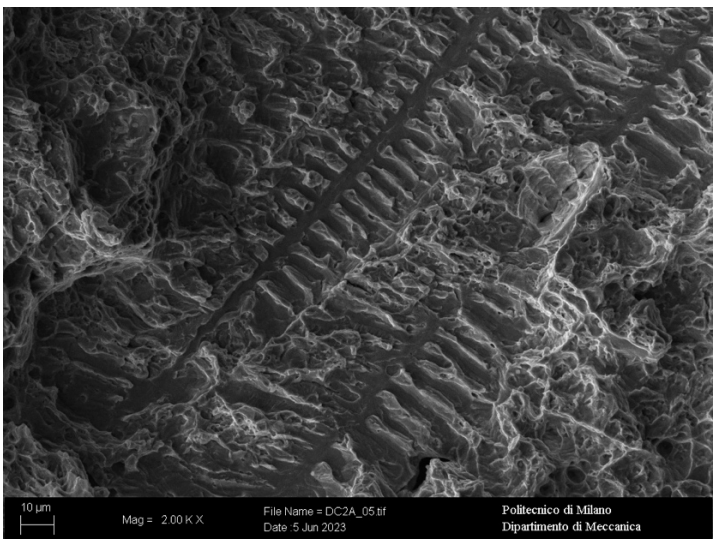

Figure 104: Dendrite detail on the fracture surface of the DC2 butt weld specimen

Chapter 6

Conclusions

Several conclusions can be derived from this study:

- the chemical composition of the alloy enables to reach a reduction in density of approximately 10% compared to the main alloys used in the automotive industry for structural components;
- in all the examined conditions, with the exception of the hot-rolled state, ferrite precipitation was observed within the austenitic matrix. Conversely, κ-carbides were not detected under any rolling condition;
- the main deformation mechanisms acting on this alloy are the MBIP and the TWIP. In fact, SEM observations had demonstrated the presence of a high amount of micro-bands in the cold-rolled specimens; simultaneously, at the OM it was possible to observe in all conditions a high amount of twins.
- the corrosion potential and the passivation current density derived form the potentiodynamic corrosion tests are respectively ~910 mV and ~0.0039 $\mu A/cm^2$; These values confirm the lower corrosion resistance of this alloy compared to stainless steels and other lightweight steels with higher Al and Mn concentrations (such as the Fe-24.4Mn-9.2Al-0.40C and the Fe-24.8Mn-7.3Al-0.90C).
- the hot-rolled material exhibited a complete anisotropic behavior ($r_m \sim 1$). Through the bending test it was possible to bend the material up to an angle of 75° without initiating any cracks on the material's surface. Furthermore, the springback factor obtained from the bending tests was 0.77 for the 5 mm specimens and 0.88 for the 3 mm specimens.

In particular, regarding the combination of hot-rolling and solution treatment:

- the initial hot-rolled condition had shown a very fine microstructure (MLI of ~14 μm) with equiaxal and randomly oriented austenitic grains. These is mainly related to the dynamic recrystallization which takes place during the hot-rolling operation;
- solution treatments at 900°C and 950°C induced the precipitation of ferrite, mainly concentrated at the edges of the samples in form of thin bands;
- even with solution treatments, some signs of the plastic deformation (such as micro-bands and twins) are not removed;
- the hardness in the hot-rolled state remained fairly stable, even after solution treatments at 900°C and 950°C. This shows that the recovery

of plastic deformation stresses has already started in the hot-rolling process.

Regarding the effect of cold rolling:

- the cold-rolled microstructure exhibits in very fine and slightly elongated austenitic grains;
- cold-rolling de-stabilize the austenitic matrix, inducing the precipitation of ultra-fine ferritic grains at grain boundary;
- thanks to the high deformation and the residual stresses induced by this operation, the hardness is the highest among all the conditions analyzed (~510 HV for the 1 mm specimen).

Regarding the effect of solution treatment on the cold-rolled material:

- considering the heat treatments performed for 30 minutes, the temperature that allows the lowest final fraction of ferrite is 900°C;
- the ferrite precipitation does not increase linearly with the treatment time in the range 15-30 minutes. The optimal treatment time to minimize the fraction for the analyzed samples was found to be 20 minutes;
- solution treatments, which allow the recovery of the residual stresses, significantly decrease the hardness of the cold-rolled material. In particular, the hardness after the heat treatment (at 900°C and 950°C) is higher for the hot-rolled material than for the cold-rolled one.

Regarding the material's behavior after the welding operation:

- alternate current has been demonstrated to be more effective than direct current for welding the Fe-15Mn-8Al-1C-40ppmB steel. Alternate current has shown the capability to break down the oxide layer present on the material's surface, which could potentially consist of a combination of alumina and iron manganese oxide;
- the microstructure of the welds exhibited significant variation across different zones of the welding joint. In the weld zone, a fine dendritic structure was identified, while the heat-affected zone showed coarsened austenitic grains. Additionally, the HAZ exhibited lower hardness values (ranging from 240 to 250 HV) compared to the base material's hardness of ~290 HV;
- SEM analysis has demonstrated that the dendrites in the weld zone primarily consist of ferrite. Furthermore, in the region of the base material adjacent to the HAZ, nanoscale κ-carbides have been observed. These κ-carbides undoubtedly contribute to the increased hardness of the material in this zone but could potentially pose issues related to reduced ductility.

- Tensile tests conducted on double-V butt welds produced using alternating current exhibited an elongation at fracture of ~45% and UTS exceeding 900 MPa. In contrast, the joints obtained using direct current yielded less favorable results, as two out of the three tested specimens failed at the center of the weld. Analysis of the fracture surfaces revealed the presence of oxides and porosity within these welds, probably due to the lower effectiveness of direct current welding.

Future developments

The characterization of the Fe-15Mn-8Al-1C-40ppmB lightweight steel considered in this study still requires further developments. For the actual industrialization of this material, achieving a comprehensive understanding of the effects of thermo-mechanical treatments and welding on its microstructure and mechanical properties is crucial. Additionally, further investigation is needed on certain properties not addressed in this study, such as wear resistance and fatigue strength. To complete the characterization of this alloy, it shall be included:

- the optimization of thermodynamic databases to obtain accurate equilibrium phase diagrams, enabling the correct prediction of constituent phases following thermo-mechanical treatments;
- understanding the inability of the solution treatment to remove signs of plastic deformation, such as twin boundaries and micro-bands;
- further investigation is needed to gain a deeper understanding of the ferrite precipitation in the cold-rolled samples followed by subsequent solution treatment;
- integrating FLD formability tests, CVN (Charpy V-notch) toughness tests, and tensile testing on both hot-rolled and cold-rolled material to complete the mechanical characterization of the alloy;
- a study to determine the optimal parameters for TIG welding in alternating current, aiming to minimize the heat input's impact on the material. It is crucial to minimize grain coarsening and the precipitation of κ-carbides that occur in proximity of the weld joint.

Bibliography

[1] O. A. Zambrano, “A General Perspective of Fe-Mn-Al-C Steels.”

[2] A. P. Bentley, “Ordering in Fe-Mn-AI-C austenite,” 1986.

[3] _____ J C Benz and H. W. Leavenworth, “An Assessment of Fe-Mn-AI Alloys as Substitutes for Stainless Steels.”

[4] S. C. Tjong, “AQUEOUS CORROSION PROPERTIES OF AUSTENITIC Fe-8.7A1-29.7Mn-1.04C ALLOY,” 1986.

[5] R. Rana, C. Lahaye, and R. K. Ray, “Overview of Lightweight Ferrous Materials: Strategies and Promises,” *JOM*, vol. 66, no. 9. Minerals, Metals and Materials Society, pp. 1734–1746, Sep. 01, 2014. doi: 10.1007/s11837-014-1126-5.

[6] R. Rana, “Low-Density Steels,” *JOM*, vol. 66, no. 9. Minerals, Metals and Materials Society, pp. 1730–1733, Sep. 01, 2014. doi: 10.1007/s11837-014-1137-2.

[7] L. Mereghetti, “Effects of the thermo-mechanical processing on the microstructural evolution of a Fe-Mn-Al-C austenitic lightweight steel.,” 2021.

[8] H. Kim, D. W. Suh, and N. J. Kim, “Fe-Al-Mn-C lightweight structural alloys: A review on the microstructures and mechanical properties,” *Science and Technology of Advanced Materials*, vol. 14, no. 1. Feb. 2013. doi: 10.1088/1468-6996/14/1/014205.

[9] S. Chen, R. Rana, A. Haldar, and R. K. Ray, “Current state of Fe-Mn-Al-C low density steels,” *Progress in Materials Science*, vol. 89. Elsevier Ltd, pp. 345–391, Aug. 01, 2017. doi: 10.1016/j.pmatsci.2017.05.002.

[10] Z. H. Lai, Y. H. Sun, Y. T. Lin, J. F. Tu, and H. W. Yen, “Mechanism of twinning induced plasticity in austenitic lightweight steel driven by compositional complexity,” *Acta Mater*, vol. 210, May 2021, doi: 10.1016/j.actamat.2021.116814.

[11] G. Zhang *et al.*, “Investigation on the microstructural evolution and mechanical properties of partially recrystallized Fe-27Mn-10Al-1.4C steel,” *Materials Science and Engineering A*, vol. 833, Jan. 2022, doi: 10.1016/j.msea.2021.142545.

[12] J. Xing, Y. Wei, and L. Hou, “An Overview of the Effects of Alloying Elements on the Properties of Lightweight Fe-(15–35) Mn-(5–12) Al-(0.3–1.2) C Steel,” *JOM*, vol. 70, no. 6. Minerals, Metals and Materials Society, pp. 929–937, Jun. 01, 2018. doi: 10.1007/s11837-018-2837-9.

[13] I. Gutierrez-Urrutia and D. Raabe, “High strength and ductile low density austenitic FeMnAlC steels: Simplex and alloys strengthened by nanoscale ordered carbides,” *Materials Science and Technology (United Kingdom)*, vol. 30, no. 9, pp. 1099–1104, 2014, doi: 10.1179/1743284714Y.0000000515.

[14] S. Pramanik and S. Suwas, “Low-Density Steels: The Effect of Al Addition on Microstructure and Properties,” *JOM*, vol. 66, no. 9, pp. 1868–1876, Sep. 2014, doi: 10.1007/s11837-014-1129-2.

[15] S. S. Sohn, S. Lee, B. J. Lee, and J. H. Kwak, “Microstructural Developments and Tensile Properties of Lean Fe-Mn-Al-C Lightweight Steels,” *JOM*, vol. 66, no. 9, pp. 1857–1867, Sep. 2014, doi: 10.1007/s11837-014-1128-3.

[16] D. W. Kim, J. Yoo, S. S. Sohn, and S. Lee, “Austenite reversion through subzero transformation and tempering of a boron-doped strong and ductile medium-Mn lightweight steel,” *Materials Science and Engineering A*, vol. 802, Jan. 2021, doi: 10.1016/j.msea.2020.140619.

[17] L. Xia, L. Yan, H. Zhang, Y. Li, Z. Jiang, and G. Li, “Factors Affecting the Mechanical Performance of High Manganese Austenitic Steel,” *Metals*, vol. 12, no. 9. MDPI, Sep. 01, 2022. doi: 10.3390/met12091405.

[18] O. A. Zambrano, J. Valdés, Y. Aguilar, J. J. Coronado, S. A. Rodríguez, and R. E. Logé, “Hot deformation of a Fe-Mn-Al-C steel susceptible of κ-carbide precipitation,” *Materials Science and Engineering A*, vol. 689, pp. 269–285, Mar. 2017, doi: 10.1016/j.msea.2017.02.060.

[19] K. H. Han and W. K. Choo, “Phase Decomposition of Rapidly Solidified Fe-Mn-AI-C Austenitic Alloys.”

[20] W. C. Cheng, C. Y. Cheng, C. W. Hsu, and D. E. Laughlin, “Phase transformation of the L12 phase to kappa-carbide after spinodal decomposition and ordering in an Fe-C-Mn-Al austenitic steel,” *Materials Science and Engineering A*, vol. 642, pp. 128–135, Aug. 2015, doi: 10.1016/j.msea.2015.06.096.

[21] W. C. Cheng, “Phase Transformations of an Fe-0.85 C-17.9 Mn-7.1 Al Austenitic Steel After Quenching and Annealing,” *JOM*, vol. 66, no. 9, pp. 1809–1820, Sep. 2014, doi: 10.1007/s11837-014-1088-7.

[22] W. C. Cheng, C. Y. Cheng, C. W. Hsu, and D. E. Laughlin, “Phase transformation of the L12 phase to kappa-carbide after spinodal decomposition and ordering in an Fe-C-Mn-Al austenitic steel,” *Materials Science and Engineering A*, vol. 642, pp. 128–135, Aug. 2015, doi: 10.1016/j.msea.2015.06.096.
[23] W. C. Cheng, “Phase Transformations of an Fe-0.85 C-17.9 Mn-7.1 Al Austenitic Steel After Quenching and Annealing,” *JOM*, vol. 66, no. 9, pp. 1809–1820, Sep. 2014, doi: 10.1007/s11837-014-1088-7.
[24] J. Xing, L. Hou, H. Du, B. Liu, and Y. Wei, “Effects of Pre-deformation on the Kinetics of β-Mn Phase Precipitation and Mechanical Properties in Fe–30Mn–9Al–1C Lightweight Steel,” *Metall Mater Trans A Phys Metall Mater Sci*, vol. 50, no. 6, pp. 2629–2639, Jun. 2019, doi: 10.1007/s11661-019-05173-5.
[25] J. Moon *et al.*, “Phase transformation mechanism and hardness during ageing of an austenitic Fe-30Mn-10.5Al-1.1C-3Mo lightweight steel,” *J Alloys Compd*, vol. 804, pp. 511–520, Oct. 2019, doi: 10.1016/j.jallcom.2019.06.362.
[26] X. P. Chen, Y. P. Xu, P. Ren, W. J. Li, W. Q. Cao, and Q. Liu, “Aging hardening response and β-Mn transformation behavior of high carbon high manganese austenitic low-density Fe-30Mn-10Al-2C steel,” *Materials Science and Engineering A*, vol. 703, pp. 167–172, Aug. 2017, doi: 10.1016/j.msea.2017.07.055.
[27] J. D. Yoo and K. T. Park, “Microband-induced plasticity in a high Mn-Al-C light steel,” *Materials Science and Engineering A*, vol. 496, no. 1–2, pp. 417–424, Nov. 2008, doi: 10.1016/j.msea.2008.05.042.
[28] D. Hua, H. Li, Z. Wu, H. Mingli, H. Li, and Q. Xin, “Microstructural evolution and deformation behaviors of Fe-Mn-Al-C steels with different stacking fault energies,” *Steel Res Int*, vol. 84, no. 12, pp. 1288–1293, Dec. 2013, doi: 10.1002/srin.201300052.
[29] L. Zhang, R. Song, C. Zhao, and F. Yang, “Work hardening behavior involving the substructural evolution of an austenite-ferrite Fe-Mn-Al-C steel,” *Materials Science and Engineering A*, vol. 640, pp. 225–234, Jul. 2015, doi: 10.1016/j.msea.2015.05.108.
[30] O. Acselrad, J. Dille, L. C. Pereira, and J.-L. Delplancke, “Communications Room-Temperature Cleavage Fracture of FeMnAlC Steels.”
[31] K. T. Luo, R.-W. Kao, and D. Gan, “Letter Low temperature mechanical properties of Fe-28Mn-5Al-1C alloy,” 1992.
[32] C. W. Shao, P. Zhang, R. Liu, Z. J. Zhang, J. C. Pang, and Z. F. Zhang, “Low-cycle and extremely-low-cycle fatigue behaviors of high-Mn austenitic TRIP/TWIP alloys: Property evaluation, damage mechanisms and life prediction,” *Acta Mater*, vol. 103, pp. 781–795, Jan. 2016, doi: 10.1016/j.actamat.2015.11.015.
[33] S. W. Song, Y. J. Kwon, T. Lee, and C. S. Lee, “Effect of Al addition on low-cycle fatigue properties of hydrogen-charged high-Mn TWIP steels,” *Materials Science and Engineering A*, vol. 677, pp. 421–430, Nov. 2016, doi: 10.1016/j.msea.2016.09.082.
[34] B. Kim, S. Jeong, S. J. Park, J. Moon, and C. Lee, “Local brittle cracking in the heat-affected zone of lightweight steels,” *Mater Chem Phys*, vol. 238, Dec. 2019, doi: 10.1016/j.matchemphys.2019.121904.
[35] C. E. Coronado-Alba, I. Mejía, and J. M. Cabrera, “Metallographic, Structural, and Mechanical Characterization of Weld Nuggets in Fe–Mn–Al–C Low-Density Steels Microalloyed with Ti/B and Ce/La by Gas Tungsten Arc Welding Process,” *Steel Res Int*, vol. 92, no. 11, Nov. 2021, doi: 10.1002/srin.202100229.
[36] S. Jeong, G. Park, B. Kim, J. Moon, S. J. Park, and C. Lee, “Heat-Affected Zone Characteristics with Post-Weld Heat Treatments in Austenitic Fe–Mn–Al–C Lightweight Steels,” *Metals and Materials International*, vol. 28, no. 10, pp. 2371–2380, Oct. 2022, doi: 10.1007/s12540-021-01133-0.
[37] M. Tao, L. Huirong, G. Jianxin, and L. Yungang, “Effect of Al Content and Solution Treatment on Tensile and Corrosion Resistance of Fe–Mn–Al–C Low-Density Steel,” *TMS2020*, San Diego, USA, pp. 537–548, Feb. 23, 2020.
[38] V. F. C. Lins, M. A. Freitas, and E. M. Paula e Silva, “Corrosion resistance study of Fe-Mn-Al-C alloys using immersion and potentiostatic tests,” *Appl Surf Sci*, vol. 250, no. 1–4, pp. 124–134, Aug. 2005, doi: 10.1016/j.apsusc.2004.12.040.
[39] P. P. Erez, F. J. P. Erez, C. G. Omez B, and P. Adeva, “Oxidation behaviour of an austenitic Fe±30Mn±5Al±0.5C alloy.” [Online]. Available: www.elsevier.com/locate/corsci
[40] Y. J. Gau and J. K. Wu, “Galvanic corrosion behaviour of F e-M n-A I alloys in sea water,” 1992.

[41] S. C. Tjong, “AQUEOUS CORROSION PROPERTIES OF AUSTENITIC Fe-8.7A1-29.7Mn-1.04C ALLOY,” 1986.
[42] “Standard Test Methods for Vickers Hardness and Knoop Hardness of Metallic Materials 1 Verification of Vickers and Knoop Hardness Testing Machines Annex A1 Vickers and Knoop Hardness Standardizing Machines Annex A2 Standardization of Vickers and Knoop Indenters Annex A3 Standardization of Vickers and Knoop Hardness Test Blocks Annex A4 Correction Factors for Vickers Hardness Tests Made on Spherical and Cylindrical Surfaces Annex A5”, doi: 10.1520/E0092-17.
[43] “Standard Test Method for Plastic Strain Ratio r for Sheet Metal 1 This international standard was developed in accordance with internationally recognized principles on standardization established in the Decision on Principles for the Development of International Standards, Guides and Recommendations issued by the World Trade Organization Technical Barriers to Trade (TBT) Committee”, doi: 10.1520/E0517-19.
[44] “Designation: E8/E8M − 22 Standard Test Methods for Tension Testing of Metallic Materials 1”, doi: 10.1520/E0008_E0008M-22.
[45] “Standard Test Methods and Definitions for Mechanical Testing of Steel Products 1”, doi: 10.1520/A0370-22.
[46] “Standard Specification for Steel, Sheet and Strip, Alloy, Hot-Rolled and Cold-Rolled, General Requirements for”.
[47] W. D. , Jr. Callister, *Material Science and Engineering*, 5ISBN 9780471135760. 2003.
[48] Susanne Page, Reto Maurer, and Arne Gericke, “Physical-Mechanical Properties of Extrudates and Tablets Manufactured thereof,” Basel, Switzerland, 2015. [Online]. Available: http://www.wpi.edu/Academics/Projects.
[49] Marcolongo Andrea, “ANALISI NUMERICA E SPERIMENTALE DEL PROCESSO DI PIEGATURA DI LAMIERA,” *Università degli Studi di Padova*, 2013.
[50] “Standard Test Methods for Bend Testing of Material for Ductility 1”, doi: 10.1520/E0290-22.
[51] “Standard Practice for Conventions Applicable to Electrochemical Measurements in Corrosion Testing 1”, doi: 10.1520/G0003-14R19.
[52] “Standard Reference Test Method for Making Potentiodynamic Anodic Polarization Measurements 1”, doi: 10.1520/G0005-14R21.
[53] F. J. Khusiafan, “Advance High Strength Steels: The Solution in Lightweighting our Future Automobiles,” *International Journal of Current Engineering and Technology*, vol. 8, no. 04, Jul. 2018, doi: 10.14741/ijcet/v.8.4.15.
[54] World Material, “Weight & Density Of Stainless Steel 304, 316, 316L & 303 In Lb/In3, G/Cm3, Lb/Ft3, Kg/M3.”
[55] “Designation: E112 − 13 Standard Test Methods for Determining Average Grain Size 1”, doi: 10.1520/E0112-13R21.
[56] “Standard Test Methods for Characterizing Duplex Grain Sizes 1”, doi: 10.1520/E1181-02R15.
[57] X. F. Zhang, H. Terasaki, and Y. Komizo, “Correlation of delta-ferrite precipitation with austenite grain growth during annealing of steels,” *Philos Mag Lett*, vol. 91, no. 7, pp. 491–497, Jul. 2011, doi: 10.1080/09500839.2011.587464.
[58] T. Oikawa and M. Enomoto, “Pinning Effects on Grain Growth of Ferrite in an Fe-C-B Alloy,” *Journal of the Iron and Steel Institute of Japan*, vol. 97, no. 1, pp. 584–591, 2011.
[59] B. Mishra *et al.*, “Effect of cold rolling and subsequent heat treatment on microstructural evolution and mechanical properties of Fe-Mn-Al-C-(Ni) based austenitic low-density steels,” *Materials Science and Engineering A*, vol. 861, Dec. 2022, doi: 10.1016/j.msea.2022.144324.
[60] G. FARGAS, N. AKDUT, M. ANGLADA, and A. MATEO, “Microstructural Evolution during Industrial Rolling of a Duplex Stainless Steel,” *ISIJ International*, vol. 48, pp. 1596–1602, 2008.
[61] C. Zheng, Q. Liu, S. Zheng, X. Chong, Y. Jiang, and J. Feng, “Effect of solution treatment on mechanical properties and microstructure of welded joints of Fe-29Mn-9Al-0.9c low-density steel,” *J Micromech Mol Phys*, vol. 5, no. 2, Jun. 2020, doi: 10.1142/S242491302050006X.
[62] S. Fajardo, I. Llorente, J. A. Jiménez, J. M. Bastidas, and D. M. Bastidas, “Effect of Mn additions on the corrosion behaviour of TWIP Fe-Mn-Al-Si austenitic steel in chloride solution,” *Corros Sci*, vol. 154, pp. 246–253, Jul. 2019, doi: 10.1016/j.corsci.2019.04.026.
[63] D. B. Lee and I. R. Sohn, “Oxidation of Fe-18%Mn-0.6%C steels in air and a N 2-CO 2-O 2 mixed gas atmosphere at 1273-1473K,” in *Steel Research International*, Apr. 2012, pp. 398–403. doi: 10.1002/srin.201100323.

[64] F. Miyasaka, T. Okuda, and T. Ohji, “Effect of current wave form on AC TIG welding for aluminum alloys,” *Yosetsu Gakkai Ronbunshu/Quarterly Journal of the Japan Welding Society*, vol. 22, no. 3, pp. 364–368, 2004, doi: 10.2207/qjjws.22.364.
[65] Y. Jiang and C. Xie, “Microstructure and mechanical properties of 980MPa grade Fe-Mn-Al-C lightweight steel,” in *IOP Conference Series: Materials Science and Engineering*, Institute of Physics Publishing, Jun. 2017. doi: 10.1088/1757-899X/207/1/012053.
[66] Z. Sun, H. A. Davies, and J. A. Whiteman, “Phasestructure and morphology of rapidly solidified Fe-15Mn-8Ai-2C alloy,” *Metal Science*, vol. 18, no. 9, pp. 459–463, 1984, doi: 10.1179/030634584790419818.
[67] R. H. Larn and J. R. Yang, “The effect of compressive deformation of austenite on the Widmanstätten ferrite transformation in Fe-Mn-Si-C steel,” 1999.
[68] X. Wang and K. H. Spitzer, “High-Temperature Properties of High Mn Steel with Al, Si, and C,” *Steel Res Int*, vol. 93, no. 10, Oct. 2022, doi: 10.1002/srin.202200173.

Appendix A. OES measurements

Wt. %	1	2	3	4	5	6	7	8	9
C	1.013	1.007	1.029	0.901	0.981	1.004	0.973	1.017	1.021
Si	0.021	0.021	0.020	0.021	0.020	0.020	0.020	0.020	0.018
Mn	15.78	15.82	15.69	15.80	15.72	15.19	15.34	15.42	15.02
P	0.0045	0.0044	0.0047	0.0043	0.0047	0.0044	0.0044	0.0044	0.0042
S	0.012	0.012	0.012	0.012	0.012	0.013	0.014	0.012	0.012
Cr	0.052	0.053	0.052	0.052	0.054	0.054	0.054	0.053	0.054
Mo	0.013	0.013	0.012	0.013	0.013	0.013	0.012	0.013	0.011
Ni	0.0074	0.0072	0.0074	0.0075	0.0077	0.0076	0.0076	0.0073	0.0071
Cu	0.0089	0.0088	0.0087	0.0088	0.0091	0.0092	0.0089	0.0089	0.0086
Al	7.633	7.533	7.449	7.597	7.531	7.751	7.638	7.548	7.547
As	0.016	0.016	0.017	0.016	0.017	0.017	0.016	0.016	0.016
B	0.0045	0.0046	0.0049	0.0037	0.0041	0.0044	0.0044	0.0046	0.0047
Bi	0.0064	0.0058	0.0052	0.0060	0.0064	0.0060	0.0063	0.0059	0.0053
Ce	0.0091	0.0074	0.0082	0.0075	0.0078	0.0077	0.0057	0.0056	0.0052
Co	0.0058	0.0056	0.0055	0.0056	0.0056	0.0057	0.0057	0.0058	0.0059
Mg	0.0009	0.0009	0.0009	0.0009	0.0009	0.0010	0.0011	0.0010	0.0009
Nb	0.0057	0.0058	0.0058	0.0056	0.0060	0.0063	0.0063	0.0059	0.0060
Pb	0.169	0.176	0.186	0.187	0.194	0.204	0.194	0.199	0.210
Sb	0.076	0.076	0.076	0.075	0.077	0.076	0.077	0.076	0.077
Sn	0.0046	0.0045	0.0046	0.0047	0.0047	0.0046	0.0046	0.0047	0.0047

Ta	0.216	0.210	0.200	0.205	0.216	0.223	0.218	0.218	0.216
La	0.0062	0.0061	0.0059	0.0058	0.0062	0.0060	0.0054	0.0058	0.0053
Ti	0.0025	0.0023	0.0025	0.0026	0.0024	0.0026	0.0023	0.0025	0.0026
V	0.021	0.021	0.024	0.023	0.024	0.029	0.025	0.026	0.028
W	0.099	0.100	0.106	0.099	0.106	0.106	0.108	0.117	0.120
Zn	0.012	0.013	0.015	0.012	0.014	0.015	0.011	0.014	0.013
Zr	0.0085	0.0082	0.0081	0.0091	0.0082	0.0082	0.0094	0.0080	0.0082
Se	0.050	0.049	0.047	0.051	0.049	0.051	0.054	0.052	0.049
N	0.022	0.025	0.025	0.023	0.022	0.027	0.024	0.018	0.016
Ca	<0.000 10	<0.000 10	<0.000 10	<0.000 10	<0.000 10	<0.000 10	<0.000 10	<0.000 10	<0.000 10
Te	0.066	0.069	0.074	0.069	0.071	0.072	0.071	0.070	0.076
Fe	74.65	74.71	74.90	74.77	74.80	75.07	75.07	75.04	75.43

Table 23: OES measurements

Appendix B. Bending Samples

Rolling direction, 5 mm - RD1G

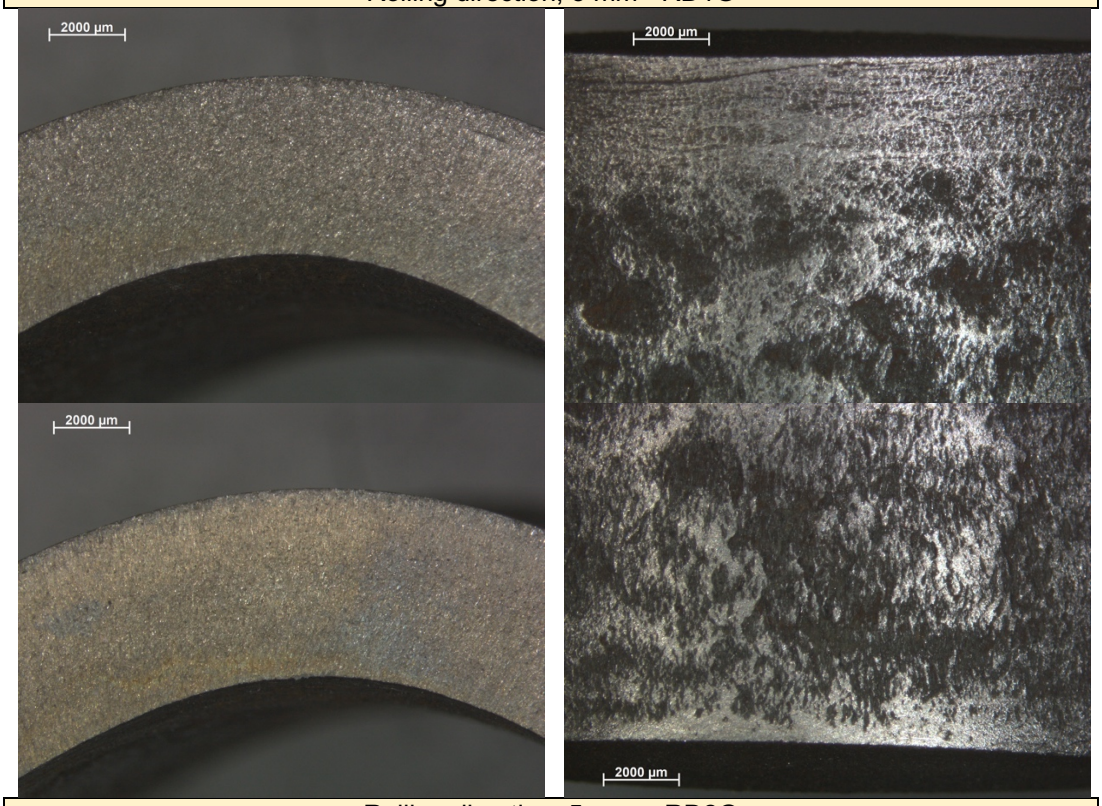

Rolling direction, 5 mm – RD2G

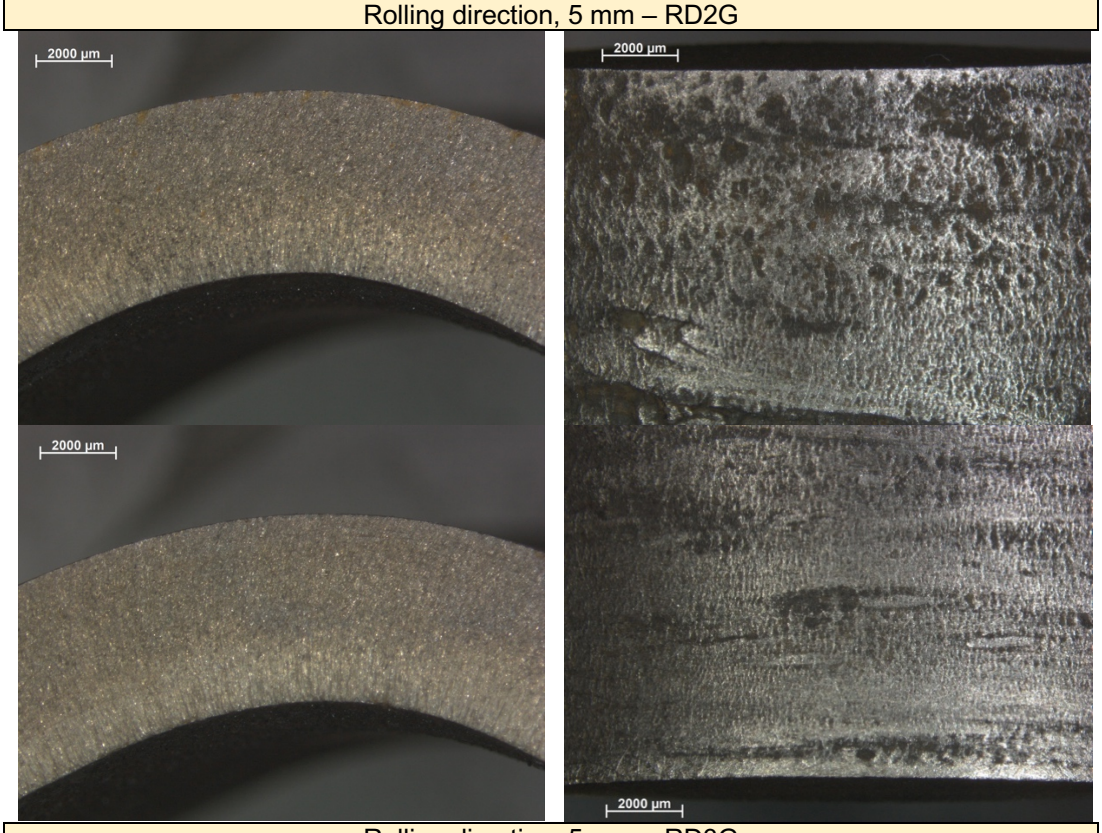

Rolling direction, 5 mm – RD3G

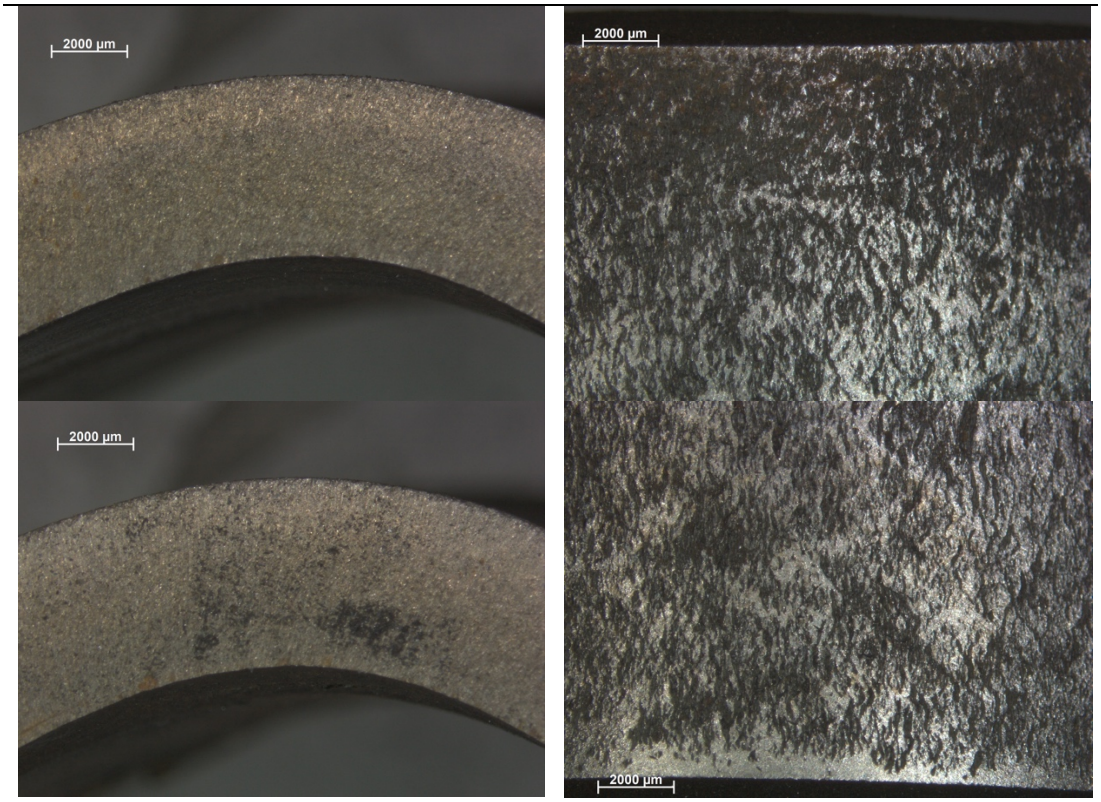

Figure 105: RDG samples after the bending test

Rolling direction, 3 mm - RD1S

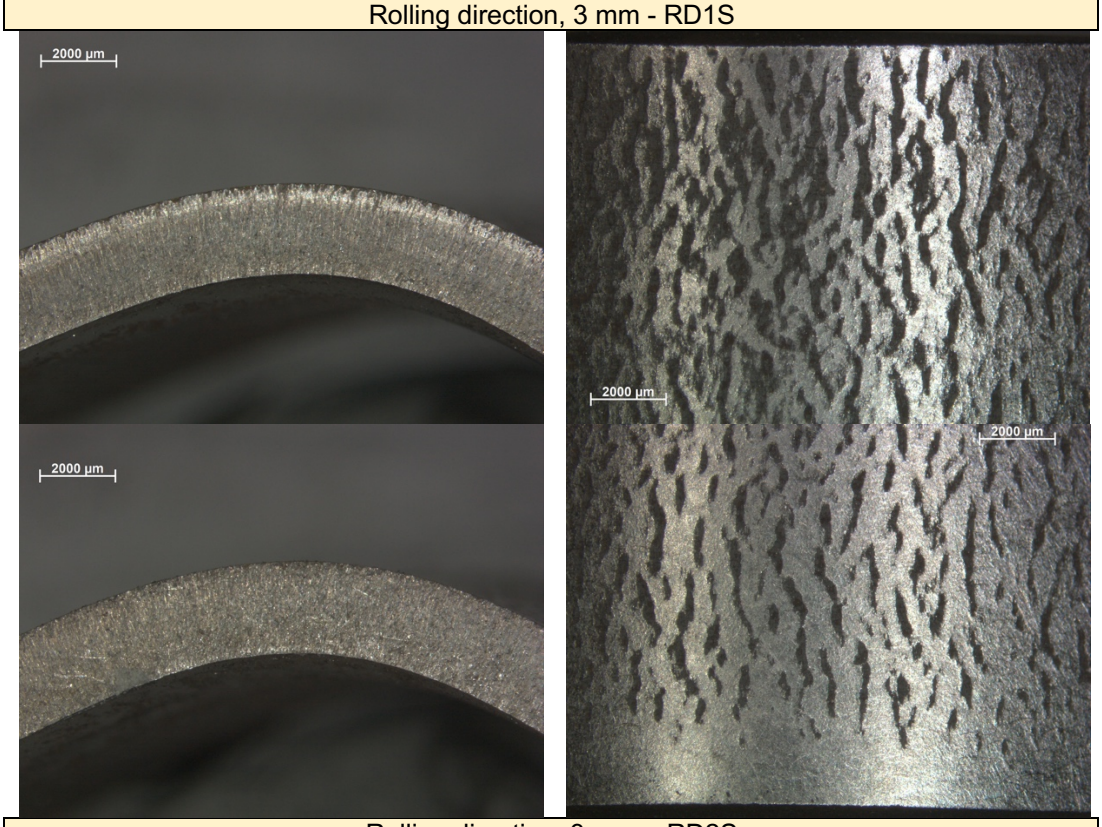

Rolling direction, 3 mm – RD2S

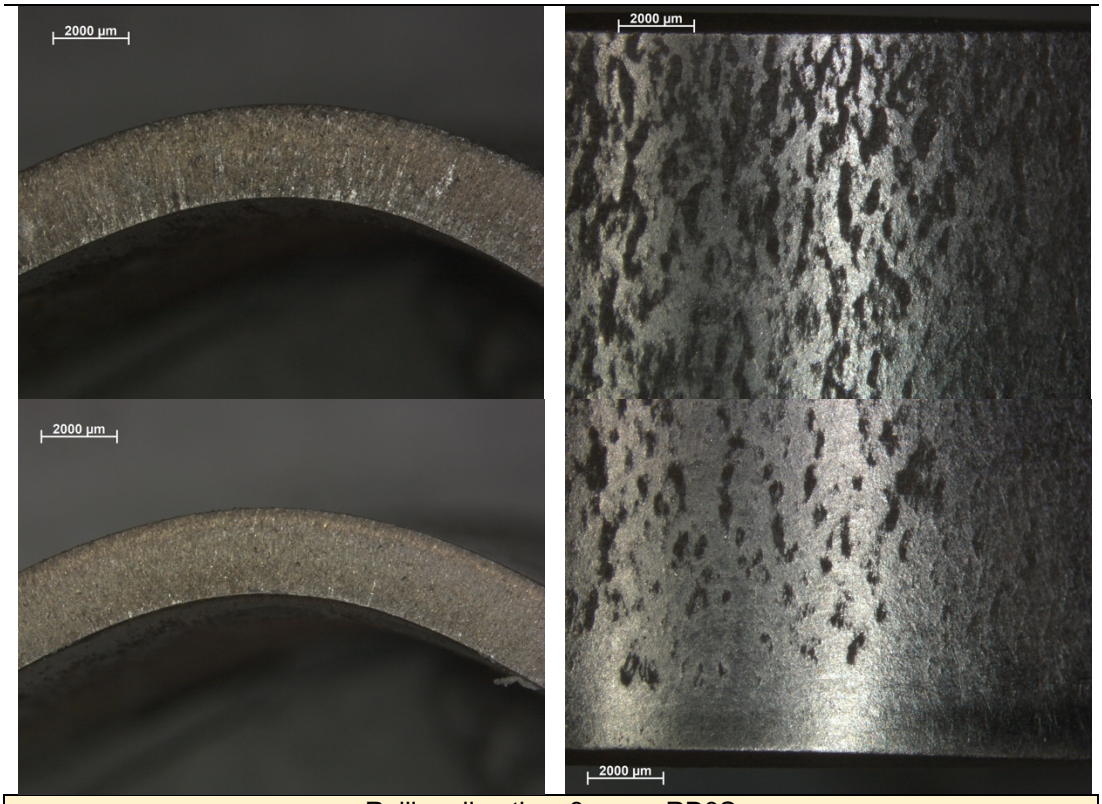

Figure 106: RDS samples after the bending test

Transverse direction, 5 mm – TD1G

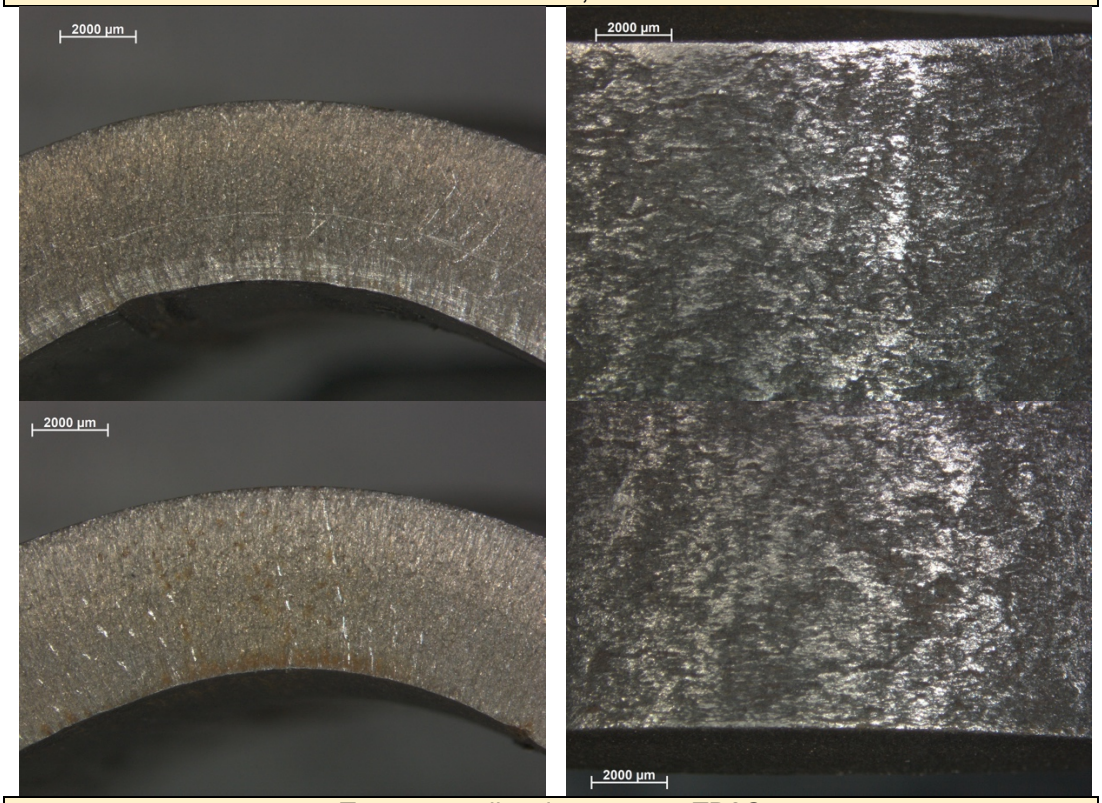

Transverse direction, 5 mm – TD2G

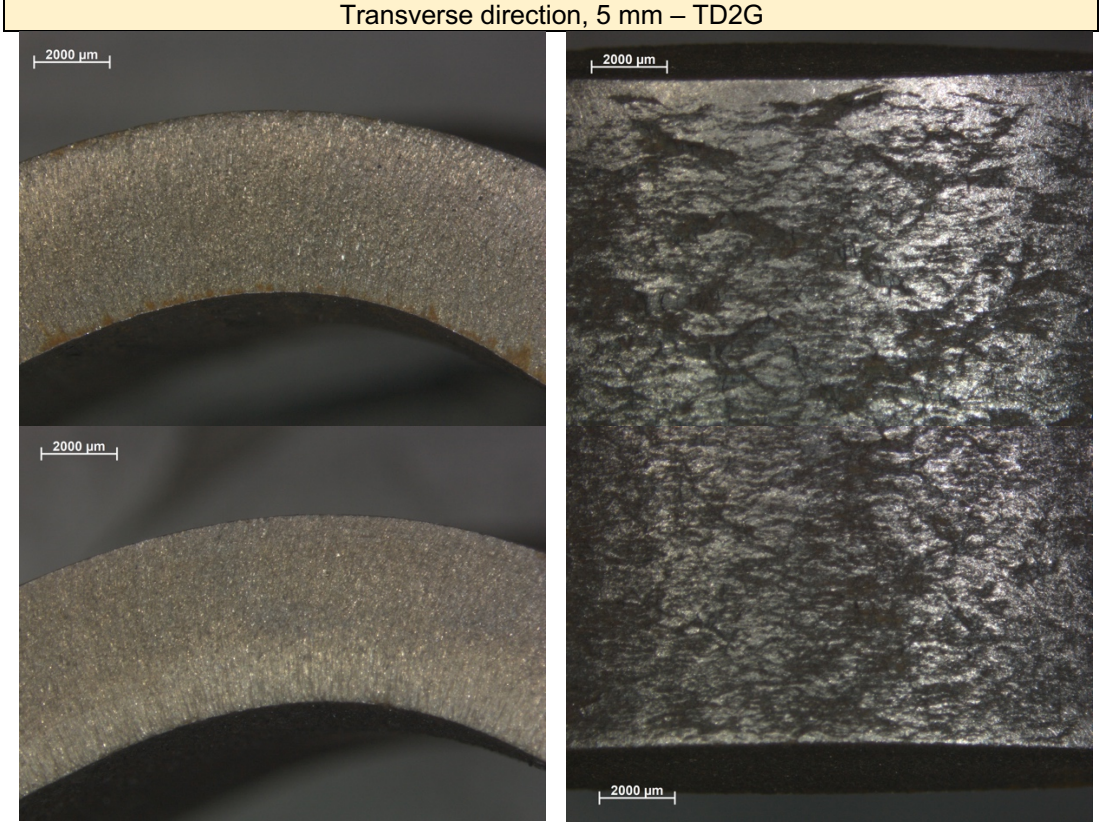

Transverse direction, 5 mm – TD3G

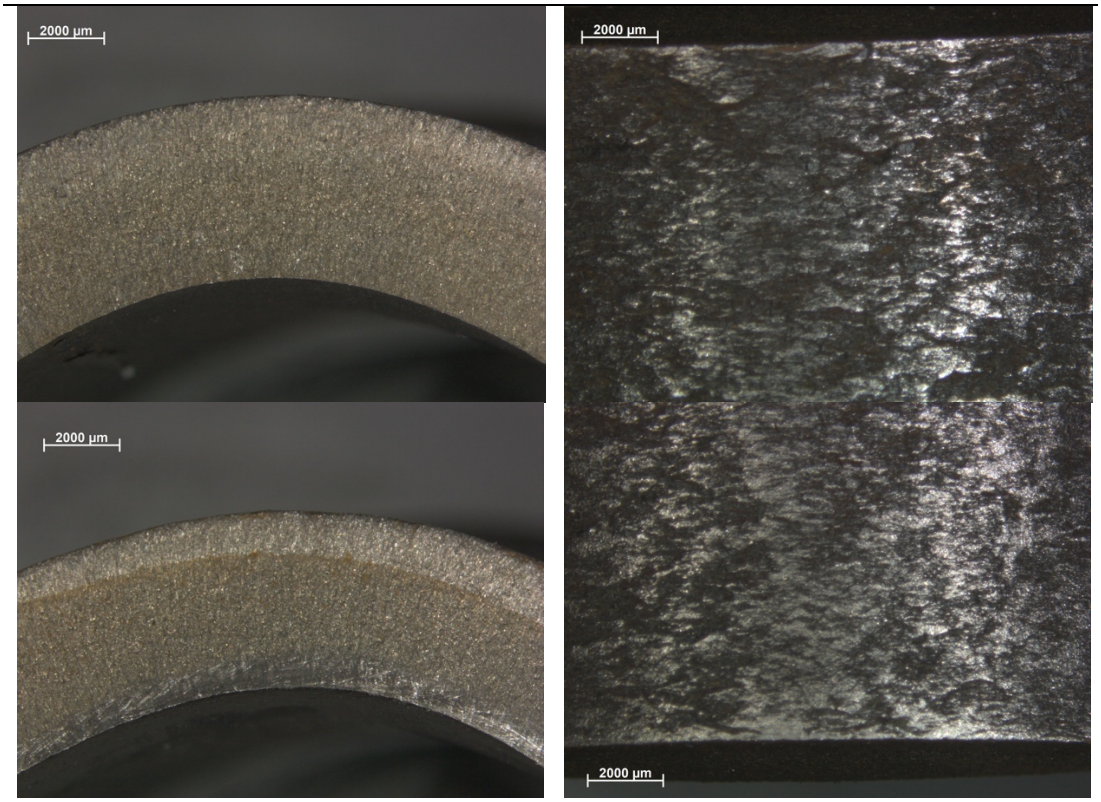

Figure 107: TDG samples after the bending test

Transverse direction, 3 mm – TD1S

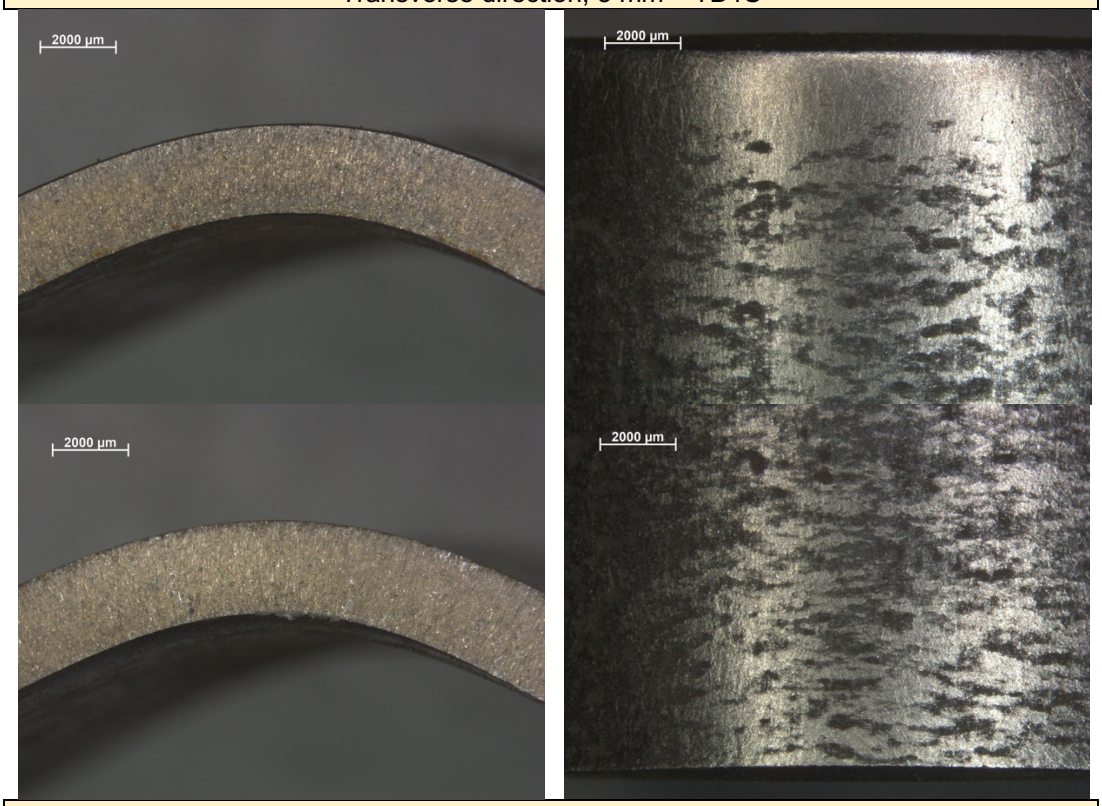

Transverse direction, 3 mm – TD2S

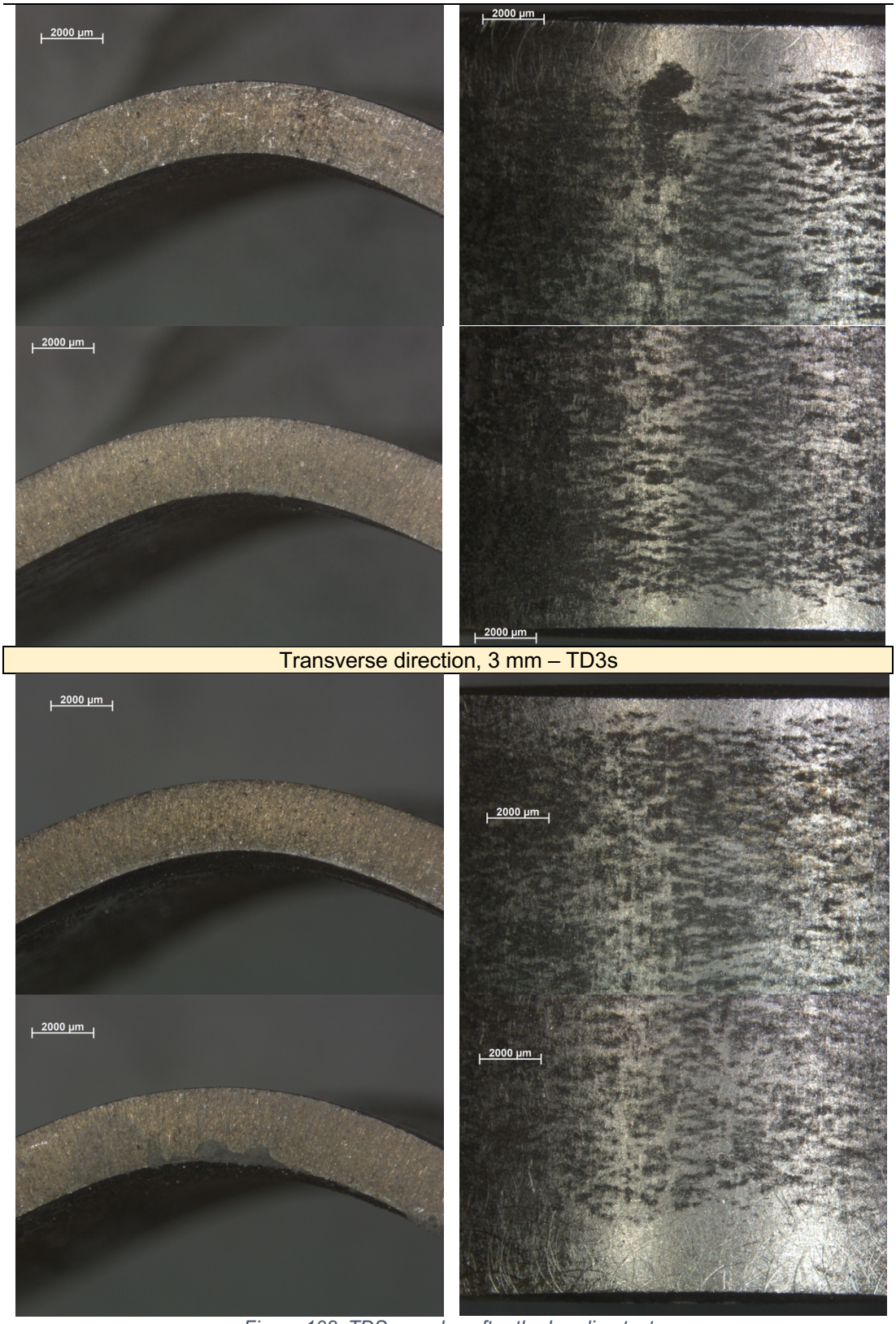

Figure 108: TDS samples after the bending test

Appendix C. Polarization Plots Database

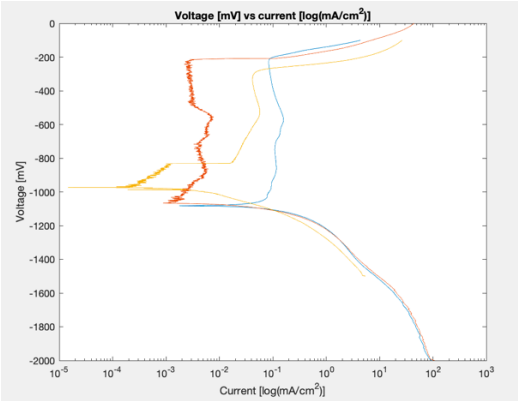

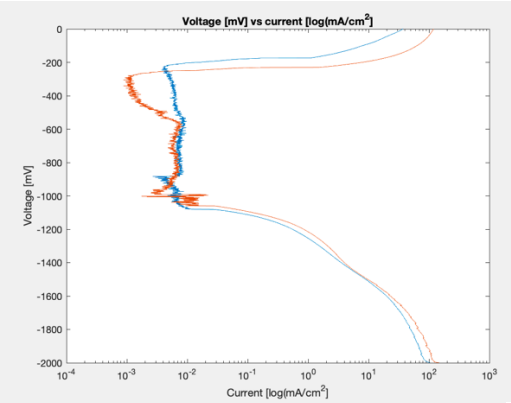

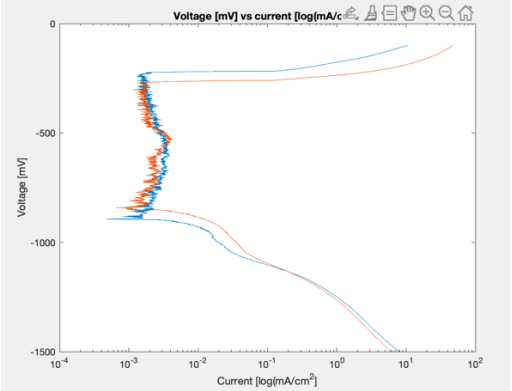

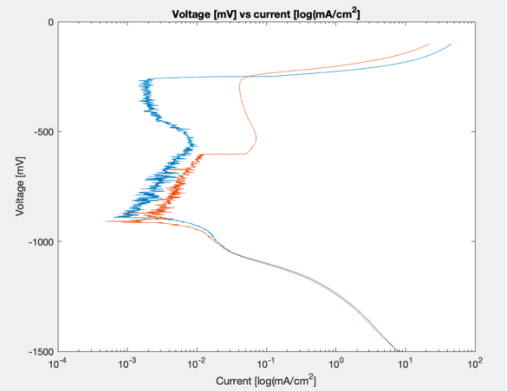

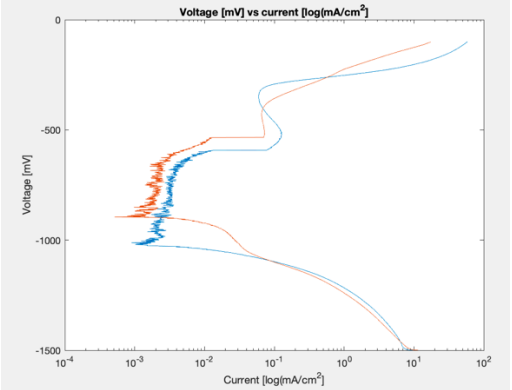

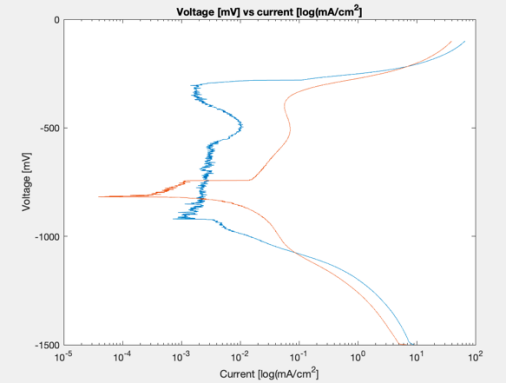

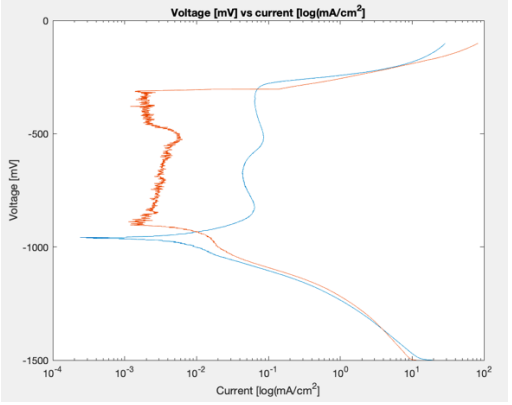

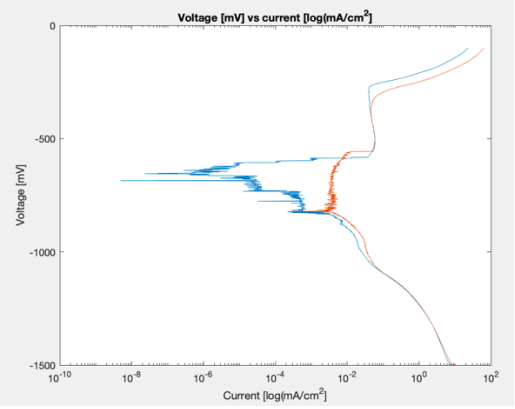

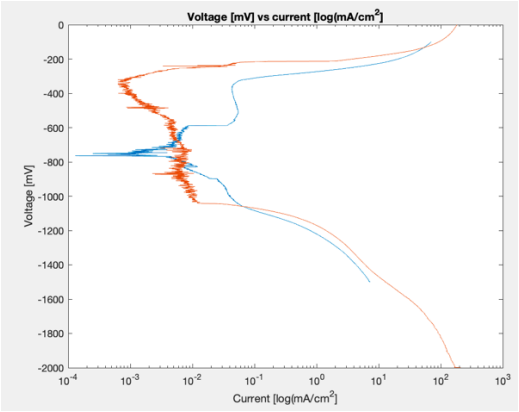

Figure 109: Polarization plots for passive anode. Each Figure represents the tests conducted on a single specimen

Appendix D. OM Database

Hot rolled (HR)		
x50	x100	x200
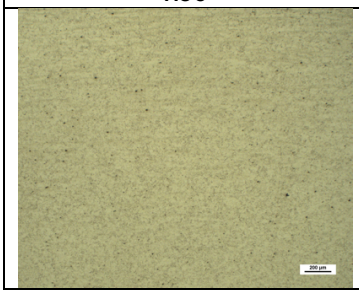	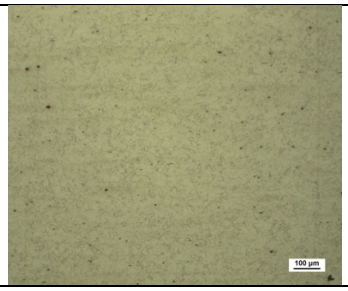	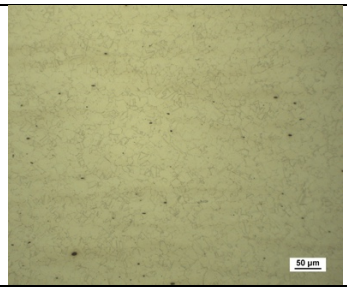

Figure 110: Hot-rolled (HR) microstructure at the optical microscope

Hot rolled – solutioned at 900°C (SHT900)		
x50	x100	x200
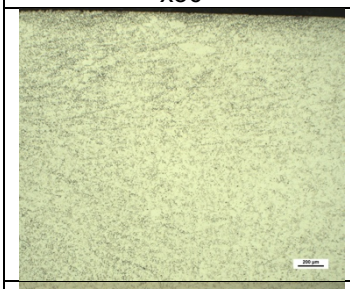	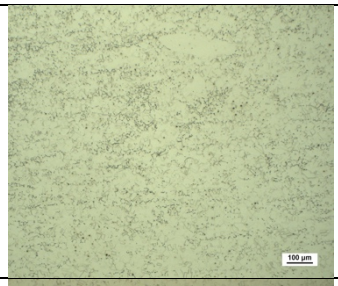	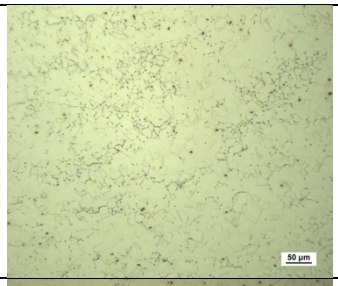
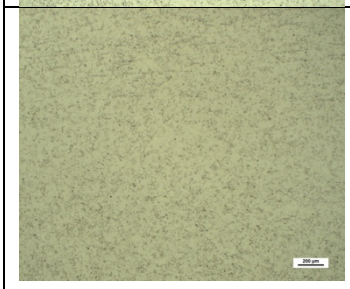	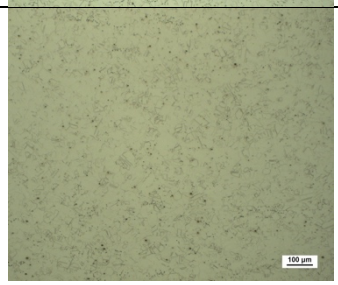	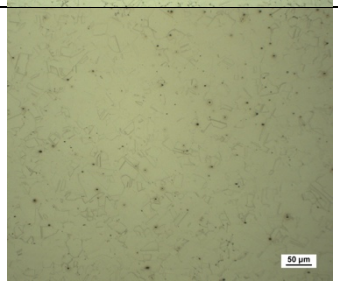

Figure 111: Hot-rolled and solutioned at 900°C (SHT900) microstructure at the optical microscope

Hot rolled – solutioned at 950°C (SHT950)		
x50	x100	x200
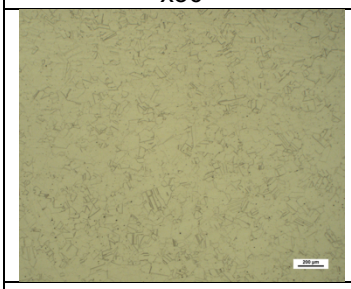	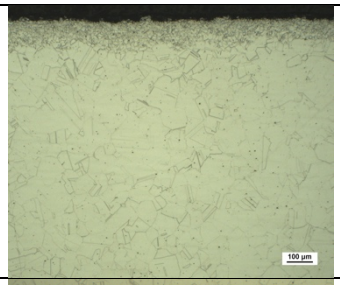	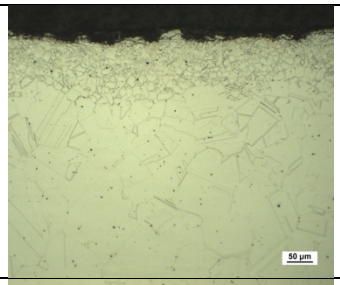
	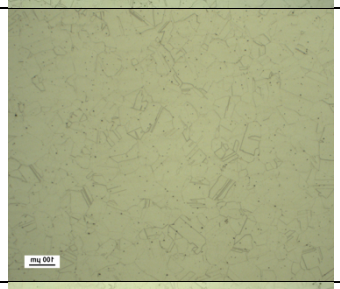	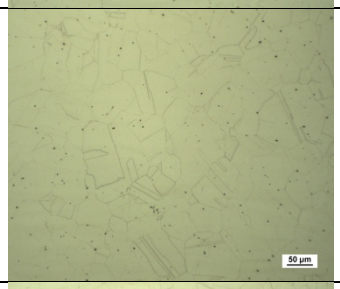
	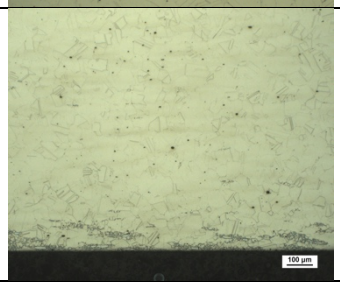	

Figure 112: Hot-rolled and solutioned at 950°C (SHT950) microstructure at the optical microscope

Hot rolled – anisotropy tested (HRTT)		
x50	x100	x200
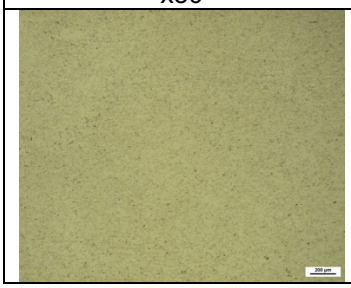	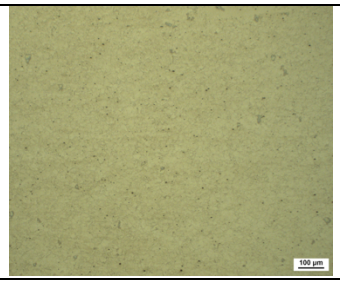	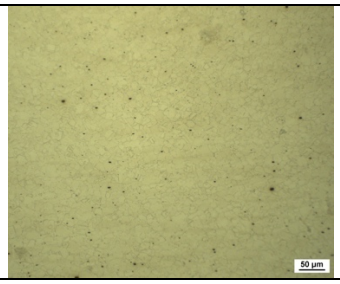

Cold rolled – 2 mm (CR)		
x100	x200	x500
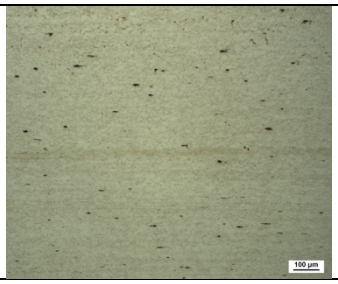	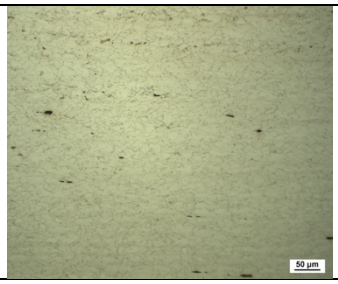	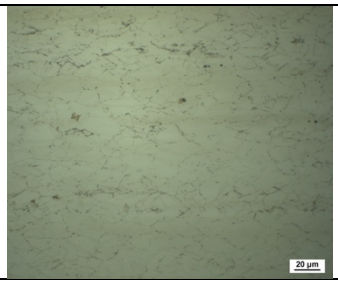

Figure 113: Cold-rolled at 2 mm (CR) microstructure at the optical microscope

Cold rolled – 1 mm (CRE)		
x100	x200	x500
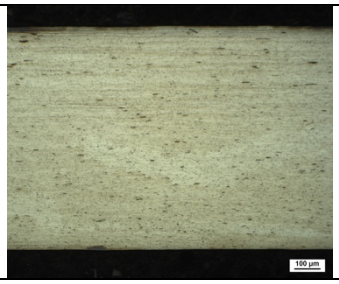	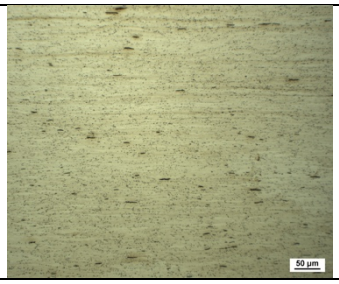	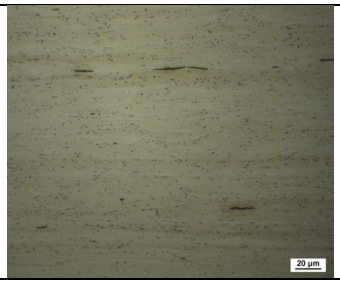

Figure 114: Cold-rolled at 1 mm (CRE) microstructure at the optical microscope

Cold rolled – 1 mm – solutioned at 900°C		
x100	x200	x500
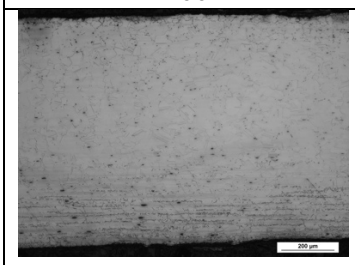	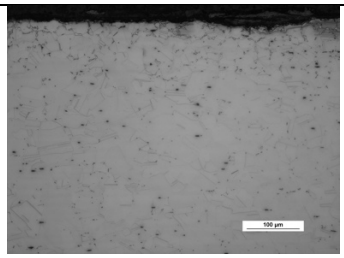	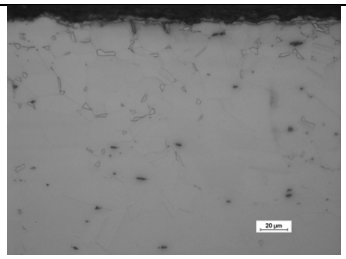
	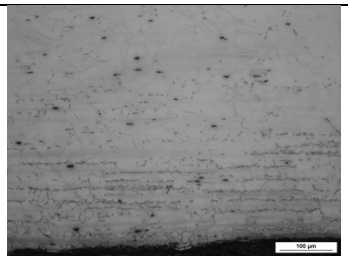	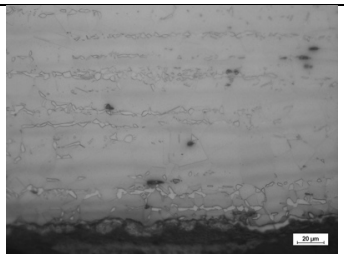

Figure 115: Cold-rolled at 1 mm and solutioned at 900°C microstructure at the optical microscope

Cold rolled – 1 mm – solutioned at 950°C		
x100	x200	x500
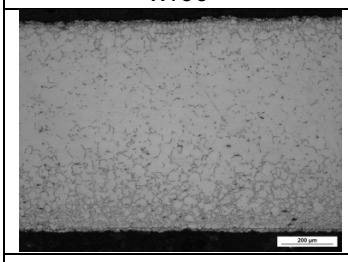	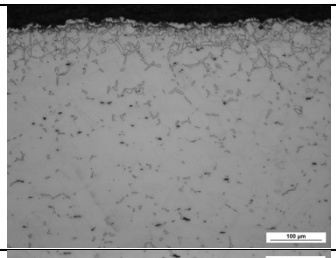	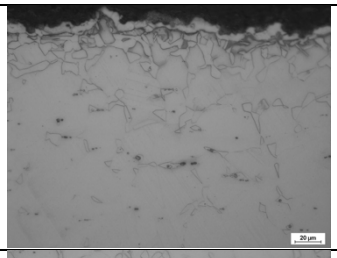
	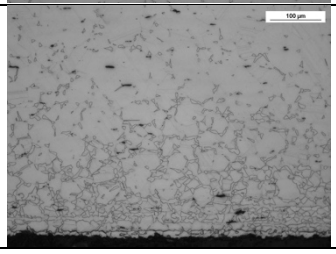	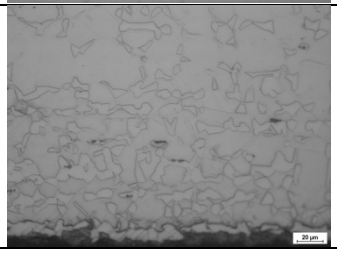

Figure 116: Cold-rolled at 1 mm and solutioned at 950°C microstructure at the optical microscope

Cold rolled – 1 mm – solutioned at 1000°C		
x100	x200	x500
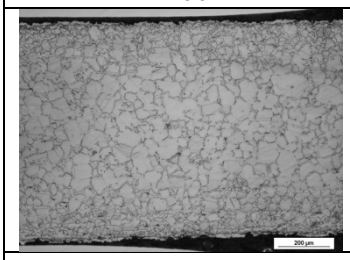	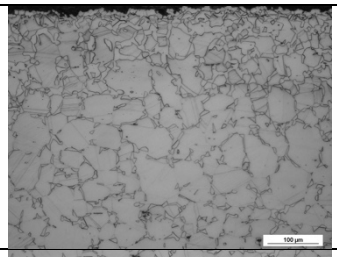	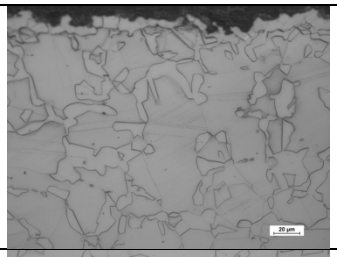
	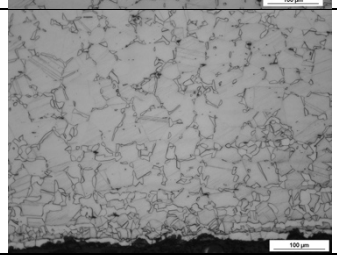	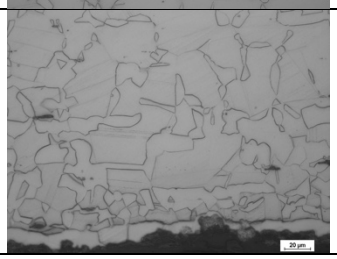

Figure 117: Cold-rolled at 1 mm and solutioned at 1000°C microstructure at the optical microscope

Cold rolled – 1 mm – solutioned at 1050°C	
x100	x200
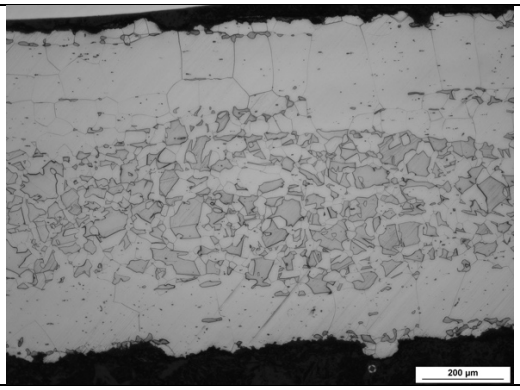	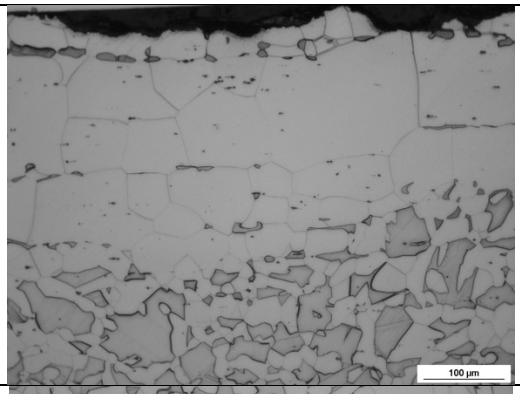
	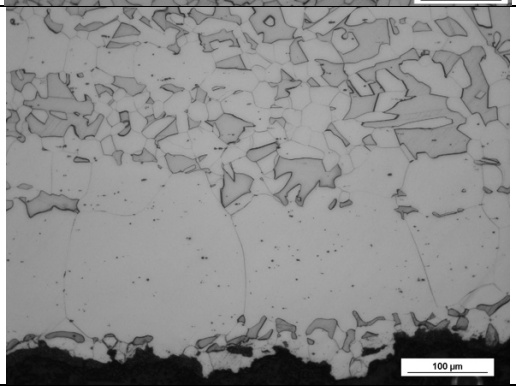

Figure 118: Cold-rolled at 1 mm and solutioned at 1050°C microstructure at the optical microscope

Cold rolled – 1 mm – solutioned at 1100°C	
x100	x200
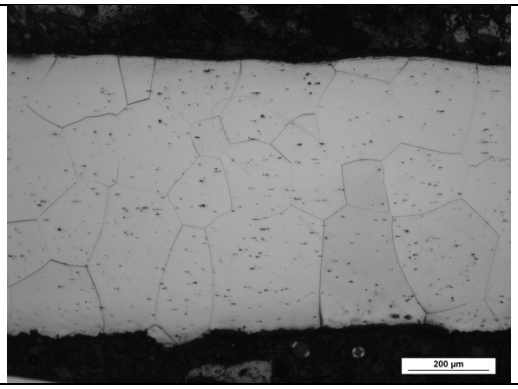	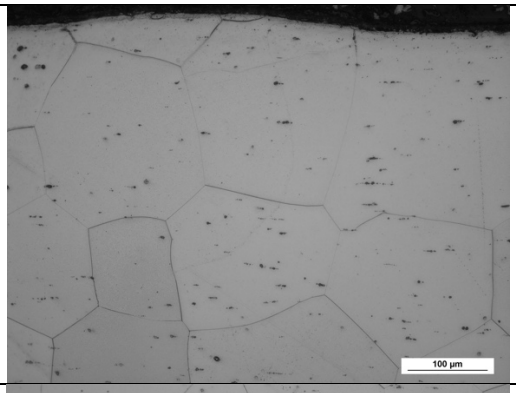
	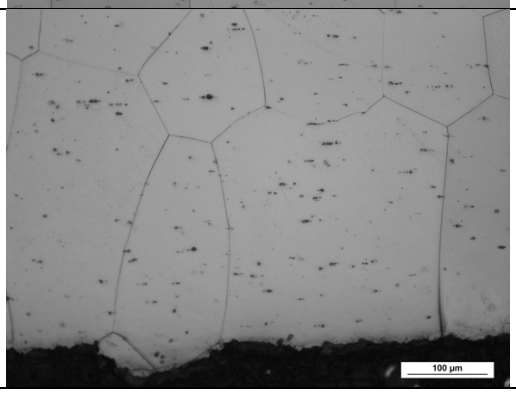

Figure 119: Cold-rolled at 1 mm and solutioned at 1100°C microstructure at the optical microscope

Cold rolled – 1 mm – solutioned at 900°C – 15 minutes		
x100	x200	x500
	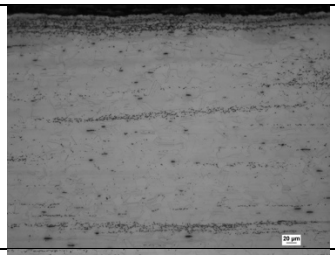	
	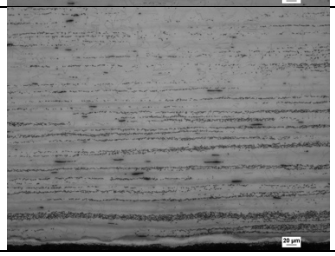	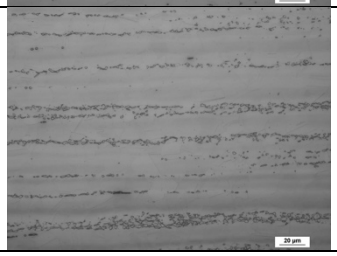

Figure 120: Cold-rolled at 1 mm and solutioned at 900°C for 15 minutes microstructure at the optical microscope

Cold rolled – 1 mm – solutioned at 900°C – 20 minutes		
x100	x200	x500
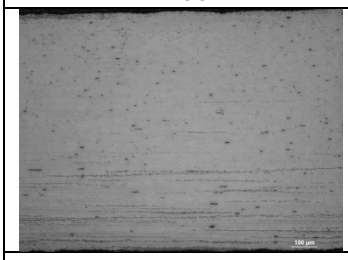	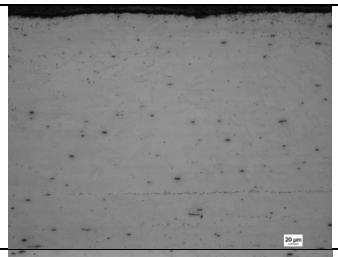	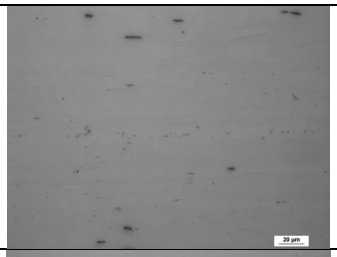
	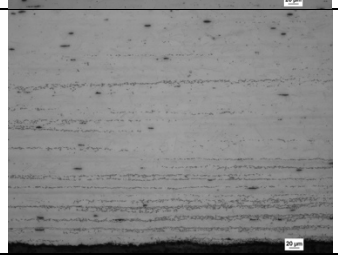	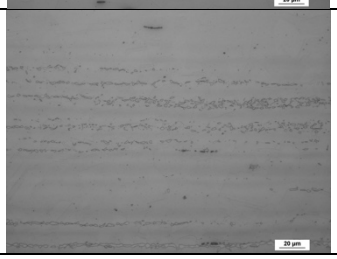

Figure 121: Cold-rolled at 1 mm and solutioned at 900°C for 20 minutes microstructure at the optical microscope

Cold rolled – 1 mm – solutioned at 900°C – 25 minutes		
x100	x200	x500
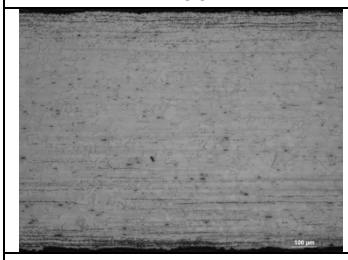		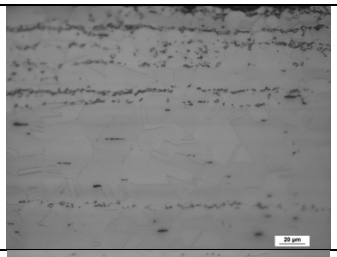
	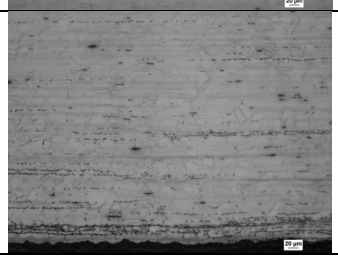	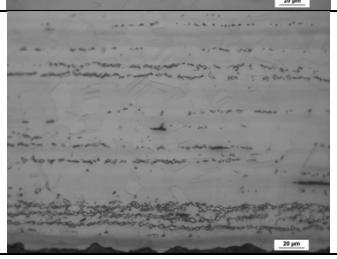

Figure 122: Cold-rolled at 1 mm and solutioned at 900°C for 25 minutes microstructure at the optical microscope

Cold rolled – 1 mm – solutioned at 925°C – 15 minutes		
x100	x200	x500
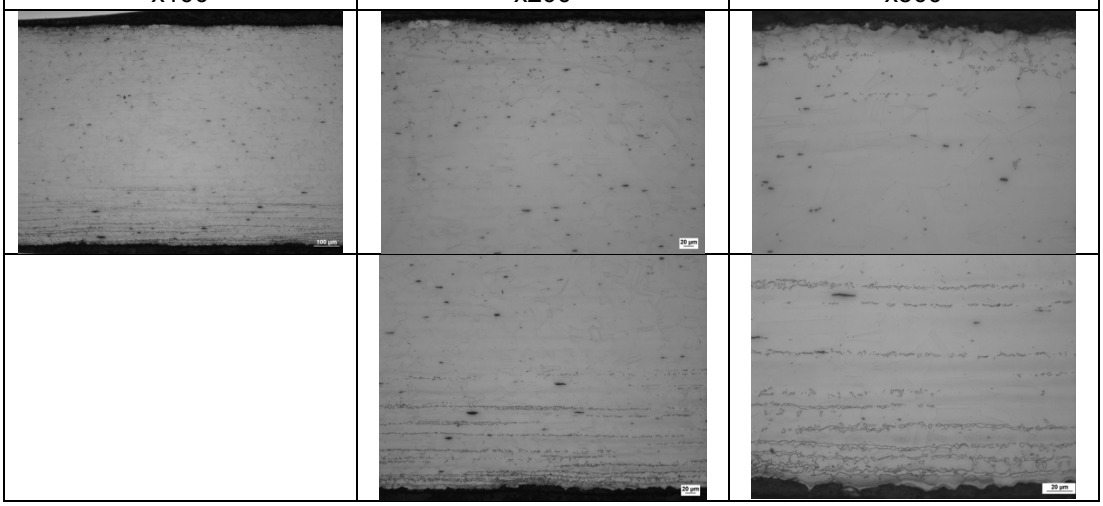		

Figure 123: Cold-rolled at 1 mm and solutioned at 925°C for 15 minutes microstructure at the optical microscope

Cold rolled – 1 mm – solutioned at 925°C – 20 minutes		
x100	x200	x500
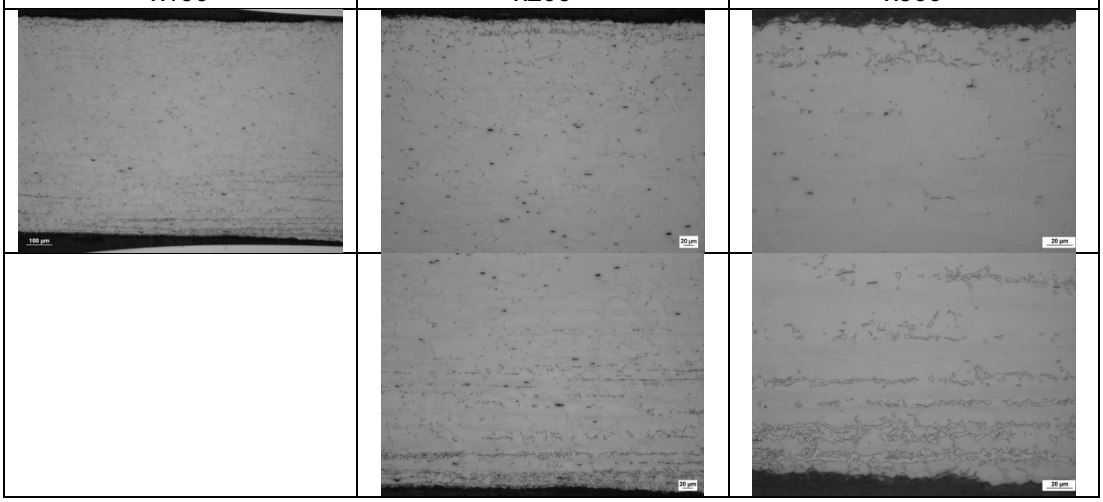		

Figure 124: Cold-rolled at 1 mm and solutioned at 925°C for 15 minutes microstructure at the optical microscope

Cold rolled – 1 mm – solutioned at 925°C – 25 minutes		
x100	x200	x500
	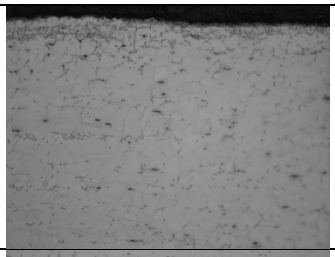	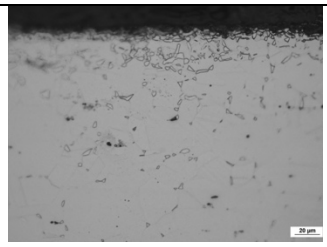
	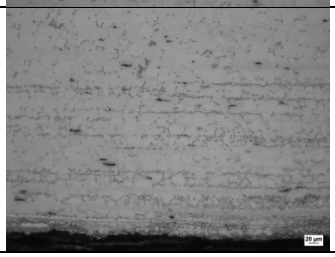	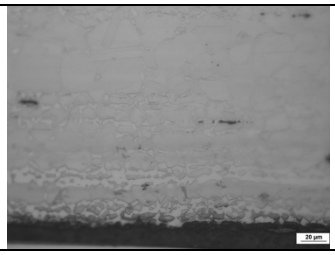

Figure 125: Cold-rolled at 1 mm and solutioned at 925°C for 25 minutes microstructure at the optical microscope

Cladding – DC1		
WZ (x500)	HAZ (x200)	BM (x500)
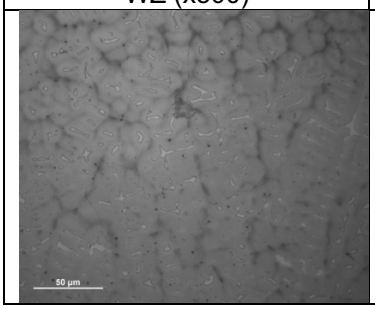	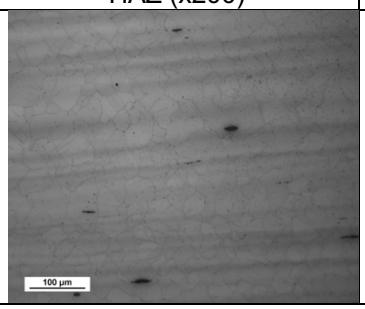	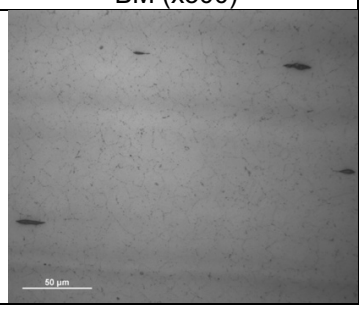

Figure 126: DC1 cladding sample at the optical microscope

Cladding – DC2		
WZ (x500)	HAZ (x200)	BM (x500)
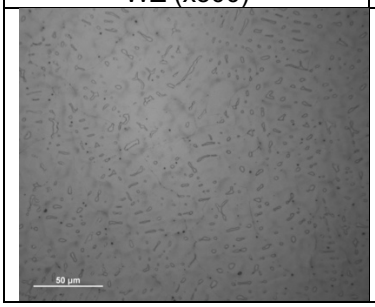	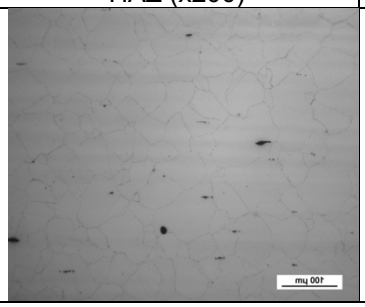	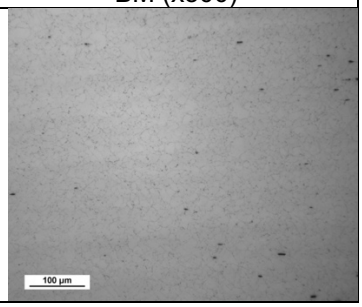

Figure 127: DC2 cladding sample at the optical microscope

Cladding – DC3		
WZ (x500)	HAZ (x200)	BM (x500)
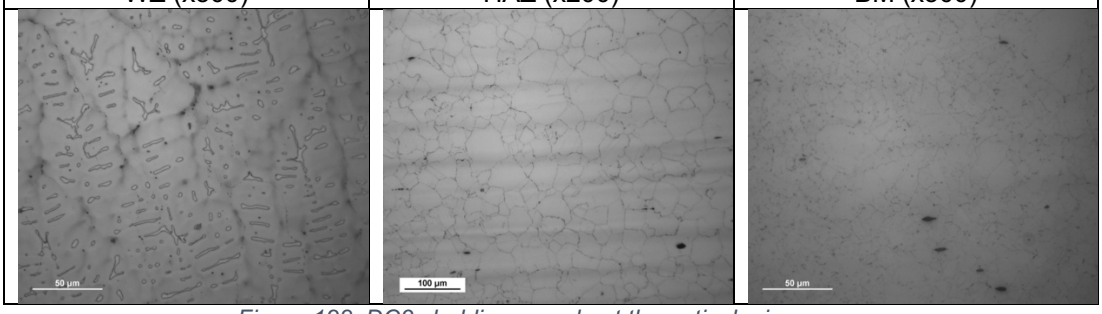		

Figure 128: DC3 cladding sample at the optical microscope

Cladding – DC4		
WZ (x500)	HAZ (x200)	BM (x500)
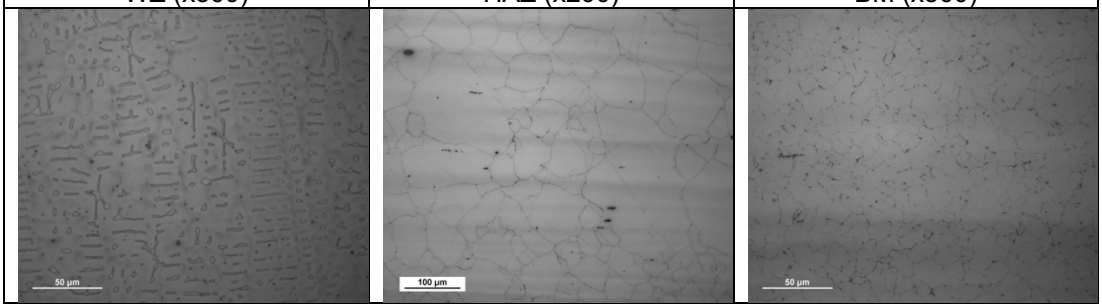		

Figure 129: DC4 cladding sample at the optical microscope

Cladding – AC1		
WZ (x500)	HAZ (x200)	BM (x500)
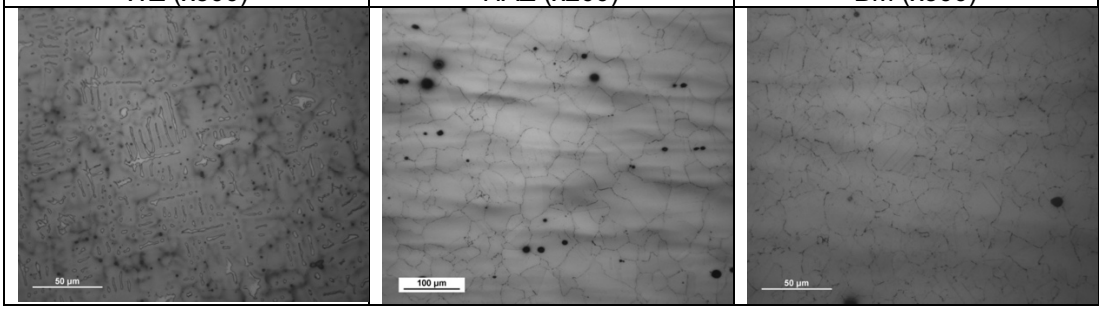		

Figure 130: AC1 cladding sample at the optical microscope

Cladding – AC2		
WZ (x500)	HAZ (x200)	BM (x500)
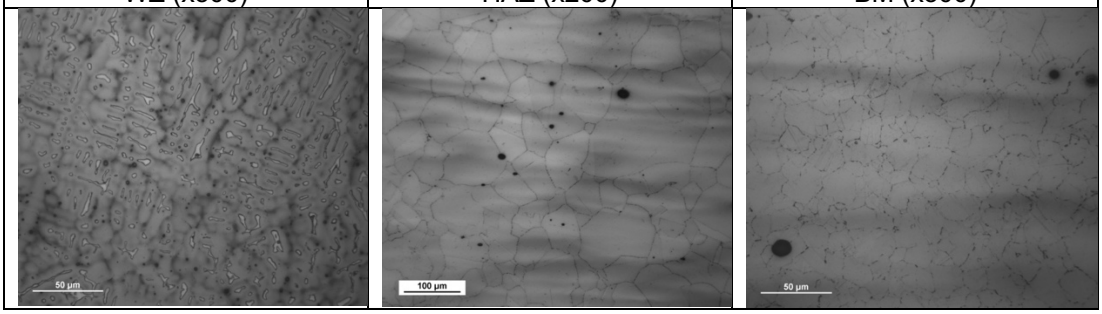		

Figure 131: AC2 cladding sample at the optical microscope

Cladding – AC3		
WZ (x500)	HAZ (x200)	BM (x500)
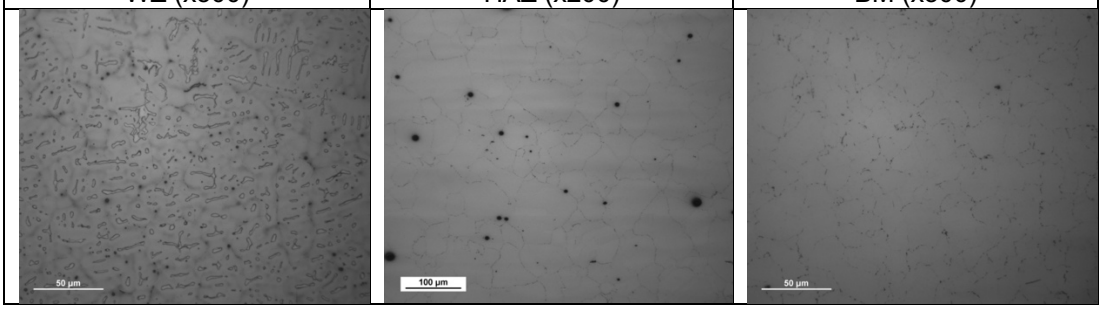		

Figure 132: AC3 cladding sample at the optical microscope

Cladding – AC4		
WZ (x500)	HAZ (x200)	BM (x500)
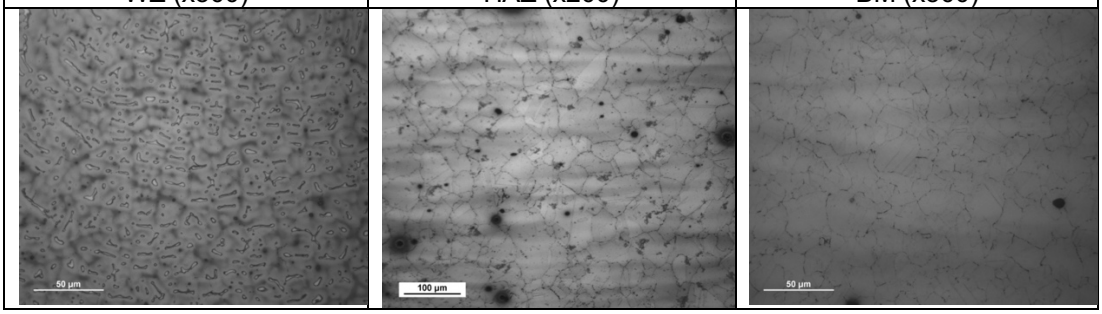		

Figure 133: AC4 cladding sample at the optical microscope

Double-V Butt Weld – DC1		
WZ (x500)	HAZ (x200)	BM (x500)
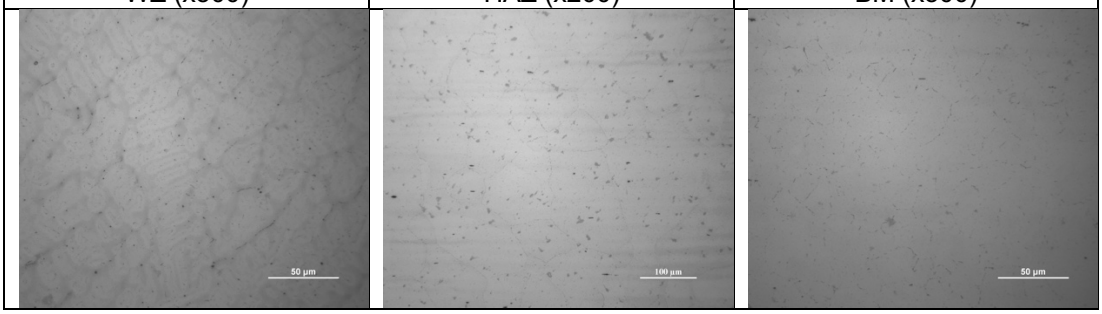		

Figure 134: DC1 Double-V butt weld sample at the optical microscope

Double-V Butt Weld – DC2		
WZ (x500)	HAZ (x200)	BM (x500)
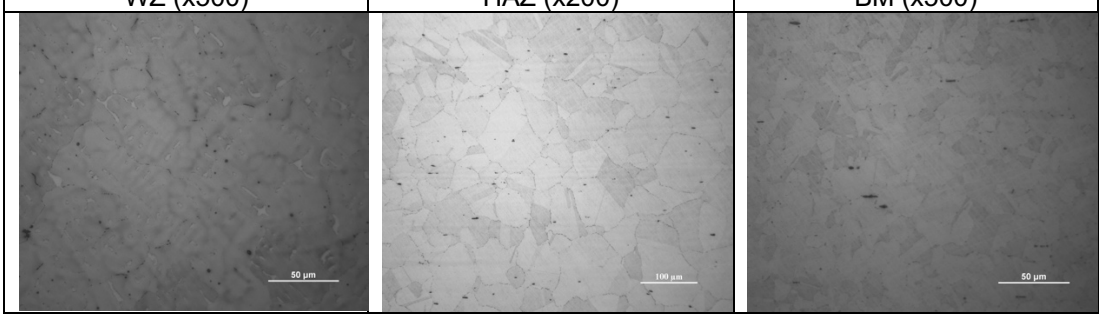		

Figure 135: DC2 Double-V butt weld sample at the optical microscope

Double-V Butt Weld – DC3		
WZ (x500)	HAZ (x200)	BM (x500)
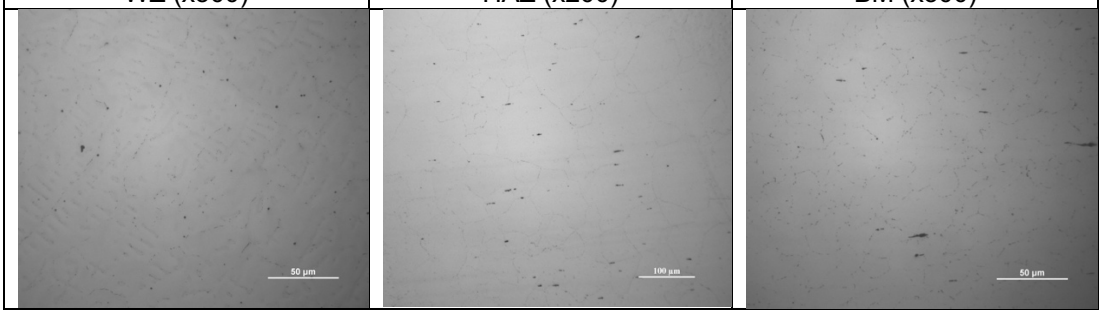		

Figure 136: DC3 Double-V butt weld sample at the optical microscope

Double-V Butt Weld – DC4		
WZ (x500)	HAZ (x200)	BM (x500)
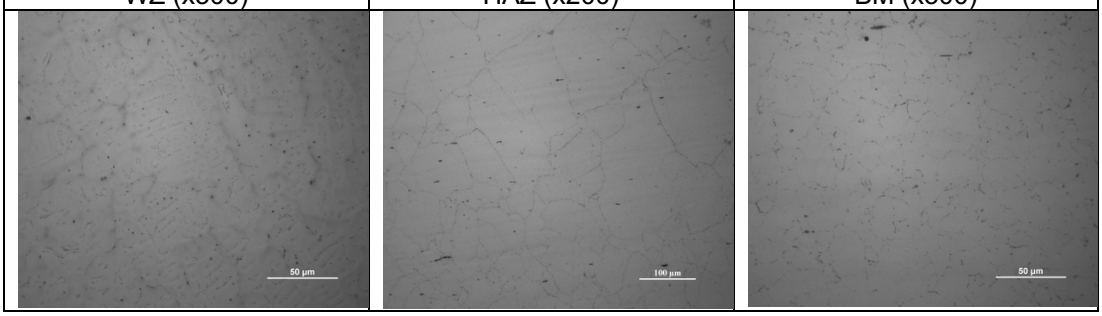		

Figure 137: DC4 Double-V butt weld sample at the optical microscope

Double-V Butt Weld – AC1		
WZ (x500)	HAZ (x200)	BM (x500)
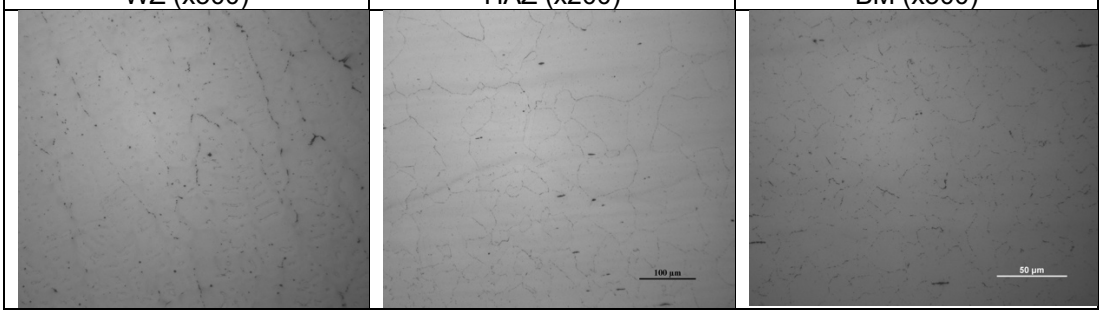		

Figure 138: AC1 Double-V butt weld sample at the optical microscope

Double-V Butt Weld – AC2		
WZ (x500)	HAZ (x200)	BM (x500)
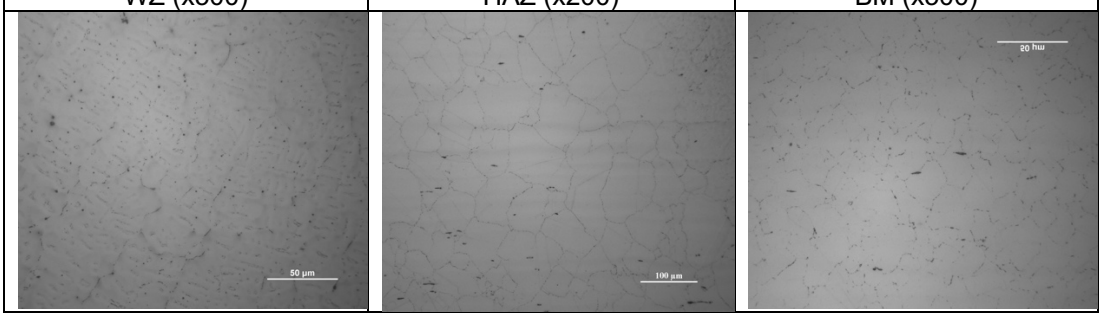		

Figure 139: AC2 Double-V butt weld sample at the optical microscope

Double-V Butt Weld – AC3		
WZ (x500)	HAZ (x200)	BM (x500)
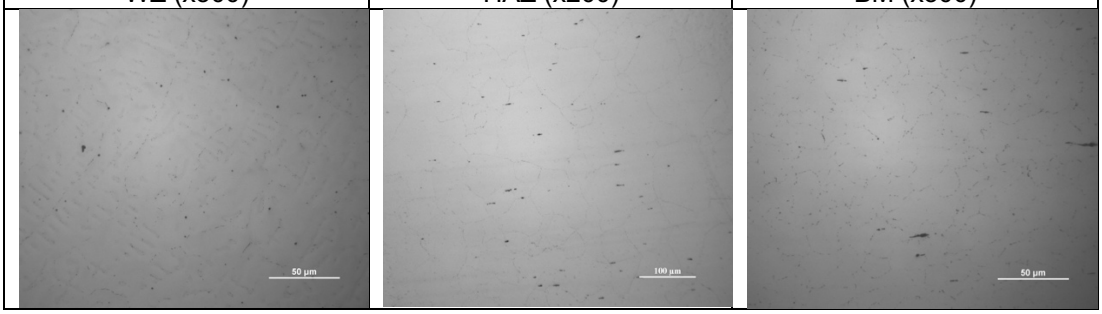		

Figure 140: AC3 Double-V butt weld sample at the optical microscope

Double-V Butt Weld – AC4		
WZ (x500)	HAZ (x200)	BM (x500)
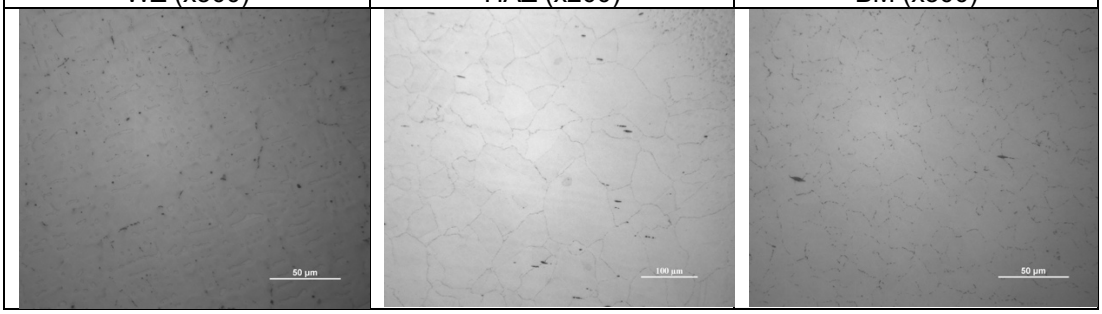		

Figure 141: DC1 Double-V butt weld sample at the optical microscope